GAMMA-RAY

FLOW IMAGING

CAND. SCIENT. THESIS

BY

TORBJØRN FRØYSTEIN

DEPARTMENT OF PHYSICS
UNIVERSITY OF BERGEN
MARCH 1992

Torbjørn Frøystein
Phone: +47 928 199 20
email: tfroystein@gmail.com

Preface

The work described in this thesis was carried out at the Department of Physics, University of Bergen, from August 1988 to March 1992; it is a part of a project concerned with the development of a flow imaging system based on γ-ray attenuation measurements. I wish to thank my supervisor, Professor Erling A. Hammer, for bringing this very interesting problem to my attention. I would also like to thank Cand. Scient. Olav Gaute Hellesø, for laying the groundwork for the project through his feasibility study of the system, and for useful cooperation during the initial part of my work.

Further, I wish to express my gratitude to Dr. Geir A. Johansen, who has been an invaluable source of information on the subject of radiation detectors; Dr. Jan Erik Nordtvedt also deserves special mention, for reading the thesis manuscript and making useful comments and suggestions.

Finally, I would like to thank my friends and fellow students for their continuous supply of encouragement and support during this work.

Bergen, March 1992

Torbjørn Frøystein

Contents

1. Introduction

1.1. Motivation

The problem of accurate measurement of multiphase flow arises in a variety of situations, such as multiphase transport of hydrocarbons, control of thermoelectric power plants and in assorted types of process industry. In many cases, conventional flow meters are unsuitable for multiphase operation, because their response is strongly dependent on the actual flow regime, which generally varies with space and time in a non-stationary manner.

For this reason, it is of great interest to develop techniques for on-line flow imaging, i.e. measurement of the crossectional phase distribution of the flow. This information can be combined with readings from ordinary flow meters to obtain corrected, and hence more accurate flowrate measurements. Alternatively, a flow imaging system might be used on its own for monitoring or design purposes, e.g. in reactor safety and process industry applications.

It is obvious that the different situations in which flow imaging might be used put varying demands to the imaging equipment used. When imaging is used for the correction of readings from standard flowmeters and for process monitoring, an indication of the type of flow regime may be adequate; on the other hand, much better spatial resolution and image precision are required for producing true images of the phase distribution, or for regime independent multiphase fraction measurement.

There is also the question of dynamic response; in some applications, the flowing media may travel at several meters per second and with rapidly changing flow regimes, therefore, a response time in the millisecond range could sometimes be needed. Conversely, in other applications with lower flow velocity and/or near stationary regimes, a response time of several seconds may be acceptable.

Further, it is clearly desirable to have a non-invasive and non-intrusive imaging system, as this ensures maximum integrity of the pipeline, that the instrument is protected from being damaged by the flowing medium, and that the flow is not disturbed or obstructed in any way. Finally, if the instrument can be made as a “clamp-on” design, installation and maintenance will be greatly simplified.

1.2. Previous work

There have been made a few attempts to design systems for flow imaging or regime identification, and a number of different measurement techniques have been proposed; we will describe very briefly the more important:

1.2.1. Ultrasound imaging

At UMIST[1], the possibility of using ultrasound techniques for flow imaging have been investigated [1]. Several ultrasound transducers are positioned around the pipe circumference, and the reflection (echo) generated by a pulsed ultrasound beam is measured. An image of the flow regime section is then reconstructed using a simple backprojection algorithm.

1.2.2. Capacitance techniques

Two-component oil-gas flow regimes can be successfully identified using capacitance methods. Because the dielectric constants of oil and gas are different, the measured capacitance between a pair of electrodes placed on the outside of an insulated pipe section will depend on the relative fractions of the phases between the electrodes. By using several electrodes and measuring the capacitance between all combinations of electrode pairs, a coarse image of the flow can be reconstructed using backprojection. Imaging systems based on capacitance techniques have been investigated at UMIST [2] and at UofB [3]. It should be noted that a capacitance imaging system may become unusable for gas-oil-water or oil-water flows if water is the continuous phase, as this short-circuits the electrodes.

1.2.3. Imaging systems based on radiation absorbtion techniques

The ultrasound and capacitance based systems described above are both capable of very good dynamic response, but the measurement principles used have inherent limitations that preclude the use of the more accurate and efficient image reconstruction methods used in medical X-ray CT[2] (see Chapter 3): The sensitivity for a unit change in the measured parameter is not uniform within the “region of influence” for a measurement (e.g. the region between an electrode pair), and the extent of this region of influence and the sensitivity within it both depend on the phase distribution, or flow regime.

---

[1]University of Manchester, Institute of Science and Technology.

[2]Computerized Tomography.

Such problems are nonexistent or negligible in radiation-based medical imaging; therefore, it seems reasonable to expect X-ray or γ-ray techniques to be suitable for flow imaging as well. The following systems, which are more thoroughly discussed in Chapter 4, represent attempts in this direction:

- A *rotating γ-ray scanner* design for flow imaging has been investigated at the Ohio State University [4][5]; this system offers good spatial and density resolution, as well as reasonable dynamic response; however, the system is rather complex and has moving parts, which is a definite disadvantage.

- The *scattering/transmission* nonmoving system based on γ-ray attenuation measurements has been developed at UMIST [6]: A linear array of photon sources is generated by an external scatterer rod and two γ-sources situated at each end of the rod. The flow cross section is illuminated by the photon field emanating from the scatterer, and two energy-discriminating detectors oppositely positioned measure the average density in several chords through the pipe. This system has no moving parts, but its dynamic response is very poor, due to the use of the external scatterer concept.

- At the Department of Physics, University of Bergen, a project was started in 1987, with the intention of designing a *multisource+multidetector direct transmission γ-ray flow imaging system*. Using this concept, the shortcomings of the systems described above (moving parts, or inferior dynamic response) may be circumvented. The basic principle of γ-ray attenuation density measurement has been tested using a system with one source and one detector, and images of static models of flow regimes have been successfully reconstructed using standard algorithms known from medical CT [7].

1.3. Scope of work

The present work is concerned with the analysis of the latter of the three concepts described above; i.e. a flow imaging system based on the γ-ray attenuation technique, utilizing several fixed γ-sources and detectors. The geometrical problem of the source positioning will be considered in Chapter 4, where we will also investigate the image errors arising from reconstruction algorithm related factors. In Chapter 5, we describe the principle and the accuracy of the density measurements on which the image reconstruction is based. Finally, in Chapter 6 we will discuss how reconstruction error and measurement uncertainty together determine the overall precision of the image.

However, before attacking these tasks, it is necessary to establish some general γ-ray theory (Chapter 2), and discuss the basic principles of CT (Chapter 3).

2. Basics of γ rays: Transport theory, detection and application to densitometry

2.1. Introduction

In this chapter we will discuss how γ rays interact with matter and what methods which may be used for γ-ray transport calculations. We will also consider the subject of γ-ray detection, and how γ rays can be used for density measurement.

2.2. Definitions

Gamma rays are electromagnetic radiation resulting from *nuclear* processes, with frequency higher than approximately 10^{18} Hz (or wavelength shorter than $300 \cdot 10^{-12}$ m), propagating in free space with the velocity of light. The term X rays is also frequently used more or less interchangeably with "gamma rays" to denote *any* electromagnetic radiation with frequency higher than that of ultraviolet light (>10^{15} Hz), although "X rays" are normally used of electromagnetic radiation resulting from an *atomic* process.

The behaviour of electromagnetic radiation of frequency lower than that of infrared light is exactly described by classical electrodynamics; that is, it is treated as a wave phenomenon. However, this classical theory fails to explain emission, propagation and absorption of radiation in the X- and γ-ray range, and a quantum mechanical approach is needed. Quantum electrodynamics describes the radiation as a beam consisting of energy quanta called photons, each having an energy E, which is related to the frequency ν and wavelength λ by

$$E = h\nu = \frac{hc}{\lambda} \tag{2.1}$$

where E is the energy of the photon, h is Planck´s constant, c is the velocity of light in vacuum and where $c = \lambda\nu$. When the frequency is equal to or higher than that of visible light, it is indeed possible to measure the effect of individual photons; this demonstrates the corpuscular behaviour of electromagnetic radiation in this range.

At this point, we may add a few comments on our use of units: It is customary to express the energy E in electron volts when dealing with radiation in this energy range; alternatively, one can express the energy in units of the electron rest mass energy (i.e. in multiples of mc^2, equal to 0.511 MeV). We shall use E to denote energy in eV units, and k to denote energy in mc^2

units. Furthermore, we shall sometimes (when dealing with X or γ rays) express wavelengths in *Compton units*; that is, $\lambda = 1/k = 0.511/E$[MeV].

We have already mentioned that the origin of γ rays is nuclear processes. The α- or β- decay of an unstable isotope may be followed by emission of γ rays; normally, β-isotopes are used as sources of γ rays because of higher emission intensity and easier production. The γ rays emitted from isotopes have an energy spectrum composed of one or more lines, with photon energies ranging from a few keV to a few MeV. Because of this, we shall restrict our discussion of photon interaction with matter to the energy range of 1 keV to 10 MeV.

2.3. Attenuation processes and secondary effects

2.3.1. Cross sections and linear attenuation coefficients

When a photon propagates through matter, it may interact with the individual atoms of a material through several processes, some of which causes the outright absorption of the photon, and others which changes its direction of travel. We may define the *cross section* σ as the probability that a photon will undergo an interaction with an absorber (material) containing one atom per square centimetre. The cross section has the dimension of area and its unit is the barn (b); one barn equals 10^{-24} cm^2.

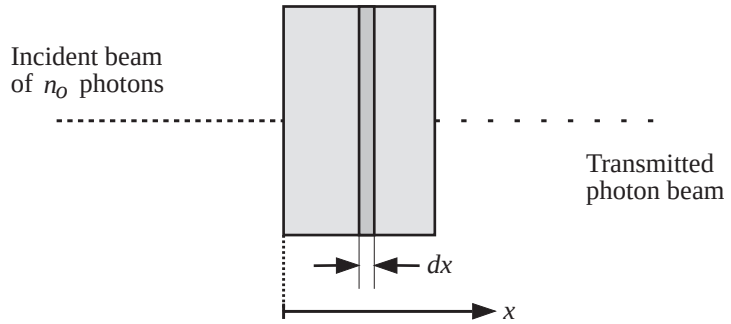

Figure 2.1 Geometry used for derivation of the attenuation formula for a narrow, monoenergetic photon beam incident on a slab of a homogeneous material.

Let us now consider the situation in which a narrow beam of monoenergetic photons is incident on a slab of homogeneous material (Figure 2.1), which is assumed to consist of a single element. In a slice of thickness *dx* and at depth *x* and within the slab, *dn* photons will be removed from the beam by absorption or scattering. The number of photons removed, *dn*, is proportional to the number of incident photons, *n*, and the slice thickness *dx*; the proportionality factor is the total photon interaction probability, which is equal to the total interaction cross section σ_{tot} times the number of atoms per cubic centimetre, *N*:

$$-dn = n\sigma_{tot}Ndx \tag{2.2}$$

which may be written

$$\begin{aligned} -dn &= n\mu_{tot}dx \\ \mu_{tot} &= \sigma_{tot}N \end{aligned} \tag{2.3}$$

The quantity μ_{tot} is called the total *linear attenuation coefficient* and may be defined as the probability per unit pathlength that a photon will interact with the absorber. It has the unit of inverse length (usually the pathlength is expressed in centimeters; hence, the unit of the linear attenuation coefficient is [cm^{-1}]). Since the total cross section σ_{tot} depends in a complex manner on the photon energy E and the atomic number Z of the medium, so does the linear attenuation coefficient. It does not, however, depend on the position in the medium where the interaction takes place, because the atoms contribute independently to the total cross section, and eq 2.3 can be solved by simple integration. The equation for the number of photons transmitted through position x is then

$$n(x) = n_0 e^{-\mu_{tot}x} \tag{2.4}$$

where n_0 is the number of photons incident on the slab. If the medium is inhomogeneous, however, the value of the attenuation coefficient will depend on the position in the medium, and in this case the number of transmitted photons is:

$$n(x) = n_0 \exp\left\{-\int_0^x \mu_{tot}(x')dx'\right\} \tag{2.5}$$

2.3.2. The mass attenuation coefficient

From eq 2.3 we know that μ_{tot} is proportional to the number of atoms per cubic centimetre, N; this is given by

$$N = \rho\frac{N_A}{M} \tag{2.6}$$

where ρ is the density of the medium, M is its atomic mole weight and N_A is Avogadro's number, which is equal to $6.02252 \cdot 10^{23}$.

The linear attenuation coefficient may then be written as

$$\mu_{tot} = \sigma_{tot}\rho\frac{N_A}{M} \tag{2.7}$$

Because the linear attenuation coefficient depends on the density of the absorber, and therefore to some degree on its physical state , it is customary to use the so-called *mass attenuation*

coefficient, $(\mu/\rho)_{tot}$, when tabulating attenuation coefficients. The mass attenuation coefficient is defined as

$$(\frac{\mu}{\rho})_{tot} = \sigma_{tot}\frac{N_A}{M} \tag{2.8}$$

and is usually expressed in units of [$cm^2 \cdot g^{-1}$].

2.3.3. Attenuation coefficients for chemical compounds and mixtures

When the linear and mass attenuation coefficients were defined in the preceding section, it was assumed for simplicity that the medium consisted of atoms of a single element. In practice, we will also encounter absorbers which are homogeneous mixtures or chemical compounds, and we will now develop approximate formulas for finding the attenuation coefficients in such cases; our derivation is partly based on [8, pp. 40-42 and 193-194] and [9, p. 7].

Equation 2.3 states that the linear attenuation coefficient for a single-element medium is equal to the product of the cross section and the number of atoms/cm^3, which means that the individual atoms contribute independently to the total interaction probability. But this is also true when the medium consist of more than one element, and we may write the following expression for the attenuation coefficient of the "mixture":

$$\mu_{mix} = \sum_{\forall i} N_i \sigma_i \tag{2.9}$$

where N_i is the number of atoms of element i , σ_i is the corresponding cross section and the summation is done over all elements in the "mixture". To find the N_i, we note that the total number of *molecules* per cubic centimetre, N_m, is equal to

$$N_m = \rho_{mix}\frac{N_A}{M_{mol}} \tag{2.10}$$

where M_{mol} is the molecular mole weight :

$$M_{mol} = \sum_{\forall i} M_i x_i \tag{2.11}$$

Here the M_i's are the atomic weights for the individual elements, and the x_i's are the number of atoms of element i in the molecule. Obviously, the number of atoms/cm^3 of element i , N_i, is equal to the number of molecules/cm^3, N_m times the number of atoms x_i of element i per molecule:

$$N_i = N_m x_i$$
$$= \rho_{mix} \frac{N_A}{M_{mol}} x_i \tag{2.12}$$

We may now combine the above expressions to obtain the following formula for the calculation of the linear attenuation coefficient for a chemical compund from the interaction cross sections of its constituents:

$$\mu_{mix} = \rho_{mix} \frac{N_A}{M_{mol}} \sum_{\forall i} x_i \sigma_i$$
$$= \rho_{mix} N_A \frac{\sum_{\forall i} x_i \sigma_i}{\sum_{\forall i} M_i x_i} \tag{2.13}$$

For each element, we may write

$$\mu_i = \frac{N_A \rho_i \sigma_i}{M_i} \Leftrightarrow \sigma_i = \frac{M_i \mu_i}{N_A \rho_i} \tag{2.14}$$

where ρ_i is the density of element i when appearing on its own. Substituting this in eq 2.13, we find the following expression for the "mixture" mass attenuation coefficient:

$$\left(\frac{\mu}{\rho}\right)_{mix} = \frac{\sum_{\forall i} \left(\frac{\mu}{\rho}\right)_i M_i x_i}{\sum_{\forall i} M_i x_i} \tag{2.15}$$

The linear attenuation coefficient of the compound may then be found simply by multiplying with the "mixture" density.

We observe that the "mixture" attenuation coefficient is obtained by a weighted sum of the coefficients of the individual elements, where the weights are equal to the contribution to the total molecular mass from each element.

Strictly speaking, equations 2.13 and 2.15 are only approximations, because we have assumed that the cross sections for each element in the mixture is the same as the cross section for that element when it appears "on its own". We have thus ignored the effect on the cross section for the atoms because of changes in their molecular, chemical or crystalline environment. However, for photons in the energy range we will consider, the errors in the estimated attenuation coefficients arising from this approximation are believed to be less than 2-3% [9, p. 7].

2.3.4. Cross sections for the different photon interaction mechanisms

A photon beam passing through a medium may be attenuated by different types of processes, and the total interaction cross section is the sum of the cross sections for the individual interaction mechanisms. We may classify these mechanisms according to the type of interaction: the first kind of interaction is outright absorption, in which the photon disappears; the second is scattering, where the photon is deflected from its original direction of travel. Furthermore, scattering is said to be elastic if the photon does not suffer energy loss during the interaction; and inelastic if it does. An overview of the processes of interest to us is shown in Table 2.1, which is based on Table 1 in [9, p. 22.] and on Table 2.1 in [10, p. 663].

Table 2.1 Types of elementary photon interaction mechanisms.

		Scattering	
Interaction with:	Absorption	Inelastic	Elastic
Atomic electrons	Photoelectric effect	Compton scattering	Rayleigh scattering
Electric field surrounding charged particles	Electron - positron pair production		

We will now consider the cross sections for each process separately, discussing their dependence on the photon energy E and on the atomic number Z of the medium in which the interaction takes place, their relative contribution to the total cross section and the generation of secondary radiation. Our discussion of the photon interaction processes is based on [9, pp. 21-40], [10, pp. 662-674] and [11].

Photoelectric effect

When a photon interacts with an atomic electron through the photoelectric effect, the photon disappears and the electron is ejected from the atom. The electron carries away the energy of the incident photon minus the binding energy of the electron; that is, $E_e = E_\gamma - E_b$. For this process to occur, the photon energy must be higher than the binding energy for the electron in question, and if the photon energy is less than the binding energy for a given shell, an electron from this shell cannot be ejected. A plot of the photoeffect cross section τ_{pe} versus photon energy E (Figure 2.2) will therefore exhibit characteristic discontinuities at the binding energies for the various shells; these are called *absorption edges.*

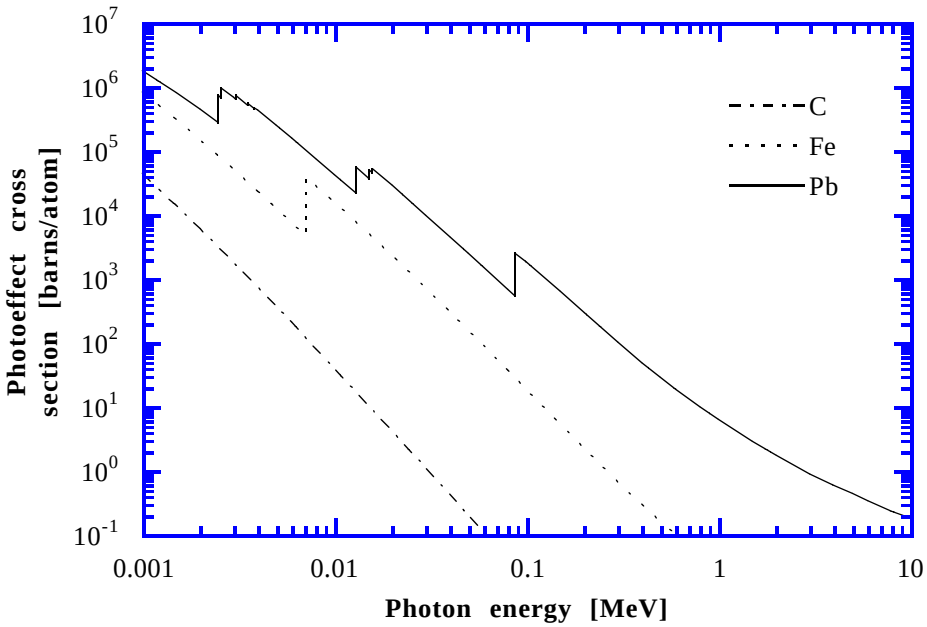

Figure 2.2 Photoelectric cross sections as function of photon energy for carbon (Z = 6), iron (Z = 26) and lead (Z = 82). The strong dependence of the cross sections on the atomic number is clearly seen, as is its steady decrease with increasing photon energy E. The plot is based on data from [12].

The K-shell electrons, which are most tightly bound to the nucleus, contribute most to the cross section in the upper part of the energy range under consideration. However, the cross section has a strong Z dependence (Figure 2.2); τ_{pe} is approximately proportional to $Z^{4.5}$, and so the contribution from electrons in the other shells become important for high-Z materials.

In addition to the discontinuities mentioned above, the energy dependence of τ_{pe} is characterized by being approximately proportional to E^{-3} at lower energies and approaching an E^{-1} dependence at energies higher than a few MeV.

Calculations of the E and Z dependence of the photoeffect cross section is in general difficult, because the electron involved in the process is not only bound to and acted upon by the nucleus, but it is also acted upon by all other electrons in the atom. Nevertheless, quite a few numerical calculations have been made, and together with experimental data they provide information on the photoelectric cross sections for wide ranges of E and Z; such data are tabulated in [9] and [12].

The generation of secondary radiation must also be mentioned: In addition to the ejected photoelectron, the filling of the resulting shell vacancy by an electron from a more distant shell is accompanied by the emission of either a characteristic photon (X ray) or an Auger electron. The probability that an X ray rather than an Auger electron is emitted is called the *fluorescence yield*; this increases with the energy of the photon to be emitted [10, p. 664].

Electron-positron pair production

This effect, which is the most probable photon interaction mechanism at high energies, takes place in the electric field surrounding a charged particle and causes the incident photon to disappear, leaving an electron-positron pair. Pair production may occur in the field of a nucleus or in the field of an electron; however, we shall ignore the latter, as its contribution to the total pair production cross section is negligible.

Nuclear field pair production is only possible if the energy of the incident photon is greater than the combined rest energies of the electron-positron pair; that is, greater than

$$E_t = 2mc^2 \tag{2.16}$$

which is equal to 1.022 MeV. The difference between the photon energy and the threshold energy E_t is shared between the electron and positron as kinetic energy.

The nuclear field pair production cross section, κ_n, is roughly proportional to Z^2 and increases approximately linearly with photon energy at first (from zero at the threshold energy), rises more slowly above 50-100 MeV, and eventually flattens out to a maximum value at very high energies. A plot of κ_n is shown in Figure 2.3 for low-, medium- and high-Z materials.

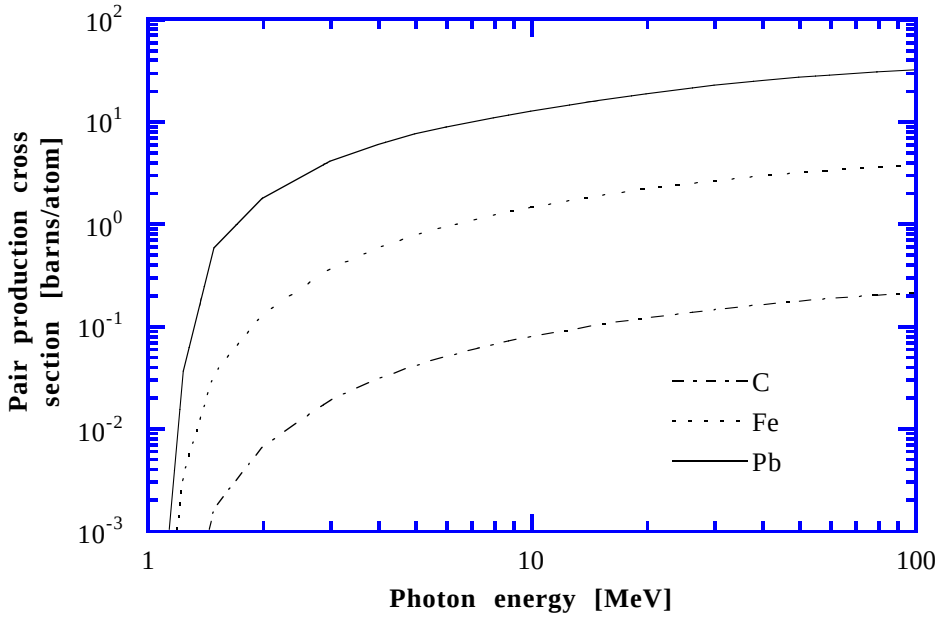

Figure 2.3 Nuclear field electron-positron pair production cross sections versus photon energy for carbon (Z = 6), iron (Z = 26) and lead (Z = 82). The plot is based on data from [12].

The direct secondary radiation resulting from this process is of course the electron-positron pair, but there is an accompanying effect which deserves special mention: When the positron loses its kinetic energy, it will be annihilated with an electron, and the combined rest energy

will be released as two photons moving in opposite directions, each with an energy equal to the rest energy of an electron (0.511 MeV).

Compton scattering

Compton scattering is a process by which a photon interacts with an atomic electron, loses some of its energy and is deflected from its original direction of travel, see Figure 2.4.

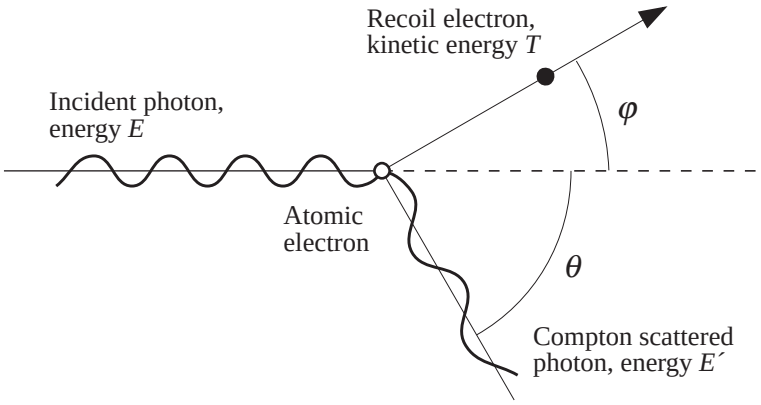

Figure 2.4 Compton scattering: a photon interacts with an atomic electron (considered to be free), loses some energy to the electron and is deflected from its original direction of travel.

Under the assumption that the binding energy of the electron in negligible, one can find the relation between the scattering angle θ and the energy E' of the scattered photon from conservation of energy and momentum:

$$E' = \frac{E}{1 + \frac{E}{mc^2}(1 - \cos\theta)} \tag{2.17}$$

where E is the energy of the incident photon. We may also express this equation in terms of the wavelength shift (in Compton units) of the photons:

$$\lambda' - \lambda = 1 - \cos\theta \tag{2.18}$$

Expressions for the total Compton scattering cross section and for the angular distribution of the scattered photons have been derived by Klein and Nishina [13] using quantum electrodynamics. Their formula for the total Compton interaction cross section, expressed as a function of the atomic number Z of the medium and the energy of the incident photon, k (i.e. energy in mc^2 units), is as follows [9, p. 28]:

$$\sigma_C^{KN} = 2Z\pi r_e^2 \left\{ \frac{1+k}{k^2} \left[\frac{2(1+k)}{1+2k} - \frac{\ln(1+2k)}{k} \right] + \frac{\ln(1+2k)}{2k} - \frac{1+3k}{(1+2k)^2} \right\} \left[\frac{10^{24}\,\text{barns}}{\text{atom}} \right] \tag{2.19}$$

where r_e , the "classical electron radius", is equal to $2.818 \cdot 10^{-13}$ cm. The Klein-Nishina cross section is plotted against photon energy in Figure 2.5.

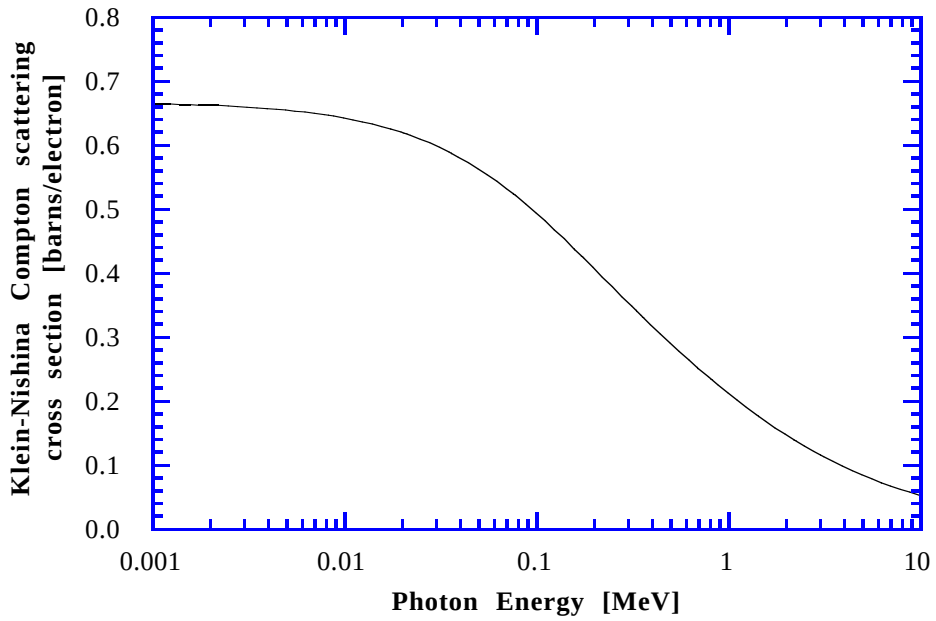

Figure 2.5 Klein-Nishina Compton scattering cross section per *electron* versus photon energy; that is, eq 2.19 with $Z = 1$.

In most cases, the Klein-Nishina theory agrees very well with experimental data: however, it is inaccurate at low photon energies because it is assumed that the binding energy of the electron is negligible. This effect become more pronounced for increasing Z because, in this case, the electrons near the nucleus are more tightly bound. Correction factors to compensate for this effect have been calculated and are included in tabulations of cross section data for the Compton effect [9] [12].

In Figure 2.6 we have plotted the ratio of the binding effect corrected Compton cross section and the Klein-Nishina cross section for some elements; it is seen that the effect becomes negligible at higher energies, but also that its influence gets larger for increasing Z.

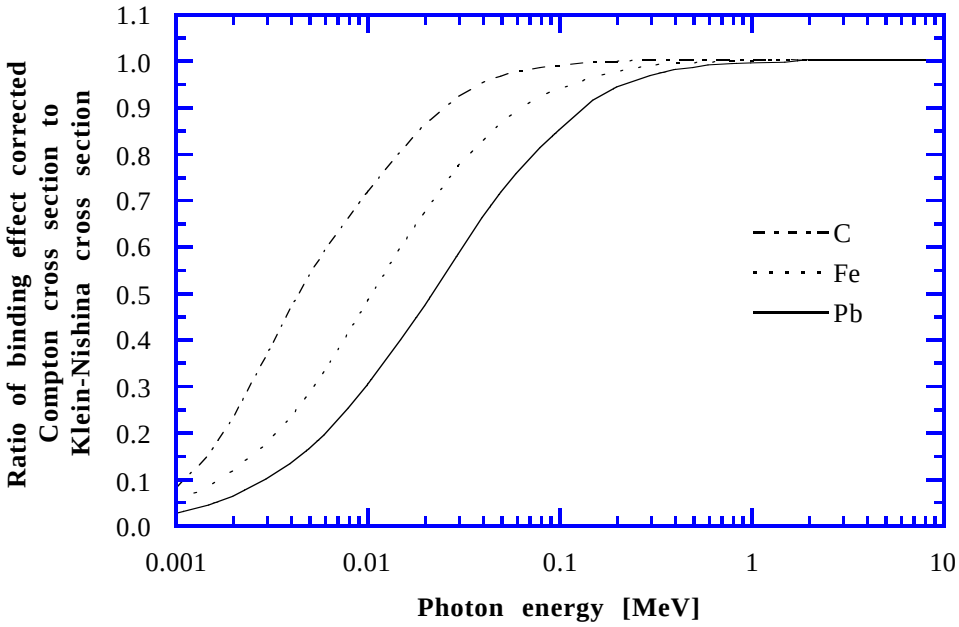

Figure 2.6 The ratio of the binding effect corrected Compton cross section to the Klein-Nishina (or free-electron) cross section plotted against photon energy for carbon (Z = 6), iron (Z = 26) and lead (Z = 82). The binding effect corrected data are from [12], and the Klein-Nishina data are computed using eq 2.19.

The angular distribution of the scattered photons is determined by the *differential* form of the Klein-Nishina formula [11, p. 253], which is the cross section for a Compton scattering of a photon into the angular interval $[\theta, \theta+d\theta]$.

$$\frac{d(\sigma_C^{KN})}{d\theta} = Z\pi r_e^2 \sin\theta \left[\frac{1}{1+k(1-\cos\theta)}\right]^2 \times \left[1+\cos^2\theta + \frac{k^2(1-\cos\theta)^2}{1+(1-\cos\theta)}\right] \left[\frac{10^{24}\ \text{barns}}{\text{atom}\cdot\text{radians}}\right] \tag{2.20}$$

This expression may be regarded as the combined probability of a Compton interaction and the probability of the photon being scattered an angle θ. Eq 2.20 is plotted in Figure 2.7 for a few values of the incident photon energy. We note that the distribution of the scattered photons shifts to a predominantly forward direction as the energy of the incident photon increases; this may be attributed to the increased momentum of the photon.

It should be pointed out that to uniquely determine the direction of the scattered photon in three-dimensional space, the *azimuthal* scattering angle α must also be specified; it represents the direction of the projection of the *scattered* photon direction, into a plane perpendicular to the *incident* photon direction. If polarization effects are ignored, all values of the azimuthal scattering angle (0 to 2π) are equally probable.

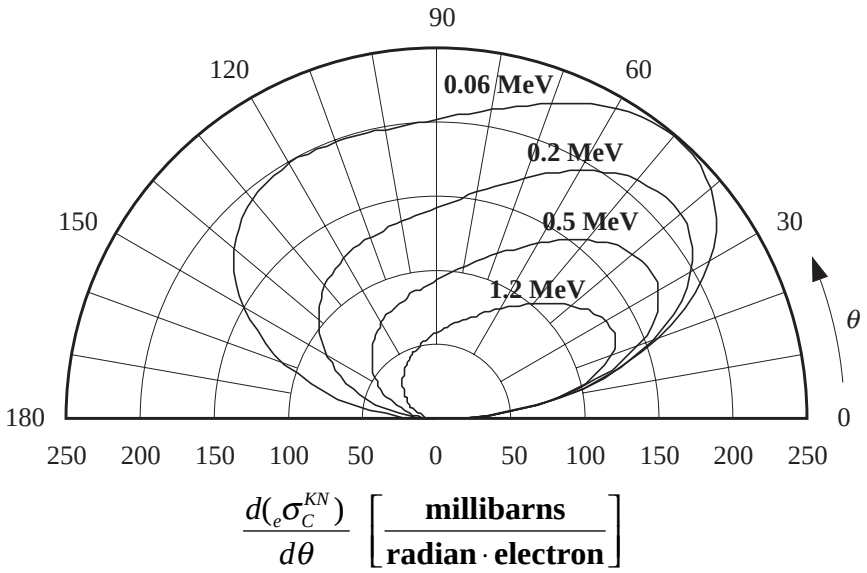

Figure 2.7 The angular distribution of Compton scattered photons according to Klein-Nishina theory (eq 2.20, with Z = 1) for incident photon energies E of 0.06 MeV, 0.2 MeV, 0.5 MeV and 1.2 MeV; adapted from Evans' Figure 20 [11, p. 253]

The secondary effect of the Compton process is the emission of a recoil electron; it receives as kinetic energy the difference between the energy of the incident photon and the energy of the scattered photon, and may in turn cause exitation or ionization when colliding with other atomic electrons. The emission angle φ of the recoil electron (see Figure 2.4) is related to the photon scattering angle θ by the following expression:

$$\tan\varphi = \frac{1}{\tan(\frac{\theta}{2})(1+k)} = \frac{1}{\tan(\frac{\theta}{2})(1+\frac{E}{mc^2})} \qquad (2.21)$$

By combining this with eq 2.20, one may find the angular distribution of the recoil electrons, see Evans [11, p. 254].

Rayleigh scattering

Under the circumstances when the Klein-Nishina theory for Compton (inelastic) scattering breaks down, i.e. when the binding energy of the atomic electron no longer is negligible compared to the energy of the incident photon, another type of scattering may occur. This is Rayleigh (or elastic) scattering, in which a photon is scattered by an atomic electron but with very little energy loss. The electron is neither ionized nor exited; the recoil is taken up by the atom as a whole. All electrons in the atom contribute coherently to the total cross section for Rayleigh scattering (σ_R); therefore, the effect is often called coherent scattering.

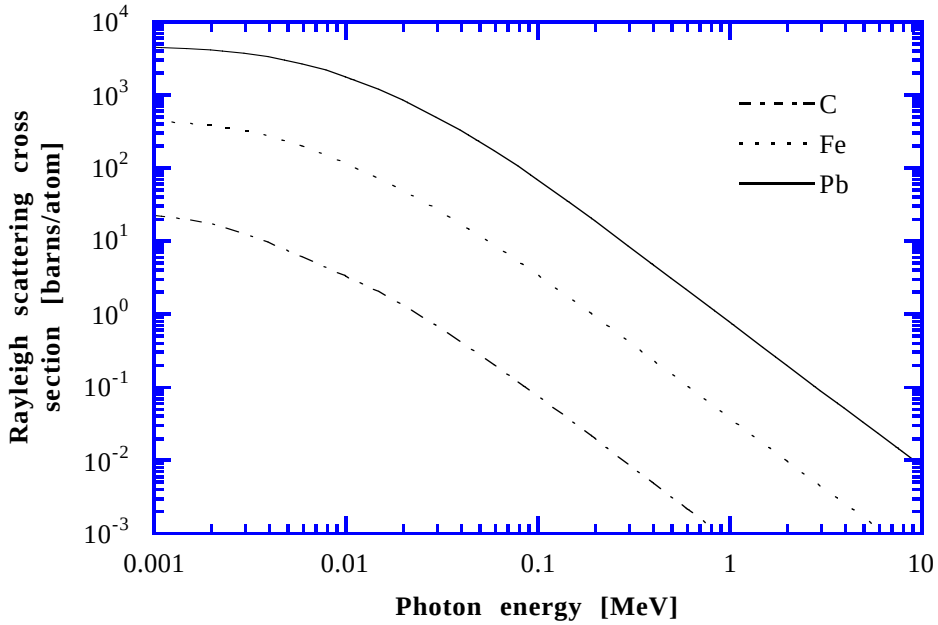

Figure 2.8 Total cross section for Rayleigh scattering, σ_R, plotted vs. photon energy for carbon (Z = 6), iron (Z = 26) and lead (Z = 82); the data are from [12].

The cross section for Rayleigh scattering is proportional to Z^2 and decreases with increasing energy, see Figure 2.8. The angular distribution of the Rayleigh scattered photons is rather broad for low photon energies, but it becomes increasingly forward peaked at higher energies.

Total photon interaction cross section

Because the individual interaction mechanisms generally occur without mutual disturbance, the total cross section is simply the sum of the individual cross sections:

$$\sigma_{tot} = \tau_{pe} + \kappa_n + \sigma_C + \sigma_R \qquad (2.22)$$

From the discussion in the preceding sections we may draw a few conclusions regarding the relative importance of the different attenuation processes for varying E and Z: For low energy photons, the attenuation is predominantly by the photoelectric effect, whose cross section increases very rapidly with decreasing energy. At intermediate energies, the attenuation is mostly due to Compton scattering, and when the photon energy increases further, pair production eventually becomes most important. The general effect of increasing Z is that the photoeffect- and Compton dominated regions are moved higher up in energy.

We also note that even though the Rayleigh process is the most probable *scattering* mechanism for low energy photons, its contribution to the total cross section is of minor importance compared to the contribution of the photoelectric effect.

These general trends are apparent from Figure 2.9 (a), (b) and (c), where we have plotted individual and total interaction cross sections against photon energy for carbon, iron and lead, respectively.

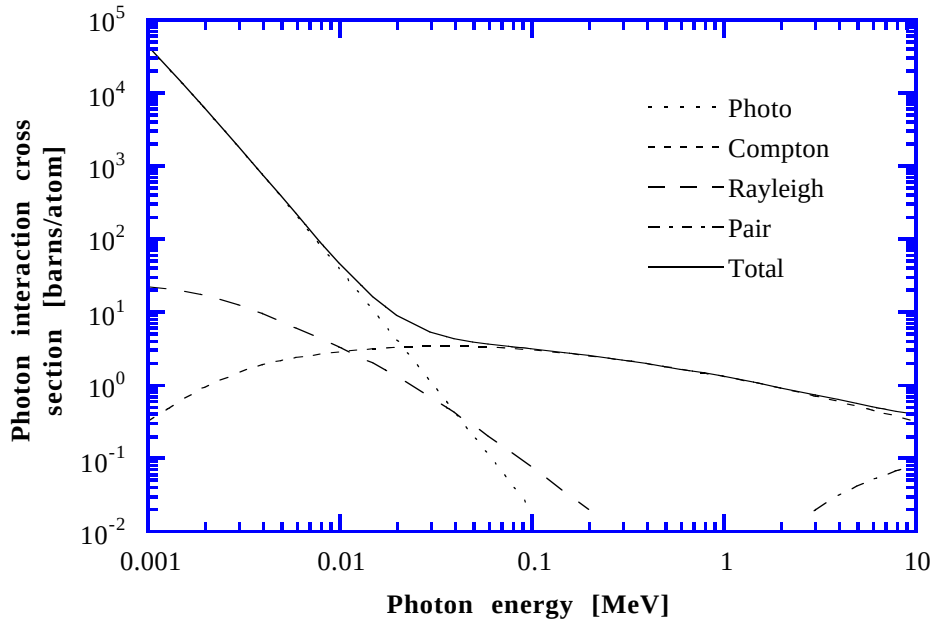

Figure 2.9 (a) Total and individual cross sections vs. photon energy for carbon ($Z = 6$). The data are from [12].

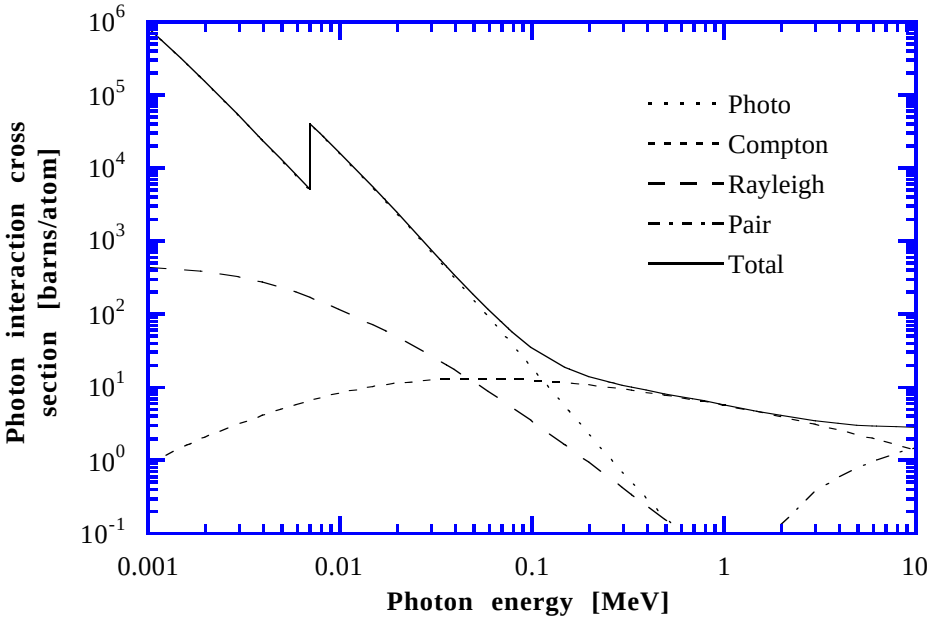

Figure 2.9 (b) Total and individual cross sections vs. photon energy for iron ($Z = 26$). The data are from [12].

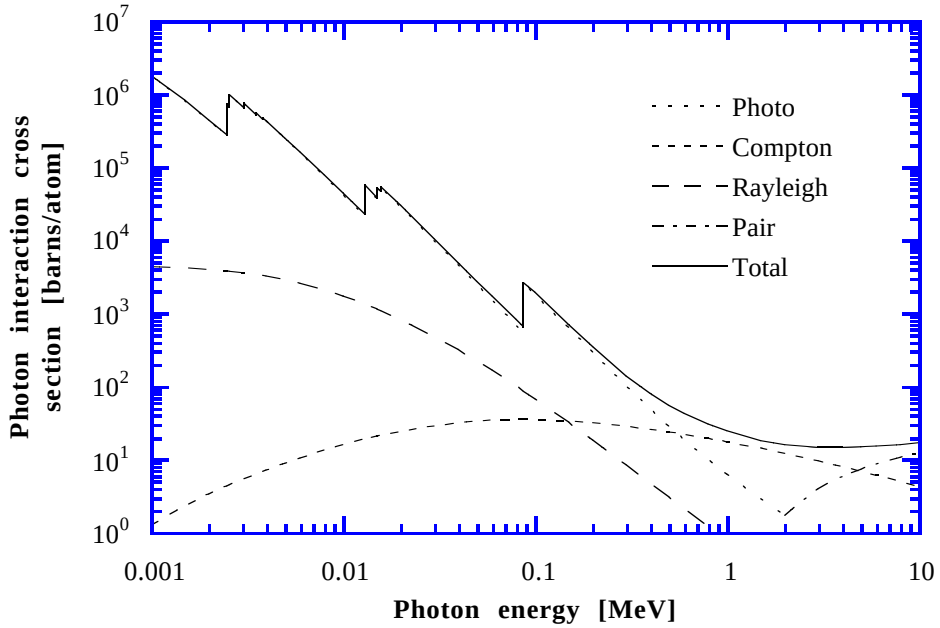

Figure 2.9 (c) Total and individual cross sections vs. photon energy for lead (Z = 82). The data are from [12].

Sources of photon cross section data

As we have already indicated, the current knowledge of numerical cross section data for the various processes is a mixture of theoretical calculations and experimental data. Several authors have compiled tabulations of such data: Hubbell [9] provide data for the photoeffect, Compton scattering and pair production, Storm and Israel [12] also include Rayleigh data, and the tabulation of Hubbell *et al* [14] contain Compton and Rayleigh scattering cross section data. For our Monte Carlo modelling work (see below), we will use data from [12].

The approximate accuracy for these tabulations is as follows: For Rayleigh and Compton scattering the accuracy is believed to be better than 3%. The pair production data have an approximate accuracy of 5%, whereas the photoeffect data are accurate to within 3% in the energy range 6 to 200 keV, and 10% outside this range. We also note that in the range 10 keV to 1 MeV, the cross section data for the dominating processes (see Figure 2.9) are accurate to within 3%.

2.4. Mathematical modelling of photon transport

In many cases, there is a need for mathematical methods for handling X- or γ-ray related problems, such as calculation of detector response functions and design of source shields. The general problem is to determine the flux of photons at a given point in a system of absorbers, due to a given distribution of photon sources. This is known as photon transport theory, which are described below, since we will need such techniques in Chapter 5 for calculation of detection efficiencies.

2.4.1. The photon transport equation

The time-constant flow of photons per unit area, of (Compton) wavelength λ and direction ω, and at position $\mathbf{r}$, is represented by the flux $I(\mathbf{r},\omega,\lambda)$. We wish to determine this flux at each point in space, given the photon source distribution and the absorber geometry. A general formalism for this type of problem is presented by Fano *et al* [10, pp. 680-681]; a description of its derivation is given below.

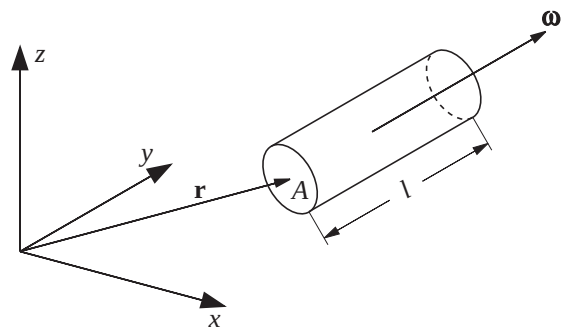

Figure 2.10 Geometry for derivation of photon transport equation: An infinitesimal cylinder of base area A and length l, positioned at $\mathbf{r}$, and pointing in the direction ω.

The starting point for this somewhat heuristic derivation is that the net flow of photons out of the infinitesimal cylinder of Figure 2.10, is equal to the difference between the outflow and inflow of photons

$$\begin{aligned} \text{net flow} &= AI(\mathbf{r}+l\boldsymbol{\omega},\boldsymbol{\omega},\lambda) - AI(\mathbf{r},\boldsymbol{\omega},\lambda) \\ &= Al\,\boldsymbol{\omega}\cdot\nabla I(\mathbf{r},\boldsymbol{\omega},\lambda) \end{aligned} \tag{2.23}$$

where we have multiplied with the infinitesimal cylinder base area A because I represents flux per unit area. There are three contributions to the net photon flow: The first is the narrow-beam *attenuation* of photons entering the cylinder base area with direction ω and wavelength λ; thus representing a *negative* contribution to the net outflow of photons:

$$\text{attenuation} = -\mu(\lambda) l A I(\mathbf{r},\boldsymbol{\omega},\lambda) \tag{2.24}$$

The second is the *scattering* term, which represents the number of photons leaving the cylinder with direction ω and with a wavelength λ, resulting from the scattering of photons entering the cylinder in *any* direction ω´, and with wavelength λ´ less than or equal to λ:

$$\text{scattering} = Al\int_0^{\lambda} d\lambda' \int_{4\pi} d\boldsymbol{\omega}' k(\boldsymbol{\omega},\lambda,\boldsymbol{\omega}',\lambda') I(\mathbf{r},\boldsymbol{\omega},\lambda) \tag{2.25}$$

The function $k(\omega,\lambda,\omega',\lambda')$ represents the probability that the scattering of an incident photon of direction ω' and wavelength λ' produces a new photon with direction ω and wavelength λ, anywhere inside the infinitesimal cylinder; the subscript "4π" of the inner integral is shorthand for "all directions". We multiply by *Al* because the integral represents flux per unit volume, and the wavelength restriction arises simply because a photon does not increase its energy in a scattering. If we ignore Rayleigh scattering, we are left with the Compton effect, and the function $k(\omega,\lambda,\omega',\lambda')$ will be a modified Klein-Nishina differential cross section [10, p. 681].

The third contribution to the net outflow comes from any photon source inside the cylinder; if $S(\mathbf{r},\omega,\lambda)$ is the source flux per unit volume, the resulting contribution is:

$$\text{source} = AlS(\mathbf{r},\boldsymbol{\omega},\lambda) \tag{2.26}$$

Since the net outflow of photons from the cylinder (eq. 2.23) is equal to the sum of the attenuation, scattering and source terms (eqns 2.24 to 2.26), we have

$$\begin{aligned} \boldsymbol{\omega}\cdot\nabla I(\mathbf{r},\boldsymbol{\omega},\lambda) = {} & -\mu(\lambda) I(\mathbf{r},\boldsymbol{\omega},\lambda) + \\ & + \int_0^{\lambda} d\lambda' \int_{4\pi} d\boldsymbol{\omega}' k(\boldsymbol{\omega},\lambda,\boldsymbol{\omega}',\lambda') I(\mathbf{r},\boldsymbol{\omega},\lambda) \\ & + S(\mathbf{r},\boldsymbol{\omega},\lambda) \end{aligned} \tag{2.27}$$

which is the *photon transport equation* [10, p. 681].

This integro-differential equation is in general difficult to solve analytically for $I(\mathbf{r},\omega,\lambda)$, as it contains six independent variables; also, $\mu(\lambda)$ and $k(\omega,\lambda,\omega',\lambda')$ are complicated functions of photon energy and scattering angle. Direct analytical solution of eq. 2.27 may be very complicated even for simple geometries, and even if simplified analytical expressions are used for the functions μ and *k*. The large number of independent variables also complicates direct numerical solution; therefore, other methods are normally used instead.

It should be noted that eq. 2.27 represents a simplification of the physical processes of photon transport, as it ignores effects associated with secondary radiation created by the photon

interaction processes: First, there is the emission of fluorescence X rays following photoelectric effect. Secondly, there are a variety of effects connected with the charged particles ejected when a photon interacts with matter; electrons and positrons loose kinetic energy by *bremsstrahlung*, and the annihilation of the positron is followed by photon emission[1] (See also Figure 1.4 of Hubbell [9, p. 15]).

X-ray fluorescence photons may be included in the "scattering" term of eq. 2.27 because they are produced locally, but as electrons and positrons may travel a considerable distance while they loose energy by bremsstrahlung (or before being annihilated), the flux of new photons created by charged particle interactions cannot generally be treated in this way, but must be calculated separately and included in the source term of the transport equation. A general model of photon transport should therefore include the transport of charged particles as well: The model thus consists of a system of three separate transport equations (similar to eq. 2.27), one each for photons, electrons and positrons, and where the flux of each quantity enters in the source terms of the equations of the other fluxes [10, p. 681].

However, if the energies of the photons, and hence, the energies of the charged particles are moderate (< 1-2 MeV), the production of secondary photons may be assumed to take place locally; this allows including the secondary photon flux in the "scattering" term of eq. 2.27[2].

Orders-of-scattering expansion

If the flux from primary photons and the flux of photons scattered once, twice, etc. are determined separately, the total flux may be written [10, pp. 686-687]:

$$I(\mathbf{r},\boldsymbol{\omega},\lambda) = I^{(0)}(\mathbf{r},\boldsymbol{\omega},\lambda) + I^{(1)}(\mathbf{r},\boldsymbol{\omega},\lambda) + I^{(2)}(\mathbf{r},\boldsymbol{\omega},\lambda) + \ldots \tag{2.28}$$

The equation for the flux $I^{(0)}$ of primary, or unscattered, photons is found by deleting the integral in eq. 2.27:

$$\boldsymbol{\omega} \cdot \nabla I^{(0)}(\mathbf{r},\boldsymbol{\omega},\lambda) = -\mu(\lambda) I^{(0)}(\mathbf{r},\boldsymbol{\omega},\lambda) + S(\mathbf{r},\boldsymbol{\omega},\lambda) \tag{2.29}$$

---

[1]The production of new photons from the charged particle emission following primary photon interaction may be repeated several times over for the secondary photons, producing many photons for a single primary photon; this is called a *cascade-shower* process [10, p. 665].

[2]The meaning of the term "scattering" would in this case be extended to include all attenuation processes which create new photons from incident ones.

The equation for the flux $I^{(1)}$ of singly scattered photons is found by ignoring the source term in eq. 2.27, and replacing I with $I^{(0)}$ in the integral, and with $I^{(1)}$ everywhere else. Proceeding in this fashion, we get the following equation for the flux of photons scattered n times, $I^{(n)}$:

$$\begin{aligned}\boldsymbol{\omega}\cdot\nabla I^{(n)}(\mathbf{r},\boldsymbol{\omega},\lambda) = &-\mu(\lambda)I^{(n)}(\mathbf{r},\boldsymbol{\omega},\lambda)+\\ &+[1-\delta_{n0}]\int_0^{\lambda}d\lambda'\int_{4\pi}d\boldsymbol{\omega}'k(\boldsymbol{\omega},\lambda,\boldsymbol{\omega}',\lambda')I^{(n-1)}(\mathbf{r},\boldsymbol{\omega},\lambda)\\ &+\delta_{n0}\,S(\mathbf{r},\boldsymbol{\omega},\lambda)\end{aligned} \tag{2.30}$$

where δ_{n0} is the Kronecker delta. The solution of eq 2.30 is [10, p. 687]

$$I^{(n)}(\mathbf{r},\boldsymbol{\omega},\lambda)=\int_0^{\infty}d\zeta\, e^{-\mu(\lambda)\zeta}S^{(n)}(\mathbf{r}-\boldsymbol{\omega}\,\zeta,\boldsymbol{\omega},\lambda)$$

where

$$S^{(0)}=S(\mathbf{r},\boldsymbol{\omega},\lambda)\text{ and }S^{(n)}=\int_0^{\lambda}d\lambda'\int_{4\pi}d\boldsymbol{\omega}'k(\boldsymbol{\omega},\lambda,\boldsymbol{\omega}',\lambda')I^{(n-1)}(\mathbf{r},\boldsymbol{\omega},\lambda) \tag{2.31}$$

i.e., the solution of the transport equation may be found by evaluating a sequence of multiple integrals, analytically or numerically.

However, since the multiplicity of the integrals increases rapidly with the order of scattering n, it is clear that this method also has its limitations; the unavoidable truncation of the series in eq. 2.28 will always introduce errors in the calculated flux $I(\mathbf{r},\omega,\lambda)$. Also, complex absorber geometries will invariably cause difficulties for numerical evaluation, therefore, it is clear that a different approach is generally needed.

2.4.2. Monte Carlo photon transport calculation

The photon transport problem is probabilistic in its nature, because of the inherent randomness of the quantum processes involved: The trajectory of a photon undergoing scatterings, and finally absorption, cannot be predicted exactly; only the probability distributions of the outcome of the individual interaction processes are known in advance. The "trick" of the Monte Carlo method is to imitate the actual physical processes by an analog numerical random process; this is known as straightforward sampling or analog Monte Carlo [10, p. 772].

Basis for photon transport Monte Carlo

To demonstrate the basis for the Monte Carlo photon transport calculation, we first describe the sequence of events taking place from a photon leaves its source until it disappears in an absorption; an "algorithmic" description is shown in the flow chart of Figure 2.11:

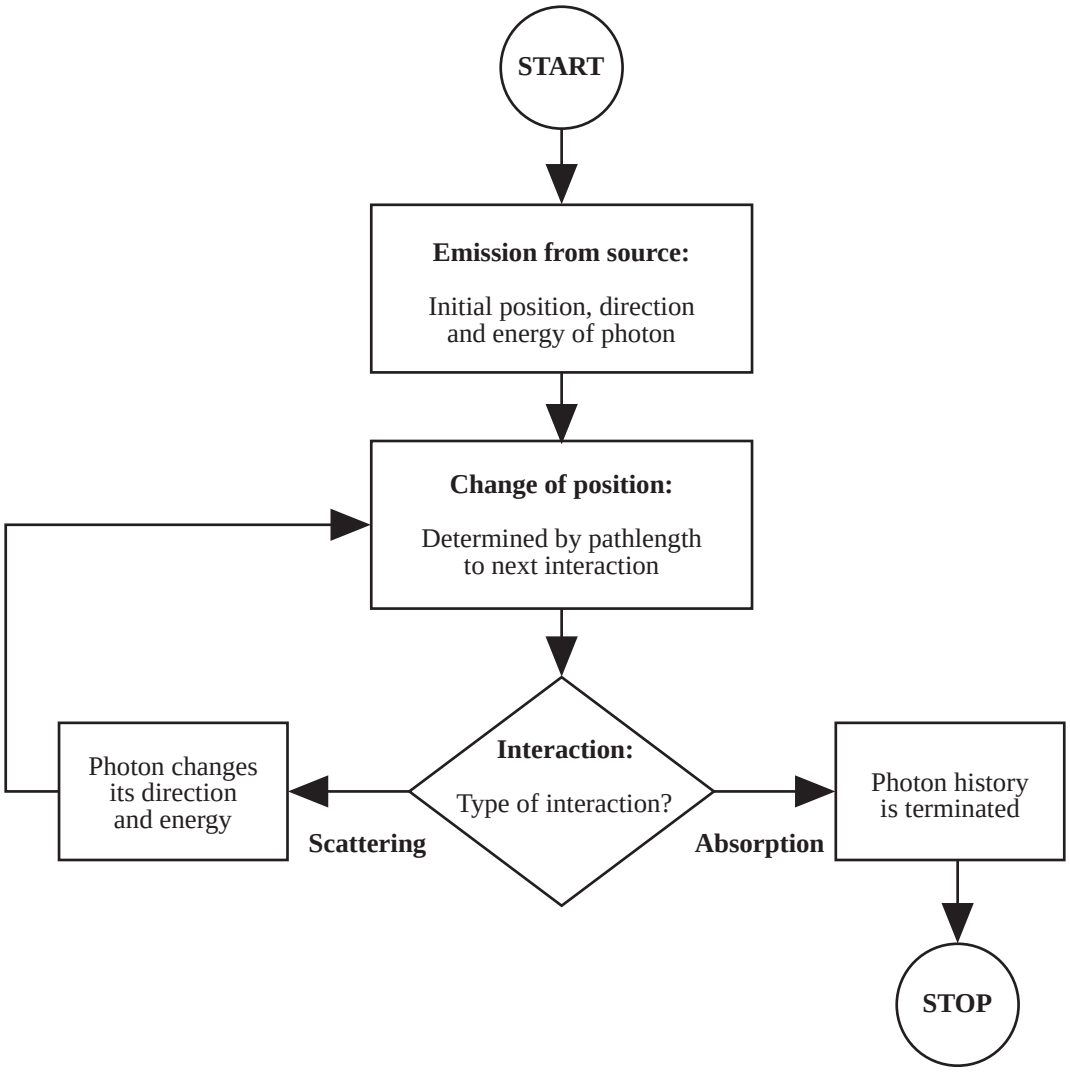

Figure 2.11 The basic sequence of events in photon transport: Emission of a photon from the source, scattering interactions, and the final disappearance by absorption. Emission of fluorescence radiation is ignored, as is charged particle transport.

The history of a photon being scattered several times before being absorbed is characterized by a set of variables describing its position **r**, direction ω and wavelength λ immediately *before* each interaction:

$$\left.\begin{array}{l} \mathbf{r}_1,\ \mathbf{r}_2,\ldots,\ \mathbf{r}_n,\ldots,\ \mathbf{r}_N \\ \boldsymbol{\omega}_1,\boldsymbol{\omega}_2,\ldots,\boldsymbol{\omega}_n,\ldots,\boldsymbol{\omega}_N \\ \lambda_1,\ \lambda_2,\ldots,\ \lambda_n,\ldots,\ \lambda_N \end{array}\right\} \qquad (2.32)$$

Interactions $n = 1$ to $n = N$-1 are scatterings, while $n = N$ represents the absorption event terminating the photon history. Together with the source position , which we may call $\mathbf{r}_0$ (assuming a point source), the variables in eq. 2.32 thus specifies the photon trajectory completely. The direction ω_0 and wavelength λ_0 of the photon as it leaves the source are of course equal to ω_1 and λ_1, respectively.

Before we describe the flow chart of Figure 2.11 more closely, we note that the unit direction vector ω is conveniently determined by the two angles φ and ν, as shown in Figure 2.12:

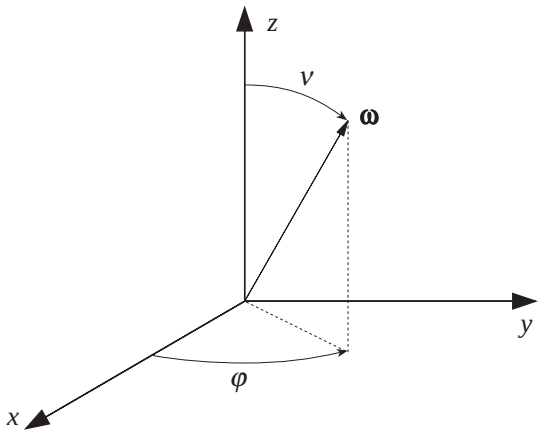

Figure 2.12 The unit direction vector ω is uniquely specified by the angles φ and ν. The former lies within the interval [0, 2π], the latter in [0, π].

Thus, in Carthesian representation, ω is given by:

$$\boldsymbol{\omega} = \left[\sin\nu\cos\varphi, \sin\nu\sin\varphi, \cos\nu\right] \tag{2.33}$$

We now proceed to describe each part of the flow diagram of Figure 2.11.

If we consider an *isotropic point source*, all emission directions are equally probable, so φ and ν have the following probability distribution functions

$$\begin{aligned} f(\varphi) &= \frac{1}{2\pi}\ ;\ 0 \le \varphi < 2\pi, \\ f(\nu) &= \frac{\sin\nu}{2};\ 0 \le \nu < \pi \end{aligned} \tag{2.34}$$

in the "spherical" representation.

The *change of position* of the photon is determined by its current direction of travel and the *pathlength* ζ_n between interactions n - 1 and n, so that:

$$\mathbf{r}_n = \mathbf{r}_{n-1} + \zeta_n \boldsymbol{\omega}_n \tag{2.35}$$

The pathlength (in an infinite homogeneous medium) is governed by the following probability density distribution function:

$$f(\zeta_n) = \mu(\lambda_n) e^{-\mu(\lambda_n)\zeta_n}\ ;\ \zeta_n \ge 0 \tag{2.36}$$

The *type of interaction* may be either an absorption (photoelectric absorption or pair production), or a scattering (Compton or Rayleigh); the relative probabilities are given by:

$$p_{PE} = \frac{\mu_{PE}}{\mu_{tot}}(\lambda_n) \; ; \quad p_{PP} = \frac{\mu_{PP}}{\mu_{tot}}(\lambda_n)$$
$$p_C = \frac{\mu_C}{\mu_{tot}}(\lambda_n) \; ; \quad p_R = \frac{\mu_R}{\mu_{tot}}(\lambda_n) \tag{2.37}$$

An *absorbtion event* causes the photon to disappear, thus terminating the history[1]. Note that the probability of a pair production event is identically zero if the photon energy is below the threshold energy.

After a *scattering event*, the photon continues in a new direction and, in the case of a Compton interaction, with lower energy. Rayleigh scattering is frequently ignored in Monte Carlo modelling because of its low relative probability; in this case, the direction and energy of the scattered photon are governed by the probability distributions of the Compton scattering angles:

$$f(\alpha) = \frac{1}{2\pi} \; ; \; 0 \le \alpha < 2\pi,$$
$$f(\theta) = \frac{1}{{}_e\sigma_C^{KN}} \frac{d({}_e\sigma_C^{KN})}{d\theta}; \; 0 \le \theta < \pi \tag{2.38}$$

where α, the azimuthal scattering angle, is uniformly distributed and θ is determined by the Klein-Nishina differential cross section of eq. 2.20. The new direction vector ω may then be found using eq. 2.33 and a little algebra, and the new wavelength λ using the Compton energy-scattering angle relationship, i.e. from eq. 2.17 or eq. 2.18.

We now see that photon transport problems may be solved by performing a "computer experiment": Based on the flow chart of Figure 2.11, and on random sampling from the associated probability distributions for each event in the interaction sequence, an artificial photon history can be generated, which is in fact a computer imitation of the real physical process taking place. An experiment is simulated by generating a high number of different histories, and the flux $I(\mathbf{r},\omega,\lambda)$ may be determined by tallying the photons within the interesting range of $\mathbf{r}$, ω and λ. This is the basic principle of Monte Carlo photon transport calculation.

Random sampling of probability distributions

When constructing the artificial photon histories required in a Monte Carlo simulation, it is necessary to perform random sampling from the probability distributions governing the

[1]Note that photoelectric absorption may be followed by the emission of a fluorescence X-ray; also, the annihilation of the pair production positron results in photon emission.

various parts of the sequence of events taking place. Loosely defined, random sampling of a given probability distribution involves generating a set of random numbers, whose distribution in the long run approach the required probability distribution. In the following section, we will consider general techniques for doing this, and then we proceed to study the sampling of distributions specific to photon transport Monte Carlo.

General

The random sampling of probability distributions is invariably done using techniques based on *uniform random numbers*, i.e. numbers which are uniformly distributed in the interval [0, 1] and do not exhibit any correlation. Psuedorandom numbers may be generated by means of computer algorithms [15, pp. 204-213]; while this of course implies that such numbers are really not totally random in a strict statistical sense, their degree of "randomness" is adequate for any practical purpose in Monte Carlo work. We will now describe three methods for random sampling of probability density distribution functions; all methods are based on the use of uniform random numbers.

The *inverse method*, relies on the fact that any random variable, of any distribution, can be expressed as a function of another random variable which is uniformly distributed between zero and one. If $p(x)$ is the probability density distribution of the random variable x, its cumulative distribution $P(x)$ is given by:

$$P(x) = \int_{-\infty}^{x} p(x')dx' \tag{2.39}$$

$P(x)$ is itself a random variable, distributed uniformly between zero and one; therefore, a random variable x with distribution $p(x)$ may be obtained by selecting an uniform random number ρ and solving the equation:

$$\rho = P(x) \;\Rightarrow\; x = P^{-1}(\rho) \tag{2.40}$$

The main drawback of this method is that it may be impossible to find an expression for the inverse of the cumulative distribution function.

Another method, originally proposed by von Neumann [16], is the *rejection method* [17, pp. 36-37]: If the distribution $p(x)$ of the variable x is restricted to the interval $[0, a]$, and the maximum of $p(x)$ is L, we may sample from the distribution in the following way: First, we select two uniform random numbers ρ_1 and ρ_2; next, we compute $x_1 = \rho_1 a$. Now, if $\rho_2 L \leq p(x_1)$, x_1 is accepted as a random variable from the distribution $p(x)$, if not, the process is repeated with a new pair of uniform random numbers.

The efficiency of this sampling method depends on the characteristics of the distribution function; the relative portion of *rejected* random number pairs is given by the quantity

$$1-\frac{1}{aL}\int_0^a p(x)dx \;=\; 1-\frac{1}{aL} \tag{2.41}$$

which is called the *rejection rate*.

The third random sampling scheme we will discuss, is the *composition + rejection method*, which is a slight twist to the combination of the two methods mentioned above [10, pp. 777-778][17, p. 40]. If $p(x)$ and $p_i(x)$ are probability density distributions, α_i are positive real numbers, and $g_i(x)$ are confined to the range [0, 1], the density function

$$p(x)=\sum_{i=1}^{n}\alpha_i\, p_i(x)g_i(x) \tag{2.42}$$

may be sampled in the following way: First, choose three uniform random numbers ρ_1, ρ_2 and ρ_3. Second, find i so that

$$\sum_{j=1}^{i-1}\alpha_j < \rho_1\sum_{j=1}^{n}\alpha_j \le \sum_{j=1}^{i}\alpha_j \tag{2.43}$$

i.e., select α_i with relative probability $\alpha_i/(\alpha_1 + ... + \alpha_n)$. Third, select x from the distribution $p_i(x)$, e.g. by solving $P_i(x) = \rho_2$ (inverse method). Finally, accept x if $\rho_3 \le g_i(x)$; if not, repeat from the beginning. The trick is of course to "decompose" the desired density function $p(x)$ in such a way that the resulting p_i´s can be sampled by the inverse method.

Sampling of distributions specific to photon transport

Using the techniques described in the previous section, we will now describe the sampling of probability distributions specific to photon transport Monte Carlo:

An *isotropic source* emits photons in directions determined by the generic distributions of eq. 2.34; the sampling of the angles φ and ν is easily accomplished using the inverse method:

$$\begin{aligned} F(\varphi)=\frac{\varphi}{2\pi} \;&\Rightarrow\; \varphi = 2\pi\rho \\ F(\nu)=\frac{1-\cos\nu}{2} \;&\Rightarrow\; \nu = \arccos(1-2\rho) \end{aligned} \tag{2.44}$$

where the ρ´s denote uniform random numbers. It is seen that the angles φ and ν generated in this way are contained in the correct intervals [0, 2π] and [0, π], respectively. The direction vector ω may then be found using eq. 2.33.

The *change of position* of the photon is computed from eq. 2.35, after sampling the *pathlength* distribution function of eq. 2.36; using the inverse sampling method we get:

$$F(\zeta_n) = 1 - e^{-\mu(\lambda_n)\zeta_n} \;\Rightarrow\; \zeta_n = -\frac{\ln(\rho)}{\mu(\lambda_n)} \tag{2.45}$$

where ρ denotes an uniform random number. At this point, we note that eqns. 2.36 and 2.45 apply to the case of an homogeneous medium: However, if the medium consists of several regions, each consisting of different but homogeneous materials, we must take into account what happens if a photon, in travelling the distance ζ_n, crosses a boundary between two different materials. Thus, if the linear attenuation coefficient $\mu(\lambda_n)$ of the material of the next region is smaller than that of the current region, ζ_n should be stretched; conversely, if $\mu(\lambda_n)$ increases upon crossing the boundary, ζ_n should be shortened.

If the distance ζ_b along the current direction of travel, from the position of the most recent scattering (or from the source position) to a boundary between different materials, is less than the sampled pathlength between interactions ζ_n, the total effective pathlength should be corrected as follows:

$$\zeta_n' = \zeta_b + (\zeta_n - \zeta_b)\frac{\mu_{current}(\lambda_n)}{\mu_{next}(\lambda_n)} \tag{2.46}$$

Here, $\mu_{current}(\lambda_n)$ and $\mu_{next}(\lambda_n)$ are the attenuation coefficients of the materials in question; the pathlength is shortened or stretched as required, i.e. depending on which is the larger of the two attenuation coefficients. Note that this correction process must be carried out several times if the photon should cross more than one material boundary; i.e. the second correction is based on the first corrected pathlength, and so forth.

The *interaction type* distribution is discrete, so it is sampled simply by using the probabilities of the interaction processes in question; if there are n possible interaction types, with probabilities p_i, type i is chosen when

$$\sum_{j=1}^{i-1} p_j < \rho \sum_{j=1}^{n} p_j \le \sum_{j=1}^{i} p_j \tag{2.47}$$

where ρ is an uniform random number. The relative probabilities of the interaction processes are defined in eq. 2.37.

As we have mentioned above, Rayleigh scattering is frequently ignored in photon transport calculations; moreover, pair production may be ignored if the photon source energy is less than the threshold energy for this process. Under these circumstances, the type of interaction is selected simply by chosing the photoeffect if $\rho < p_{pe}$, and Compton scattering if not.

If we consider the sampling of *scattering angles* for a Compton interaction, we first note that the azimuthal scattering angle α is uniformly distributed in the interval [0, 2π]; thus, it is sampled in exactly the same way as the azimuthal photon emission angle φ of eq. 2.44:

$$F(\alpha) = \frac{\alpha}{2\pi} \;\Rightarrow\; \alpha = 2\pi\rho \tag{2.48}$$

For the sampling of the Compton scattering angle distribution, the composition+rejection method is used, but the selection of θ is *not* based directly on eq. 2.38; instead, we use the following method [10, pp. 777-778]:

The Klein-Nishina differential cross section in eq. 2.20 is expressed as cross section per unit angle; for the sake of simpler sampling, we will use the differential cross section per unit *solid angle* instead. Because the solid angle per unit angle is given by

$$\frac{d\Omega}{d\theta} = 2\pi\sin\theta \tag{2.49}$$

we get the following expression for the Klein-Nishina cross section per unit angle:

$$\begin{aligned}\frac{d({}_e\sigma_C^{KN})}{d\Omega} = \frac{r_e^2}{2}\left[\frac{1}{1+k(1-\cos\theta)}\right]^2 \times \\ \left[1+\cos^2\theta+\frac{k^2(1-\cos\theta)^2}{1+(1-\cos\theta)}\right]\;\left[\frac{10^{24}\,\text{barns}}{\text{atom}\cdot\text{steradian}}\right]\end{aligned} \tag{2.50}$$

Obviously, if the scattering angle is sampled such that the resulting cross section per unit solid angle distribution is correct, the scattering angle itself should also be correctly distributed, i.e. according to eq. 2.20. However, instead of sampling the scattering angle directly, we sample the relative wavelength change ε, i.e. we use (see eq. 2.18)

$$\varepsilon = \frac{\lambda'}{\lambda} \;\;;\;\; \cos\theta = 1-\lambda'+\lambda = 1-\lambda(\varepsilon-1) \tag{2.51}$$

so that eq. 2.50 may be written:

$$\frac{d({}_e\sigma_C^{KN})}{d\Omega} = \frac{r_e^2}{2}\left\{\frac{1}{\varepsilon^2}\left[(1-\lambda(\varepsilon-1))^2+\frac{1}{\varepsilon}\right]+\left[\frac{1}{\varepsilon}-\frac{1}{\varepsilon^2}\right]\right\}\;\left[\frac{10^{24}\,\text{barns}}{\text{atom}\cdot\text{steradian}}\right] \tag{2.52}$$

If we define, in the fashion of eq. 2.42

$$f(\varepsilon,\lambda) = \alpha_1 f_1(\varepsilon,\lambda)g_1(\varepsilon,\lambda) + \alpha_2 f_2(\varepsilon,\lambda)g_2(\varepsilon,\lambda) \tag{2.53}$$

where the α´s, f´s and g´s are given by:

$$\alpha_1 = \frac{\lambda+2}{9\lambda+2}, \qquad \alpha_2 = \frac{\lambda}{9\lambda+2},$$
$$f_1(\varepsilon,\lambda) = \frac{\lambda}{2}, \qquad f_2(\varepsilon,\lambda) = \frac{\lambda+2}{2\varepsilon^2}, \tag{2.54}$$
$$g_1(\varepsilon,\lambda) = 4\left[\frac{1}{\varepsilon} - \frac{1}{\varepsilon^2}\right], \quad g_2(\varepsilon,\lambda) = \frac{1}{2}\left[(1-\lambda(\varepsilon-1))^2 + \frac{1}{\varepsilon}\right]$$

equation 2.52 can be expressed as:

$$\frac{d({}_e\sigma_C^{KN})}{d\Omega} = \frac{r_e^2}{2}\left(\frac{9\lambda+2}{2\lambda(\lambda+2)}\right) f(\varepsilon,\lambda) \quad \left[\frac{10^{24}\,\text{barns}}{\text{atom}\cdot\text{steradian}}\right] \tag{2.55}$$

For a given wavelength, the cross section per unit solid angle is equal to the function $f(\varepsilon,\lambda)$ except for a constant, and we may sample the relative Compton wavelength change from eqns. 2.53 and 2.54, using the composition + rejection method described earlier. The distributions f_1 and f_2 are easily sampled using the inverse method:

$$F_1(\varepsilon) = \frac{\lambda}{2}(\varepsilon-1) \;\Rightarrow\; \varepsilon = \frac{2\rho}{\lambda}+1$$
$$F_2(\varepsilon) = \frac{\lambda+2}{2}\left(1-\frac{1}{\varepsilon}\right) \;\Rightarrow\; \varepsilon = \frac{2+\lambda}{2\rho+\lambda} \tag{2.56}$$

where the ρ´s are uniform random numbers[1]. After a successful completion of the composition + rejection algorithm, the scattering angle θ and the wavelength λ' of the scattered photon may be found using eq. 2.51.

Accuracy of Monte Carlo method

Analog Monte Carlo is akin to an experiment in the sense that the results are subject to statistical fluctuations, in contrast to average values obtained by analytical calculations. In general, we attempt to estimate the probability p of a given event, such as the escape of a photon from a shield surrounding an isotope, by generating N photon histories and counting the number of interesting cases, i.e. the number of escaped photons, L. The quantity L/N is thus an estimate of the desired probability. This corresponds to sampling from a binomial distribution, with N trials and L successes, and the absolute and relative standard deviations of p are therefore given by [17, p. 21]:

[1]When solving $F_2(\varepsilon) = \rho$ for ε, we have utilized the fact that if ρ is uniformly distributed between zero and one, so is $(1-\rho)$.

$$\sigma_p = \sqrt{\frac{p(1-p)}{N}} \quad ; \quad \frac{\sigma_p}{p} = \sqrt{\frac{(1-p)}{pN}} \tag{2.57}$$

It is seen that the relative standard error is inversely proportional to the square root of the number of trials *N*, i.e. the number of photon histories. This means that reducing the relative error by an order of magnitude requires increasing the number of photon histories by two orders of magnitude; thus the accuracy of the Monte Carlo method is limited by the available computer resources[1]. We also note that the smaller the probability to be estimated, the greater are the number of histories needed to achieve a given accuracy. Finally, when a numerical value for the standard error is required, it is usual to replace *p* by its estimate *L*/*N* in eq. 2.57.

Apart from errors due to statistical fluctuations, there are various others sources of error associated with Monte Carlo photon transport calculations. First, it should be remembered that no model of a physical process is perfect, so analytical expressions used for the probability distributions for the interaction processes are of course not exact.

The tabulations of cross sections and linear attenuation coefficients vs. photon energy, on which the pathlength and interaction type sampling are based, are a mixture of theoretical and experimental data, with an accuracy of about 3% for the dominating process in a given energy range; this will influence the accuracy of the Monte Carlo simulation results. In addition, interpolation is necessary to obtain values for other energies than the tabulated ones; however, the interpolation errors are believed to be insignificant.

As we have already indicated, Rayleigh scattering is ignored in our Monte Carlo modelling work; the justification for this is the low relative probability of this interaction process.

Because the model would otherwise become extremely complicated and computer time consuming, the treatment of charged particle transport is omitted. Also, emission of fluorescence X rays following photoelectric absorption have not been included in our model. The possible errors arising from these omissions, or because of any simplification of the system geometry model, will be discussed further when we describe the particular problems we have attacked by Monte Carlo.

---

[1]Some techniques exist which increase the efficiency of Monte Carlo by incorporating into the simulation information obtained by other means [10, pp. 780-789] [17, pp. 100-104]; however, they may be awkward to use when simulating complex systems.

2.5. Detection of X rays and γ rays

With the exception of Rayleigh scattering, in which the photon suffer negligible energy loss, the interaction of photons with matter generally cause transfer of energy from the photon to electrons (and positrons, in the case of pair production). These primary electrons in turn interact with other electrons, producing ionization and exitation; the total ionization is ideally proportional to the energy loss suffered by the photon. Therefore, the detection of X rays and γ rays is accomplished by detecting either the free charge or the fluorescence emission produced by ionization in the detector material following photon interaction.

In the energy range of interest to us, the important processes for detector operation are the photoelectric effect, Compton scattering and pair production; because the energy transfer from the interacting photons to the primary electrons are wildly different for these three processes, the response function of a photon detector is in general very complicated [18, pp. 24-34].

2.5.1. Energy deposition in a detector by photon interaction

Consider the situation in which a monochromatic beam of photons of energy E is incident on a detector of finite size. If a photon interact by the photoelectric effect, the photoelectron will receive a kinetic energy T_{pe} given by

$$T_{pe} = E - E_b \tag{2.58}$$

where E_b is the binding energy of the electron.

For a Compton interaction, the kinetic energy of the electron, T_c, is equal to the difference in energy between the incident and scattered photon; using eq 2.17 we find:

$$\begin{aligned} T_c &= E - E' \\ &= E\left(\frac{\frac{E}{mc^2}(1-\cos\theta)}{1+\frac{E}{mc^2}(1-\cos\theta)}\right) \end{aligned} \tag{2.59}$$

We see that the energy of the recoil electrons is distributed between zero and a maximum energy T_{cm} given by

$$T_{cm} = \frac{E}{1+\frac{mc^2}{2E}} \tag{2.60}$$

corresponding to a 180˚ scattering of the photon. The shape of the distribution may be found using the energy - angle relationship for the Compton effect (eq 2.17) and the formula for the angular distribution of the scattered photons (eq 2.20).

If the photon energy E is greater than $2 \cdot mc^2$, interaction by pair production is possible; the result is the generation of an electron-positron pair, the combined kinetic energy of which is equal to the difference between the photon energy and the sum of the rest energies for the electron and positron:

$$T_{pp} = E - 2mc^2 \tag{2.61}$$

The contribution to the primary electron energy spectrum from each group of electrons is determined by the relative probability of each interaction process for the energy and medium in question. If we assume that the photon energy is high enough for pair production to occur, the general shape of the primary electron spectrum is as in Figure 2.13.

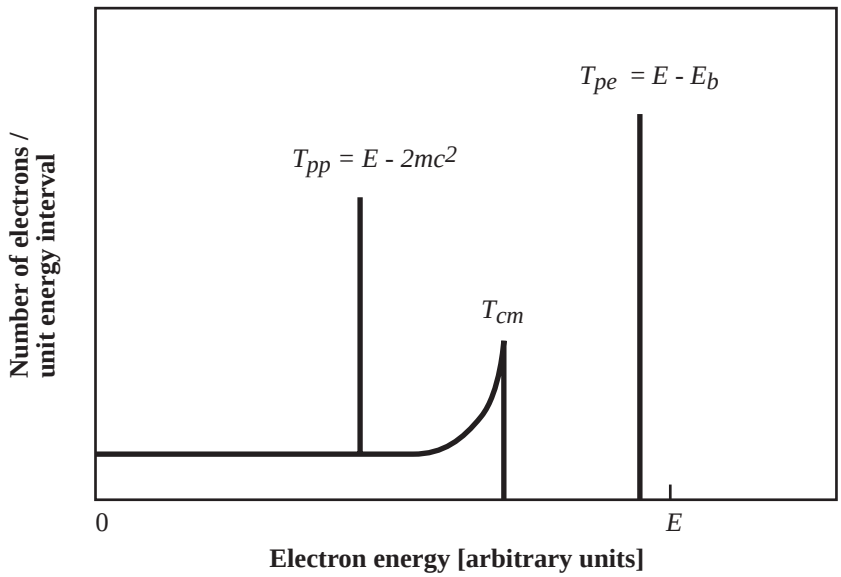

Figure 2.13 Energy spectrum of primary electrons produced by monochromatic photons of energy E ($>2mc^2$) in a detector [18, p. 33].

The situation is further complicated by the fact that characteristic photons emitted following the photoeffect, Compton scattered photons or even annihilation quanta (resulting from the positron created by pair production) may undergo further interactions in the detector. The electrons liberated in this way contribute coincidently with the primary electrons to the detected energy spectrum, the shape of which will differ from the electron spectrum shown in Figure 2.13. We will now discuss the possible combinations of interaction mechanisms.

If the interaction is by the photoeffect, the binding energy is present in the detector as a characteristic X ray (or as Auger electrons); if this is absorbed in a subsequent interaction, the total energy transferred to electrons within the detector is equal to the photon energy; thus the photon is detected in the "full energy peak". The probability for this to happen depend on the X-ray energy and the size and material type of the detector, as well as where in the detector the

interaction takes place. Some X rays will leave the detector anyway, giving rise to the so called "X-ray escape peak". The situation is shown schematically in Figure 2.14.

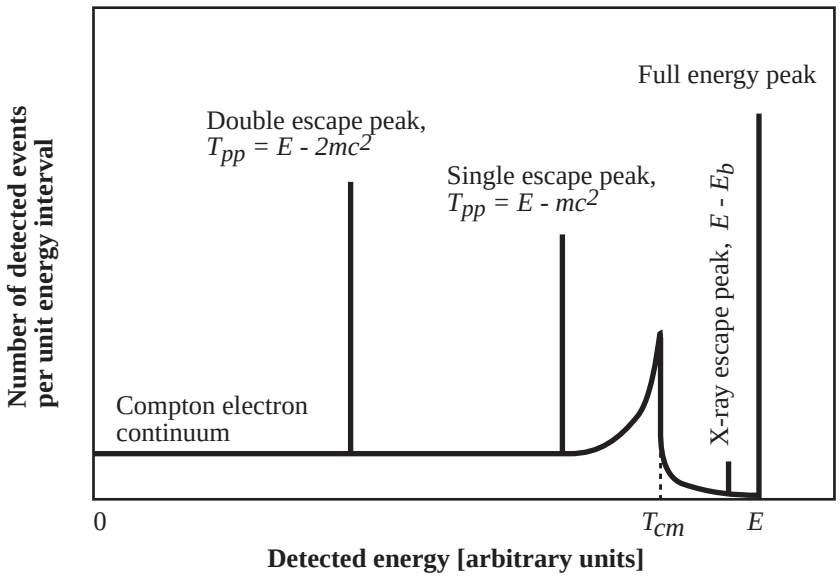

Figure 2.14 Idealized detector energy spectrum produced by monochromatic photons of energy E ($>2mc^2$). Note that the single and double escape peaks also may have associated X-ray escape peaks. The main peaks may have several X-ray escape peaks; each of which correspond to the possible characteristic X-ray energies for the different shells.

If we consider a Compton interaction, after which the scattered photon escapes the detector, the contribution to the detected energy spectrum will simply be the energy spectrum of the recoil electron alone, i.e. as the Compton continuum outlined in Figure 2.13. However, there is the possibility of the scattered photon interacting with the detector; for example, a contribution to the full energy peak in the detected energy spectrum may consist of a series of Compton scatterings followed by a photoelectric interaction. Finally, the photon may escape after several scattering events, giving a detected energy somewhere between the primary Compton electron spectrum and the full energy peak, see Figure 2.14. In general, the contribution of Compton events to the detected spectrum depends in a complex manner on the photon energy, on the detector material characteristics and geometry.

A pair production event is followed by the annihilation of the positron, producing two 0.511 MeV photons moving in opposite directions. If both are completely absorbed within the detector, the total energy deposited by the pair production/annihilation events is equal to the energy of the incident photon and there is a contribution to the full energy peak of the detector spectrum. If both annihilation quanta escape, there will be a contribution to the "double escape peak" which is the same as the T_{pp} peak in Figure 2.13; if one annihilation photon escapes and the other is totally absorbed, the event contributes to the "single escape peak", which correspond to an energy of $E - mc^2$ being deposited in the detector; see Figure 2.14. Finally, the annihilation quanta may also only partly deposit their energy, for

example by photoeffect interaction with X-ray escape, or Compton interaction with escape of the scattered photon, causing further confusion of the detected energy spectrum.

In the above discussion we have tacitly assumed that once photon energy is transferred to electrons, it is to be regarded as totally absorbed in the detector. However, electrons produced by photon interaction processes may have appreciable ranges in matter, and for high photon energy and/or small detectors there is a possibility that the electron may escape the detector before all its energy is expanded in ionizations.

2.5.2. Overview of detector types

Before discussing the performance and principles of operation for a few types of X- and γ-ray detectors, we will make a few comments on the parameters characterizing the detectors: efficiency, energy resolution, timing resolution and countrate capability.

The *total detection efficiency*, ε_{tot}, of a detector for a given photon energy E is in principle determined by the total interaction probability (or *interaction ratio*) which is equal to

$$\varepsilon_{tot} = 1 - \exp(-\mu d) \tag{2.62}$$

for a narrow monochromatic photon beam normally incident on a detector of thickness d. It may be defined as the probability that a photon striking the detector will produce a counted event. However, the energy with which the event is registered may be anywhere in the spectrum outlined in Figure 2.14. Therefore, the *full energy*, or *photopeak*, detection efficiency, ε_p, is often of greater interest for many applications; this is defined as the ratio of the number of events registered in the full energy peak to the number of (monochromatic) photons striking the detector. The photopeak efficiency depends on the photon energy and the geometry and material of the detector; in general, high density, high-Z materials improve the efficiency. Finally, the *photofraction* ε_0 is defined as the fraction of detected events that is registered in the full energy peak; the photofraction is seen to be equal to $\varepsilon_p/\varepsilon_{tot}$.

The *energy resolution* R, or the ability of the detector to distinguish between photons with nearly equal energy, is often the most important parameter characterizing a detector. It is defined as

$$R_{\%} = 100 \times \frac{FWHM}{E} \tag{2.63}$$

where FWHM is the linewidth (full width at half maximum) of the observed full energy peak resulting from a monochromatic photon beam of energy E. The resolution of a detector is generally energy dependent; hence, R is always specified for a given E.

The *timing resolution* of a detector determine how closely spaced in time two photons may be and still be registered as separate events. Its limit is determined by the charge collection time of the detector (or scintillation decay time, see below). Generally, there is a trade off between timing and energy resolution, because the time constant of the readout electronics may be set shorter than the detector charge collection time to improve timing resolution; however this reduces the signal/noise ratio and hence the energy resolution.

The *countrate capability* of a detector may be defined as the maximum intensity for which the difference between the number of interacting photons and the number of registered events is acceptably small, or alternatively, as the maximum countrate for which the worsening of the energy resolution is acceptable. In any case, the countrate capability is limited by the charge collection time (or scintillation decay time) of the detector and the performance of the readout electronics.

We will now discuss some X- and γ-ray detector types in the light of the comments of the above paragraphs.

Gas filled detectors

Basically, this is a metal case filled with gas (usually, noble gases are used), also containing an anode wire, which is positively biased with respect to the case. When the photons traverse the gas, the various interaction mechanisms produce electrons and positive ions, which are attracted to the anode wire and the case (cathode), respectively. Thus an electric pulse is generated, which is then registered by suitable electronic circuitry. Because the absorbing medium of this detector is a gas, its detection efficiency decreases rapidly as the photon energy increases.

The gas detector can be operated in three different modes, depending on the magnitude of the bias voltage applied. At low voltages, when the bias is just adequate to collect all the charge before the electrons and ions recombine and is lost, the detector is known as an ionization chamber. Because the signals generated are very small, this mode is most often used for detecting high photon fluxes, which can generate high total currents.

When the bias voltage is increased, electrons are accelerated towards the anode, acquiring enough kinetic energy to produce further ionization in the gas, and the original signal is thus amplified. In this range, individual photons may easily be detected, and there is proportionality between the photon energy and the output signal. This type of gas detector is called a proportional counter. It is used in the X-ray range and has moderate energy resolution, which is limited by statistical fluctuations in the amplification process.

At even higher bias voltages, the amplitude of the output signal is independent of the initial amount of ionization produced by the photon. A detector operated in this mode has no energy discrimination capability and is known as a Geiger-Müller counter.

The countrate capability of the gas detector is limited by the charge collection (ion drift) time; this is usually in the 1-10 μs range, varying with gas type, bias voltage and detector size. For the Geiger-Müller counter there is the additional problem that, due to the extreme amplification, the detector is driven into continuous discharge: This must be quenched by using a halogen gas mixture or special electronic circuitry; the detector may require hundreds of microseconds to recover [19, p. 6].

Semiconductor detectors

Semiconductor detectors, or "solid state" detectors, SSD's, basically have a PIN diode structure, where the insintric (I) region is created by the application of a reverse bias voltage across the diode; the region is depleted of free charge carriers because the holes and electrons are swept away by the electric field. When a photon interact within the depletion zone, free charge carriers are created and are collected by the electric field (analogous to the principle of operation of the gas detector) to the anode and cathode of the diode. The charge accumulated across the diode is then detected by a charge sensitive amplifier, which produces a proportional voltage pulse.

Silicon (Si) and Germanium (Ge), which have atomic numbers $Z = 14$ and $Z = 32$, respectively, are the commonly used materials for semiconductor detectors. The amount of dissipated energy required to liberate an electron-hole pair is 3.61eV for Si and 2.98eV for Ge at room temperature; these values are independent of the bias voltage and only very slightly temperature dependent, resulting in excellent stability. Furthermore, a very high number of charge carriers are produced since little energy is required per electron-hole pair; this means that fluctuations in charge carrier production are small and the result is excellent energy resolution. The other contributions to the linewidth are preamplifier noise, and electronic noise caused by the reverse leakage current of the detector.

Efficient detection of energetic X rays and γ rays require large volume detectors, and because the reverse leakage current (caused by thermal generation of charge carriers) of SSD's is proportional to the depletion volume, they are usually operated at liquid nitrogen temperature (77 K) to minimize the contribution of this noise to the linewidth. Often, the input FET of the preamplifier is cooled as well to reduce amplifier noise.

The energy resolution of Si and Ge detectors is extremely good, making them first choice for X-ray and γ-ray spectroscopy, respectively. The countrate capability and timing resolution

are determined by the amplifier time constant and the charge collection time of the detectors; the latter is usually a few microseconds. Countrates up to about 100 cps (counts per second) are possible without too much worsening of the energy resolution.

It should also be mentioned that thin, small area Si detectors (e.g. 100 mm^2 area and 300 μm thickness) may be operated at room temperature because the small depletion volume ensure low leakage current anyway; although such devices are primarily used for charged particle detection, they may be used to detect photons with energy of a few tens of keV. There has also been some interest in using other semiconductor materials as room temperature detectors: Cadmium Telluride (CdTe), which has a higher bandgap than Si and consequently lower leakage current, has been used for making detectors having reasonable detection efficiency for photon energies up to about 100 keV, with moderate energy resolution.

Scintillation counters

A scintillation counter detector exploits the fact that some solids, liquids and gases emit UV or visible light when they are exposed to radiation [18]. The intensity of the light pulse is (ideally) proportional to the energy deposited in the detector by the interacting X- or γ-ray photons. A light detection device, such as a photomultiplier tube (PMT) or a photosensitive diode, may then be used to obtain an electric pulse proportional to the light intensity, and hence, the X- or γ-ray energy.

The desirable properties of a scintillation crystal[1] are good stopping power, high conversion efficiency (i.e. the fraction of X- or γ-ray energy converted to scintillation photon energy), good transparency for the scintillation light and short light pulse decay time.

Several of the common scintillation materials are of high density and atomic number, and because the fabrication of rather large detectors is possible, a scintillation detector is often chosen when optimum stopping power is required.

There are several factors affecting the energy resolution: First, there are fluctuations in the number of emitted scintillation photons and to some degree nonlinearity between the intensity of the emitted light and the energy deposited by X and γ rays. Second, the collection and transfer of light to the readout device may be nonuniform. Third, there is the contribution to the linewidth from the readout device itself: for PM tube readout, fluctuations in the electron multiplication process set the limit for the resolution, whereas in the case of semiconductor

[1]Not all solid scintillation materials are crystalline, but the term “scintillation crystal” is often used nevertheless.

photodiode readout, the resolution is mainly determined by the electronic noise in the diode and the associated charge amplifier. In any case, the best possible scintillation conversion efficiency is desired, as this will maximize the output signal amplitude and reduce the relative linewidth.

The possible timing resolution is determined by the decay time of the scintillation pulse; most scintillator crystals have decay times ranging from a few hundred nanoseconds to a few microseconds, but plastic (organic compound) scintillators exist which have decay times of a few nanoseconds. For a sub-microsecond decay time scintillator, countrates of 10^5–10^6 cps may be achieved using either PM tube or photodiode readout; if the energy resolution requirement is relaxed and a fast PM tube is used, timing resolution in the nanosecond range is possible. Plastic scintillators are used for sub-nanosecond timing, at the expense of poorer detection efficiency.

In applications where the photon flux is very large and the energy of the individual photons is uninteresting, both PM tubes and photodiodes may by operated in "current mode"; that is, one measures the total continuous current through the readout device; this current is proportional to the total energy flux in the detector.

Summary

If we consider energy discriminating devices only, the following conclusions may be drawn from the above discussion of detector types:

- Proportional gas detectors and room temperature semiconductor detectors are suitable for X-ray measurements where moderate energy and timing resolution is adequate.
- Cryogenic Si and Ge detectors are suitable for X- and γ-ray measurements in applications where excellent energy resolution is at premium; however, the cooling system adds to their complexity and make them rather less than compact. The detection efficiency is limited at higher energy, because of their low atomic numbers and the fact that fabrication of very large crystals is difficult.
- Scintillation detectors offer moderate to good resolution, excellent detection efficiency and timing capabilities over entire γ-ray range. As for the type of readout device, PM tubes offer better timing capabilities in general, and better energy resolution at lower photon energies, but unlike photodiodes, they are bulky and sensitive to magnetic fields and temperature variations. Thus compactness and stability are the attractive properties of photodiode readout scintillation detectors.

2.6. γ-densitometry

The average density of an absorber may be found by measuring the attenuation of a photon beam passing through it; this technique is called γ-densitometry. We will now describe very briefly the general principle of the method and the main sources of error associated with it.

2.6.1. Basic principles

If we consider the attenuation of a narrow, monochromatic photon beam traversing a slab of inhomogeneous material of thickness *d*, the number of transmitted photons is (see eq 2.5 and Figure 2.1)

$$n = n_0 \exp\left\{ -\int_0^d \mu_{tot}(x)\,dx \right\} \tag{2.64}$$

where n_o is the number of photons incident on the slab. The average linear attenuation coefficient (along the photon beam direction) of the inhomogeneous medium can therefore be found by performing an attenuation measurement; it is given by:

$$\bar{\mu}_{tot} = \frac{1}{d}\int_0^d \mu_{tot}(x)\,dx = \frac{1}{d}\ln\left(\frac{n_0}{n}\right) \tag{2.65}$$

By eq 2.7 and eq 2.22, the total linear attenuation coefficient (for a given photon energy) of an element is equal to

$$\mu_{tot} = \rho\,(\tau_{pe} + \kappa_n + \sigma_C + \sigma_R)\frac{N_A}{M} \tag{2.66}$$

where the cross sections for the individual attenuation processes depend in different ways on the atomic number of the material. However, if Compton scattering is the dominating interaction process, we may write

$$\mu_{tot} = \rho Z\,\sigma_C^{KN}\frac{N_A}{M} \tag{2.67}$$

where we have used the Klein-Nishina formula for the Compton interaction cross section for a single electron (eq 2.19 with $Z = 1$). The justification for this is that the binding effect error of the Klein-Nishina expression is negligible in the Compton dominated region, see Figures 2.6 and 2.9. The cross section depends on energy only, and since N_A is a constant and Z/M is nearly constant (0.45±0.05 for all elements except Hydrogen, for which $Z/M = 1$), we see that the density is approximately proportional to the linear attenuation coefficient, for photon energies and media where Compton scattering is the dominating interaction mechanism. Thus, we may write:

$$\mu_{tot} \approx \rho \, {}_e\sigma_C^{KN} N_A k_r \quad ; \quad \frac{Z}{M} \approx k_r = 0.45 \tag{2.68}$$

If we consider the attenuation coefficient of a chemical compound or mixture and assume that photon interactions are mainly by Compton scattering, the following is true (see eq 2.13):

$$\begin{aligned} \mu_{mix} &= \rho_{mix} N_A \frac{\sum_{\forall i} \sigma_{C_i}^{KN} x_i}{\sum_{\forall i} M_i x_i} \\ &\approx \rho_{mix} \, {}_e\sigma_C^{KN} N_A \frac{\sum_{\forall i} Z_i x_i}{\sum_{\forall i} \frac{Z_i}{k_r} x_i} \\ &= \rho_{mix} \, {}_e\sigma_C^{KN} N_A k_r \end{aligned} \tag{2.69}$$

where we have used $Z_i/M_i \approx k_r$. Hence, proportionality between the linear attenuation coefficient and absorber density may be assumed also for chemical compounds or homogeneous mixtures.

To ensure that our assumption of Compton scattering being the dominating interaction process is valid, it is necessary to restrict the photon energy E to the range 0.1 to 10 MeV, and to require that the atomic number Z of the absorber is less than 20. A look at Figures 2.9(b) and (c) also reveal that no totally Compton-dominated energy range exist for high Z materials.

We may now combine eq 2.65 and eq 2.68 (see also eq 2.69) to obtain an approximate formula for the average density, valid within the above limits for E and Z :

$$\bar{\rho} = \frac{1}{d}\int_0^d \rho(x)dx \approx \frac{\bar{\mu}_{tot}}{N_A k_r ({}_e\sigma_C^{KN})} = \frac{\ln(n_0/n)}{d N_A k_r ({}_e\sigma_C^{KN})} \tag{2.70}$$

This expression is of fundamental importance in γ-densitometry: It states that, under certain restrictions of the atomic number of the medium and the photon energy used, the average density along a path through an absorber may be found by performing a measurement of the attenuation of a narrow monochromatic γ beam traversing the medium in the same direction[1].

---

[1]There is a definite advantage of using the monochromatic photon beam from a γ source instead of an X-ray tube generated beam, as the latter introduces the problem of "beam hardening": An X-ray tube has a broad, continuous photon emission energy spectrum; because the low energy photons are removed more quickly from the beam than the higher energy photons, the average attenuation coefficient for the *beam* decreases as it penetrates deeper into the absorber.

It should be noted that although the proportionality factor between the average density and the average linear attenuation coefficient can be evaluated directly from eq 2.70, it is usually found by a calibration measurement. Therefore, when we study the practical problems and the accuracy of γ-densitometry, we will discuss them in terms of linear attenuation coefficient measurement.

2.6.2. Practical problems of attenuation coefficient measurement

When deriving the formula for the attenuation of a photon beam, eq 2.5, it was assumed that the photon beam is monochromatic and infinitesimally narrow, see Figure 2.1. In practice, this is not the case; a more realistic situation is outlined in Figure 2.15:

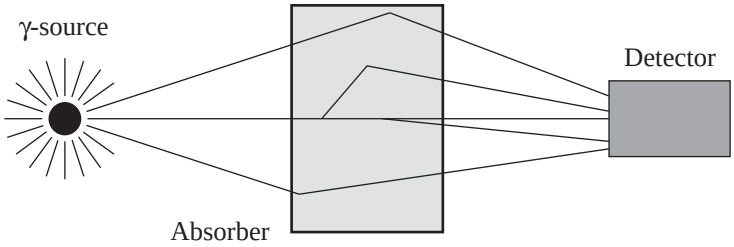

Figure 2.15 How measurement of the linear attenuation coefficient of an absorber is complicated by single or multiple photon scattering and finite beam width effects.

It is seen that practical linear attenuation coefficient measurement is complicated by two factors: First, as the source emits photons in all directions, and both the source and the detector are of finite size, the photon beam is no longer infinitesimally narrow; second, the photons detected are no longer primary source photons only, but scattered photons as well. We will now discuss these problems separately.

Finite beam width effects

For finite size sources and detectors, the pathlength travelled by the photons through the absorber is not constant and equal to the absorber thickness *d*, but varies from this value and upwards, depending on where in the source a photon is emitted and where it hits the detector. This may introduce a small error in the measured attenuation coefficient, but is usually insignificant, provided that the photon beam is approximately parallel; this is ensured by keeping the source-detector distance large compared to the detector and source widths.

If the attenuation coefficient varies across the beam width at a given depth within the absorber, an error is introduced in the calculated μ (eq. 2.65) even under parallel beam conditions, because of the exponential attenuation of a photon beam. This error may be significant if the nonuniformity is severe; the error is minimized by keeping the beam width small compared to the absorber thickness. We will discuss this effect further in Chapter 4.

Scattered photons

The detection of scattered photons introduces an error in the measured attenuation coefficient, because the total number of detected photons is clearly greater than the number of directly transmitted primary source photons (see Figure 2.15). We will now discuss two different techniques for reducing this error.

The first method is to use a collimated photon beam to approximate narrow beam conditions; this principle is shown schematically in Figure 2.16.

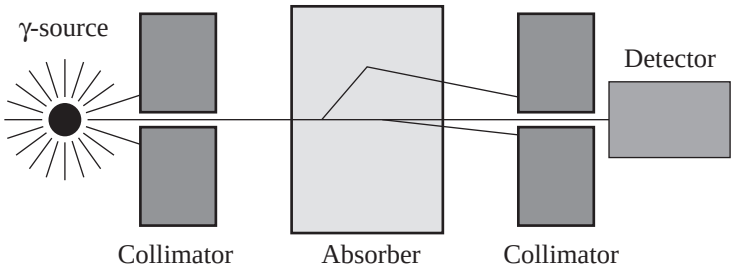

Figure 2.16 Using collimators to prevent the detection of unwanted scattered radiation when measuring the linear attenuation coefficient of an absorber.

Narrow-aperture collimators, made of high density, high-*Z* materials like lead or tungsten (which have large attenuation coefficients), are put between the γ-source and the absorber, and between the absorber and the detector. In this way, most of the unwanted scattered radiation is prevented from reaching the detector, and an ideal narrow beam geometry is approximated; the effective beam width is determined by the size of the collimator apertures.

The other technique, which we may call "energy filtering", exploits the fact that a Compton-scattered photon have a lower energy than the primary, or unscattered photons (eq 2.17). By using an energy-discriminating detector, it is possible to avoid counting scattered photons, and the assumption of a monochromatic beam is once again valid[1]. The effective width of the photon beam is in this case determined by the size of the source and the detector.

How effectively this method reduces errors due to scattered photons, depends on the γ-energy used and the energy resolution of the detector. From eq 2.17 we see that the energy loss of the scattered photon depends on the energy of the primary photon; for a given angle, the energy loss is greater for higher primary energies. This is clearly seen from Figure 2.17,

[1]Even though Rayleigh scattered photons do not suffer any significant energy loss, and hence cannot be "energy-filtered" away, they may be safely ignored, because the Rayleigh interaction cross section is negligible in the Compton-dominated energy range under consideration.

where we have plotted the ratio between scattered and incident photon energies, as a function of scattering angle and incident photon energy.

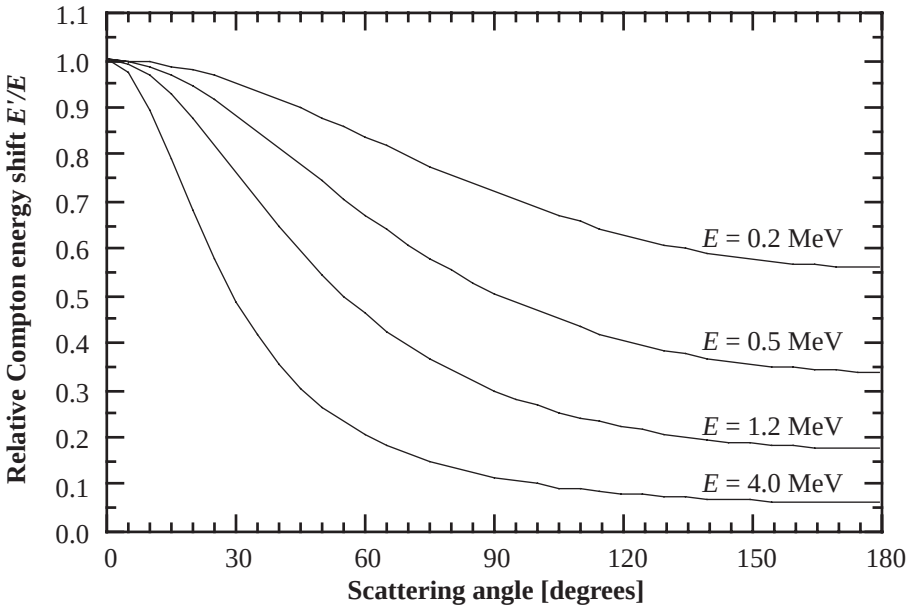

Figure 2.17 Relative energy shift of Compton-scattered photon, E'/E; plotted against scattering angle θ and with the energy E of the incident photon as a parameter.

Hence, if the detector is supposed to discriminate against photons scattered a given angle, better relative energy resolution is required at lower primary photon energies than at higher energies. This is counteracted to some degree by the fact that the angular distribution of the scattered photons (eq 2.20 and Figure 2.7) gets increasingly forward peaked for higher incident photon energy; still, it is clear that a detector having good energy resolution is required for the energy filtering method.

2.6.3. Statistical fluctuation error and choice of isotope

The nuclear decay of an isotope occur randomly in time; because of this, a measurement of a number of events during a given time interval will not be exact, but instead it represents an average value with some uncertainty. Nuclear decay processes follow a Poisson distribution, which states that the probability of observing N events if the average is $\overline{N}$ is equal to

$$P_N = \frac{\overline{N}^N \exp(-\overline{N})}{N!} \tag{2.71}$$

and that the standard deviation of N is given by:

$$\sigma_N = \sqrt{\overline{N}} \tag{2.72}$$

When eq 2.65 is used to calculate the linear attenuation coefficient, it is assumed that n_o and n are measured during equal periods of time, but in many cases this is not so; it is then

convenient to use measured intensity (the number of photons per unit time) instead of using the number of detected photons directly. The measured intensity and its standard deviation are given by

$$I = \frac{n}{\tau} \quad ; \quad \sigma_I = \frac{\sqrt{n}}{\tau} \tag{2.73}$$

where n is the number of photons and τ is the measurement time. The formula for the linear attenuation coefficient is then:

$$\mu = \frac{1}{d} \ln\left(\frac{I_0}{I}\right) \tag{2.74}$$

where I_o and I are the incident and transmitted intensities, respectively.

We will now consider the effect of statistical fluctuations in the measured intensities on the accuracy of the calculated linear attenuation coefficient. Assuming that the absorber thickness is known exactly, the standard deviation of the linear attenuation coefficient is given by:

$$\sigma_\mu = \frac{1}{d}\sqrt{\frac{1}{I_0}\left(\frac{1}{\tau_0} + \frac{\exp(\mu d)}{\tau}\right)} \tag{2.75}$$

where τ and τ_0 are the measurement periods for I and I_0, respectively. We see that the uncertainty in the measured attenuation coefficient is proportional to the inverse of the square root of the incident beam intensity I_o, which in turn is proportional to the γ-source intensity. To study the variation of the uncertainty with μ and d, it is more convenient to use the expression for the relative error:

$$\frac{\sigma_\mu}{\mu} = \frac{1}{\mu d}\sqrt{\frac{1}{I_0}\left(\frac{1}{\tau_0} + \frac{\exp(\mu d)}{\tau}\right)} \tag{2.76}$$

Alternatively, if the incident beam intensity, I_0, is measured during much longer time than the transmitted intensity I, the fluctuations in I_0 contribute negligibly to the relative error (see eq 2.73), which is then given by:

$$\frac{\sigma_\mu}{\mu} = \frac{1}{\mu d}\sqrt{\frac{\exp(\mu d)}{I_0 \tau}} \tag{2.77}$$

We see that the ratio of these two expressions approach unity for large μd, but also that the relative error is slightly less for small μd when eq 2.77 is used; that is, when the incident intensity I_0 is measured over much longer time than the transmitted intensity I. Equation 2.77 is plotted in Figure 2.18.

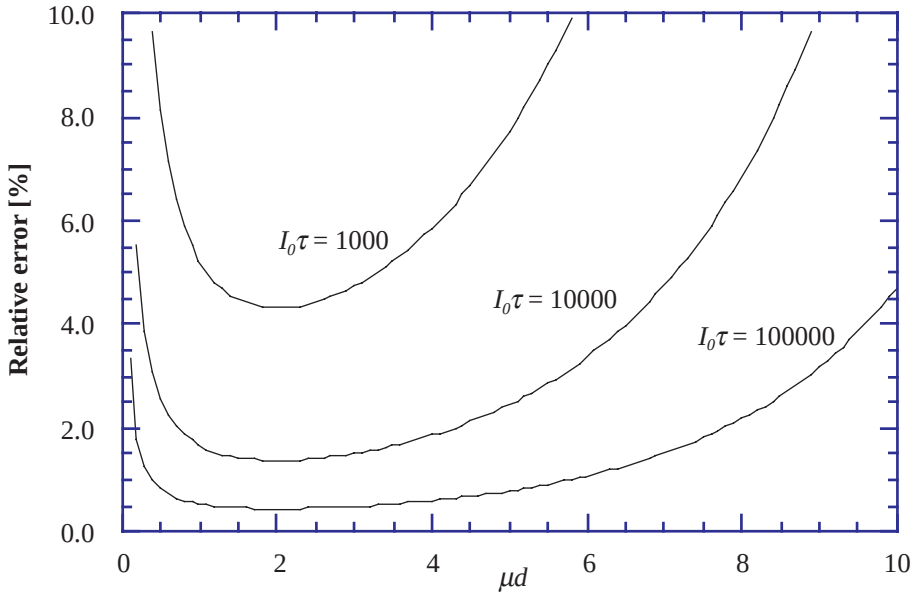

Figure 2.18 Relative error σ_μ/μ due to statistical fluctuations in the measured beam intensity I, assuming that incident intensity I_0 is known without error (eq 2.77); plotted against μd and with the product $I_0\tau$ as a parameter.

The above expressions for the relative error may be used to select the optimum γ-energy for a given application, by finding the energy corresponding to the optimum value of μd. The value of μd which minimizes the relative error is 2.2 for eq 2.76 and 2.0 for eq 2.77, respectively; however, it is seen from Figure 2.18 that the minimum of the relative error curve is rather shallow, so the actual value of μd is not very critical. Therefore, it is usually possible to find a suitable γ-source, although the range of isotopes is limited in practice, especially when the isotope lifetime requirement is taken into account.

The required source activity is determined by the maximum acceptable level of statistical error, the measurement time, the detector efficiency and the solid angle subtended at the source by the detector.

3. Basic principles of CT

3.1. Introduction

For our purposes, computerized tomography (CT) may be defined as the reconstruction of the density distribution function of a two-dimensional object from a set of "one-dimensional" density measurements called *raysums*, in many directions through the object. The theory of the reconstruction techniques used is a well developed topic within applied mathematics; the rapid progress of this field has mainly been motivated by the widespread use of CT in medical applications.

We will need some background for our system geometry and reconstruction analysis work in Chapter 4; therefore, we will now give a brief overview of the mathematical methods used for CT image reconstruction, mainly based on the review article by Brooks and DiChiro [20], but also on [21] and [22]. However, we will first take a look at some types of data collection systems used in medical CT scanning.

3.2. CT scanning methods

In medical CT, the raysums are found by measuring the attenuation of an X-ray beam. The first generation of scanners used a single X-ray source and detector in a translate-rotate system, which measure a single raysum, or *chordal density*, at a time; see Figure 3.1.

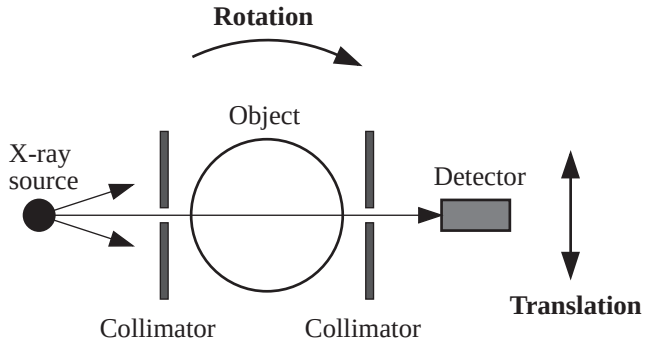

Figure 3.1 Single source, single detector translate-rotate parallel beam scanner.

Because it is desirable to minimize the radiation exposure to the patient and reduce the scanning time, more efficient scanning geometries have been developed, such as the rotating fan beam scanner (Figure 3.2) and the stationary detector ring scanner (Figure 3.3).

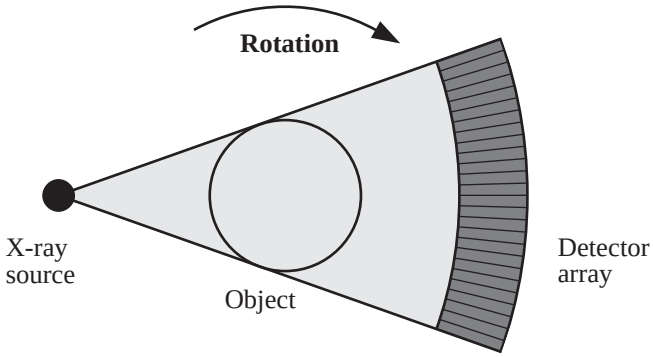

Figure 3.2 Original fan beam scanner: The source and the detector array rotate around the object.

The standard fan beam scanner uses one X-ray source and an opposing array of detectors, both of which are rotated around the stationary object. In this way, several raysums are measured simultaneously (one for each detector in the array) and the scanning time is reduced drastically.

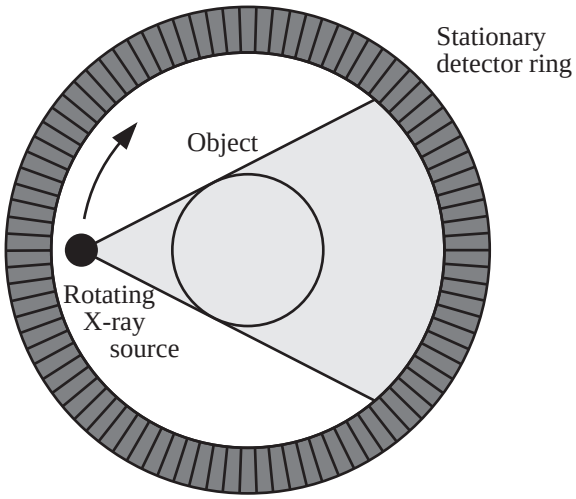

Figure 3.3 Stationary detector ring scanner: Only the X-ray source is rotated, making faster scanning possible.

Even shorter scanning times can be achieved by using the stationary detector ring scanner. At the expense of the large number of detectors needed, this technique offers very fast data collection: Because only the source need to be rotated, very fast rotation may be used, resulting in short scanning time.

For the translate-rotate system in Figure 3.1, the raysums for a given rotation angle are parallel; hence, the term “parallel beam” geometry is used to describe this scanning scheme. The scanners of Figures 3.2 and 3.3, however, collect data in the “fan beam” geometry; this simply means that, for a given rotation angle, the raysums are measured in directions diverging from the source.

3.3. Reconstruction of a function from projections

We will now turn to a mathematical description of image reconstruction methods; for simplicity, the derivations are for the parallel beam geometry, but all techniques have been adapted to fan beam systems as well.

For the parallel beam geometry, the coordinate systems used are shown in Figure 3.4, see [20, p. 696]:

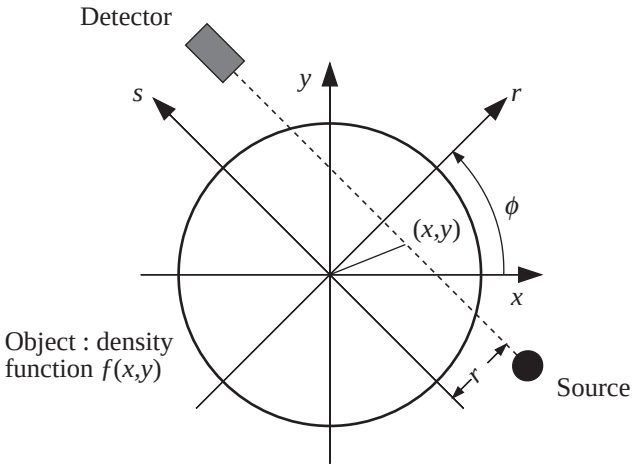

Figure 3.4 Coordinate systems for parallel beam geometry: The density function f of the object is specified in a fixed (x,y) system. Rays (source-detector line) are specified in a rotated coordinate system by the rotation angle ϕ and the normal distance r from the origin to the ray. The variable s represents distance along the ray.

We see that the path of a ray is specified in (r,s) coordinates, rotated an angle ϕ with respect to the (x,y) system. For a given rotation angle, a ray is specified by the r variable. The object is described by the density function[1] $f(x,y)$. We may now define a raysum p, or chordal density measurement, as the line integral of the density function along the ray:

$$p(r,\phi) = \int_{r,\phi} f(x,y)ds \tag{3.1}$$

The set of raysums for varying r but fixed ϕ is known as a projection; hence, equation 3.1 is often called the projection equation.

We see that reconstruction of an image requires the projection equation to be solved for the density function; ideally, f is a continuous function in x and y, so an exact solution would require an infinite number of projections (and an infinite number of rays per projection),

[1]The term "density" is not to be taken too literally; in X-ray imaging, it would represent the average linear attenuation coefficient.

which is clearly impossible. Therefore, all reconstruction algorithms must somehow limit the spatial resolution of the image in order to make reconstruction possible; in practice, a finite number of projections is available, and the density function is reconstructed at a finite number of points.

Reconstruction methods may be classified according to how they attempt to solve the projection equation and how they incorporate the necessary spatial resolution limiting. Basically, there are two different classes of techniques; in the first, the projection equation is solved directly, or analytically, but bandwidth limiting of the density function is incorporated in the numerical implementation; in the second, the object function is discretized before the density function is reconstructed. We will now describe these methods separately.

3.3.1. Direct solution of projection equation: Analytic reconstruction

Analytic reconstruction methods attempt to solve the projection equation (eq 3.1) directly. The starting point for the derivation of these methods is the fact that the object density function $f(x,y)$ may be written as a two-dimensional Fourier integral

$$f(x,y) = \int_{-\infty}^{\infty}\int_{-\infty}^{\infty} F(k_x,k_y)\exp[2\pi i(k_x x + k_y y)]dk_x dk_y \tag{3.2}$$

i.e. $f(x,y)$ is represented by a superposition of sinusoids, with spatial frequencies (wavenumbers) k_x and k_y in the x and y directions, respectively. We also have

$$F(k_x,k_y) = \int_{-\infty}^{\infty}\int_{-\infty}^{\infty} f(x,y)\exp[-2\pi i(k_x x + k_y y)]dxdy \tag{3.3}$$

We now transform this integral from the (x,y) system to the (r,s) coordinates; from Figure 3.4 we have

$$\begin{aligned} x &= r\cos\phi - s\sin\phi \\ y &= r\sin\phi + s\cos\phi \end{aligned} \tag{3.4}$$

where ϕ is the angle of rotation of the (r,s) system. If we define

$$\begin{aligned} \phi &= \arctan\left(\frac{k_y}{k_x}\right) \\ k &= \sqrt{k_x^2 + k_y^2} \end{aligned} \tag{3.5}$$

the spatial frequencies can be written:

$$\begin{aligned} k_x &= k\cos\phi \\ k_y &= k\sin\phi \end{aligned} \tag{3.6}$$

Using this, we may write eq 3.3 as:

$$F(k_x,k_y) = \int_{-\infty}^{\infty}\int_{-\infty}^{\infty} f(x,y)\exp(-2\pi ikr)drds \tag{3.7}$$

Exchanging the order of integration and using eq 3.1 we find:

$$\begin{aligned} F(k_x,k_y) &= \int_{-\infty}^{\infty}\left\{\int_{-\infty}^{\infty} f(x,y)ds\right\}\exp(-2\pi ikr)dr \\ &= \int_{-\infty}^{\infty} p(r,\phi)\exp(-2\pi ikr)dr \\ &\Downarrow \\ F(k_x,k_y) &= P(k,\phi) \end{aligned} \tag{3.8}$$

Here, $P(k,\phi)$ is the Fourier transform of $p(r,\phi)$ with respect to r. Equation 3.8 states that the Fourier coefficient , or wave amplitude, of the density function in the direction specified by the angle of rotation ϕ, is equal to the Fourier transform of the projection taken in the same direction. This equation is the basis for all analytical reconstruction methods.

2D Fourier method

The 2D Fourier reconstruction method is based directly on Equation 3.8: By taking the one-dimensional transform of the projections $p(r,\phi)$, $P(k,\phi)$ is found; the density function $f(x,y)$ is then found by taking the inverse two-dimensional Fourier transform of $F(k_x,k_y) = P(k,\phi)$. Of course, only a finite number of projections are available, each specified at a finite number of values of r, so discrete Fourier transforms (DFT) must be used. This is where the bandwidth limiting is introduced: By the sampling theorem, the DFT is exact, provided the object function $f(x,y)$ does not contain spatial frequencies greater than

$$k_{\max} = \frac{1}{2w} \tag{3.9}$$

where w is the pixel width, or spacing between the reconstruction points.

Because the DFT's can be computed using the FFT algorithm, the Fourier reconstruction method is potentially very fast. The major problem of the method is that the inverse 2D transform require the Fourier coefficients to be known on a rectangular grid, that is, as $F(k_x,k_y)$, whereas $P(k,\phi)$ (computed from measured projections) is specified on a polar grid. Therefore, interpolation is required, which adds some computational overhead because it must

be done fairly accurately to avoid errors in the reconstructed image (see [20, p. 709] and [21, p. 120]).

Filtered Backprojection

To explain how this technique works, we will first take a look at a very crude "reconstruction" method called backprojection, which is described mathematically by the following expression:

$$\hat{f}(x,y) = \int_0^{\pi} p(r,\phi)d\phi = \int_0^{\pi} p(x\cos\phi + y\sin\phi, \phi)d\phi \tag{3.10}$$

Thus, the value of the approximate object function as "reconstructed" by backprojection in the point (x,y), is simply the sum of the values of all projections in this point; that is, each projection contribute with the value of the raysum passing through the point. It is obvious that this method cannot be very accurate, as the full value of each raysum is added indiscriminately to *all* points along the ray, and not only where "needed", i.e. to the high density points of the object function.

However, if we write

$$p(r,\phi) = \int_{-\infty}^{\infty} P(k,\phi)\exp(2\pi ikr)dk \tag{3.11}$$

we can express eq 3.10 as:

$$\begin{aligned}\hat{f}(x,y) &= \int_0^{\pi}\left\{\int_{-\infty}^{\infty} P(k,\phi)\exp(2\pi ikr)dk\right\}d\phi \\ &= \int_0^{\pi}\int_{-\infty}^{\infty} \frac{P(k,\phi)}{|k|}\exp(2\pi ikr)|k|dkd\phi\end{aligned} \tag{3.12}$$

This double integral is in the form of an inverse 2D Fourier transform in polar coordinates (k,ϕ); i.e. we have

$$\begin{aligned}&\hat{F}(k_x,k_y) = \frac{P(k,\phi)}{|k|} \\ &\qquad\Downarrow \\ &F(k_x,k_y) = P(k,\phi) = \hat{F}(k_x,k_y)|k|\end{aligned} \tag{3.13}$$

where we have used eq 3.8. Equation 3.13 suggests that backprojection could perhaps work if the projections $p(r,\phi)$ are modified before they are backprojected. This technique is called filtered backprojection (FBP); as an example, we will now consider the most frequently used variation of this method.

FBP with convolution filtering

If equation 3.2 is transformed to polar coordinates (r,ϕ) and (k,ϕ), we have:

$$f(x,y) = \int_0^{\pi} \int_{-\infty}^{\infty} P(k,\phi) \exp(2\pi i k r) |k| dk d\phi \tag{3.14}$$

We now define

$$p^*(r,\phi) = \int_{-\infty}^{\infty} P(k,\phi) \exp(2\pi i k r) |k| dk \tag{3.15}$$

and eq 3.14 may then be written:

$$f(x,y) = \int_0^{\pi} p^*(r,\phi) d\phi \tag{3.16}$$

Equation 3.16 also represents a backprojection, but instead of backprojecting p directly as in eq 3.10, the function p^* is used, and the result is the object density function as required. The use of eq 3.16 for reconstruction require the computation of p^* from p; this may at first sight seem a little tricky because the integrand of eq 3.15 is not bandlimited due to the $|k|$ term. However, it is assumed that $f(x,y)$, and hence $p(r,\phi)$, does not contain spatial frequencies higher than k_{max}, and we may rewrite eq 3.15

$$p^*(r,\phi) = \int_{-\infty}^{\infty} P(k,\phi) H(k) \exp(2\pi i k r) dk \tag{3.17}$$

where the filter function $H(k)$ is given by:

$$H(k) = \begin{cases} |k|, & |k| \le k_{max} \\ 0, & |k| > k_{max} \end{cases} \tag{3.18}$$

The spatial domain representation of $H(k)$, $h(r)$ is:

$$h(r) = 2k_{max}^2 \operatorname{sinc}[2\pi k_{max} r] - k_{max}^2 \operatorname{sinc}^2[\pi k_{max} r] \tag{3.19}$$

The modified projection function, p^*, may now be evaluated as a convolution integral:

$$\begin{aligned} p^*(r,\phi) &= \int_{-\infty}^{\infty} p(r',\phi) h(r-r') dr' \\ &= k_{max} p(r,\phi) - k_{max}^2 \int_{-\infty}^{\infty} p(r',\phi) \operatorname{sinc}^2[\pi k_{max}(r-r')] dr' \end{aligned} \tag{3.20}$$

Apart from the assumption that the object function is bandlimited, no approximations have been used in this derivation. The numerical implementation of eq 3.20 is uncomplicated, because the integrand does not contain frequencies greater than k_{max} and the integral can be replaced by a summation, with summation points spaced $w = (2k_{max})^{-1}$ [20, p. 714].

The reconstruction procedure is then as follows: First, each projection is modified using eq 3.20, then the modified projection is backprojected (eq 3.16). When this has been done for all projections, the reconstruction is complete.

Convolution-filtered backprojection is almost as fast as the 2D Fourier method described above and does not involve any interpolation, which complicates the implementation of the Fourier method. Therefore, FBP is the most used reconstruction technique for CT.

3.3.2. Discretized object function; iterative methods

To limit the spatial resolution of the image, the object function is discretized, or approximated by an array of cells of uniform density, or pixels (picture elements), as shown in Figure 3.5.

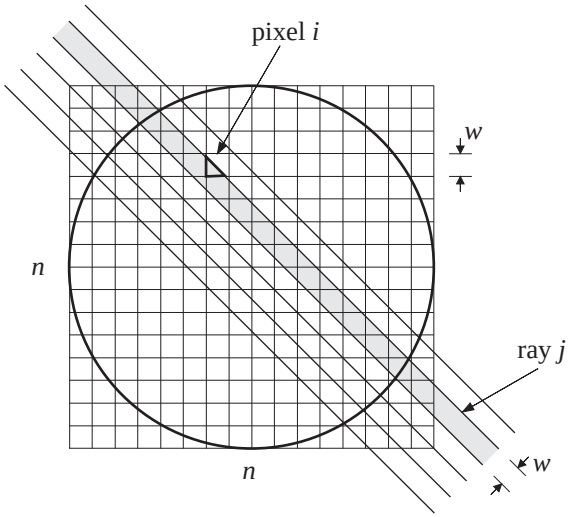

Figure 3.5 Array of $n \times n$ pixels for the discretization of the object function; the object is bounded by the circle [20, p. 700]. The rays have finite width, here equal to the pixel width *w*.

The projection equation (eq 3.1) may now be written as a summation instead of an integral:

$$p_j = \sum_{i=1}^{N} w_{ji} f_i \qquad \begin{cases} N \approx \dfrac{\pi n^2}{4} \\ j = 1, \ldots, M \end{cases} \tag{3.21}$$

Here p_j is the raysum of ray j, f_i is the density of pixel i, and w_{ji} is the contribution to raysum j from pixel i; this is equal to the area of intersection between the ray and the pixel for finite beam width, see Figure 3.5. The summation is to be taken over the total number of pixels

constituting the object, N, and for all raysums of the scan, M. Equation 3.21 represent a system of M linear equations in N unkown pixel densities f_i, and may be expressed as

$$\mathbf{p} = \mathbf{W}\mathbf{f} \tag{3.22}$$

where the raysum vector **p**, the pixel density vector **f** and the projection matrix **W** is given by:

$$\begin{aligned} \mathbf{p} &= \left[p_j \right], && j = 1,\ldots,M \\ \mathbf{f} &= \left[f_i \right], && i = 1,\ldots,N \\ \mathbf{W} &= \left[w_{ji} \right], && \begin{cases} j = 1,\ldots,M \\ i = 1,\ldots,N \end{cases} \end{aligned} \tag{3.23}$$

As mentioned above, the components w_{ji} of the projection matrix are the contribution to raysum j from pixel i; these are determined by the measurement geometry and the pixel array used. It is important to realize that although we have indicated the use of a rectangular reconstruction grid and parallel beam geometry in Figure 3.5, *any* type of reconstruction grid and measurement geometry is easily handled by a discrete method, simply by calculating an appropriate projection matrix **W**.

We will now consider how to reconstruct the image by solving eq 3.21 or eq 3.22.

Matrix inversion

Generally, N and M are not equal, which means that eq 3.22 cannot be solved by direct inversion of the projection matrix **W**. Furthermore, if $M<N$, the system is underdetermined, in which case many solutions may exist. There are problems even for $M \geq N$, because measurement errors in the raysums may cause the system to be inconsistent, which means that no possible solution exists. However, it is possible to redefine the problem in such a way that a mathematically well-behaved $N \times N$ system of equations is the result[1] [22] [20, p. 701], which can be solved by standard matrix inversion techniques.

The main problem of this image reconstruction method is that it is computationally inefficient. Even for a rather coarse reconstruction grid, the matrix which must be inverted is quite large, and even though the inversion only need to be done once for a given scanning scheme, the iterative techniques described below are actually faster [20, p. 701]. Therefore, the matrix inversion reconstruction method is not very much used in practice.

---

[1] The actual method used is to pick the solution vector **f** which fits the raysum measurements best in the least-squares sense; i.e. the measurement errors are also taken into account.

Iterative techniques

The principle of iterative reconstruction methods is to apply corrections to arbitrary initial pixel density values in such a way that raysums calculated from the corrected pixel values (eq 3.22) agree better with the measured raysums than raysums calculated from the initial density values. The process is then repeated, with the corrected densities of the previous iteration as new initial values, until satisfactory accuracy is achieved.

The correction of the density of pixel *i* during iteration *l* may be expressed mathematically as

$$f_i^{l+1} = f_i^l + \sum_{j=1}^{M} \Delta f_{ij}^l \tag{3.24}$$

where the total correction to the density of pixel *i* is expressed as the sum of the corrections to this pixel from each ray. To find the correction factors, we first determine the difference between the measured and computed raysums:

$$\Delta p_j^l = p_j - p_{cj}^l = p_j - \sum_{i=1}^{N} w_{ji} f_i^l \tag{3.25}$$

We shall require the corrections to be calculated in such a manner that if all pixels constituting ray *j* is corrected, the raysum is increased by the difference given in eq 3.25. One possibility is to define the correction terms the following way:

$$\Delta f_{ij}^l = \frac{w_{ji} \Delta p_j^l}{\sum_{k=1}^{N} w_{jk}^2} \tag{3.26}$$

It is seen that each pixel is corrected in proportion to w_{ji}, i.e. as the contribution of the pixel density to the raysum.

We may classify the iterative reconstruction techniques according to in what sequence the corrections are computed and applied during the iteration; the three main types of schemes are point-by-point correction (SIRT), ray-by-ray correction (ART) and simultaneous correction (ILST).

SIRT: Simultaneous Image Reconstruction Technique

In the point-by-point correction technique, all raysums containing a given pixel are calculated and then the pixel density is corrected for the total density deficit. The process is repeated for each pixel, incorporating the adjusted pixel values before moving to the next pixel. An iteration is complete when all pixels have been treated. The disadvantage of this method is that

it is not very computationally efficient compared to the two other variations of iterative techniques.

ART: Algebraic Reconstruction Technique

The most efficient of the three methods is ART, or ray-by-ray correction. The difference between the measured and the computed raysum is computed for one ray at a time; then a correction is applied to all pixels contributing to this raysum before moving to the next ray. However, the convergence properties of this technique is sensitive to errors in the raysum measurements, and it should therefore be used with caution.

ILST: Iterative Least Squares Technique

In this technique, all raysums are computed from the pixel densities of the previous iteration; then corrections to all pixels are computed and applied simultaneously. It is necessary to introduce a damping factor when applying the corrections of eq 3.26, because otherwise each pixel is corrected many times for each ray passing through it. However, if this precaution is taken, ILST is a good compromise between the two other methods: It is faster that SIRT, and handles noisy raysum data more gracefully than ART. The method owes its name to the fact that the corrections and the damping factor are found by requiring the corrected densities to fit the measured raysums best possible, in the least-squares sense.

Because we will use ILST for image reconstruction in the present work, we include the equations for this method as described in [22]: As all density adjustments for one iteration are done at the same time, we may express the procedure for iteration l as

$$\mathbf{f}^{l+1} = \mathbf{f}^{l} + \delta^{l}\Delta\mathbf{f}^{l} \tag{3.27}$$

where δ^l is the damping factor mentioned above. If the *calculated* raysums are written as

$$p_{cj}^{l} = \sum_{k=1}^{N} w_{jk}\, f_k^{l} \;, \quad j = 1,\ldots,M \tag{3.28}$$

the pixel density corrections are given by

$$\Delta f_i^{l} = \frac{\sum_{j=1}^{M} \left\{ \frac{w_{ji}}{\sigma_j^2}(p_j - p_{cj}^{l}) \right\}}{\sum_{j=1}^{M} \frac{w_{ji}^2}{\sigma_j^2}}, \qquad i = 1,\ldots,N \tag{3.29}$$

where σ_j is the measurement error (standard deviation) of raysum j. The overall damping factor δ^l is equal to:

$$\delta^l = \frac{\sum_{j=1}^{M} \left\{ \frac{w_{ji}}{\sigma_j^2} (p_j - p_{cj}^l) \right\}}{\sum_{j=1}^{M} \frac{c_{ji}^2}{\sigma_j^2}} \quad ; c_j = \sum_{i=1}^{N} w_{ji} \Delta f_i^l , \qquad j = 1, \ldots, M \tag{3.30}$$

Equations 3.27 to 3.30 thus describe one iteration. The initial density values used, $\mathbf{f}^0$, are not critical; often the same initial value are assigned to all pixels . The number of iterations used are normally determined by experiment, but a value in the range of 3 to 10 iterations seem to be suitable in most cases [7, p. 84][22].

3.4. Discussion of reconstruction methods

In the preceding sections we have studied the principles of operation of the more important reconstruction methods; we will now discuss some practical questions.

3.4.1. Scanning strategies

From our study of reconstruction methods, we have seen that the object density function may be exactly reconstructed, provided one can assume that it is suitably bandlimited. In this context, "suitably bandlimited" means bandlimited with respect to the chosen resolution of the reconstruction grid: For a given application, the grid spacing must be chosen according to the smallest detail the object function is expected to contain, and then the necessary number of raysum measurements needed may be found.

Natterer [21, pp. 71-84] has determined the optimum scanning strategies for the parallel and fan beam geometries, by applying the Nyquist criterion to the sampling of the object density function by raysum measurement. The results may be summarized as follows:

If we consider a circular object of diameter d, and assume that the object function $f(x,y)$ does not contain details of smaller size than w, then an exact reconstruction of $f(x,y)$ on an $n \times n$ grid may be done, with $n = d/w$, if the following scanning strategies are used:

For *standard parallel beam scanning*, the optimum scanning scheme is described by

$$\begin{cases} \phi_j = \dfrac{\pi\ (j\ -1)}{m_p} & ,\ \ j\ = 1, \ldots, m_p \\ r_l = \dfrac{wl}{2} & ,\ \ l\ = -n, \ldots, n \end{cases}$$
$$m_r = 2n\ + 1, \quad m_p \approx \pi n\ , \tag{3.31}$$
$$M\ = m_r m_p \approx\ 2\pi n^2$$

where r_l specifies the rays for the projection specified by the angle ϕ_i, see Figure 3.4. Also, we use m_r for the number of rays per projection, m_p for the number of projections and M denotes the total number of rays needed. We see that the optimum ratio of m_p and m_r is approximately equal to $\pi/2$.

Interlaced parallel beam scanning is a more efficient scheme, which requires half as many raysum measurements as the standard parallel beam scanning for a given spatial resolution of the reconstructed image; it is defined by:

$$\begin{cases} \phi_j = \dfrac{\pi\,(j-1)}{m_p} \quad , \quad j = 1,\ldots,m_p \\ r_l = \dfrac{wl}{2} \quad , \quad \begin{cases} l = -n,\ldots,n \\ j + l \ \text{ even} \end{cases} \end{cases} \tag{3.32}$$

$$m_r \approx n \ , \quad m_p \approx \pi n \ ,$$

$$M = m_r m_p \approx \pi n^2$$

We note that both parallel beam scanning schemes require projections in an angular interval of π radians only, because oppositely situated source positions give identical information in these geometries.

The geometry for the *fan beam scanning* scheme is specified by the rotation angle of the source, β, the ray angles α_l and the radius r_s of the circle on which the source rotates, see Figure 3.6:

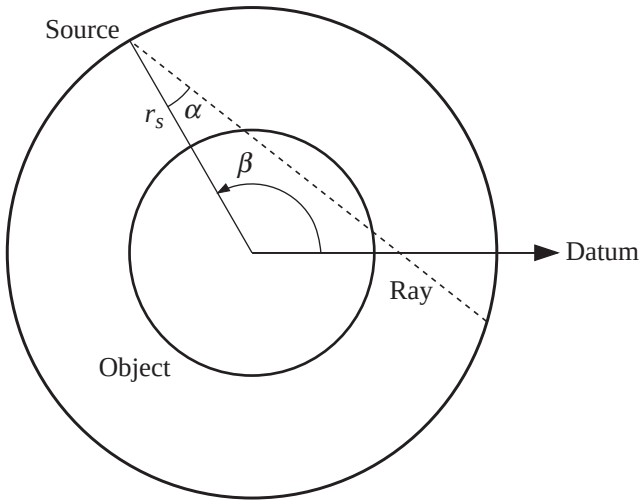

Figure 3.6 Fan beam scanning scheme: For each source position specified by β, raysums are measured for a set of α. It should be noted that β does not correspond directly to the projection angle ϕ defined in Figure 3.4.

The optimum scanning scheme for the fan beam geometry is then given by:

$$\begin{cases} \beta_j = \dfrac{2\pi\ (j\ -1)}{m_s} & , j\ = 1, \ldots, m_s \\ \alpha_l\ = \dfrac{\pi l}{2q} & , \begin{cases} l\ = -q\ , \ldots, q\ \ , \ \ q\ \approx \frac{n\pi r_s}{d} \\ \alpha_l\ \le \alpha_{\lim}(r_s) = \arcsin\ (\frac{d}{2r_s}) \end{cases} \end{cases} \tag{3.33}$$

$$m_a \approx \frac{4nr_s\alpha_{\lim}\ (r_s\ )}{d} + 1\ , \quad m_s \approx 2\pi n$$

$$M\ \ = m_a m_s \approx \frac{8\pi n^2 r_s \alpha_{\lim}(r_s\ )}{d}$$

Here, m_a is the number of rays per source position and m_s is the number of source positions; we also see that source positions in a 2π interval is used, because opposite source positions does not produce equal information for fan beam scanning.

From eq 3.33 (where $r_s > d/2$), it is seen that the fan beam geometry is not as efficient as the parallel geometries as far as the number of necessary raysum measurements for a given spatial resolution is concerned. However, its great advantage in scanning speed makes it widely used in CT nevertheless.

We also note that the number of raysum measurements required for the exact reconstruction of a circular object on an $n \times n$ grid, is considerably greater than the number of points contained within the object, $N = \pi n^2/4$. In situations where the scanning scheme and number of raysums are suboptimal, one will have to expect loss of accuracy in the reconstructed image.

3.4.2. Accuracy considerations

Provided the necessary number of raysum data is available, both analytic and iterative reconstruction techniques produce exact results under the assumption that the object function is suitably bandlimited. However, this requires that the measurements are error-free; in practice, if the measured raysums p contain errors σ_p (standard deviation), the resulting relative error of the reconstructed pixel density is approximately [22][20, p. 718]:

$$\left(\frac{\sigma_f}{f}\right) \cong \sqrt{\frac{n^3}{M}}\left(\frac{\sigma_p}{p}\right) \tag{3.34}$$

where n is the number of pixels across the diameter of the object and M is the total number of measured raysums.

As we have already mentioned, nonoptimal scanning conditions will also introduce artifacts and inaccuracies in the reconstructed image. Examples of such conditions are too few projections or raysums per projection for the chosen reconstruction grid, or confinement of all projections to a limited angular interval (i.e. less than the full interval of π or 2π radians, for

parallel or fan beam scanning, respectively). We will discuss the topic of suboptimal scanning more thoroughly in the next chapter.

3.4.3. Choice of technique

As the methods described have similar performance as far as the quality of the reconstruction is concerned, the choice of technique for a given application must be based on the computational speed required and the scanning geometry to be used: The analytic methods are faster, but the iterative techniques are more flexible, as they can easily accommodate any type of scanning geometry. Because flow imaging systems have relatively low spatial resolution compared to medical CT systems, the reconstruction computation time is no problem, and we have therefore chosen the iterative technique ILST for our reconstruction error analysis in the next chapter.

4. Measurement geometries for γ-ray flow imaging

In this chapter, the possible strategies for measurement of adequate raysum data for CT reconstruction of the cross-sectional density distribution of two phase or multiphase flow will be discussed. After a brief literature review, the description and performance analysis of the system geometries which are investigated in this work will be addressed.

4.1. Introduction

Because it is desirable to image flow inside steel process pipes, X-ray tubes are out of the question as radiation sources because the low energy photons generated have too poor penetration capability. Besides, they generate photons in a broad energy spectrum; this produces errors in the density measurements due to the beam hardening effect [20, p. 720].

A γ-ray system seems to be the better choice; some systems have been proposed [4][5][6][7], of varying complexity and performance.

4.1.1. Rotating scanner

The most obvious system geometry for γ-ray tomographic flow imaging is a high speed rotating fan-beam scanner, see section 3.2. Indeed, this possibility has been investigated, a parameter analysis and a feasibility study for such a system are found in Refs. [4] and [5]. The proposed system consisted of a fixed detector ring and a rotating γ source. For a 48-detector system with an 18.2 mCi ^{137}Cs source, a scan time of 1 second were expected to give a pixel density resolution of 0.03 g/cm^2, with spatial resolution of 1.15 cm for a 15.24 cm (6 inch) steel pipe (i.e. ≈130 pixels inside pipe). By increasing rotation speed and source intensity, the dynamic response may be further enhanced, with no deterioration of the resolution parameters.

Note, however, that the quoted density resolution only includes the effect of statistical fluctuations in the measured raysums, and since this system does not conform to the optimum scanning conditions described in Section 3.4.1, there might also quite possibly be a reconstruction error contribution to the uncertainty of the pixels in the image.

While the specifications of this system are impressive, with the possibility of subsecond scanning times, the fact still remains that it is a *rotating* scanner: As the flow may move at several meters per second, the density distribution within the measurement plane will change during the scan, causing inconsistencies between raysums measured for different source

positions. Therefore, the rotation speed must be high enough to ensure that the density distribution in the measurement plane may be assumed to be constant during the scan; otherwise the reconstructed density image will be of doubtful value. Thus a fixed, or nonmoving, system would be desirable: while the raysum measurements are still averaged over the flow moving through the measurement plane, all raysums would be measured simultaneously, ensuring consistency of the data.

4.1.2. The scattering + transmission technique

A nonmoving γ-ray flow imaging system using very few sources and detectors has been investigated at UMIST [6]. The measurement principle is shown schematically in Figure 4.1.

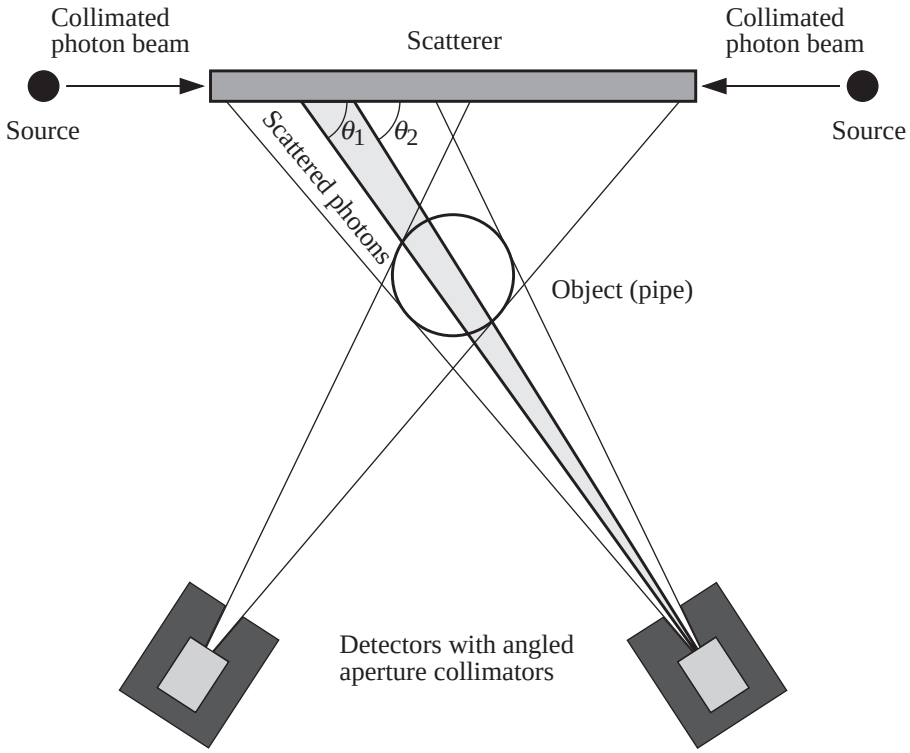

Figure 4.1 The scattering + transmission flow imaging system: An external low-Z scatterer generates a field of Compton scattered photons which traverse the pipe cross section. The detected energy of a photon uniquely determines the path by which it has traversed the pipe; thus finite width beams across the pipe are defined by a small energy interval.

Two 50 mCi ^{137}Cs sources illuminate a low-*Z* scatterer rod, from which a field of singly Compton scattered photons emerge, thus simulating a linear array of sources of different energies. The pipe is placed in this photon field, and two NaI(Tl)+PMT detectors with narrow aperture collimators are positioned to detect the photons which traverse the pipe. The path by which a photon has traversed the pipe cross section is uniquely determined by its energy, through the Compton energy - scattering angle relationship (eq 2.17) and the setup geometry. Thus, a raysum measurement is defined by the detected photon flux in a narrow

energy interval, corresponding to a narrow beam through the pipe. By measuring the number of photons in several energy intervals, a number of raysums are measured simultaneously for each detector, provided corresponding calibration measurements are available.

In the UMIST system, 7 raysums were measured for each detector, giving a total of 14 raysums. The cross sectional density distribution were then reconstructed on a 7×7 pixel grid using iterative techniques. Considering the discussion in section 3.4.1, it is obvious that the system is highly underdetermined; still, identification of simple, idealized models of flow regimes were possible.

The small amount of available raysum measurements is a definite disadvantage, especially if accurate void fraction and density distribution measurements are attempted. However, the main problem with this system is that the external scatterer concept require extreme source intensities to keep the errors due to statistical fluctuations acceptably small for short measurement times. For the setup described above, the counting time were six hours, when performing measurements on a 76 mm diameter perspex pipe containing air/water mixture.

4.1.3. Direct transmission raysum measurement system

The concept of the systems with which this project are concerned, is to improve the dynamic response of a nonmoving setup by using direct transmission measurement of raysums, as in a rotating CT scanner. However, several fixed groups of sources and detectors are placed around the pipe, each group corresponding to a certain rotation angle of a moving scanner. In this way, a nonmoving system with much better dynamic response and more raysum data than a scattering/transmission system may be realized.

So far, the work on this project has been a basic feasibility study [7]; this includes testing of reconstruction algorithms and reconstruction of images from simple single-source, single-detector raysum measurements on static flow regime models inside a steel pipe. The results of this work indicate that reconstruction of images adequate for regime identification is possible using a very low number of raysum measurements. However, a more detailed analysis is required to determine the possible performance of such systems; this is the scope of the present work. We start by giving brief descriptions of three different nonrotating system concepts which uses several sources and detectors.

Single energy, multisource, multidetector system

This concept uses several fixed sources of equal γ-energy at different angular positions, each placed in the same radial distance from the pipe centre, and each source illuminating its own set of detectors placed on the opposite side of the pipe. A system using three sources is shown schematically in Figure 4.2.

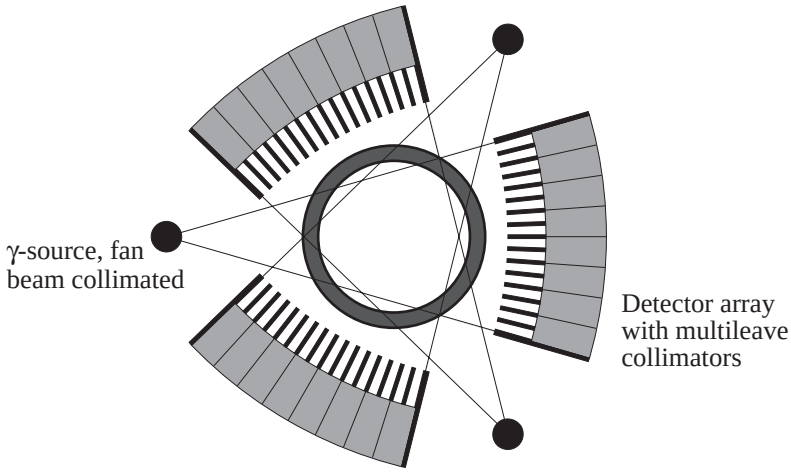

Figure 4.2 A single energy, multisource, multidetector imaging system using collimators to minimize the effect of Compton scattered radiation. All raysums are measured simultaneously; one for each detector used.

Collimators are used to minimize the possibility of scattered photons reaching the detectors; however, the use of several γ-sources simultaneously means that photons from a source "aimed at" one particular set of detectors may undergo large angle Compton scattering and hit a detector of another set. Therefore, energy filtering must be used to counteract this effect, which become more pronounced as the number of source-detector array groups is increased.

It is also seen that the pipe-source distance and source-detector distance must be increased when larger number of sources are used, in order to provide a "clear field of view" for each source-detector group. This imposes geometrical constraints on the number of source positions used, and also on the total number of simultaneous raysum measurements: Apart from the fact that a system using many sources will have large dimensions, the photon intensity registered by a detector is inversely proportional to the square of the source-detector distance; hence, the measurement error due to statistical fluctuations will increase with increasing source-detector distance for a given measurement time and source intensity, if not the detector size is increased as well.

Given the pipe dimensions and the attenuation coefficients of the pipe material and the heaviest phase of the flow, the optimum γ-energy can be found by the techniques outlined in Section 2.6.3, and a suitable isotope may then be chosen. For steel pipes, energies of several hundred keV or more will be required; because the detectors need to be rather compact for good spatial resolution, it is obvious that high-Z detectors must be used to achieve adequate detection efficiency. Further, the detectors must have a reasonable energy resolution to be able to discriminate against Compton scattered photons. Finally, good countrate capability is required

when using intense sources in order to reduce the necessary measurement time. We will take a closer look at the selection of isotopes and detectors in Chapter 5.

Multienergy, multisource, multidetector system

The single energy system described above requires one detector per raysum measurement, which, compared to a rotating scanner, makes it inefficient with regard to the number of detectors needed. While this may be said to be an obvious tradeoff between a rotating scanner and a nonrotating system, better "detector economy" can be accomplished for a fixed system as well; the principle is shown in Figure 4.3.

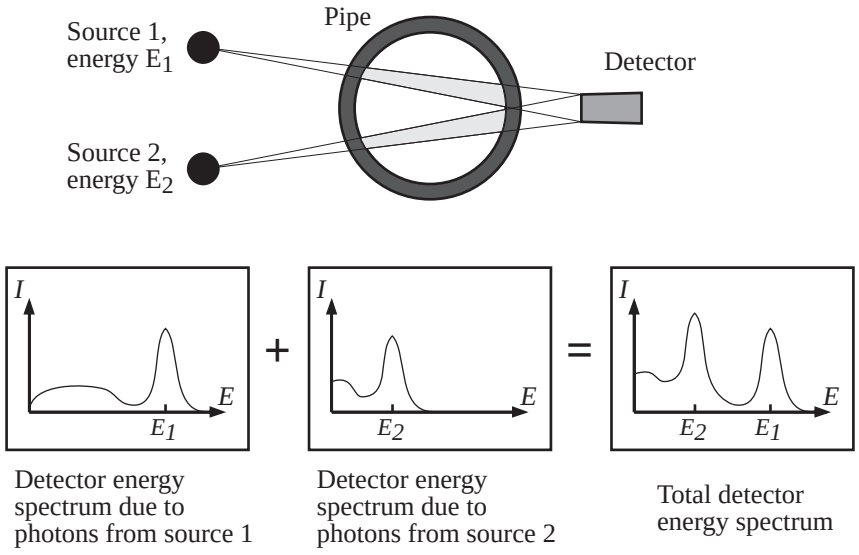

Figure 4.3 Principle of dual energy raysum measurement: By using sources of different energy and position, two separate raysums can be measured with one energy sensitive detector. Only counts in the full energy peaks of the detectors may be used, to avoid registering unwanted scattered photons, and the counts in the peak corresponding to the source of the lowest energy must be corrected for the influence of the higher source energy.

If the detectors are illuminated by γ-sources of different energies, it is possible to measure several raysums with one detector, provided its energy resolution is sufficient. By counting full-energy peak events only, it is possible to separate the events due to each source used. Thus, simultaneous measurement of photon transmisson for several different rays through the pipe is possible, much in the same way as the scattering + transmission technique described above. However, it is possible to use a much shorter measurement time, because the pipe is illuminated directly by the sources.

It is obvious that the detectors used must have better energy resolution and countrate capability than is needed for a single energy system. This is because buildup of scattered radiation will have to be removed by energy filtering as conventional collimators cannot be used (see Figure

4.3), and that the total detected intensity will increase when more than one source is directed at each detector.

The possible number of measured raysums per detector depends on the energy resolution of the detector and the availability of suitable isotopes. The γ-sources used should ideally be monochromatic, and their energies should be chosen to suit the given pipe material and pipe dimension; more on this in Chapter 5. Because of the lifetimes of the isotopes also must be considered, it follows that the range of suitable choices is limited; however, 2-3 isotopes should be possible to find in most energy ranges (see e.g. Table 5.1). A system using two different source energies and three detector arrays is shown in Figure 4.4.

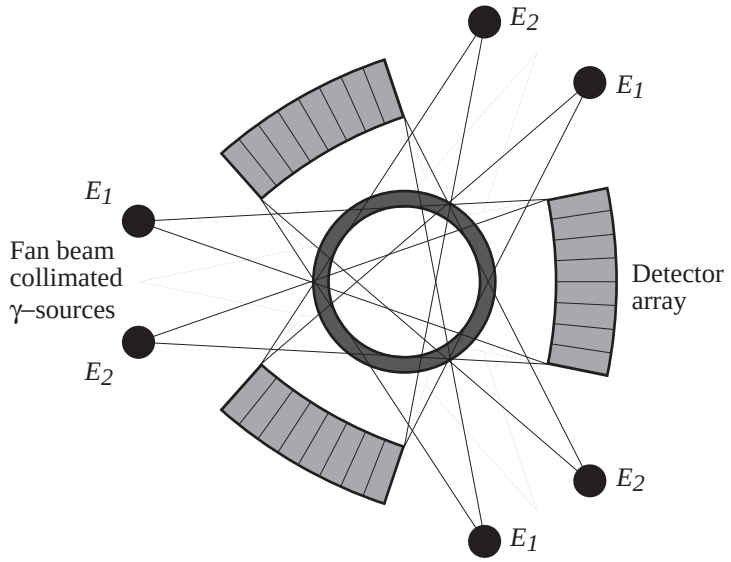

Figure 4.4 Dual energy, multisource, multidetector flow imaging system, relying on energy filtering to avoid the problem of scattered radiation. Two raysums are measured per detector.

We see that geometrical constraints similar to those of the single energy system also apply here. However, note that the fan spanned by one source and its corresponding detector array does not cover the entire flow cross section, and that the angular spacing of the sources is not uniform; the possible effect of this will be discussed later.

It should be mentioned that although it is in principle possible to use energy filtering to remove the effect of scattered radiation, the detector energy resolution needed may not be compatible with the requirement of good detection efficiency and compactness.

Another approach is to try and compensate for buildup using an adaptive image reconstruction algorithm. If an initial reconstruction is done based on raysum data containing some buildup error, the amount of scattered radiation detected could be estimated from the initial image; afterwards, the raysum data could be corrected accordingly and used for an improved

reconstruction. A mathematical model of the photon transport in the entire system would then be required.

Multiplane system

By using several parallel measurement planes, it is possible to increase the number of source positions without increasing the radial dimensions of the system [7]. The spacing of the measurement planes is determined by how much shielding material is required to prevent directly transmitted photons emanating from sources belonging to one plane, to reach the detector arrays of the other planes. Hellesø estimates the required spacing to be in the region of 5 - 8 cm [7, p. 20]; however, it would depend strongly on the isotope energy used.

The obvious advantage of a multiplane system, is that the source-detector distance is kept at a minimum, which minimize the statistical fluctuation error for a given source intensity and measurement time. However, using a multiplane system is only permissible if the flow regime is relatively stable over the time taken for the flow to travel past all measurement planes, or if the measurement period is much longer than this time Because of this, we will discuss single-plane systems only; however, note that the performance figures for multiplane systems may easily be derived from the analysis of single plane systems.

4.2. Analysis of ideal nonrotating systems

In this section, we will attack the task of determining what reconstruction accuracy to expect from nonrotating systems; we start by deriving some basic geometry relations for these systems.

4.2.1. Geometry relations for single, dual, and triple energy systems

The most important parameters for the nonrotating system geometries, are the minimum distances between the pipe centre and the sources and detector arrays needed to ensure a clear "field of view" for each source-detector group. From Figures 4.2 and 4.4, it is obvious that these distances increase when the number of source-detector groups increases, and that a fixed system may assume impractical dimensions even for rather modest number of source-detector groups, or *views*.

First, we will consider an idealized *single energy* system: We assume that the fan defined by the source and the detector array cover the entire object, i.e. the pipe interior, and that the source is an ideal point source, with photon emission limited to the fan beam angular interval. Further, we define r_o as the pipe radius, r_s as the distance from the pipe centre to the source,

and r_d as the distance from the pipe centre to the endpoints of the detector array. Figure 4.5 shows the single energy geometry for the cases $r_s > r_d$ and $r_s < r_d$, respectively.

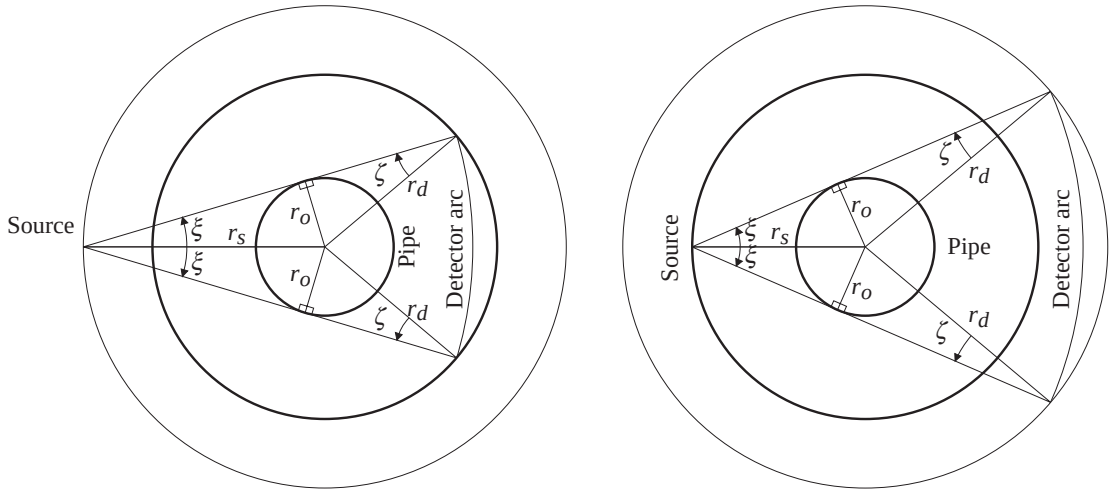

Figure 4.5 Basic source-detector group geometries for single energy system, with $r_s > r_d$ (left) and $r_s < r_d$ (right), respectively.

The angles ξ and ζ are given by

$$\xi = \arcsin\left(\frac{r_o}{r_s}\right)$$
$$\zeta = \arcsin\left(\frac{r_o}{r_d}\right) \tag{4.1}$$

and the distance r_{ds} between the source and any detector in the corresponding array is equal to:

$$r_{ds} = \sqrt{r_s^2 - r_o^2} + \sqrt{r_d^2 - r_o^2} \tag{4.2}$$

If we define ψ to be the total angular interval, relative to the smaller of the circles of radii r_s and r_d, which is occupied by the fan defined by the source and the detector array, it may be shown from Figure 4.5 that:

$$\psi = \begin{cases} 4\xi & , r_s < r_d \\ 4\zeta & , r_s > r_d \end{cases} \tag{4.3}$$

In general, the angular interval available for each view is equal to

$$\psi = \frac{2\pi}{m_s} \tag{4.4}$$

when there are m_s equispaced views. At this point, it should be mentioned that equispaced views over the full 2π interval is only possible if m_s is an odd number. The reason for this is that an even number of equispaced views requires the source-detector groups to be pairwise

situated directly oppositely of each other, which is clearly impossible in a fixed system[1]. If we define

$$r_{\min} = \inf\{r_s, r_d\} \tag{4.5}$$

we find the following expression for the minimum r_S or r_d required for a system of m_S views:

$$\frac{r_{\min}}{r_o} = \frac{1}{\sin\left(\frac{\pi}{2m_s}\right)} \; ; \quad m_s = 3,5,7,\ldots \tag{4.6}$$

Because the photon intensity at the detectors is inversely proportional to the square of the source-detector distance r_{ds}, it is desirable to minimize this distance in order to keep the error due to statistical fluctuations in the number of detected photons as small as possible. From the above considerations we see that r_S and r_d must be greater than or equal to the r_{min} defined by eq. 4.6 for a system of m_S views; hence, a system of minimum r_{ds} is obtained with $r_S = r_d = r_{min}$; the source-detector distance is in this case given by:

$$(r_{ds})_{\min} = 2\sqrt{r_{\min}^2 - r_o^2} \tag{4.7}$$

The basic geometry of a single energy system of this specification is shown in Figure 4.6; in this case, we have $\psi = 4\xi = 4\zeta$, since $r_S = r_d$.

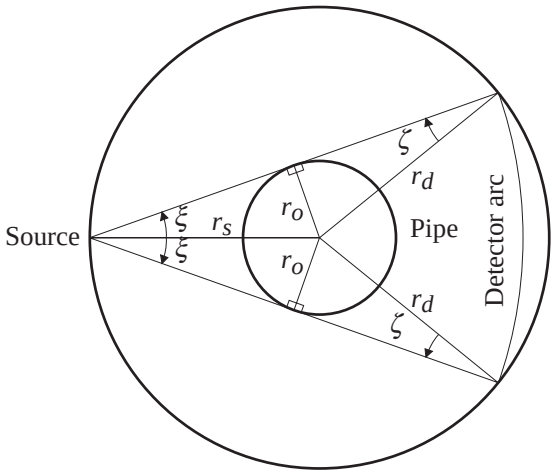

Figure 4.6 Basic geometry of an idealized single energy system of minimum source-detector distance r_{ds}, i.e. for the case of $r_S = r_d$.

[1]A system using an even number of views is possible if the views are spaced over less than the full 2π range, however, the unused angular interval is in fact exactly adequate for accommodating one extra view, i.e. a system where m_S is an odd number.

Next, we will take a look at dual-energy and triple-energy systems: The positioning of the detector array is similar to a single-energy system, but the detector arc is narrower, i.e. the fan does not cover the whole object. Figure 4.7 shows the basic geometry for such systems.

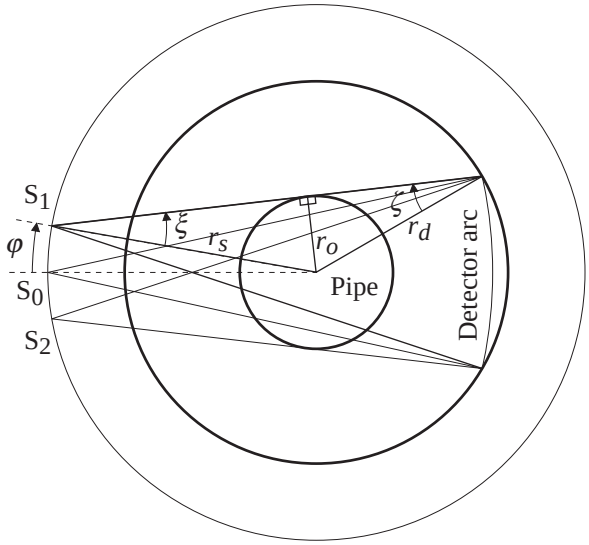

Figure 4.7 Basic geometry for dual- and triple energy systems for the case $r_s > r_d$; for the dual energy system, source positions S_1 and S_2 are used, while the triple energy system uses S_0 as well. The angular spacing of the sources (within a source-detector group) is 2φ for the dual energy system and φ for the triple energy system.

From Figure 4.7 we can derive similar geometrical constraints to those of the single energy system discussed above. It turns out that exactly the same relation (eq. 4.6) between the number of source-detector groups m_s and r_{min} (minimum r_s or r_d) applies to the dual and triple energy systems, i.e. r_s and r_d remain unchanged for single, dual or triple energy systems for a given m_s. Further, r_s and r_d are independent of the angular spacing of the sources, φ. However, if we consider the source-detector distance, we see that this is no longer constant for sources S_1 and S_2; for S_0 it is given by

$$(r_{ds})_0 = \sqrt{r_s^2 + 2r_s r_d \cos(\zeta + \xi - \varphi) + r_d^2} \qquad (4.8)$$

while for S_1 and S_2, r_{ds} varies around this value depending on where in the array the detector is positioned. It is seen from Figure 4.7 that this variation is small for moderate values of φ. Note that increasing the source spacing angle φ causes the fans to become narrower.

Figure 4.7 also shows that increasing the number of energies used imply either *less coverage of the object* for each source-detector fan, or *smaller angular spacing* between fans within one group of sources and detectors; in either case, not much new information is gained. Hence, it is probably pointless to use a system of more than two or three energies, which is the practical limit anyway because the availability of a suitable group of isotopes is limited.

Although the number of raysum measurements per detector is doubled or trebled (without increasing r_{min}) when dual of triple energy systems are used, a penalty is paid in that the fans spanned by S_0, S_1, S_2 and the detector array does not cover the entire pipe interior, since a certain source spacing φ is required for the three fans to give different raysum information, see Figure 4.7. In addition, the rays in fans 1 and 2 will not be equispaced; neither will the views of different source-detector groups.

Therefore, the multi-energy measurement geometry differs somewhat from the single-energy geometry, as well as from the ideal conditions described in Section 3.4.1. Thus for a given number of measured raysums, the quality of the reconstructed image must be expected to be somewhat poorer for the multi-energy system than for the single energy system.

4.2.2. Reconstruction performance of nonrotating systems

Because the fan beam geometry ideal sampling conditions described in Section 3.4.1 dictates the use of a large number of views even for systems of low spatial resolution, a nonrotating system conforming to these conditions will be rather large even for modest resolutions. In order to limit the size of the instrument, it may therefore be necessary to use a suboptimal sampling scheme; that is, to use fewer views than ideal for the reconstruction grid used.

Conversely, if the grid resolution is reduced in order to limit the number of necessary raysum data, an error is introduced because the bandlimiting assumption of CT reconstruction theory is violated, see Section 3.3. To analyze these effects, we have developed a simulation program called TOM1, which we will now describe in some detail.

Introduction to simulator TOM1

The idea of TOM1 is to investigate the performance of a measurement geometry by feeding ideal (error-free) raysum data for a given regime to the reconstruction algorithm; afterwards, the *reconstructed* pixel density values are compared to *ideal* pixel densities for the regime and reconstruction grid in question. The errors occuring in the reconstructed pixel densities must then be caused by insufficient resolution of the reconstruction grid (i.e. violation of the bandlimiting requirement), or a nonideal scanning scheme, or both.

By testing each combination of grid resolution and scanning scheme for different regimes, one may use TOM1 to determine a suitable measurement setup for the desired spatial resolution and pixel density accuracy. An overview of the simulator is shown in Figure 4.8.

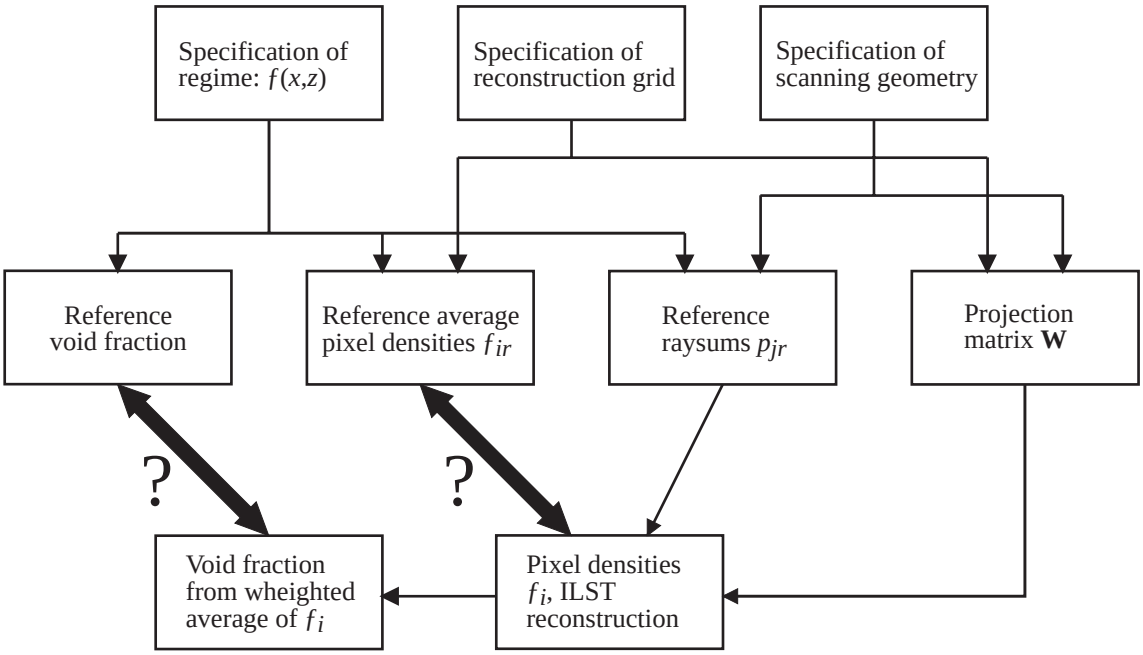

Figure 4.8 Simulator TOM1: Based on the specified regime, scanning geometry and reconstruction grid, reference pixel densities and raysums are computed, as well as the projection matrix required for ILST reconstruction. The reconstructed pixel values may then be compared to the reference values to determine the performance of an ideal system, i.e. with error-free raysum measurements.

In its present form, TOM1 is restricted to handle two-phase gas/fluid flow, with fully separate phases distributed as idealized annular or stratified flow regimes. Further, it is assumed that the density distribution f is constant along the axial direction of the pipe (see Figure 4.9), i.e. that the density distribution function is independent of y and may be written as $f = f(x,z)$.

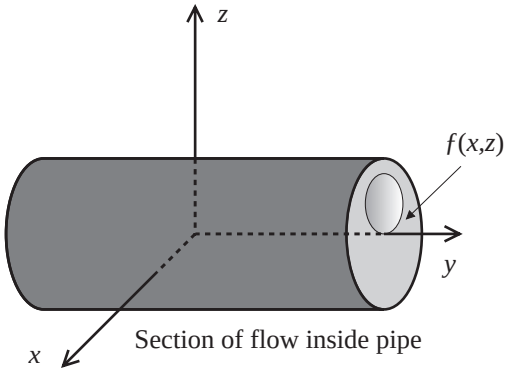

Figure 4.9 Coordinate system for simulation program TOM1: the density distribution f is assumed to be independent of y and may thus be written $f(x,z)$.

In general, regimes are defined as a two-dimensional density distribution for the flow cross section, see Figure 4.10 (left); this distribution is the basis for the calculation of ideal average pixel densities and raysums.

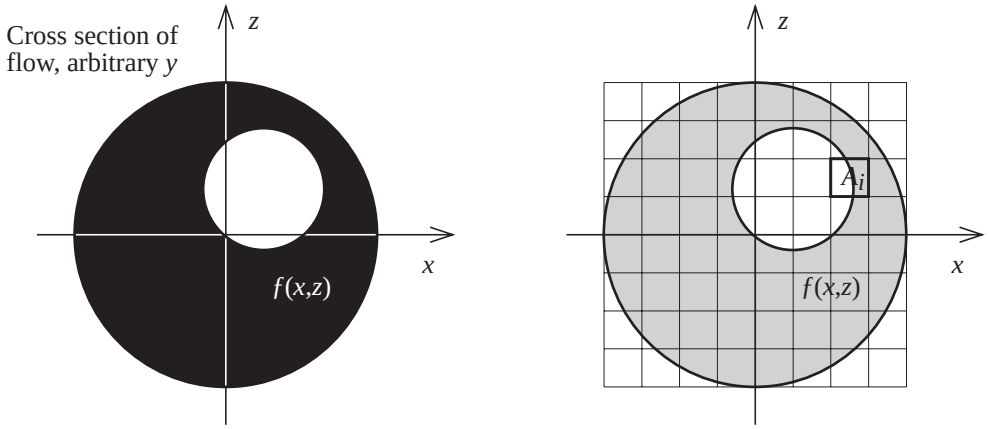

Figure 4.10 A flow regime is defined by its 2D density distribution function $f(x,z)$ (left). A typical discretizing grid is shown at the right; pixel i is defined by the region A_i.

The calculation of the *pixel densities* for a given regime and grid resolution are done in the following way: For pixel i, the average density f_{ir} is found by integrating the density distribution function of the regime over the region A_i in the xz-plane, and normalizing to the area of the region (see right-hand side of Figure 4.10):

$$f_{ir} = \frac{\iint_{A_i} f(x,z)\,dx\,dz}{\iint_{A_i} dx\,dz} \tag{4.9}$$

This is repeated for every pixel in the grid, the result is an array of average pixel densities as shown in Figure 4.11.

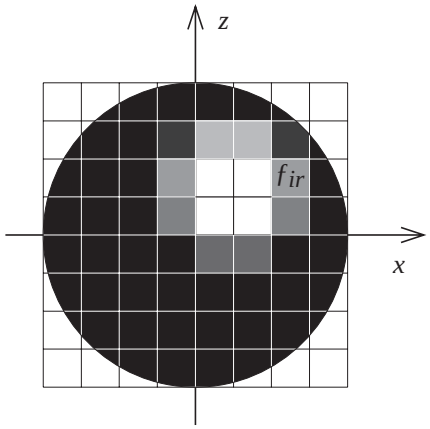

Figure 4.11 Image of average pixel densities f_{ir} for the density distribution and grid in Figure 4.10.

The geometry used for the calculation of the *raysums* (or average chordal densities) is shown in Figure 4.12; in addition to the density distribution of the flow regime, it is necessary to know the positions and widths of the source and detector for the ray in question.

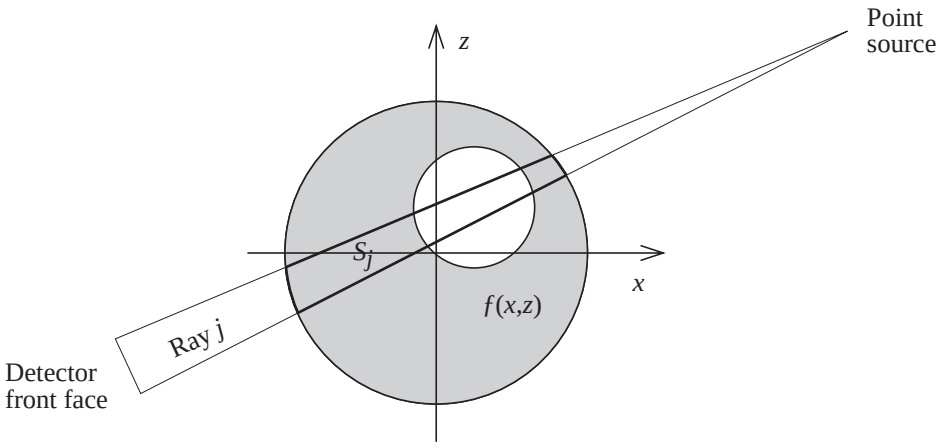

Figure 4.12 Geometry used for raysum calculation; S_j defines the region of influence for ray j.

Raysum p_{jr} for ray j are found in a similar way to the above procedure for calculating the pixel densities; i.e. as a normalized integral of $f(x,z)$ over the region S_j, where S_j is the region of intersection between the flow cross section and the ray.

$$p_{jr} = \frac{\iint_{S_j} f(x,z)\,dxdz}{\iint_{S_j} dxdz} \tag{4.10}$$

This is done for every ray[1] defined by the given scanning geometry, giving a set of ideal raysum values for the regime in question. It should be noted that the normalization to the area of S_j restricts p_{jr} to lie in the interval $[0, f_{max}]$, where f_{max} is the maximum of the density distribution function within the flow cross section. We use this definition to "harmonize" our notation with the notation used for *measured* raysums, which are also normalized quantities (see Chapter 5).

In order to be able to reconstruct images from the raysums using ILST (or any iterative technique), it is necessary to calculate the weights w_{ji}, which are the components of the projection matrix **W** defined by eq. 3.23. The weight w_{ji} may be defined as the contribution of the density of pixel i, f_i, to the raysum p_j of ray j; normally, w_{ji} would be equal to the area of intersection between regions S_j and A_i (see Figure 4.13), but because we have used normalized raysums (see the previous paragraph), the weights must be normalized as well.

[1]The term "ray" is a little misleading, because the beams are not infinitesimally narrow, but have finite width.

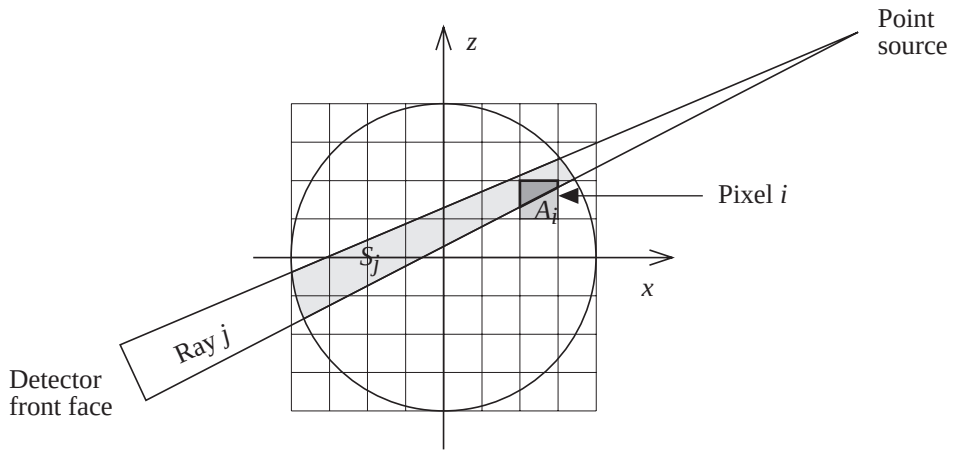

Figure 4.13 Geometry for the calculation of the components of the projection matrix W.

The proper normalization is achieved by defining w_{ji} as the area of intersection between S_j and A_i, divided by the total area of S_j:

$$w_{ji} = \frac{\iint_{(A_i \cap S_j)} dxdz}{\iint_{S_j} dxdz} \tag{4.11}$$

Equations 4.9 to 4.11 thus provide the basis for the simulation program together with equations 3.27 to 3.30, which define the ILST algorithm.

Reconstruction error estimators

Herman [23, p. 66] has proposed a number of estimators for the evaluation of image reconstruction error, some of which were used in the introductory work for this project [7]. The *normalized average absolute pixel error, r,* is defined by:

$$r = \frac{\sum_{i=1}^{N} |f_i - f_{ir}|}{\sum_{i=1}^{N} |f_{ir}|} = \frac{\sum_{i=1}^{N} |f_i - f_{ir}|}{N f_{max}(1-\alpha_e)} \tag{4.12}$$

It is seen that this estimator is normalized to the average of the flow cross section density function (α_e is the void fraction); for the sake of simple comparison between regimes of different average density we shall use the *average absolute error per pixel*, r_{abs}, instead:

$$r_{abs} = \tfrac{1}{N} \sum_{i=1}^{N} |f_{ir} - f_i| \tag{4.13}$$

In addition to using this estimator, we will compare the exact value of the void fraction α_e with an estimated void fraction α_r computed from the reconstructed pixel values. The void

fraction is defined as the relative volume occupied by the gas phase; because we have assumed that the density distribution function is independent of y, α_e is given by:

$$\alpha_e = 1 - \frac{\iint_{S_{flow}} f(x,z)\,dxdz}{f_{max} \iint_{S_{flow}} dxdz} \tag{4.14}$$

The "reconstructed" void fraction α_r is computed as an weighted average of the reconstructed pixel densities, where the weights are just the relative areas of each pixel:

$$\alpha_r = 1 - \frac{\sum_{i=1}^{N} \left(f_i \iint_{A_i} dxdz \right)}{f_{max} \iint_{S_{flow}} dxdz} \tag{4.15}$$

In both cases, the integral in the denominator is simply the total area of the flow cross section

$$\iint_{S_{flow}} dxdz = \pi r_o^2 \tag{4.16}$$

and the region S_{flow} is defined by:

$$S_{flow} : (x,z) \text{ for which } \quad x^2 + z^2 \le r_o^2 \tag{4.17}$$

Then we may define our second error estimator, the *absolute void fraction error*, as follows:

$$e_{void} = |\alpha_e - \alpha_r| \tag{4.18}$$

Notes on the implementation

The program handles grid resolutions of 2×2 to 16×16, the maximum number of views is 100, and the maximum number of rays per view is 33; the latter restrictions correspond to fan beam optimal scanning conditions for the maximum grid resolution (with $d = 2r_0$ and $r_s \ge 4r_0$), see eq 3.33. Based on the specified geometry and density function, f_{ir}, p_{jr} and w_{ji} are computed using simple numerical integration of equations 4.9 - 4.11. The raysums and the projection matrix **W** are input to the ILST algorithm defined by equations 3.27 - 3.30. An initial value of 0.5 is assigned to all pixels (since $f_{max} = 1$); then 7 iterations are done to complete the reconstruction, see Section 3.3.2.

A slight modification of the ILST algorithm is incorporated: Because it is known in advance that the f_i´s should lie in the interval [0, f_{max}], values of f_i below or above this interval are set to zero or f_{max}, respectively, after each iteration. We have also cancelled the raysum

measurement errors σ_j from eqns 3.29 and 3.30, because we are using "exact" raysum data, believed to be accurate to 6 significant digits, which is the precision of the numerical integration procedure used.

Regime definitions and strategy for simulations

As mentioned above, TOM1 is restricted to handle simple models of two-phase stratified and annular flows, see Figure 4.14. The stratified regimes are specified by the interface level and the angle between the interface and the *x*-axis, while the annular regimes are defined by the radius and position of a single circular annulus (void). The gas density f_{gas} is set equal to zero, while the fluid density f_{fluid} is equal to one.

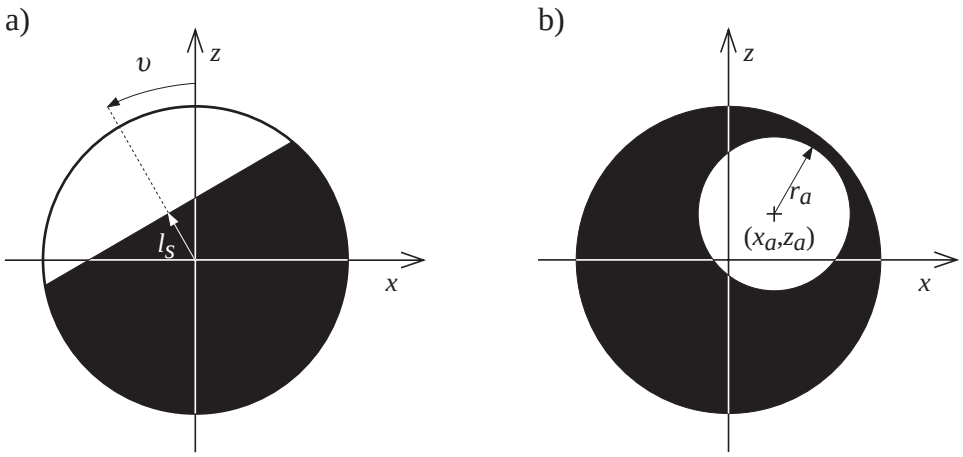

Figure 4.14 Density distributions of the regime models handled by TOM1: a) Stratified flow, with interface level l_s and angle υ, and b) annular flow, with a void (gas) region of radius r_a centred at (x_a,z_a). The value of $f(x,z)$ is zero for gas (white) and one for fluid (black).

The stratified regime in Figure 4.14(a) may be defined mathematically as

$$f_{stratified}(x,z) = \begin{cases} 0 : z > \dfrac{x\sin\upsilon + l_s}{\cos\upsilon} \\ 1 : \text{otherwise} \end{cases} \qquad (4.19)$$

$$\text{for } (x,z) \in S_{flow}, \text{ with } l_s \in \langle -r_0, r_o \rangle \text{ and } \upsilon \in \langle -\tfrac{\pi}{4}, \tfrac{\pi}{4} \rangle$$

where l_s is the interface level and υ is the rotation angle relative to the *x*-axis. For the annular regime of Figure 4.14(b), the expression is:

$$f_{annular}(x,z) = \begin{cases} 0 : z > (x-x_a)^2 + (z-z_a)^2 \le r_a^2 \\ 1 : \text{otherwise} \end{cases} \qquad (4.20)$$

$$\text{for } (x,z) \in S_{flow}, \text{ with } \sqrt{x_a^2 + z_a^2} - r_a \le r_o$$

where r_a is the radius of the annulus and (x_a,z_a) is the position of its centre.

We must now decide upon some strategy for the testing of various system geometries. Because we are dealing with systems of relatively poor spatial resolution and/or limited numbers of raysum data, the accuracy of the reconstructed image must be expected to depend strongly on the flow regime in question.

In order to be able to compare the performance of different systems, it is therefore necessary to compensate for this regime dependence; our counsel of desperation is to test each system for a number of regimes, calculate the average error for all regimes and then compare the systems with respect to this average error. Thus we may define the average pixel error per regime as

$$R_{abs} = \frac{1}{M_r} \sum_{k=1}^{M_r} r_{abs}(k) \tag{4.21}$$

and the average void fraction error per regime as

$$E_{void} = \frac{1}{M_r} \sum_{k=1}^{M_r} e_{void}(k) \tag{4.22}$$

where M_r is the number of regimes, and $r_{abs}(k)$ and $e_{void}(k)$ are defined in eq 4.13 and 4.18, respectively.

The next problem is of course to compose a representative selection of flow regimes: As it is impossible to know in advance what suite of regimes which provides the best basis for comparison of system geometries, we content ourselves with choosing the following mixture of 52 different regimes, which at least ensures good variation:

•19 simple *stratified* regimes: $\nu = 0^\circ$, $l_s = \{-0.9, -0.8, \ldots, 0.8, 0.9\}$

•19 simple *annular* regimes: $x_a = 0$, $z_a = 0$, $r_a = \{0.05, 0.10, \ldots, 0.90, 0.95\}$

•14 *angled* or *offset* regimes:

a) Stratified (6): $\nu = 15^\circ$, $l_s = \{-0.5, 0.0, 0.5\}$
$\nu = -30^\circ$, $l_s = \{-0.8, 0.0, 0.8\}$

b) Annular (8): $x_a = -0.4$, $z_a = 0.4$, $r_a = \{0.20, 0.40\}$
$x_a = 0.4$, $z_a = -0.4$, $r_a = \{0.20, 0.40\}$
$x_a = 0.5$, $z_a = 0.1$, $r_a = 0.30$
$x_a = 0.4$, $z_a = -0.4$, $r_a = \{0.25, 0.50, 0.80\}$

The interface level l_s, the void radius r_a and the void position coordinates x_a and z_a are in units of r_0, i.e. the radius of the flow cross section. The angled stratified and the offset annular regimes are shown in Figure 4.15.

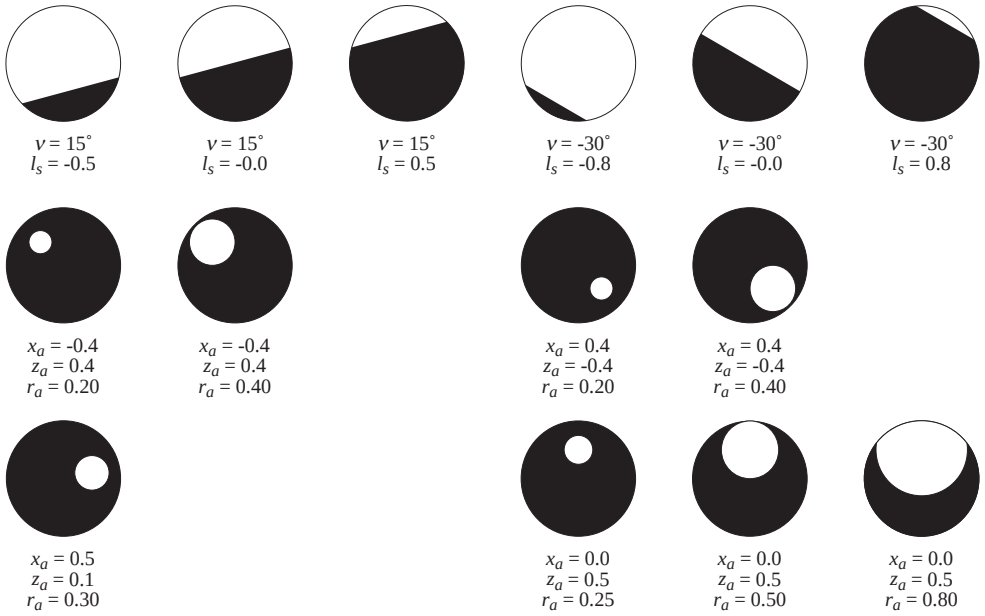

Figure 4.15 Angled stratified and offset annular regimes.

The general *modus operandi* for testing the performance of a given system geometry and grid resolution is then as follows: First, calculate the projection matrix; next, compute the reference pixel densities and raysums for each regime. Then perform reconstruction and compute error estimators r_{abs} and e_{void} for the regime in question. When this has been done for all regimes in the test suite, the average errors R_{abs} and E_{void} are computed.

We will now describe and discuss the various system geometries which have been simulated.

Simulations: Optimum scanning conditions

We start by simulating a system which uses the optimum fan beam scanning conditions defined by eq 3.33; while this system is really not practical in a fixed version due to the high number of views, it is useful to include as a reference. By using $r_s = 4r_0 = 2d$, the number of rays per view m_a is equal to $2n+1$, where n is the grid resolution. The number of views m_s is approximately $2\pi n$, see Table 4.1.

Table 4.1 Optimum scanning conditions for grid resolution n of 2×2 to 16×16 pixels. The angular spacing of rays and views are given by eq 3.33, with $r_s = 4r_0$ and $d = 2r_0$.

	n														
	2	3	4	5	6	7	8	9	10	11	12	13	14	15	16
m_a	5	7	9	11	13	15	17	19	21	23	25	27	29	31	33
m_s	12	18	25	31	37	43	50	56	62	69	75	81	87	94	100

The source-detector distance used is $2r_s$, and the detector width is chosen so that the detectors are stacked edge-to-edge, i.e. the angular interval occupied by a detector is equal to the angular spacing of the rays, see eq 3.33. Finally, we have used zero source width, i.e. a point source is assumed.

The resulting values of R_{abs} and E_{void} are plotted against the grid resolution n in Figures 4.16 and 4.17, respectively. Values are plotted for each separate group of regimes (simple stratified, simple annular, and angled stratified + offset annular), as well as for the entire suite; however, note that we have not considered the standard deviation of the values, so it is not known if the differences between the curves for the various regime groups are statistically significant. In any event, the curves are quite similar for all groups.

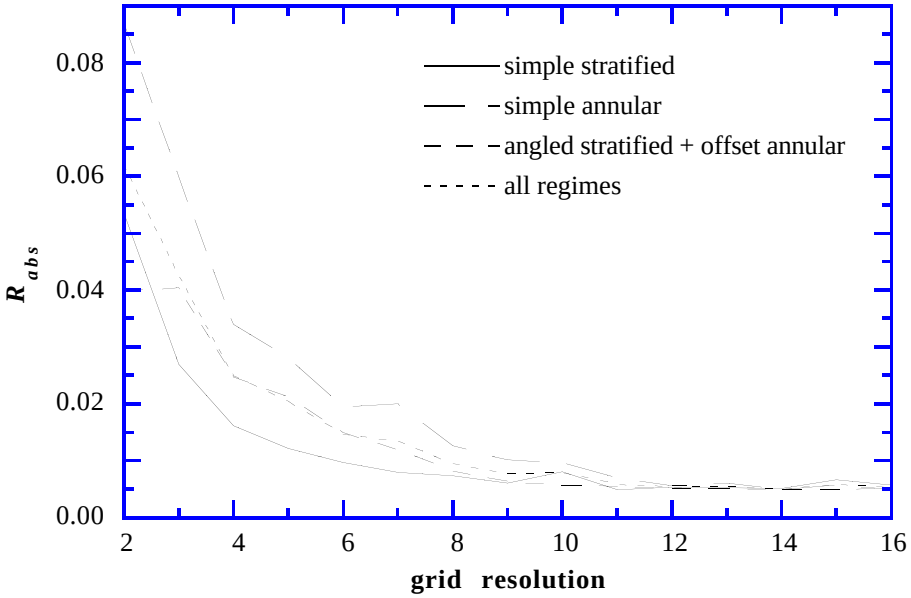

Figure 4.16 R_{abs} plotted against reconstruction grid resolution n for the different groups of regimes (see text) for optimum scanning conditions.

From Figure 4.16 we see that there are errors present in the reconstructed images, even if exact raysum data are used and the scanning conditions for the different grid resolutions are optimal. This may seem to contradict our earlier statement (see Section 3.4.2), that the different reconstruction algorithms produce error-free images from exact raysum data under optimum scanning conditions. However, if the spatial resolution of the reconstruction grid is insufficient, the bandwidth limiting assumption on which reconstruction theory is based is not fulfilled, and there will be errors present in the resulting images, even if the scanning conditions are optimal with respect to the grid resolution.

The reconstruction error in the "optimum conditions" simulations may then be explained from the fact that all 52 regimes in our test suite have *discontinuous* density distribution functions;

therefore, errors will be present for any finite grid resolution, because a discontinuity represents infinite bandwidth in the spatial frequency domain.

It is seen that the reconstruction error decreases with increasing grid resolution, which is clearly because the violation of the bandlimiting requirement gets less severe for better resolution. A rough estimate of the dependence of the average error per pixel R_{abs} on the grid resolution may be done as follows: For both annular- and stratified- type regimes, the number of pixels affected by the discontinuity are proportional to n (which is the number of pixels across the diameter of the flow cross section). If it is assumed that only these pixels, in the "neighbourhood" of the discontinuity, contain errors, the average error per pixel should be proportional to n^{-1}, because the total number of pixels in the image is proportional to n^2.

We may compare this with the actual R_{abs} by normalizing at $n = 16$, which corresponds to the smallest error due to bandwidth effects; there is reasonable agreement for higher values of n, but it turns out that R_{abs} rises more sharply when n decreases than a simple n^{-1} dependence for very small n. This is a consequence of the inability of a coarse grid to accurately represent the features of the density distribution; also, the relative portion of pixels affected by a discontinuity may be greater for very small n.

If we consider the actual magnitude of the reconstruction errors, we see that the average absolute error per pixel per regime, R_{abs}, is about 0.01 for the entire test suite of 52 regimes for a grid resolution of 8×8 pixels; this corresponds to a 1% full scale error, since the density function values are confined to the interval [0, 1].

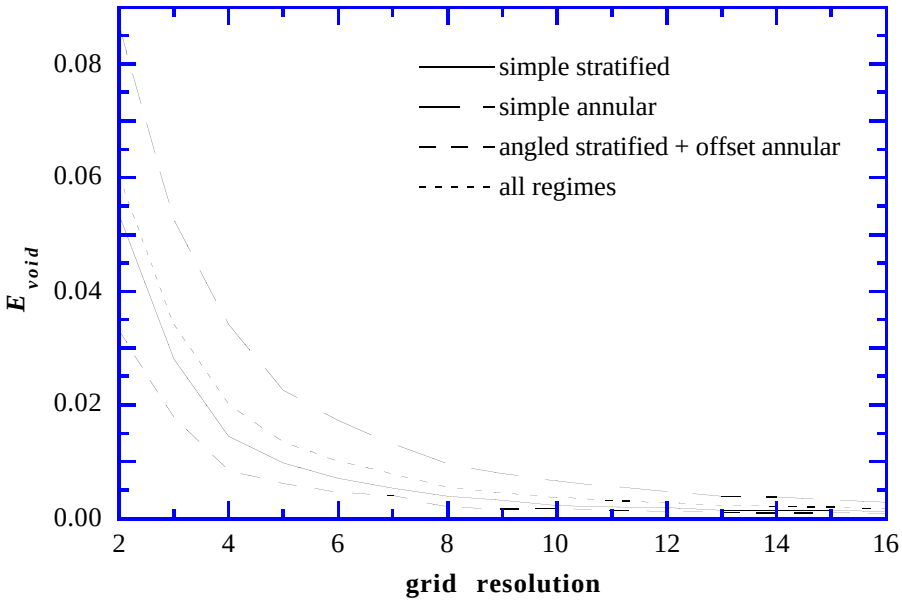

Figure 4.17 E_{void} plotted against reconstruction grid resolution n for the different groups of regimes (see text) for optimum scanning conditions.

Similarly, we see from Figure 4.17 that the absolute void fraction error per regime, E_{void}, is about 0.005 for the same grid resolution, i.e. a 0.5% full scale error. The absolute void fraction error exhibit a similar dependence on the grid size n as the average absolute pixel error R_{abs}, but is smaller, because positive and negative pixel errors tend to cancel each other to some extent in the calculation of the void fraction.

Finally, we note that although a $n = 8$ system using optimum scanning has nice performance figures, it is clearly impossible to implement as a fixed system, because it requires no fewer than 50 views (each of 17 rays): Such a system would have a minimum detector-source distance r_{ds} of about $64r_0$, or 32 times the pipe diameter, see eqns 4.6 and 4.7[1]. Of course, the radial dimension of the imaging instrument could be reduced by reducing the grid resolution, but even a modest $n = 4$ system require 25 views, resulting in a minimum r_{ds} of about 16 pipe diameters. Therefore, it is clear that we are forced to tolerate suboptimal scanning strategies in fixed imaging systems.

Simulations: Single energy systems

Motivated by the concluding remarks of the previous section, we now proceed to consider fixed (nonrotating) single energy systems of more manageable proportions: We will study the performance of systems where the number of views, m_s, ranges from 3 to 15 (odd m_s only), which corresponds to minimum detector-source distances (eqns 4.6 and 4.7) from 1.7 to 9.5 pipe diameters. A complete overview of the source radii r_s and minimum detector-source distances r_{ds} (i.e. the detector array endpoint radius r_d is equal to r_s) for the values of m_s used, is presented in Table 4.2.

Table 4.2 Source radii r_s and minimum source-detector distances r_{ds} (i.e. for $r_d = r_s$) expressed as multiples of the inner pipe radius and diameter, respectively, for the simulated single-energy systems. The number of views, m_s, varies from 3 to 15.

	m_s						
	3	5	7	9	11	13	15
r_s	2.00	3.24	4.49	5.76	7.03	8.30	9.57
$(r_{ds})_{\min}$	1.73	3.08	4.38	5.67	6.96	8.24	9.51

[1]Actually, we have used $m_s = 51$, since only odd m_s are permissible in a fixed (nonrotating) system.

A look at Table 4.1 (see the previous section) reveals that all optimal systems require more than 15 views, so all systems that are discussed in the current section are "suboptimal", except the n = 2 system with 13 or 15 views.

For each value of m_s, simulations are performed for grid resolutions n ranging from 2 to 16; the angular position β_j (relative to the x-axis) of the views (sources) and the ray angles α_l (defining detector angular spacing) are given by the following expressions (see Figure 3.6 and eq 3.33):

$$\beta_j = \frac{2\pi(j-1)}{m_s}, \quad j = 1,\ldots,m_s$$

$$\alpha_l = \frac{\pi l}{2q}, \qquad \begin{cases} l = -n,\ldots,n \\ q \le \dfrac{n\pi r_s}{d} < q+1 \end{cases} \tag{4.23}$$

It is seen that the views are spaced uniformly over the full 2π interval, and that the ray spacing is the same as for the optimal scanning conditions. The number of rays per view, m_a, is equal to $2n + 1$ with this specification, which ensures that the whole pipe cross section is covered by the fan of rays; however, note that two of the systems which have been simulated use *fewer* rays per view than this; also, one of them uses a different detector spacing, see below.

Four different nonrotating single energy systems have been considered:

System 1: The number of rays per view, m_a, is equal to $2n$ +1, and the ray spacing is as defined by eq 4.23. The detector width is chosen so that the detectors are stacked edge-to-edge, just as for the "optimal" system above.

System 2: The ray spacing, and the number of rays per view, are identical to those of System 1, but the detectors are half as wide, i.e. a detector occupies an angular interval which is half the angular spacing of the rays.

System 3: The number of rays per view, m_a, is equal to n , and the spacing of the rays are exactly *twice* the spacing of Systems 1 and 2. The detector width is twice that of System 1, so the detectors are stacked edge-to-edge for this system as well.

System 4: The ray spacing, and detector width, are identical to System 1, but the number of rays per view is chosen as the minimum number required for the fan beam to fully cover a circle around the pipe axis, whose radius is 3/4 of the inner pipe radius r_o.

System 1 is similar to the "optimal" system of the previous section, except that the number of views used are smaller in most cases; the other three systems are variations of the first one:

System 2 is included to investigate the effect of varying the detector width, which is important because it influences the solid angle subtended by the detector at the source, and hence, the statistical fluctuation error of the raysum measurements. System 3 is included to study the effect of "saving" detectors by doubling the spacing of the rays. Finally, the simulation of System 4 is intended to reveal what error that may be introduced when the fan beam of each view does not cover the entire pipe cross section; this is of interest because the statistical error will be large for raysums measured close to the inner circumference of the pipe, due to heavy attenuation in the pipe material and little attenuation in the flow [7, p. 32]; see also Chapter 5.

We will now present the simulation results for these four fixed single-energy systems, i.e. as plots of average absolute pixel error per regime, R_{abs}, and void fraction error per regime, E_{void}, along with the results of the "optimal" system simulation. Note that although all simulations have been performed separately for the three groups of regimes defined above, and the simulation results for the optimal systems are presented both "groupwise" and for all 52 regimes together, we have chosen to include only the results for the entire test suite.

The justification for this is that, in virtually all cases, it turns out that the general shape of the error-versus-gridsize curves for a given system are very similar for the individual regime groups as well as for the entire test suite. Figures 4.16 and 4.17 are in fact typical examples of this, see also our above comments to these plots. Also, the relative error level for the different groups are similar to the "optimal case" for all four systems (the errors are worse for the annular group than for the whole suite, while the errors are smaller for the stratified group).

System 1: $m_a = 2n + 1$, edge-to-edge detectors, fan covers pipe

The R_{abs} and E_{void} plots resulting from this simulation are shown in Figures 4.18 and 4.19, respectively; the values for the optimal system configuration are also included for reference purposes.

If we first consider the average absolute pixel error R_{abs} (Figure 4.18), we see that the performance is quite close to optimum for all values of m_s when n is small, and in fact slightly better than optimum for higher number of views. The latter effect may be explained from the fact that high-m_s, low-n systems use near-optimal or even "superoptimal" scanning conditions, see the comments to Table 4.2.

For higher grid resolutions, the general improvement in image quality with increasing number (but fixed n) of views is clearly demonstrated. Also, for a given number of views, the error at first decreases with increasing n, then stabilizes or even increases slightly for high n and low

m_s. This increase occurs because the amount of available raysum data becomes somewhat sparse for the high grid resolution and low m_s.

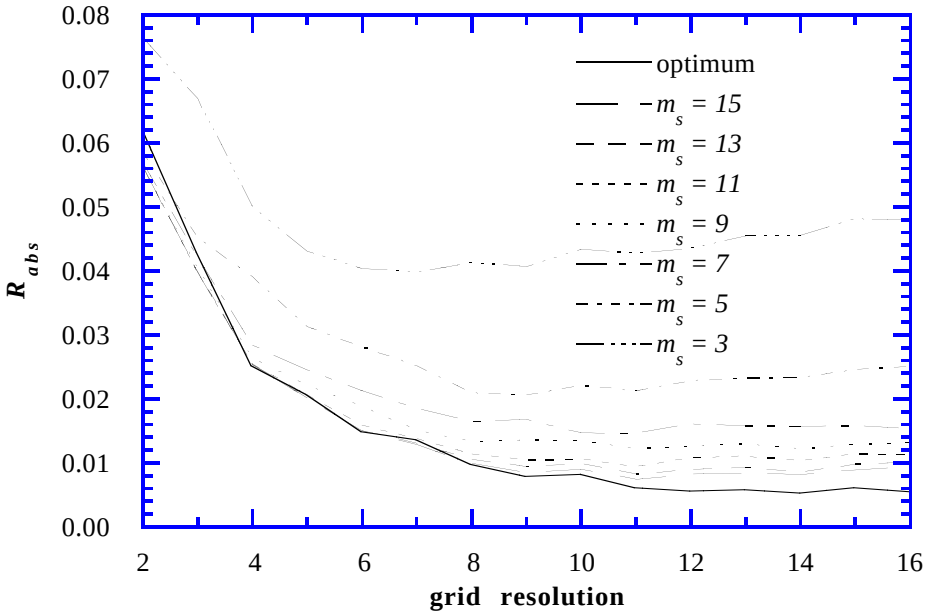

Figure 4.18 R_{abs} results for System 1, with the number of views, m_s, as a parameter, plotted against reconstruction grid resolution n for the entire test suite of 52 regimes. Results for optimal system are included for comparison.

Conversely, the difference in error between optimum and suboptimal systems decreases for very small n, which may seem a little peculiar; however, this effect may be explained as follows:

For low grid resolution, different rays passing through a given pixel may receive wildly different raysum contributions, because the regime density function may vary strongly within the region defining the pixel. As the reconstruction process is based on the assumption of uniform pixel densities, it is clear that it may be impossible for the reconstruction to converge to a pixel density which satisfies all raysums involving that pixel; i.e. there is a "raysum ambiguity" with respect to the reconstructed pixel densities. Now, because more rays pass through each pixel in a system using many views than systems using a low number of views, this ambiguity effect error increases with increasing m_s, and is especially severe for low grid resolutions, as a greater portion of the pixel are affected by such errors for small n.

Thus, for low grid resolution, the extra ambiguity error for high m_s outweighs the expected error reduction due to a greater amount of raysum information; at better grid resolution, the ambiguity error is insignificant compared to errors caused by bandlimiting effects and insufficient amounts of raysum data.

We now turn the attention to the E_{void} results plotted in Figure 4.19: Note that with the chosen vertical scale, the data for the lower grid resolutions are not visible; however, they approach very closely the optimal data, so we have concentrated on the data for the higher grid resolutions instead.

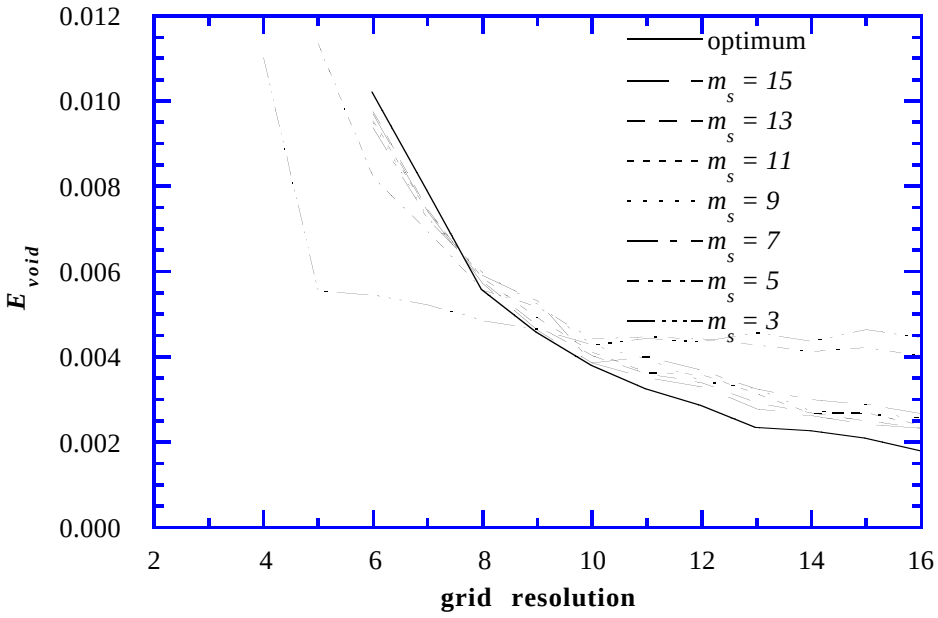

Figure 4.19 E_{void} results for System 1, with the number of views, m_S, as a parameter, plotted against reconstruction grid resolution n for the entire test suite of 52 regimes. Results for optimal system are included for comparison.

For n smaller than 8, and regardless of the number of views used, the void fraction error for this system is in fact less than for the optimal system; further, the error is not very much larger than in the optimal case for higher grid resolutions. Also, for low grid resolution, the void fraction error is at minimum when the smallest number of views are used. These phenomena may be caused by the "ambiguity effect" described above: Adding extra views at low grid resolution does not increase the precision of the void fraction estimate, but rather increases the confusion!

The fact that the void fraction error E_{void} is smaller than for the optimal case for small n, even if the converse is true for the pixel error R_{abs}, must be because positive and negative pixel errors cancel each other when the void fraction is calculated from pixel densities.

The most important observation to be made from the simulation results of this section, is perhaps that it is possible to achieve performance nearly equal to that of the "optimal" system with systems using a much smaller number of views. While this at first may seem a little strange, it may be explained from the fact that the density functions of all regimes in the test suite exhibit piecewise homogeneity and varying degree of symmetry; therefore, except for the discontinuities, their information content is lower than for the general case from which the

optimal scanning conditions are derived, and they may be successfully reconstructed from a suboptimal number of views [21, pp. 175-178].

Apart from the peculiarities mentioned above, the void fraction error of this system seems to be relatively insensitive to the number of views used, and the error level is similar to that of the optimal system. The average pixel error, on the other hand, gets steadily smaller when the number of views is increased. However, the pixel density accuracy does not improve very much when m_s is increased beyond 7 or 9; this may then be a suitable compromise for the number of views used, with respect to the tradeoff between accuracy and complexity.

System 2: $m_a = 2n + 1$, narrow detectors, fan covers pipe

The R_{abs} versus n , or pixel error versus grid resolution plot, for this system is shown in Figure 4.20, together with the optimal system results.

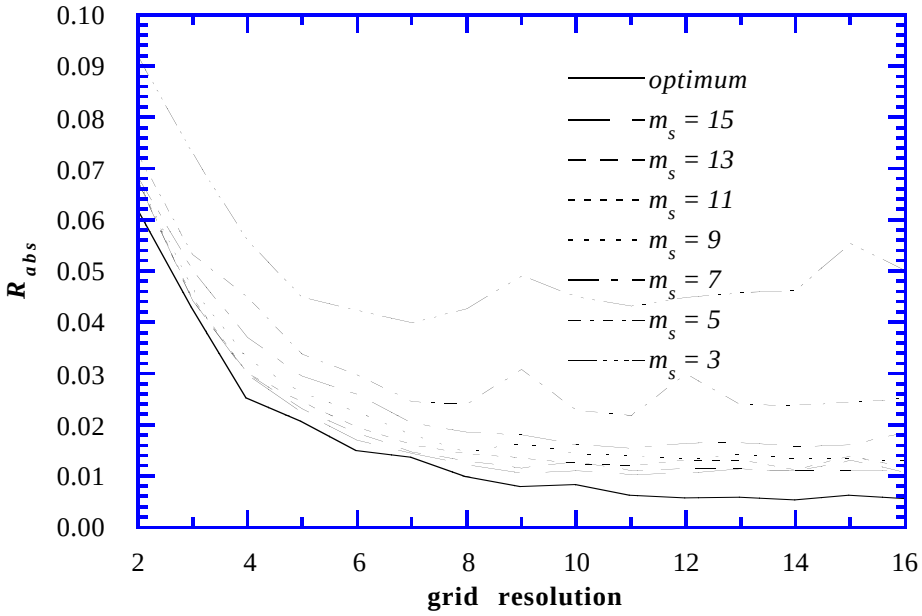

Figure 4.20 R_{abs} results for System 2, with the number of views, m_S, as a parameter, plotted against reconstruction grid resolution n for the entire test suite of 52 regimes. Results for optimal system are included for comparison.

It is seen that this system behaves in a very similar manner to System 1, except that the errors are slightly larger. For the 3 view and 5 view systems, the error curves does exhibit some small irregularities compared to System 1; these are probably caused by the difference in ray-pixel and ray-regime intersection patterns. While these “bumps” are clearly insignificant from an error level variation point of view, they are interesting because they give some indication of the sensitivity of the reconstruction to changes in the regime-ray intersection pattern, or the “regime dependence” of the image accuracy.

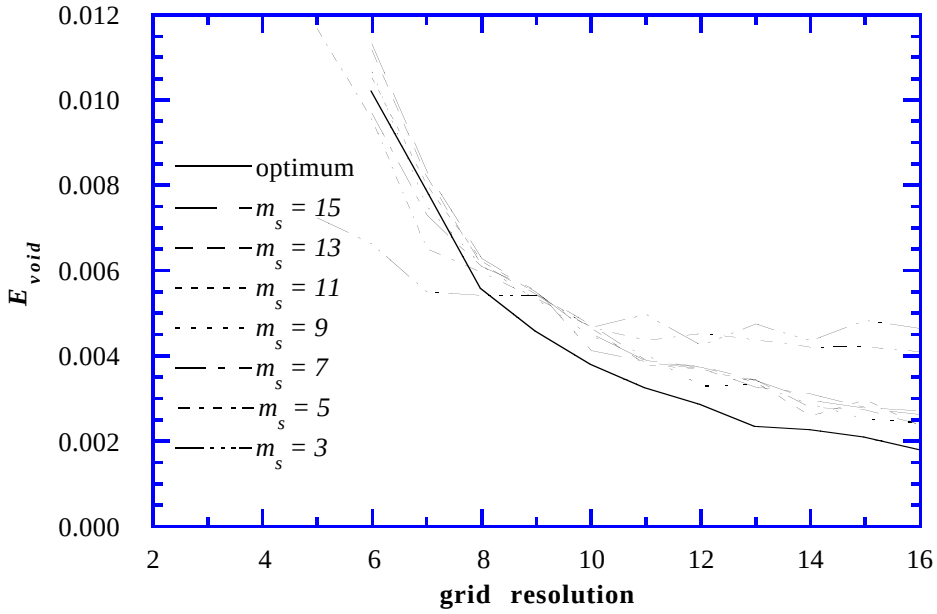

Figure 4.21 E_{void} results for System 2, with the number of views, m_s, as a parameter, plotted against reconstruction grid resolution n for the entire test suite of 52 regimes. Results for optimal system are included for comparison.

If we consider the E_{void} data, plotted in Figure 4.21, we see that the error curves resemble the corresponding System 1 data quite closely (see Figure 4.19), except that the errors are slightly larger for low grid resolution. Thus, it may be concluded that Systems 1 and 2 behave almost identically as far as the precision of the void fraction estimates are concerned.

The significance of the simulation results for System 2, is that one may safely use maximum width detectors, as in System 1, without any loss of image accuracy compared to a system using narrower rays, or beams[1]. Using the widest possible detectors maximises the solid angle subtended by a detector at the source, and hence, the number of detected photons; this in turn minimize the statistical fluctuation errors of the measured raysums.

However, it should be kept in mind that increasing the beam width may introduce other raysum measurement errors; because the pathlength/beamwidth ratio is increased, the sensitivity of the measurement for a nonuniform density distribution within the ray is increased (see Section 2.6.2), thus introducing a regime dependence. We will discuss this effect in Chapter 5, along with the need to compromise between the raysum regime dependence error and the statistical fluctuation error when choosing the detector width.

---

[1]It should be noted that the optimal sampling conditions defined in Section 3.4.1 are derived for the case of infinitesimally narrow rays, see [21, pp. 54-84].

System 3: $m_a = n$, edge-to-edge detectors, fan covers pipe

The R_{abs} simulation results for this system are shown in Figures 4.22. The striking feature of this plot is the very small error for low grid resolution; this may be explained in terms of the raysum ambiguity effect discussed above, since this system uses half as many rays per view as System 1 does. For moderate and higher values of n, however, the errors are similar to those of System 1. Finally, we notice some irregularities for the error curve for $m_s = 3$, see our comments to System 2.

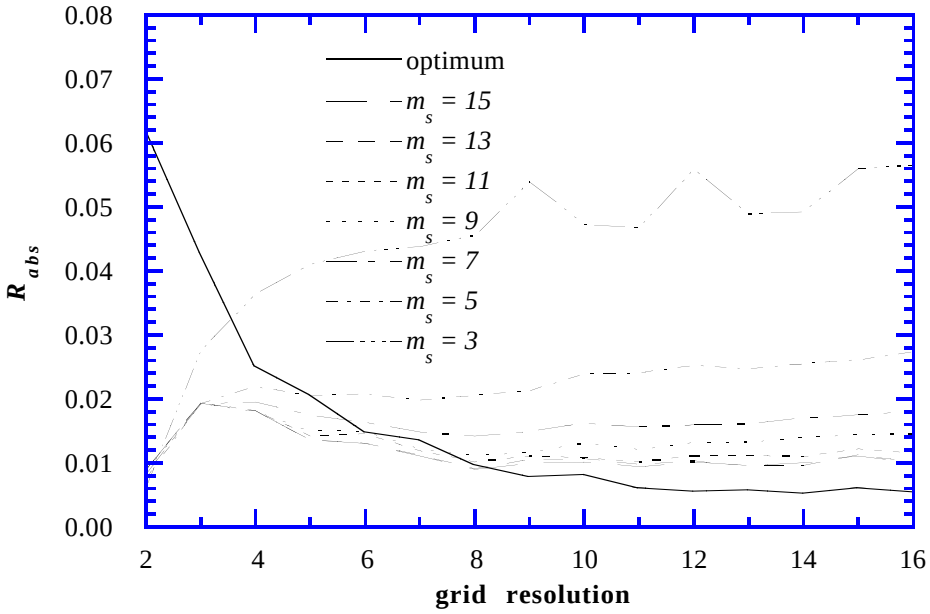

Figure 4.22 R_{abs} results for System 3, with the number of views, m_s, as a parameter, plotted against reconstruction grid resolution n for the entire test suite of 52 regimes. Results for optimal system are included for comparison.

Our comments for E_{void} plot shown in Figure 4.23 are very much the same as those for the pixel error plot above: For low grid resolution, the errors are smaller than for System 1, and than for the "optimal "system. At higher resolutions, the errors are similar to the System 1 errors, except for m_s values of 11, 13 and 15, for which the errors are slightly smaller.

Note, however, the erratic behaviour of the E_{void} curves for low n; this may indicate a high sensitivity for ray-regime intersection pattern variations for this system; similar effects are also seen in the R_{abs} plot in Figure 4.22.

To summarize the results for the double detector width system, we might conclude that this scanning strategy looks promising compared to System 1 as far as the error levels are concerned, but the peculiarities of the error curves indicate a stronger regime dependence. In addition, the use of greater detector width cause a greater raysum regime dependence error, but reduce the statistical fluctuation error, see the discussion for System 2.

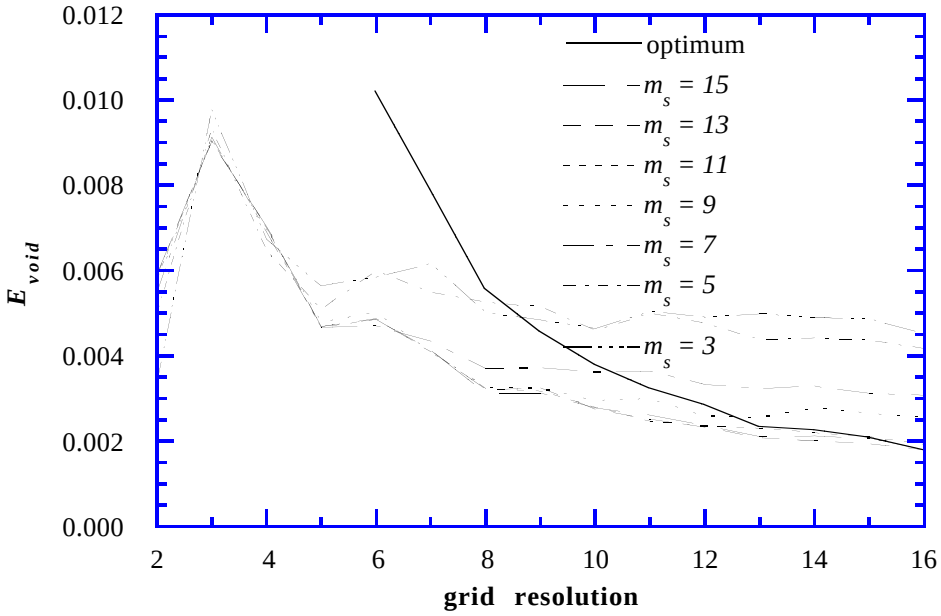

Figure 4.23 E_{void} results for System 3, with the number of views, m_S, as a parameter, plotted against reconstruction grid resolution n for the entire test suite of 52 regimes. Results for optimal system are included for comparison.

System 4: $m_a < 2n + 1$, edge-to-edge detectors, narrow fan

This system is special in the sense that the number of rays per view does not change in a simple linear fashion when the grid resolution is varied; see the R_{abs} plot of Figure 4.24.

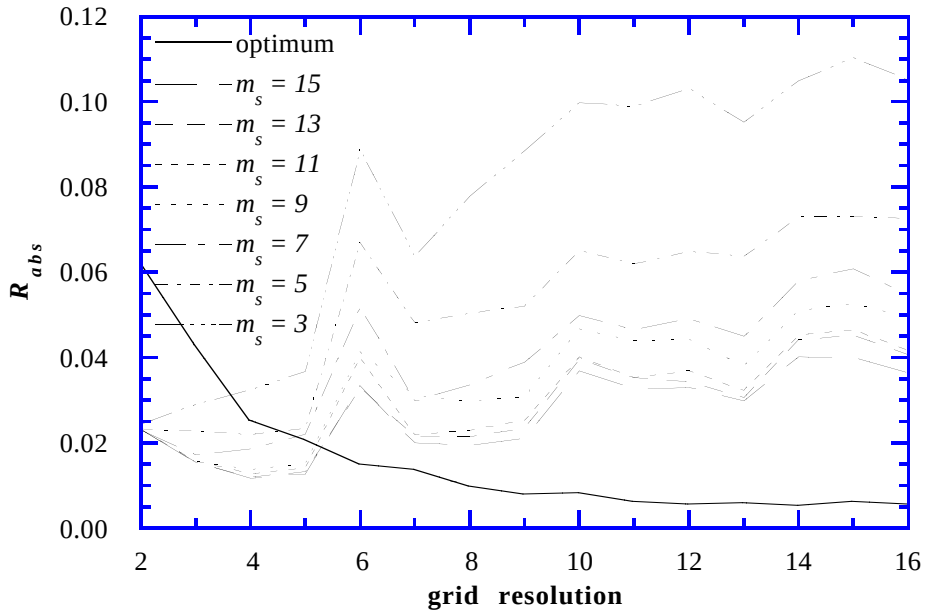

Figure 4.24 R_{abs} results for System 4, with the number of views, m_S, as a parameter, plotted against reconstruction grid resolution n for the entire test suite of 52 regimes. Results for optimal system are included for comparison.

The R_{abs} curves exhibit characteristic "jumps" for n = 6, 10 and 14, which corresponds to the "discontinuities" of the m_s versus n relation: The number of rays per view varies as follows[1]: $m_a = 2n\text{-}1$ for n = 2..5, $m_a = 2n\text{-}3$ for n = 6..9, $m_a = 2n\text{-}5$ for n = 10..13, and $m_a = 2n\text{-}7$ for n = 14..16.

Due to the reduction of the "raysum ambiguity error", the performance of this system appears to be better than System 1 for very small n. As the grid resolution is increased, the errors increase markedly at the "discontinuity points" mentioned above, because of the relative decrease in the amount of available raysum information. Between these points, the error decreases slightly with increasing n for higher m_s, is constant for intermediate m_s, and increases a little for small m_s; this behaviour is roughly the same as for System 1. As usual, the values of R_{abs} decrease when the number of views is increased.

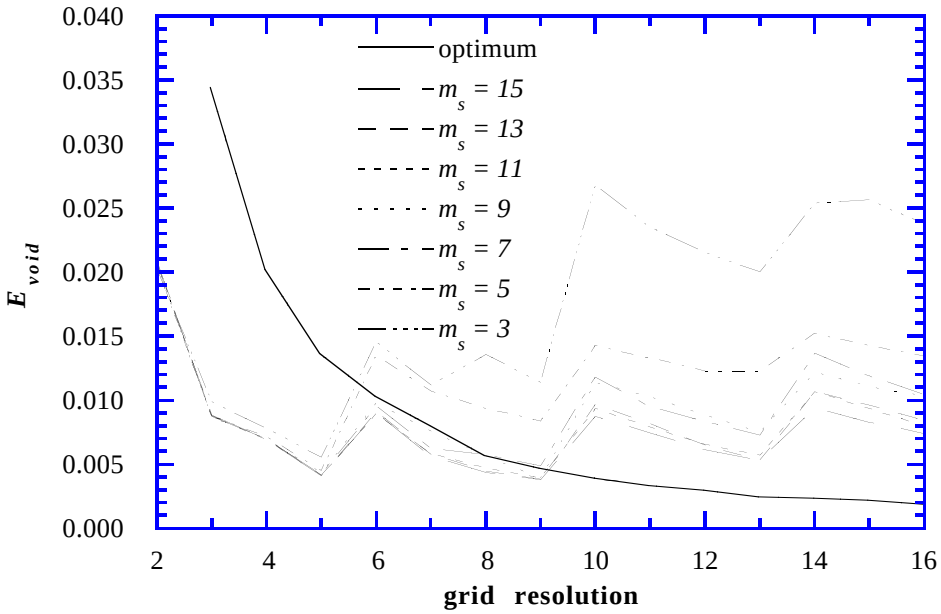

Figure 4.25 E_{void} results for System 4, with the number of views, m_s, as a parameter, plotted against reconstruction grid resolution n for the entire test suite of 52 regimes. Results for optimal system included for comparison.

The E_{void} curves shown in Figure 4.25 behave very much like the pixel error curves: At low grid resolution, the errors are smaller than for System 1, but are larger for higher resolution. As for System 1, the error decreases with increasing n, except at the m_a "discontinuity" points.

---

[1]The irregularities appear because the number of rays used is chosen to be the minimum number required to contain a circle of radius $(3/4)r_o$. Hence, there will be some overlap, which is greater in the relative number of rays for small n, since the rays are wider in this case. Also, the actual angular interval covered by the fan will vary for varying n.

Because the amount of raysum data is reduced when the angular interval of the fan is reduced, the increase of the image error for higher grid resolutions is not unexpected, nor is the error decrease for low resolutions; the latter effect is due to a reduction of the ambiguity error.

The observed "discontinuity" points of the R_{abs} and E_{void} curves are interesting because they indicate the sensitivity of the errors for a change in the angular interval covered by the fan. It is obvious that the fan of rays for each view should cover the flow cross section completely to minimize reconstruction errors; however, this may not be desirable due to large statistical fluctuation errors in raysums measured close to the inner circumference of the pipe.

Discussion: Single energy systems

The first conclusion to be drawn from the simulation results from the previous paragraphs, is the importance of choosing a reconstruction grid of adequate resolution: Both the bandlimiting error and the related "raysum ambiguity error" is severe at lower resolutions for Systems 1 and 2; this is seen from the fact that errors are much smaller for Systems 3 and 4 for low grid resolution. Regime sensitivity and intersection pattern sensitivity is much more pronounced for lower n, which means that a low resolution system is more unreliable than a high resolution one, in the sense that its performance may vary strongly with the flow regime, which is clearly undesirable in an imaging system.

The value of a low resolution image is questionable even if the average pixel densities are accurate, since some degree of spatial resolution is required to produce useful information about the features of the density distribution of the flow cross section. A reconstruction grid resolution of 7×7 is a perhaps a suitable minimum value.

When we consider the results for highest grid resolutions, we see that the pixel error curves approach a constant value, or exhibit a slight increase as n increases; this tendency is caused by a shortage of available raysum information. The "suboptimality" of the fixed measurement systems, with regard to the number of views, obviously gets worse for increasing grid resolutions, compare Table 4.1. We note the influence of the number of views used on the reconstruction error, which decrease steadily with increasing m_s. Also, for m_s higher than about 7 or 9, the performance of the best fixed systems is quite close to that of an optimal system, at least for the relatively simple regimes considered in this work.

The results for System 4, which utilizes narrower fans than the other systems, show the importance of good coverage of the pipe cross section by the fans of rays: Even if this system uses a higher number of rays than System 3, its performance is worse; moreover, the rapid change of the error level for small changes in the angular interval covered by the fan indicates

the strong effect of incomplete fan coverage of the pipe. However, this will probably have to be tolerated, as the raysum measurement error will be very large for rays close to the pipewall.

To summarize, we conclude that System 1 (or 2) is probably the best, even if other systems appear to offer better performance for some resolutions and choices of m_s. This is because the performance of the other systems are more intersection pattern and regime sensitive, which casts doubt on their reliability. Note, however, that practical considerations (raysum measurement error) may force us to choose a narrow-fan system such as System 4, although it may not be necessary to reduce the fan width to 75%. We will look into this in Chapter 5.

In the above discussion we have concentrated on the pixel error; it is seen from the average void fraction error plots that good void fraction measurement accuracy may be accomplished using quite simple systems, compared to what will be required for imaging. However, even the simplest imaging system would perhaps be a little overkill if a void fraction measurement is all that is required.

Simulations: Dual energy systems

For dual (and triple) energy systems, the quantity m_s is redefined to denote the number of detector arrays with associated groups of sources, instead of the number of views. Therefore, the number of views, and source positions, is twice or three times the value of m_s for double or triple energy systems, respectively. The basic geometry for dual (and triple) energy systems is shown in Figure 4.7; note that the angle β_j specify source position S_0, and that positions S_1 and S_2 are specified relative to this by the source spacing angle φ. Further, for a dual energy system, only positions S_1 and S_2 are used.

The dual energy system under consideration uses a detector endpoint distance r_d equal to the source radius r_s, and the source spacing angle φ is chosen to be equal to $\xi/2$ (which is equal to $\zeta/2$ for $r_s = r_d$). Hence, the source-detector distance for position S_0 is given by (see eq 4.8):

$$(r_{ds})_0 = r_s\sqrt{2(1+\cos 3\varphi)} \tag{4.24}$$

The nominal angular interval $\Delta\alpha$ covered by the fan, which is determined by the positions of the detector array endpoints and the source position, is identical for the fans defined by S_0, S_1 and S_2 for $r_d = r_s$; it is given by

$$\Delta\alpha = 2\arctan\left(\frac{\sin 3\varphi}{1+\cos 3\varphi}\right) \tag{4.25}$$

equal to $2\cdot(3\xi/4)$, which is in fact identical to the interval used for single-energy System 4. However, fans defined by S_1 and S_2 are not symmetric with respect to the source - pipe

centerline, see Figure 4.7. The number of rays per view used is the number required to contain the fan of angular extent $\Delta\alpha$ defined by source position S_0 and the detector array. The rays of the fans defined by S_1 and S_2 are in turn determined by the detector positions; note that ray spacing and width for fans 1 and 2 are not uniform.

For the simulation of the dual energy system, we have chosen the same ray spacing and detector width (relative to the position of S_0) as single-energy System 1, or as the optimal system. The actual number of detectors in each array is determined by the angular interval to be covered by the fan of rays (see previous paragraph); the values of m_a used are identical to those used in single energy System 4. The resulting R_{abs} plot is shown in Figure 4.26

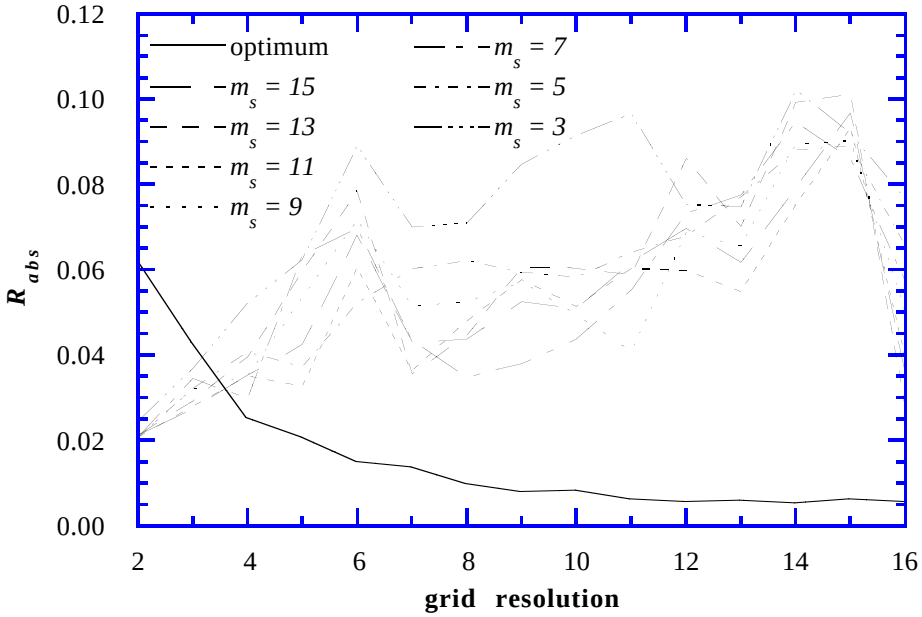

Figure 4.26 R_{abs} results for dual energy system, with the number of detector arrays, m_s, as a parameter, plotted against reconstruction grid resolution n for the entire test suite of 52 regimes. Results for optimal system are included for comparison.

The R_{abs} plot does not look very encouraging; even though this dual energy system geometry provides about 50% more raysum data than single energy System 1, its performance is inferior. There is a general increase in error level with increasing grid resolution, but with quite erratic behaviour of the error curves as well: As for the narrow fan single energy system (System 4), the error curves exhibit "jumps" at the values of n for which the fan angular interval changes abruptly. The trend of improvement of the accuracy with increasing m_s seen for the single energy systems is only partly preserved.

Similar comments apply to the E_{void} results shown in Figure 4.27; the fluctuations are smaller than for the pixel error curves, but the error level is higher than for the single energy systems considered earlier.

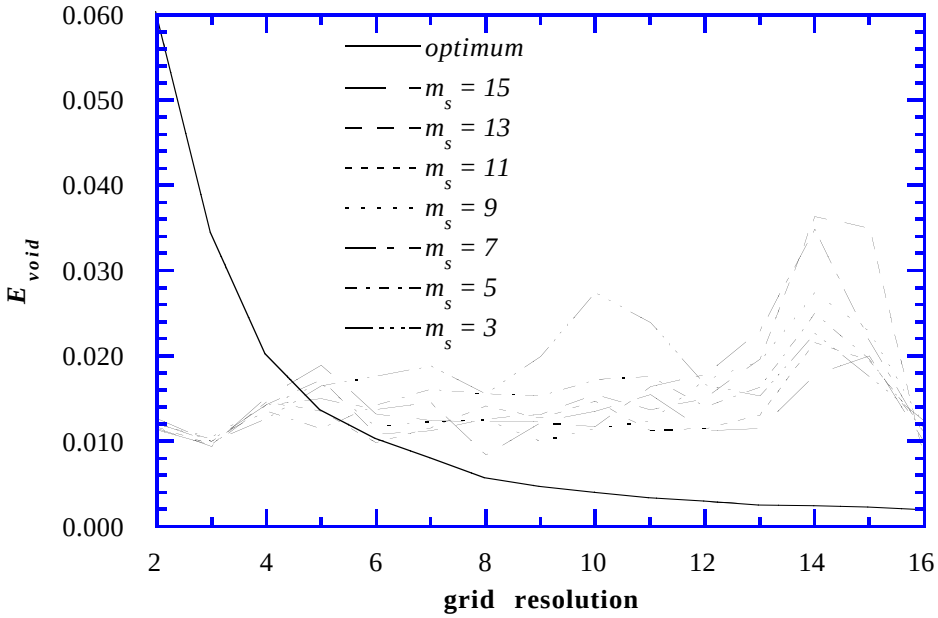

Figure 4.27 E_{void} results for dual energy system, with the number of detector arrays, m_S, as a parameter, plotted against reconstruction grid resolution n for the entire test suite of 52 regimes. Results for optimal system are included for comparison.

It may seem strange that this system, which provides exactly twice as many raysums as the single energy narrow fan system (System 4), performs so poorly: Except for the case of $m_S = 3$, for which the errors are similar to System 4, the performance is worse than for all single energy systems.

However, the dual energy system differs from the single energy systems in several respects: First, each fan (or view) does not cover the object in a symmetrical manner, see Figure 4.7. Second, the ray spacing and width will not be uniform (for fans defined by source positions S_1 and S_2). Third, the spacing of *views* will not be uniform over the 2π interval: The angular distribution of the detector arrays are uniformly spaced, and hence the pair of views associated with each array, but for the chosen φ, the spacing of the two views is such that the overall view spacing is nonuniform.

Thus there are several factors present which may account for the somewhat disappointing performance of the dual energy system. It is of some interest to establish the cause for this behaviour, and for this reason, we include the simulation of a system using exactly the same source positions (view positions) as the dual energy system, but with fans covering the entire cross section, i.e. using $m_a = 2n + 1$ rays per view. The ray width and spacing are uniform, just as for single energy System 1, as is the source radius r_S. Note, however, that because of to the nonuniform view spacing and the fact that twice as many views are used as for the single energy systems, this geometry is impossible to implement as a fixed system.

The R_{abs} and E_{void} results for this dual energy "reference system" are shown in Figures 4.28 and 4.29, respectively.

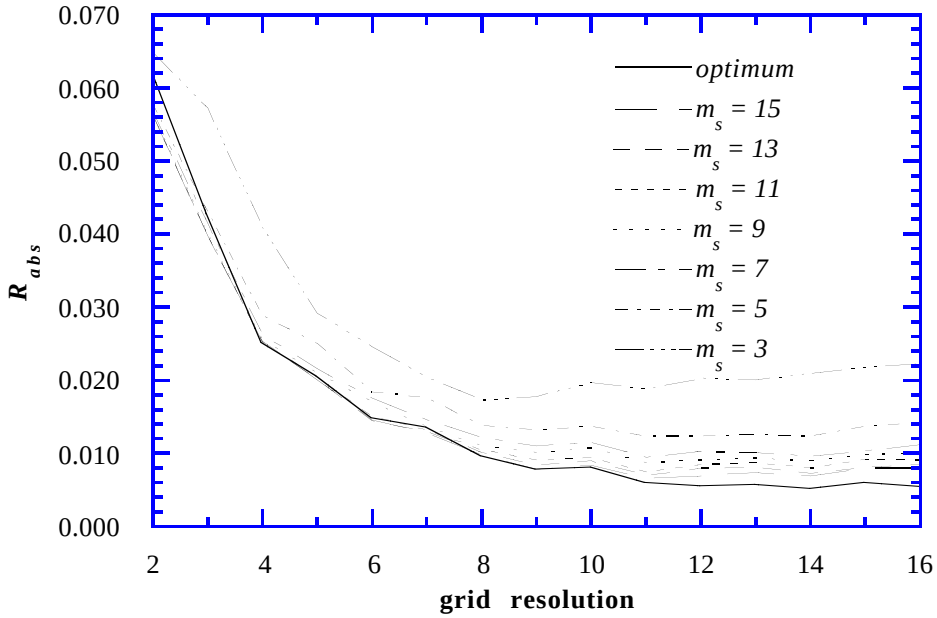

Figure 4.28 R_{abs} results for dual energy reference system, with the number of detector arrays, m_S, as a parameter, plotted against reconstruction grid resolution n for the entire test suite of 52 regimes. Results for optimal system are included for comparison.

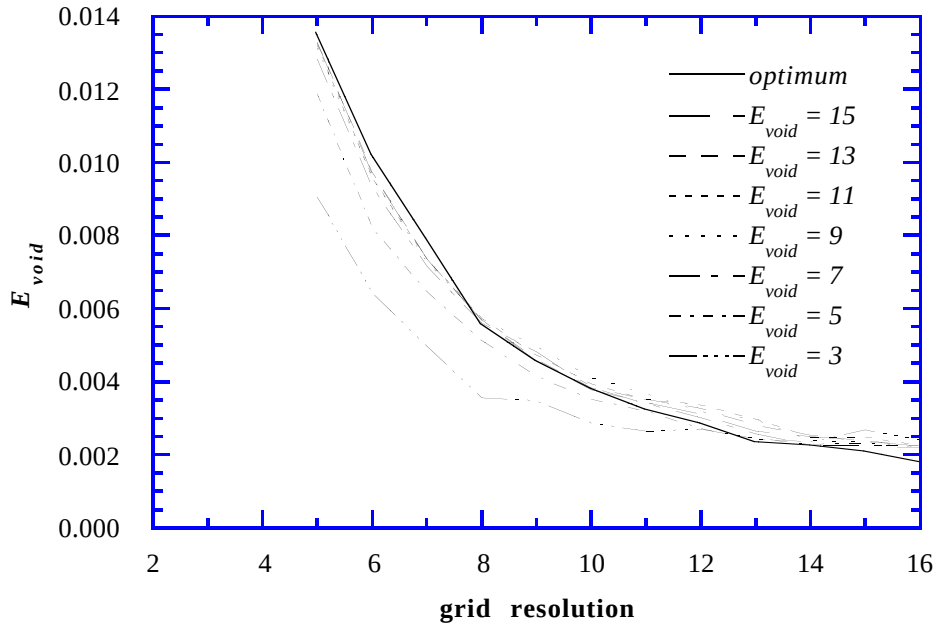

Figure 4.29 E_{void} results for dual energy reference system, with the number of detector arrays, m_S, as a parameter, plotted against reconstruction grid resolution n for the entire test suite of 52 regimes. Results for optimal system are included for comparison.

For both types of error estimators, the general n and m_s dependence is very similar to the corresponding results for single energy System 1; furthermore, the overall accuracy is as good as, or better than, System 1. Thus, we may conclude that the nonuniform view spacing is *not* the cause of the poor performance of our first dual energy system.

If we consider the other differences between the two dual energy systems, it seems improbable that nonuniform ray spacing and ray width should have any strong effect on the error level of the reconstruction image, because this nonuniformity is quite small for the rather modest value of φ which have been used.

This leaves us with the incomplete, and asymmetric, coverage of the pipe cross section by the fans of rays: From the System 4 simulation results, we already know that limiting the angular interval covered by the fans to 75% of what is required to cover the entire flow cross section, does have a negative effect on the reconstruction accuracy. The asymmetric coverage of the flow cross section by the fans is probably responsible for the further increase of the errors, along with added fluctuations of the error curves; we base this assumption on the sensitivity of the reconstruction error to fan angular interval variations observed for System 4.

From the above discussion, we conclude that dual energy systems does not seem to offer any particular advantages compared to single energy systems. Although we have not investigated the effect of varying the parameters φ and r_d, we suspect that this will not result in marked improvement of the performance. There are two reasons for this: First, while the error level will decrease if the fan angular interval is increased, it is seen from Figure 4.7 that this requires a smaller source spacing angle φ. However, by doing this, one loses the advantage of using a dual energy system in the first place, since the raysum information gathered by the two fans associated with each detector array will not be very different.

The second reason is that the System 4 simulations, and also the dual energy system simulations, indicate a strong sensitivity of the errors to variations of the fan angular interval. Therefore, we have reason to believe that dual energy systems may not be too reliable, in the sense that they would suffer from strong regime-ray intersection pattern sensitivity.

4.2.3. Comparison of results for nonrotating systems

We have now established what performance which can be expected from some types of single and dual source energy fixed measurement systems for γ-ray flow imaging. It seems clear that a single energy system using as wide fans of rays as possible is the best choice of system.

For System 1, with n = 8, the average pixel error decreases from 4% to 1% of full scale as the number of views is increased from 3 to 15; also, the performance for the higher values of m_s closely approaches that of the optimal system. For System 4, the corresponding R_{abs} values

are about twice the System 1 values. If we consider the void fraction estimate precision, we find that for $n = 8$, E_{void} is lower than 0.6% of full scale for System 1 and lower than 1.5% for System 4. In any event, this means that very respectable reconstruction precision is possible using our nonrotating single energy systems.

Although a triple energy system is a simple extension to the dual energy geometry, we have not found it worthwhile to simulate such a system, because of the poor results for the dual energy system. Adding the extra source in position S_0 is in fact the same as adding single energy System 4 to the dual energy system; while the performance certainly would improve compared to the dual energy system, such a solution would not be very effective compared to a single energy system, even if the number of detectors would be lowered. Also, as normal collimators cannot be used in a multienergy system, it is not clear if it is possible to measure raysums accurately, due to the effect of scattered radiation (see Section 4.1.3).

When we consider the question of selecting the number of views and number of rays per view for a nonrotating system, it is necessary to take raysum measurement errors into account, to determine the overall performance of the system: The main contributions to this error are statistical fluctuations in the number of detected photons, finite beam width effects, and buildup of scattered radiation, all of which are dependent on the system geometry. The analysis of these errors is the topic of the next chapter.

5. Principle and accuracy of raysum measurement

5.1. Introduction

In a γ-ray imaging system, the raysums needed for image reconstruction are found using densitometry techniques, which were described in general terms in Chapter 2. We will now describe more specifically how these techniques are applied to flow imaging raysum measurement, and then we proceed to discuss the factors influencing the accuracy of the measurements; this will serve as the basis for the selection of detectors and isotopes. In the above analysis, it turns out that it is necessary to know the photopeak and total efficiencies for the detectors used; for this purpose, we have developed the Monte Carlo detector simulator DSIM, which will also be described in this chapter.

5.2. Raysum measurement for flow imaging

The geometry for pipeflow raysum, or chordal density measurement, is shown schematically in Figure 5.1, for the case of an infinitesimally narrow photon beam.

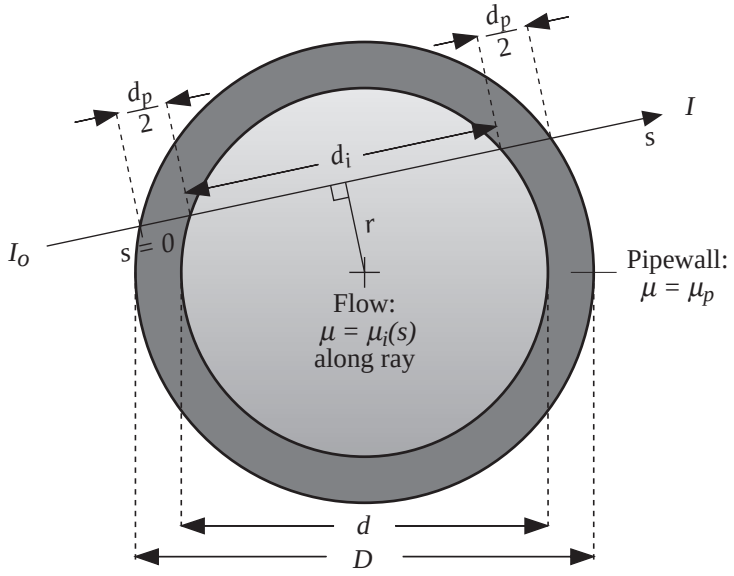

Figure 5.1 Measurement of pipeflow raysums, or chordal densities, for CT reconstruction of cross sectional density distribution image. The measurements are taken in a plane perpendicular to the pipe axis.

First, we define I_0 as the effective number of monochromatic photons per unit time registered by a detector without the absorber (i.e. the pipe) between the source and detector. This

quantity is determined by the source activity S_0, the fraction of solid angle ($\Omega_d/4\pi$) subtended at the source by the detector, and the photopeak (or full energy) detection efficiency ε_p:

$$I_0 = S_0 \varepsilon_p \frac{\Omega_d}{4\pi} = S_0 \varepsilon_p \frac{A_d}{4\pi r_{ds}^2} \tag{5.1}$$

The fraction of solid angle may be expressed as the ratio of the detector front face area A_d to the surface area of a sphere with radius equal to the source-detector distance r_{ds}, provided that the source-detector distance is not too small. We have used the photopeak efficiency rather than the total detection efficiency, because the presence of scattered radiation in a multisource system mean that only full energy detector events can be accepted if the attenuation formula (eqns. 2.64 and 2.74) is to be valid.

If it is assumed that no attenuation occurs outside the pipe, the detected full energy intensity I with the pipe in place between the source and detector is given by (see Figure 5.1)

$$I = I_0 \exp\left(-\int_0^{d_p+d_i} \mu(s)ds\right) = I_0 \exp(-\mu_p d_p) \exp\left(-\int_{\frac{d_p}{2}}^{\frac{d_p}{2}+d_i} \mu_i(s)ds\right) \tag{5.2}$$

where we have used:

$$\mu(s) = \begin{cases} \mu_p & ; 0 \le s < \frac{d_p}{2} \\ \mu_i(s) & ; \frac{d_p}{2} \le s \le \frac{d_p}{2} + d_i \\ \mu_p & ; \frac{d_p}{2} + d_i < s \le d_p + d_i \end{cases} \tag{5.3}$$

We also note that the quantities d_p and d_i are functions of the normal distance r from the pipe centre to the ray:

$$\left.\begin{aligned} d_i(r) &= \sqrt{d^2 - 4r^2} \\ d_p(r) &= \sqrt{D^2 - 4r^2} - \sqrt{d^2 - 4r^2} \end{aligned}\right\} \quad -\tfrac{d}{2} \le r \le \tfrac{d}{2} \tag{5.4}$$

We now define the ideal *normalized average raysum* ρ_N as

$$\rho_N = \frac{\overline{\rho}_i}{\rho_f} = \frac{1}{\rho_f}\left\{\frac{1}{d_i}\int_{\frac{1}{2}d_p}^{\frac{1}{2}d_p+d_i} \rho_i(s)ds\right\} \tag{5.5}$$

where ρ_i(s) denotes the flow density along the ray (see Figure 5.1), and ρ_f is the density of the heaviest fluid component. Using eq 2.70, we may write

$$\rho_N = \frac{\overline{\mu_i}}{\mu_f} = \frac{1}{\mu_f}\left\{\frac{1}{d_i}\int_{\frac{1}{2}d_p}^{\frac{1}{2}d_p+d_i}\mu_i(s)ds\right\} \tag{5.6}$$

which is a good approximation for multicomponent flow under certain restrictions of the photon energy E and the atomic number Z of the flowing media, see Section 2.6.1. Furthermore, eq 5.6 is exact for *all* E and Z in the case of two-component gas-fluid flow, since it is safe to assume that no attenuation occurs in the gas due to its low density.

By combining eqns 5.2 and 5.6, we get the following expression for the normalized raysum ρ_N:

$$\rho_N = \frac{1}{\mu_f d_i}\left(\ln\left(\frac{I_0}{I}\right) - \mu_p d_p\right) \tag{5.7}$$

Hence, it is possible to find the normalized raysum from an attenuation measurement, since d_i, d_p, μ_f and μ_p are known. However, the accuracy of these quantities will of course influence the accuracy of the calculated ρ_N, and it is therefore desirable to avoid having to know them explicitly. This may be accomplished by calculating the normalized raysum relative to suitable calibration measurements [6][7, pp. 23-25]; which is done as follows:

If it is assumed that no attenuation occurs in the gas, the detected intensity of the transmitted beam for a gas-filled, or "empty" pipe is equal to:

$$I_E = I_0 \exp(-\mu_p d_p) \tag{5.8}$$

Similarly, if the pipe is filled with the heaviest fluid phase, the detected intensity is given by

$$I_F = I_0 \exp(-\mu_p d_p - \mu_f d_i) \tag{5.9}$$

where μ_f is the attenuation coefficient of this phase. In other situations, i.e. between these two extremes, the detected intensity is given by

$$I = I_0 \exp(-\mu_p d_p - \rho_N \mu_f d_i) \tag{5.10}$$

which is an approximation for multicomponent flow and is exact for two-component gas-fluid flow, see above. We now define the *measured* normalized raysum p as follows:

$$p = \frac{\ln\left(I_E / I\right)}{\ln\left(I_E / I_F\right)} = \rho_N \tag{5.11}$$

We see that p is equal to ρ_N (within the approximations in eqns 5.6 and 5.10) provided that the conditions for the attenuation formula are fulfilled, i.e. as long as the photon beam may be regarded as monochromatic and infinitesimally narrow. Our reason for distinguishing between p and ρ_N is the fact that these assumptions have a varying degree of validity in practice, so an error will invariably be committed when estimating ρ_N by p.

5.2.1. Statistical fluctuation uncertainty and choice of γ-isotope

If the measurement time for I_E and I_F is much longer than that of I, only statistical fluctuations of the latter contribute significantly to the uncertainty in p, and we may write (compare eq 2.77):

$$\sigma_p = \frac{\exp\left[\frac{1}{2}(\mu_p d_p + \rho_N \mu_f d_i)\right]}{\mu_f d_i \sqrt{I_0 \tau}} \tag{5.12}$$

The standard deviation of p depends on the density; for a given set of values of the other parameters, it is seen that minimum and maximum σ_p occurs for ρ = 0 and ρ = 1, respectively. Thus the worst case standard deviation, with respect to the ρ dependence, is given by

$$\left(\sigma_p\right)_{\max} = \frac{\exp\left[\frac{1}{2}(\mu_p d_p + \mu_f d_i)\right]}{\mu_f d_i \sqrt{I_0 \tau}} \tag{5.13}$$

corresponding to a pipe filled with the heaviest fluid component. Note that the ratio between the maximum and minimum σ_p is given by

$$\frac{\left(\sigma_p\right)_{\max}}{\left(\sigma_p\right)_{\min}} = \exp\left(\tfrac{1}{2}\mu_f d_i\right) \tag{5.14}$$

which may be appreciable; for example, the ratio is equal to $\sqrt{2}$ for $\mu_f d_i = \ln(2)$.

We will use eq 5.13 as the basis for selection of the optimal isotope, i.e. the one that minimizes the statistical fluctuation uncertainty in the measured raysums. Because of the large number of parameters in this equation, it is necessary to introduce some simplifications:

First, we note that the normal pipe material used is steel, so μ_p equals μ_{Fe}; furthermore, the heaviest (most dense) fluid component encountered is water, i.e. $\mu_f = \mu_{Water}$. We will assume the use of these media in all subsequent calculations.

Next, we assume that the pipewall thickness is proportional to the inner diameter of the pipe:

$$d_p(0) = kd_i(0) \Leftrightarrow D - d = kd \Leftrightarrow D = d(1+k) \tag{5.15}$$

A typical value for the proportionality constant k could be $^1/_6$, we shall use $^1/_4$ as well, to show the effect of varying (relative) pipewall thickness. Eq 5.15 applies directly to a centerline ray (r = 0), but for other rays we define a modified proportionality constant between d_p and d_i:

$$d_p(r) = k'd_i(r) \Rightarrow k' = \sqrt{\frac{d^2(1+k)^2 - 4r^2}{d^2 - 4r^2}} - 1 \tag{5.16}$$

which reduces to k for r = 0. Using this, we rewrite eq 5.13 as follows:

$$\left(\sigma_p(r)\right)_{\max} = \frac{\exp\left[\frac{1}{2}d_i(r)\left(k'(r)\mu_p + \mu_f\right)\right]}{\mu_f d_i(r)\sqrt{I_0\tau}} \tag{5.17}$$

For a given pair of attenuation coefficients (i.e. for a given photon energy), we find the value of $d_i(r)$ for which the error is at minimum by first differentiating eq 5.17

$$\frac{\partial}{\partial d_i(r)}\left(\sigma_p\right)_{\max} = \left(\frac{1}{2}\left(k'(r)\mu_p + \mu_f\right) - \frac{1}{d_i(r)}\right)\left(\sigma_p\right)_{\max} \tag{5.18}$$

and then solving the equation:

$$\frac{\partial}{\partial d_i(r)}\left(\sigma_p\right)_{\max} = 0 \Leftrightarrow \left(d_i(r)\right)_{opt} = \frac{2}{k'(r)\mu_p + \mu_f} \tag{5.19}$$

This yields the optimal d_i for some value of r, but since we are really interested in the corresponding value of the inner pipe diameter, we combine eq 5.15 with the expressions for $d_i(r)$ and $k'(r)$ to find d, i.e. we must solve:

$$\sqrt{d^2 - 4r^2} = \frac{2}{\mu_p\left(\sqrt{\frac{d^2(1+k)^2 - 4r^2}{d^2 - 4r^2}} - 1\right) + \mu_f} \tag{5.20}$$

To simplify matters a little, we define r_{rel} as the normal distance from the pipe centre to the ray, normalized to the inner pipe radius (i.e. $r_{rel} \in [0,1]$):

$$r_{rel} = \frac{2r}{d} \Leftrightarrow r = \frac{r_{rel}d}{2} \tag{5.21}$$

Substituting this in eq 5.20 and solving for d yields the optimal inner pipe diameter for a given pair of fluid and pipewall attenuation coefficients:

$$d_{opt} = \frac{2}{\mu_p \sqrt{(1+k)^2 - r_{rel}^2} + (\mu_f - \mu_p)\sqrt{1 - r_{rel}^2}} \tag{5.22}$$

The actual minimum value of the worst case error (eq. 5.17) is then equal to:

$$\begin{aligned} \left(\sigma_p(r)\right)_{\max} &= \frac{e}{2\sqrt{I_0 \tau}} \left\{ 1 + \frac{\mu_p}{\mu_f} \left(\sqrt{\frac{(1+k)^2 - r_{rel}^2}{1 - r_{rel}^2}} - 1 \right) \right\} \\ &= \frac{e}{2\sqrt{I_0 \tau}} \left\{ 1 + k'(r_{rel}) \frac{\mu_p}{\mu_f} \right\} \end{aligned} \tag{5.23}$$

From eq 5.17 we see that the error increases towards infinity as r approaches $d/2$, because the $d_i(r)$ term in the denominator approaches zero. This means that measurement of raysums very close to the inner pipewall should be avoided, i.e. rays for which r is close to $d/2$, or r_{rel} is close to unity.

We will now consider the choice of optimal isotope (i.e. photon energy) for a given application, with respect to the statistical fluctuation uncertainty: Since the number of available isotopes are limited by the requirement that they should also have a reasonable long lifetime, it is more convenient to do the selection process in "reverse order", i.e. to select a few isotopes with sufficient lifetime and with different photon energies, and then find the range of pipe dimensions for which each isotope is suitable. For this purpose, we have chosen the isotopes ^{133}Ba, ^{137}Cs and ^{22}Na, whose most important characteristics are shown in Table 5.1 below.

Table 5.1 Some characteristics of the isotopes which have been considered used for raysum measurement: Energy E_γ of the main photon emission, the halflife $t_{1/2}$, and the linear attenuation coefficients for water and steel.

	Isotope		
	^{133}Ba	^{137}Cs	^{22}Na
E_γ [keV]	356	661.6	1275
$t_{1/2}$ [years]	10.8	30.2	2.6
$\mu_f = \mu_{Water}$ [cm^{-1}]	0.11	0.086	0.067
$\mu_p = \mu_{Fe}$ [cm^{-1}]	0.77	0.57	0.42

We start our investigation of the suitability of these isotopes by taking a closer look at the variation of the worst-case error with the normal distance to the ray: To get a feel for this dependence, we plot eq 5.17 as function of the pipe diameter d, and with $r_{rel} = 2r/d$ as a

parameter, for ^{137}Cs and $k = 1/6$. The plot is shown in Figure 5.2; we have used $I_0\tau = 10000$, which have been chosen more for convenience than for any other reason.

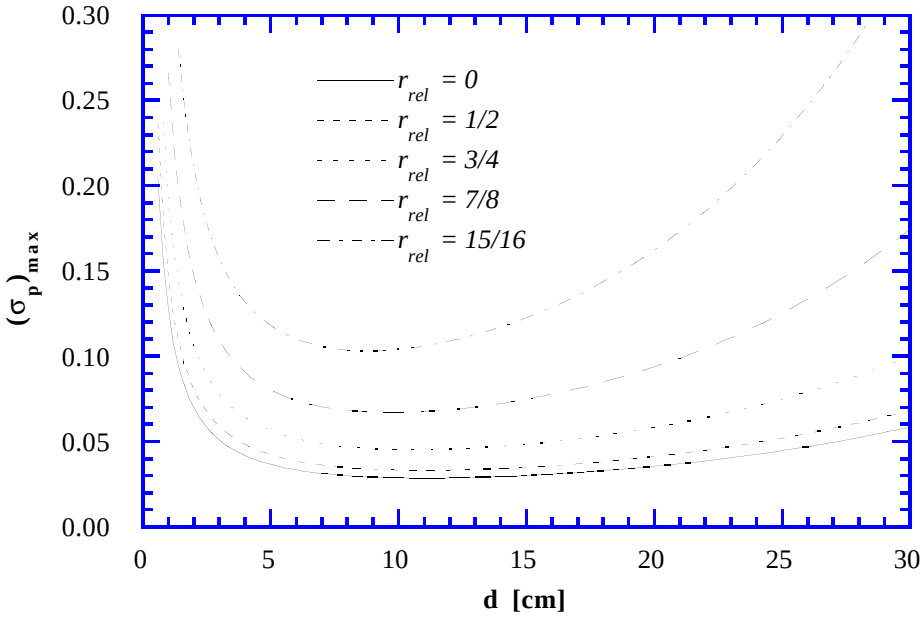

Figure 5.2 Worst-case statistical fluctuation error $(\sigma_p)_{max}$ (eq 5.17) versus pipe diameter d for ^{137}Cs, with $r_{rel} = 2r/d$ as a parameter, and with $I_0\tau = 10000$.

It is seen that the uncertainty increases very sharply as r_{rel} approaches 1, or as r approaches $d/2$. Also, the increase is more marked for higher values of d, since in that case, the relative influence of the $k'(r)\mu_p$ term in eq 5.17 is greater due to the exponential function. The results for other choices of k and the other isotopes are similar, but larger values of μ_p (i.e. lower photon energy) and k cause a more rapid increase of the uncertainty with increasing r_{rel}.

In any event, it seems reasonable to require r_{rel} to be contained within the interval $(0, 3/4)$; this will keep the error variation within a factor 2 compared to the error for a centerline ray (i.e. for $r_{rel} = 0$) for a wide range of d. This corresponds to restricting the value of r to the interval $(0, 3d/8)$; we shall use this assumption for the remainder of this work, and use $r_{rel} = 3/4$ for all uncertainty calculations.

The next point to consider, is how the error-versus-pipe-diameter curves depend on the photon energy used, i.e. the choice of isotope. From equation 5.22 it is seen that the optimum value of the pipe diameter increases with increasing energy, since the attenuation coefficients are decreasing functions of energy in this range. This trend is apparent from Figures 5.3 and 5.4, where the worst case error $(\sigma_p)_{max}$ is plotted against pipe diameter d for the three isotopes of Table 5.1 (for $r_{rel} = 3/4$), and for $k = 1/6$ and $k = 1/4$, respectively.

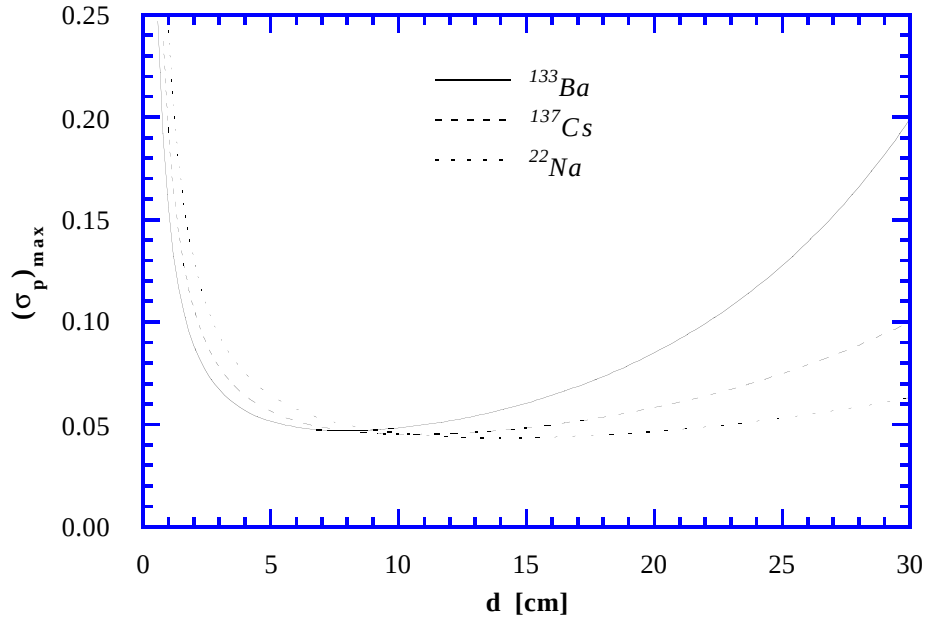

Figure 5.3 Worst-case statistical fluctuation error $(\sigma_p)_{max}$ (eq 5.17) versus inner pipe diameter d, for isotopes ^{133}Ba, ^{137}Cs and ^{22}Na, where $r_{rel} = {}^3/_4$ ($r = {}^{3d}/_8$), $k = {}^1/_6$, and with $I_0\tau = 10000$.

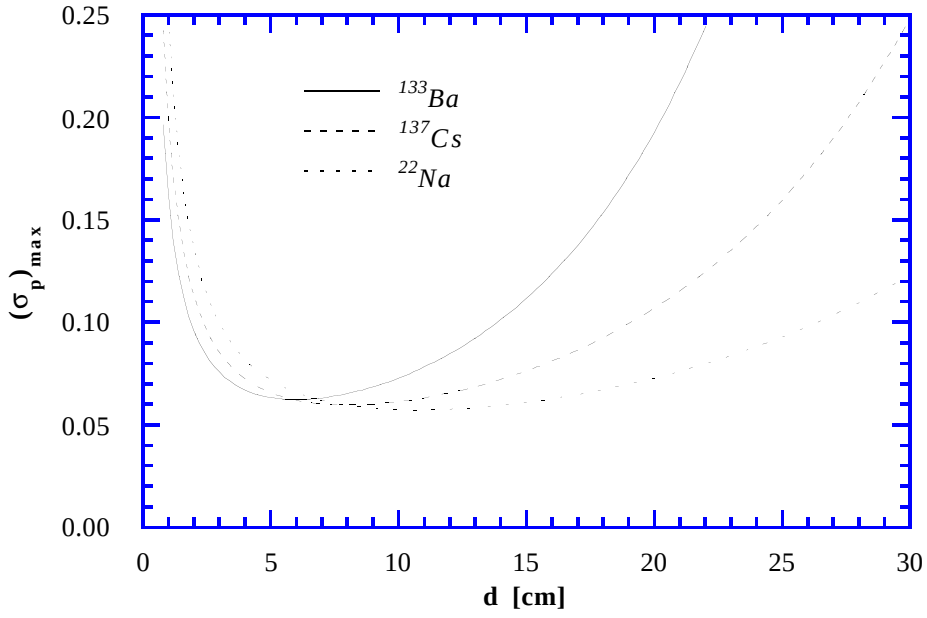

Figure 5.4 Worst-case statistical fluctuation error $(\sigma_p)_{max}$ (eq 5.17) versus inner pipe diameter d, for isotopes ^{133}Ba, ^{137}Cs and ^{22}Na, where $r_{rel} = {}^3/_4$ ($r = {}^{3d}/_8$), $k = {}^1/_4$, and with $I_0\tau = 10000$.

If we consider the expression for the actual value of $(\sigma_p)_{max}$ at the optimum inner pipe diameter, eq 5.23, we see that for a given pair of r_{rel} and k, it is determined by the ratio of the pipewall and fluid attenuation coefficients. From Table 5.1 we see that this ratio gets slightly smaller for higher energy, which means that the value of $(\sigma_p)_{max}$ at d_{opt} will also decrease slightly with increasing energy. This feature is also seen in the plots of Figures 5.3 and 5.4.

Figures 5.3 and 5.4 may give the impression that it is best to use the highest energy isotope available, since the curves for ^{22}Na represent the lowest error levels for both choices of k for all values of d except the smallest pipe diameters. However, we have not taken into account the fact that the detection efficiency ε_p depends on the photon energy in question, and because ε_p enters in the expression for I_0 (eq 5.1), this additional energy dependency also enters in the expressions for the statistical fluctuation uncertainty in p (eqns 5.12, 5.13, 5.17 and 5.23).

Since σ_p is inversely proportional to the square root of the detected intensity I_0, the same dependency applies to σ_p and ε_p, and because the photopeak detection efficiency is a decreasing function of photon energy in this range, the error level will increase with increasing energy. Clearly, high-density, high-Z detectors should be employed, as this maximizes the detection efficiency; from our discussion of detectors in Chapter 2, it is obvious that some kind of scintillation detector should be used, especially when countrate capability is taken into account. We will now give an example of the effect of the energy dependence of $(\sigma_p)_{max}$.:

Using photopeak efficiency values ε_p for a standard 3" × 3" (height × diameter) NaI scintillation detector, we have plotted $(\sigma_p)_{max}$ times $\varepsilon_p^{-1/2}$ in Figure 5.5, with the same parameters as in Figure 5.3 (i.e. $k = {}^1/_6$), except that we have used $I_0\tau/\varepsilon_p = 10000$ to facilitate the comparison; this corresponds to keeping the number of photons impinging on the detector front face constant for the different energies (isotopes).

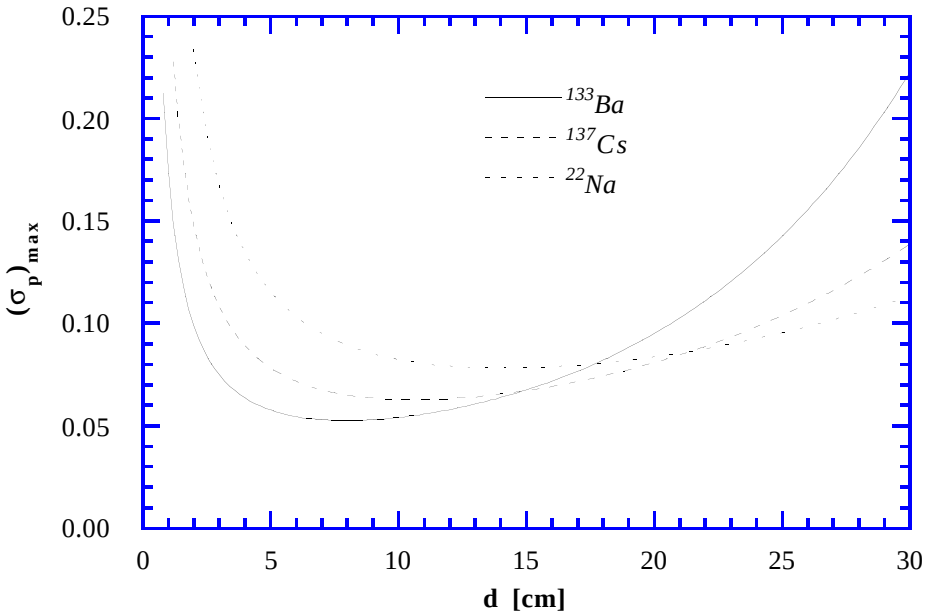

Figure 5.5 Worst-case statistical fluctuation error $(\sigma_p)_{max}$ (eq 5.17) versus inner pipe diameter d, for isotopes ^{133}Ba, ^{137}Cs and ^{22}Na, where $r_{rel} = {}^3/_4$ ($r = {}^{3d}/_8$), $k = {}^1/_6$, but with the effect of the detection efficiency included: Values from Figure 5.3 are multiplied with $\varepsilon_p^{-1/2}$ (see eq 5.1); furthermore, we have used $I_0\tau/\varepsilon_p = 10000$.

The photofraction and total detection efficiency (interaction ratio) for this detector type have been calculated by Rogers [24] for a variety of energies and source geometries; we have determined the values for the desired photon energies by interpolation, and then calculated the photopeak efficiency as the product of the photofraction and the interaction ratio: The ε_p values used for preparing Figure 5.5 are 0.80 for E_γ = 356 keV, 0.52 for E_γ = 661.6 keV and 0.31 for E_γ = 1275 keV.

It is seen that the inclusion of the detection efficiency alters the picture considerably; apart from the striking change in the relative performance of the three isotopes, we note an increase in the overall error level compared to Figure 5.3, which represented the case of a detection efficiency equal to one. This demonstrates the importance of maximizing the detection efficiency; there is certainly potential for improvement of the statistical fluctuation uncertainty, especially for higher pipe dimensions.

In addition to being a function of energy, the photopeak detection efficiency also depends strongly on the shape and size of the detector, and also on the source geometry; i.e. if the incident radiation is a narrow beam, a broad parallel beam, or if the detector is illuminated by an isotropic source at a certain distance. Since the detector dimensions and the source-detector distance depends on the reconstruction grid resolution n, the number of sources (views) m_s and also the pipe diameter, it is clear that photopeak efficiencies need to be calculated for each case in order to determine the level of statistical fluctuation uncertainty for a given system geometry. We will return to these topics in a later section.

5.2.2. Detector countrate

While the level of statistical fluctuation uncertainty is clearly the most important parameter to consider when selecting the isotope for a given system, it is a fact that most types of detectors exhibit countrate capability limitations; because of this, we will take a brief look at what maximum detector countrates to expect when measuring raysums.

Obviously, the maximum countrate occurs when the pipe is empty; furthermore, since the pathlength in the pipewall, $d_i(r)$, is at minimum for the centerline ray, the maximum countrate I_{max} will occur for r = 0 (see eq 5.4, eq 5.10 and eq 5.15):

$$I_{\max} = I_0 \exp(-kd\mu_p) \tag{5.24}$$

Equation 5.17 relates the detected intensity without absorber, I_0, to the worst case statistical fluctuation uncertainty $(\sigma_p)_{max}$; by specifying the maximum acceptable statistical uncertainty σ_p in the normalized raysum measurement, we may find the required I_0 for a given set of μ_p, μ_f, k and r:

$$I_0 = \frac{\exp\left(d_i(r)\left[k'(r)\mu_p + \mu_f\right]\right)}{\tau\left(\mu_f d_i(r)\right)^2\left((\sigma_p)_{\max}\right)^2} \tag{5.25}$$

Combining eqns. 5.24 and 5.25 yields the following expression for the maximum countrate:

$$I_{\max} = \frac{\exp\left(d_i(r)\left[k'(r)\mu_p + \mu_f\right] - kd\mu_p\right)}{\tau\left(\mu_f d_i(r)\right)^2\left((\sigma_p)_{\max}\right)^2} \tag{5.26}$$

In the previous section, we considered the relative levels of uncertainty for our selected trio of isotopes, for the case of $r_{rel} = 3/4$ and $k = 1/6$: To study the relative countrate levels for these isotopes, we have plotted eq 5.26 against pipe diameter d in Figure 5.6, for the same choice of values of r_{rel} and k, and with the product $\tau(\sigma_p)^2$ equal to one.

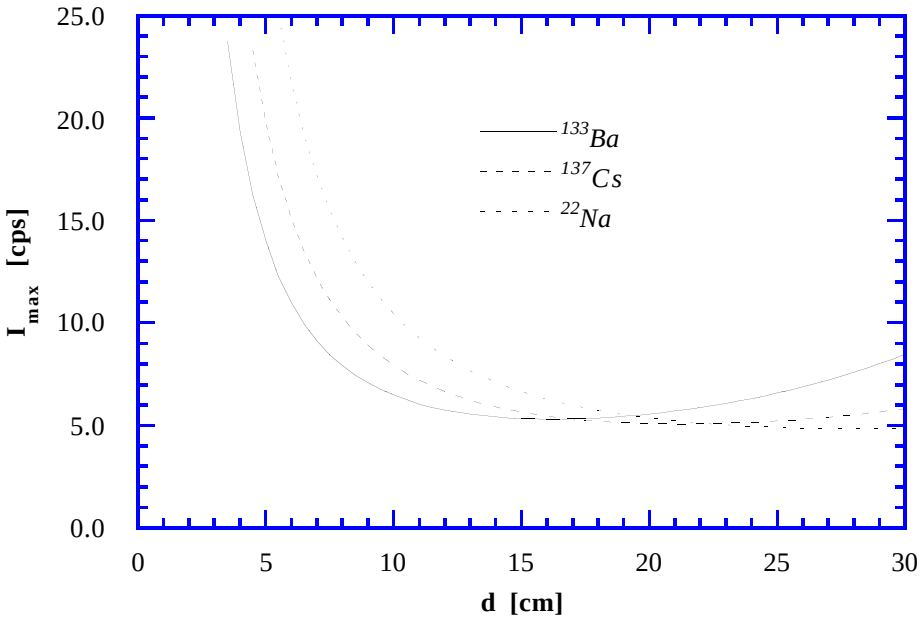

Figure 5.6 Maximum *photopeak* detector countrate I_{max} for the isotopes ^{133}Ba, ^{137}Cs and ^{22}Na, for the case of $r_{rel} = 3/4$, $k = 1/6$, and with the product $\tau(\sigma_p)^2$ equal to one.

It is seen that the countrate curves exhibit a pipe diameter dependence similar to that of the uncertainty curves: For low values of d, the beam attenuation is small, and a high countrate is needed to keep the uncertainty at the required level, since the detected intensities for a full and an empty pipe are very close; for large pipe diameters, only a small fraction of the photons are transmitted, which again cause a high I_{max} requirement for a given level of uncertainty. This also explains the differences between the three isotopes; low photon energy means stronger attenuation, so ^{133}Ba is the better choice for small d, while higher energy means less attenuation, hence ^{22}Na is best for larger pipe diameters.

Note that I_{max} represents the rate of "useful" photons, i.e. those resulting in full energy peak counts in the detector. However, the total number of interacting photons includes events not

contributing to the full energy peak as well, that is, Compton, fluorescence or annihilation radiation photon escape events. Therefore, the *total* countrate is found by dividing I_{max} by the photofraction ε_0, in order to account for all types of interactions.

As we mentioned in the previous section, Rogers [24] has calculated the photofractions for a 3" × 3" NaI detector at several photon energies (for the case of broad parallel beam); interpolation provides the following values for the energies we consider: The photofraction ε_0 equals 0.82 at 356 keV, 0.59 at 661.6 keV and 0.41 at 356 keV. In Figure 5.7, we have plotted the total countrate I_{max}/ε_0 against pipe diameter d; the values of the other parameters are the same as for the photopeak countrate plot in Figure 5.6.

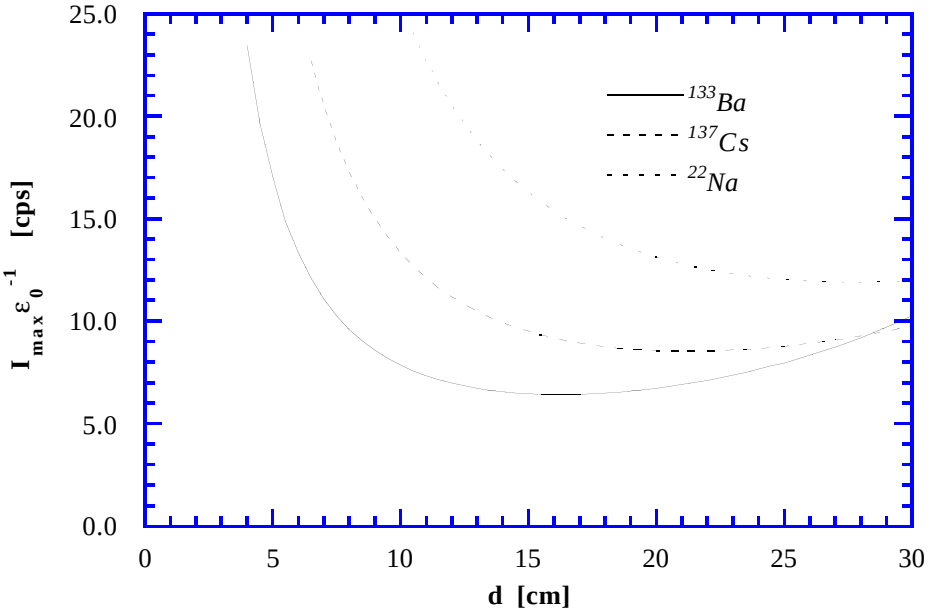

Figure 5.7 Maximum *total* detector countrate I_{max}/ε_0 for the isotopes ^{133}Ba, ^{137}Cs and ^{22}Na, for the case of r_{rel} = 3/4, k = 1/6, and with the product $\tau(\sigma_p)^2$ equal to one. The photofraction values used are for a 3″ × 3″ NaI detector, see text.

It is seen from Figure 5.7 that the countrate increase with decreasing photofraction is quite dramatic, so it is clearly desirable to maximize the photofraction. This is accomplished by maximizing the photopeak efficiency; the interaction ratio is normally not much less than unity for the detector thicknesses used.

It should be remembered that the total countrate referred to above, represents the response to directly transmitted source photons only, while in practice, the detector will also register a certain amount of externally scattered radiation; however, this contribution is difficult to estimate without a photon transport model for the entire imaging system.

Finally, we note that in order to obtain an accurate estimate of the total countrate for a given system geometry, it is again necessary to calculate photopeak and total detection efficiencies for the detectors in question.

5.2.3. Other sources of raysum measurement inaccuracy

In the above discussion we have assumed that the photon beam is infinitesimally narrow and monochromatic. However, in practice the beams will have finite width, and there will be scattered radiation present: From the discussion in Chapter 2, we know that these effects may introduce errors in the measurement of linear attenuation coefficients; hence, there will also be problems when measuring raysums. We will now take a closer look at these effects.

Finite beam width effects

In Section 2.6.2, we mentioned that nonuniform linear coefficient distribution across the beam at a given depth within the absorber volume may cause an error when measuring the average linear attenuation coefficient, since the attenuation formula is strictly not valid under non-narrow-beam conditions.

Obviously, the same applies to the raysum measurement technique considered in this chapter, and since nonuniform beam density distribution is almost the rule rather than the exception for two-phase flow, it is necessary to study the possible error introduced through the finite beam width effect.

We note in particular that since finite beam width raysum measurement errors are inherently regime dependent, it is important to have knowledge of their influence, since they cannot be eliminated directly by calibration measurements.

For the sake of simplicity, we shall assume that the raysum measurement volume has the shape of a rectangular parallelepiped, of height d and width w, see Figure 5.8; furthermore, it is assumed that any density distribution nonuniformity across the beam, occurs in the x direction only. The incident beam is assumed to be broad and parallel, having intensity I_0, while I denotes the transmitted intensity; also, we will ignore the pipewall attenuation, so $I_E = I_0$ and $I_F = I_0\exp(-\mu_f d)$. Next, we will assume that no attenuation occurs in the gas phase, while the attenuation coefficient of the fluid is denoted by μ_f. Finally, we use $\overline{\rho_N}$ to denote the average normalized density within the measurement volume.

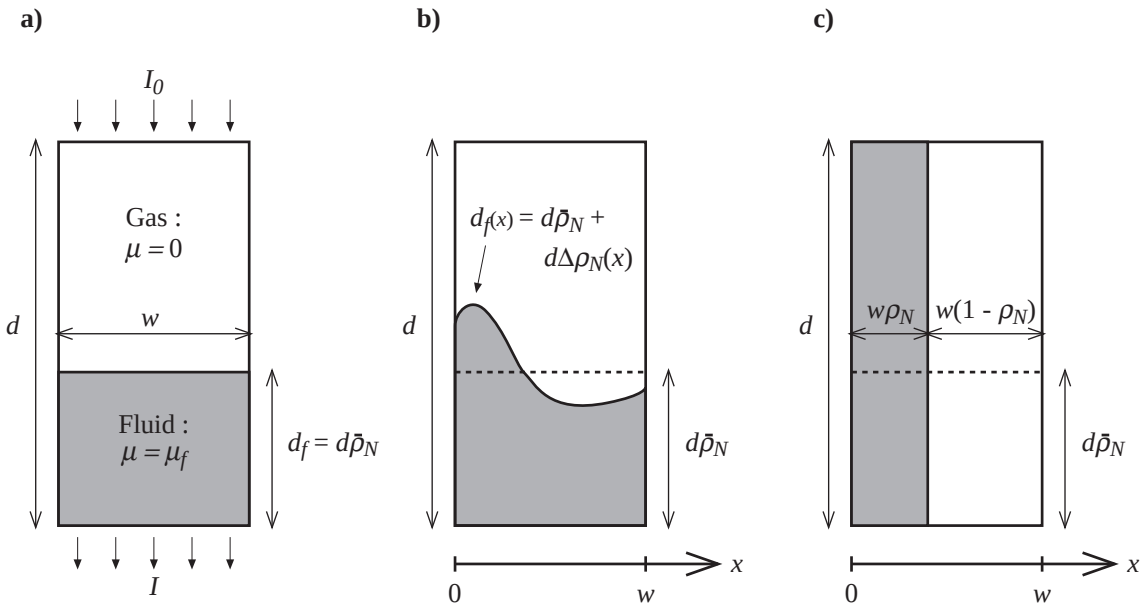

Figure 5.8 Geometries for discussion of the finite beam width effect, for gas-fluid density distribution and a broad parallel beam: a) represents the case with no error, b) represents a general case of nonuniform density across beam, and c) represents a worst case situation for finite beam width error. See text for further explanation.

Since the incident photon beam is parallel, the general expression for the transmitted intensity I is as follows:

$$I = I_0 \left\{ \frac{1}{w} \int_0^w \exp\left(-\mu_f d_f(x)\right) dx \right\} \tag{5.27}$$

where d_f is the effective pathlength in the fluid phase. For the case shown in Figure 5.8a, i.e. when there is an uniform distribution of the normalized density across the beam, the transmitted intensity is given by:

$$I = I_0 \left\{ \frac{1}{w} \int_0^w \exp\left(-\mu_f \bar{\rho}_N d\right) dx \right\} = I_0 \exp\left(-\mu_f \bar{\rho}_N d\right) \tag{5.28}$$

Noticing the similarity of eq 5.28 to 5.10, it is no surprise that the insertion of the above expressions for I_E, I_F and I in the expression for the measured (narrow-beam) normalized raysum p, eq 5.11, gives the following result:

$$p = \frac{\ln\left(I_E / I\right)}{\ln\left(I_E / I_F\right)} = \bar{\rho}_N \tag{5.29}$$

We see that when the density is uniform across the beam, eq 5.11 produces the correct result even for broad parallel beam conditions.

We now turn our attention to the case depicted in Figure 5.8b, where the average normalized density $\overline{\rho}_N$ is equal to that of Figure 5.8a, but in which there is a nonuniformity across the beam, expressed by the function $\Delta\rho_N(x)$; this represents the variation of the normalized density around its average value ρ_N, and we have:

$$\int_0^w \Delta\rho_N(x)dx = 0 \tag{5.30}$$

Using eq 5.27, we find the following expression for the transmitted intensity

$$I = I_0\left\{\frac{1}{w}\int_0^w \exp\left(-\mu_f d_f\left[\overline{\rho}_N + \Delta\rho_N(x)\right]\right)dx\right\}$$

$$\Updownarrow$$

$$I = I_0 \exp\left(-\mu_f d\overline{\rho}_N\right)\left\{\frac{1}{w}\int_0^w \exp\left(-\mu_f d\Delta\rho_N(x)\right)dx\right\} \tag{5.31}$$

Comparing this with eq 5.28, we see that the first part is equal to the expression for the transmitted intensity in the uniform case (Figure 5.8a), while the integral term is a "modifying" factor accounting for the density nonuniformity.

If $\Delta\rho_N$ is identically zero for all x, the modifying factor is equal to one, as one would expect; however, if there is a nonuniformity, the factor will be larger than unity, i.e. a higher intensity is transmitted. The reason for this is that any *positive* variation $\Delta\rho_N$ of the density, with respect to the average $\overline{\rho}_N$, is accompanied by a similar *negative* variation, see eq 5.30. A positive $\Delta\rho_N$ means a negative argument for the exponential function, i.e. the contribution to the modifying factor integral is less than one; similarly, a negative $\Delta\rho_N$ gives a contribution greater than one to the integral. Now, since $|e^C - 1| > |1 - e^{-C}|$ for positive C, we see that the total contribution of terms > 1 is greater than the sum of contributions of terms < 1, so the value of the modifying factor will be greater than one.

The fact that a nonuniform density distribution across the beam implies an increase in the transmitted intensity compared to the uniform case (which should also be evident from a consideration of the physics involved), means that when there is a density nonuniformity, the statistical raysum uncertainty σ_p is less than the uncertainty for the uniform case.

By combining eq 5.31 and 5.11, we get the following expression for the measured normalized raysum p:

$$p = \overline{\rho}_N - \left(\frac{1}{\mu_f d}\right)\ln\left\{\frac{1}{w}\int_0^w \exp\left(-\mu_f d\Delta\rho_N(x)\right)dx\right\} \tag{5.32}$$

In our discussion of eq 5.31, it was established that the modifying factor is > 1, so its natural logarithm is > 0, and the raysum error is seen to be negative in all cases, which is as expected, since a density nonuniformity causes the transmitted intensity to be higher than in the uniform case, for which the raysum formula eq 5.11 was derived.

From the above discussion, it follows that the maximum change in the transmitted intensity, and hence the maximum raysum error, occurs for the case of maximum variation of the nonuniformity function $\Delta\rho_N(x)$. This corresponds to an abrupt change in the normalized density as shown in Figure 5.8c; the average density $\overline{\rho}_N$ is the same as for the two previous cases, and the nonuniformity function is defined by:

$$\Delta\rho_N(x) = \begin{cases} 1-\overline{\rho}_N & , \quad 0 \le x \le w\overline{\rho}_N \\ \overline{\rho}_N & , \quad w\overline{\rho}_N < x \le w \end{cases} \tag{5.33}$$

The transmitted intensity is then given by (see eq 5.31):

$$I = I_0 \exp\left(-\mu_f d\overline{\rho}_N\right)\left\{\exp\left(\mu_f d\overline{\rho}_N\right)\left[\overline{\rho}_N\left(\exp(-\mu_f d)-1\right)+1\right]\right\}$$

$$\Updownarrow$$

$$I = I_0\left[\overline{\rho}_N\left(\exp(-\mu_f d)-1\right)+1\right] \tag{5.34}$$

which may easily be found directly from Figure 5.8c; also, the expression agrees with Hellesø's result for the same case [7, p. 25]. If we consider the raysum p, we find that it is given by:

$$p = \overline{\rho}_N + \Delta p \tag{5.35}$$

where Δp is the (worst case) finite beam width raysum error:

$$p = -\frac{\ln\left\{\exp\left(\mu_f d\overline{\rho}_N\right)\left[\overline{\rho}_N\left(\exp(-\mu_f d)-1\right)+1\right]\right\}}{\mu_f d}$$

$$\Updownarrow$$

$$\Delta p = -\frac{\ln\left\{\overline{\rho}_N\left(\exp(-\mu_f d)-1\right)+1\right\}}{\mu_f d} - \overline{\rho}_N \tag{5.36}$$

and the raysum p is simply:

$$p = -\frac{\ln\left\{\overline{\rho}_N\left(\exp(-\mu_f d)-1\right)+1\right\}}{\mu_f d} \tag{5.37}$$

Note that while the worst case raysum error depends on the thickness of the measurement volume, the attenuation coefficient of the fluid, and the average normalized density, it is independent of the beam width *w*.

A look at eq 5.35 reveals that the raysum error is zero for $\bar{\rho}_N = 0$ and $\bar{\rho}_N = 1$, to study the behaviour of the error for intermediate density values, we plot the Δp expression (eq 5.35) against $\bar{\rho}_N$ in Figure 5.9, for the case of $d = 10$. By using μ_f values corresponding to our usual trio of isotopes ^{133}Ba, ^{137}Cs and ^{22}Na, see Table 5.1, the energy dependence of the error is also demonstrated.

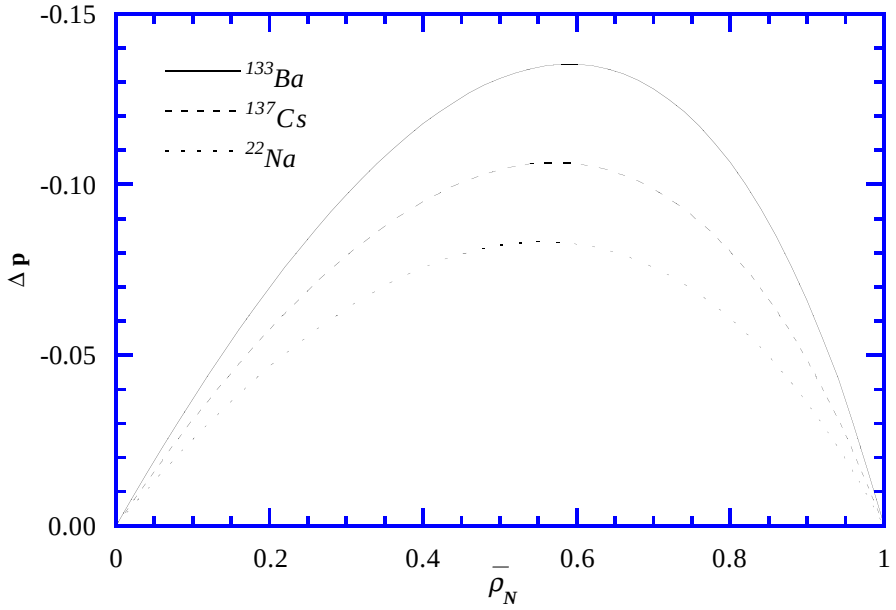

Figure 5.9 Finite beam with raysum error Δp versus average beam density $\bar{\rho}_N$, for the isotopes ^{133}Ba, ^{137}Cs and ^{22}Na, and with $d = 10$ cm.

We see that the raysum error may be considerable, for ^{133}Ba the maximum error is nearly 15% of full scale, while the error is smaller for the higher energies, which have smaller attenuation coefficients, see Table 5.1 and eq 5.36. Differentiating the absolute value of eq 5.36 with respect to $\bar{\rho}_N$, we get

$$\frac{\partial|\Delta p|}{\partial\bar{\rho}_N} = 1 + \frac{\exp(-\mu_f d) - 1}{\mu_f d\bar{\rho}_N\left(\exp(-\mu_f d) - 1\right) + 1} \tag{5.38}$$

i.e. the absolute raysum error is at maximum when

$$\frac{\partial|\Delta p|}{\partial\bar{\rho}_N} = 0 \Leftrightarrow \bar{\rho}_N = \frac{\mu_f d - \left(1 - \exp(-\mu_f d)\right)}{\mu_f d\left(1 - \exp(-\mu_f d)\right)} \tag{5.39}$$

so the actual maximum value of $|\Delta p|$ is given by:

$$|\Delta p|_{\max} = \frac{1}{\mu_f d}\left\{\ln\left(\frac{1-\exp(-\mu_f d)}{\mu_f d}\right)+\frac{\mu_f d}{1-\exp(-\mu_f d)}-1\right\} \qquad (5.40)$$

Equation 5.40 is plotted against measurement volume thickness d in Figure 5.10, for the isotopes ^{133}Ba, ^{137}Cs and ^{22}Na.

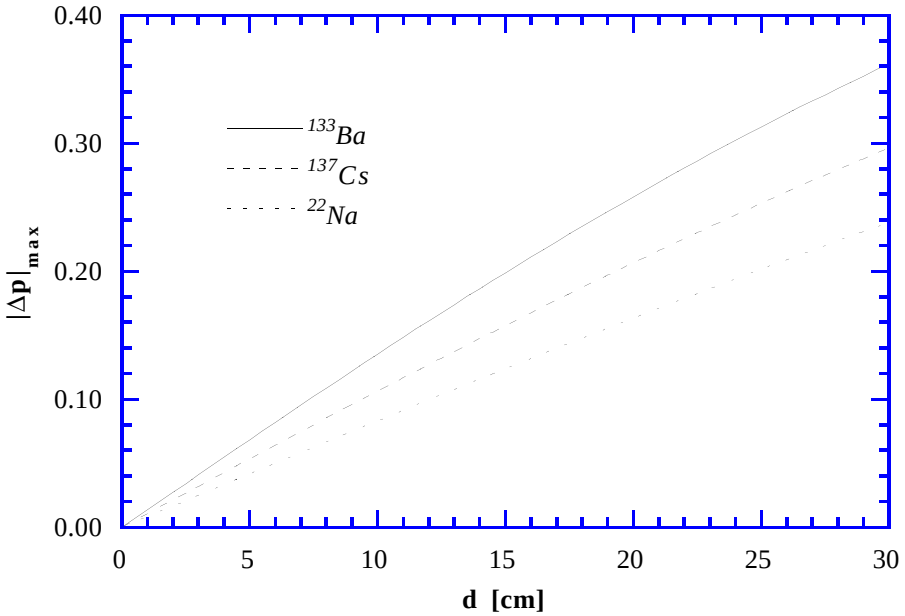

Figure 5.10 Maximum absolute finite beam width raysum error $|\Delta p|$ versus pipe diameter d for the isotopes ^{133}Ba, ^{137}Cs and ^{22}Na (eq 5.40).

We see that the magnitude of the worst case raysum error increases steadily with increasing d and μ_f, which means that the finite beam width error is minimized by using the highest possible photon energy.

The above considerations are based on the assumptions that the measurement volume has a rectangular parallelepiped shape, and that the incident beam is parallel, which corresponds to infinite source-absorber distance. In practice, however, the raysum measurement volume is defined by the intersection of the cylinder shaped pipe interior, and the beam volume, which is pyramid shaped, assuming an isotropic source and a rectangular detector front face. Thus the situation is quite different from the idealized geometry used above.

However, if the source distance is sufficiently large compared to the beam width, and if the (worst case) density nonuniformity function is such that the source is positioned on a straight line along the discontinuity, the parallelepiped geometry is an acceptable approximation to a more realistic case. Thus we may use eq 5.40 as an estimate for the worst case finite beam width error for pipe flow raysum measurement as well.

Since the effective measurement volume thickness decreases for rays not passing through the pipe centre, it is seen that the maximum error occurs for a centerline ray, if possible effects of the pipe curvature are ignored. The latter may influence the finite beam width raysum error when there is a nonuniformity of the density distribution across the beam, but nonuniform pipewall pathlength does not introduce any error as long as the density distribution of the flow medium is uniform across the beam. The pathlength effect is believed to be insignificant for the worst case (discontinuous nonuniformity) conditions, since the pathlength variation is small for reasonable beam widths.

Although the error level predicted by eq 5.40 is quite dramatic, it should be remembered that it represents the truly worst case to be encountered, and it is highly improbable that more than a small fraction of the raysums measured in an imaging system should be affected by finite beam width errors of such severity. Hellesø [7, p. 29] suggests that such errors may be compensated for by reconstructing a preliminary image from the "raw" raysum data, correcting the appropriate raysums for finite beam width error, and using the corrected data for a second - hopefully enhanced - reconstruction.

Since the worst case error is independent of the beam width, the error itself is not reduced by using narrower beams, however, the fraction of affected raysum measurements would be reduced. However, the raysum error itself may be reduced if more than one detector is used for measuring each raysum; i.e. if the detector used is divided into several segments, each measuring a "partial" raysum; the raysum for the entire beam is then taken to be the average of the partial raysums.

Provided that the photopeak efficiency of the detector segments is not seriously lowered compared to an unsegmented detector, it turns out that the statistical uncertainty of this average raysum is similar to the uncertainty for the single detector case, since negative and positive errors of different partial raysums tend to cancel each other out (the total solid angle subtended by the detector at the source is unchanged). Apart from the reduction of the finite beam width raysum error, this arrangement has the added advantage that the countrate capability requirement of the detectors is relaxed.

The effect of the finite beam width raysum error could be investigated by calculating the error for a large number of system geometries and flow regimes, i.e. by a strategy similar to the one used in Chapter 4 for estimating the reconstruction error for flow imaging systems. The 3D calculation of beam width error is complicated by the curvature of the pipe, so a numerical technique must probably be used; in fact, a simple Monte Carlo model, completely ignoring tracking of scattered photons and annihilation quanta, may prove to be the easiest way to solve this problem.

Scattered radiation

Generally, the γ-densitometry technique used for raysum measurement, is based on the assumption that the photon energy is within the range where Compton scattering is the dominating interaction mechanism for the media in question. Obviously, this means that there will be a lot of scattered photons around, and the accuracy of raysum measurements will suffer if too many of these are detected, since the basic attenuation formula is valid for unscattered radiation only. The amount of scattered photons present will generally depend on the flow regime, so the raysum error caused by detection of scattered photons will be regime dependent, and hence, it can not be eliminated by calibration.

In a single energy system, it is possible to use collimators to avoid the detection of most of the Compton quanta generated by scattering of photons originating from the source directly opposite an detector array. However, in a multisource system, there is the possibility of detecting scattered photons whose "parent" photons originate in *other* sources; this should be evident from a glance at Figure 4.2.

Furthermore, it is clear that this problem will get more serious as the number of sources increases, since the general intensity of scattered photons will increase, and the minimum scattering angle required for a photon to hit the "wrong" array will decrease.

If we consider single scattered photons only, and assume that the interaction takes place in the centre of the pipe, the mean deflection angle required to direct the photon into the middle of an array next to the one opposite the source, is simply:

$$\theta = \frac{2\pi}{m_s} \tag{5.41}$$

By using the Compton energy-angle relationship, eq 2.17, we may relate the corresponding relative energy shift to the number of sources used in the system, m_S, and the source energy used, E (see also Figure 2.17):

$$\frac{E'}{E} = \frac{1}{1+\frac{E}{m_0c^2}\left[1-\cos\left(\frac{2\pi}{m_s}\right)\right]} \tag{5.42}$$

This expression is plotted against m_S in Figure 5.11, for the sources ^{133}Ba, ^{137}Cs and ^{22}Na; note that the scattering angle used only represents some sort of average value. It is seen that the energy shift increases with increasing source energy, but decreases as the number of views increase; since the energy shift indicate the detector energy resolution required, we see in that systems using low source energy and many views, detectors of fairly good resolution would be needed.

When fewer views and higher energy isotopes are used, the resolution requirement is more moderate; however, it should be kept in mind that the angular distribution of the Compton scattered photons is more forward peaked for higher source energies, which would influence the intensity of scattered photons.

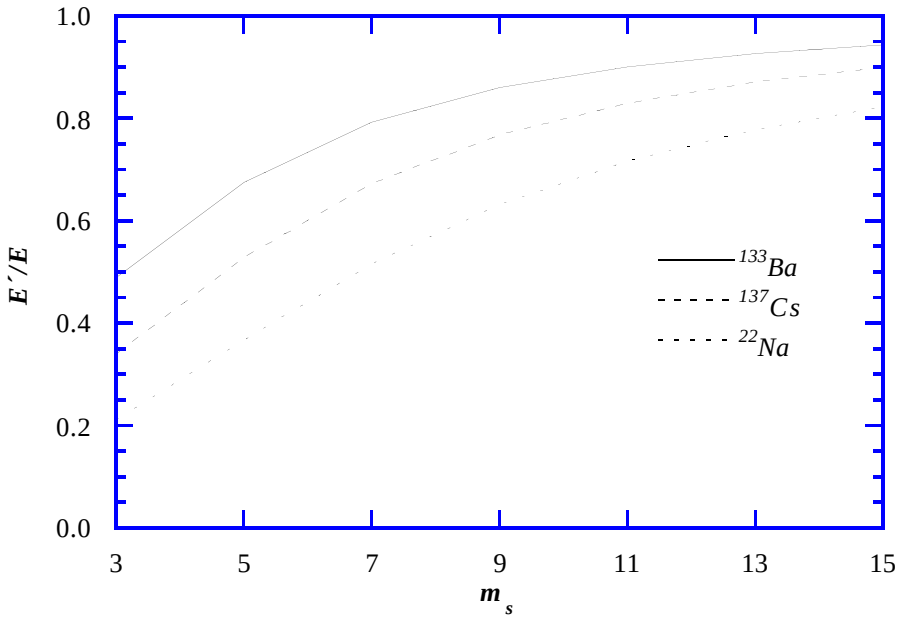

Figure 5.11 Average relative Compton energy shift E'/E versus the number of sources (views) m_S, for the isotopes ^{133}Ba, ^{137}Cs and ^{22}Na.

The considerations on which the plot in Figure 5.11 is based, do not take into account the actual intensity of scattered photons which impinges on the detector; therefore, it is quite possible that it is unnecessary to select a detector whose energy resolution is adequate for rejection of all the scattered radiation. Also, it may be possible to compensate the measured raysums for errors due to scattered radiation, by calculating corrections from a preliminary image reconstructed from raw raysum data. In any event, it is clear that a mathematical model of the photon transport in the imaging system would be required for analyzing the effect of scattered radiation.

5.3. Selection of detector type; detection efficiency calculations

In Section 5.2, we saw that the statistical raysum uncertainty depends on the photopeak detection efficiency, and that the total detector countrate needed for a given level of uncertainty depends on the photofraction of the detector. Since the uncertainty is inversely proportional to the square root of the photopeak efficiency, and the countrate requirement is inversely proportional to the detector photofraction, it is clearly important to select detectors of maximum photopeak efficiency and photofraction, as this will minimize uncertainty and countrate requirement.

In this section, we will first consider the choice of detector type and material; then we proceed to establish how detector size and shape are constrained by the choice of reconstruction gridsize n (i.e. system spatial resolution), number of views (sources) m_s and pipe diameter d. Because the detection efficiency depends on the detector shape and size, it is necessary to compute photopeak efficiencies and photofractions for each set of system parameters, in order to be able to compare uncertainty and countrate levels of different systems; for this purpose, we have developed a Monte Carlo simulation program for calculating detector efficiencies: The underlying model for this simulator is described, along with a discussion of its accuracy, and a comparison with the results of similar systems; finally, we conclude this section by calculating detector photofractions and photopeak efficiencies for a wide range of single energy systems.

5.3.1. Choice of detector material

Due to the requirement of high (photopeak) detection efficiency, it is obvious that a scintillation detector should be used: Even though a Ge(Li) detector offer efficiency comparable to NaI, its use is ruled out due to the requirement of a bulky and complex cooling system. In addition, the countrate capability of a Ge detector is inferior to scintillation detectors, because a large volume semiconductor detector exhibits charge collection times much longer than the decay times of fast scintillators. Other detector types, such as gas filled detectors or room temperature semiconductor devices, do not possess adequate stopping power for the photon energies in question.

When we consider the choice of scintillator material, we find that there is a broad range of types available, a selection of some common scintillators is presented in Table 5.2 below.

Table 5.2 Some characteristics of a selection of scintillation materials. The table is based on similar overview in [25]; the data are from [26], [27] and [28].

Material	Property			
	Density [g/cm^3]	μ_{tot} @ 511keV [cm^{-1}]	Decay constant [ns]	Light output [%]
Organic compound	1.05	0.095	2 - 20	3.0 (NE110)
NaI (Tl)	3.67	0.33	230	11.3
CsI (Tl)	4.51	0.54	1000	11.9
GSO ($Ce:Gd_2SiO_5$)	6.71	0.67	60	3.6
CWO ($CdWO_4$)	7.90	0.86	5000	3.8
BGO ($Bi_4Ge_3O_{12}$)	7.13	0.91	300	2.1

The ultra-fast but low density organic compound, or “plastic”, scintillator is included for comparison only, as its stopping power is inadequate for our purposes. The widely used NaI is seen to be a scintillator of medium detection efficiency, its popularity is mainly due to its excellent energy resolution, which is a consequence of the high light output[1]. Its main drawback is that, unlike the other materials listed, it is extremely hygroscopic, so it must be hermetically enclosed at all times. Nevertheless, NaI is chosen instead of CsI in most cases, even if the latter has similar energy resolution and higher stopping power, because NaI offers the best countrate capability; the scintillation decay constant of CsI is more than four times greater than that of NaI.

The remaining three scintillators, GSO, CWO and BGO are seen to have much lower light output than NaI and CsI, and hence, lower energy resolution; on the other hand, they offer much improved detection efficiency. Further, due to the high atomic number of their constituents, the photofraction will also be higher. GSO is an extremely fast scintillator, but its stopping power does not quite rival that of CWO or BGO. The usefulness of CWO is

[1]The light output, which is the fraction of the absorbed gamma energy that is released as scintillation light energy, is also called scintillation efficiency, conversion efficiency or quantum efficiency. In general, the higher the efficiency, the better is the energy resolution, since this minimizes the relative linewidth contribution from statistical fluctuations in the scintillation process and the readout mechanism; also, the relative linewidth contribution from electronic noise in the readout circuit is minimized.

limited in pulse-mode readout because of the very slow scintillation decay, meaning that its countrate capability is poor compared to other scintillators; however, it may be attractive for use in current-mode readout applications.

This leaves us with BGO, which offers superior detection efficiency compared to other scintillators, while its scintillation decay constant, and hence its countrate capability, is similar to that of NaI. The only drawback of BGO is its relatively low light output, which implies that the energy resolution of this scintillator will be somewhat poorer than e.g. NaI or CsI: With photomultiplier tube readout, a 3" × 3" NaI detector typically has an energy resolution of 7 % or better at 661.6 keV [26]; the resolution of BGO detectors at the same energy have been measured to 12.4% for a 6 × 20 × 30 mm device [27], and to 9.1% for a 10 × 10 × 10 mm detector [29].

Note, however, that the relative energy resolution performance of these scintillators changes in favour of NaI (and CsI) for photodiode readout, since in that case, the linewidth is largely determined by diode and readout circuit electronic noise alone [28][25, pp 73-78], while for PMT readout, the linewidth is determined mainly by quantum fluctuations in the scintillation process and the PMT electron generation and multiplication process [18, pp. 153-154]. Nevertheless, it is felt that BGO is the better choice, because of its great advantage in detection efficiency compared to e.g. NaI.

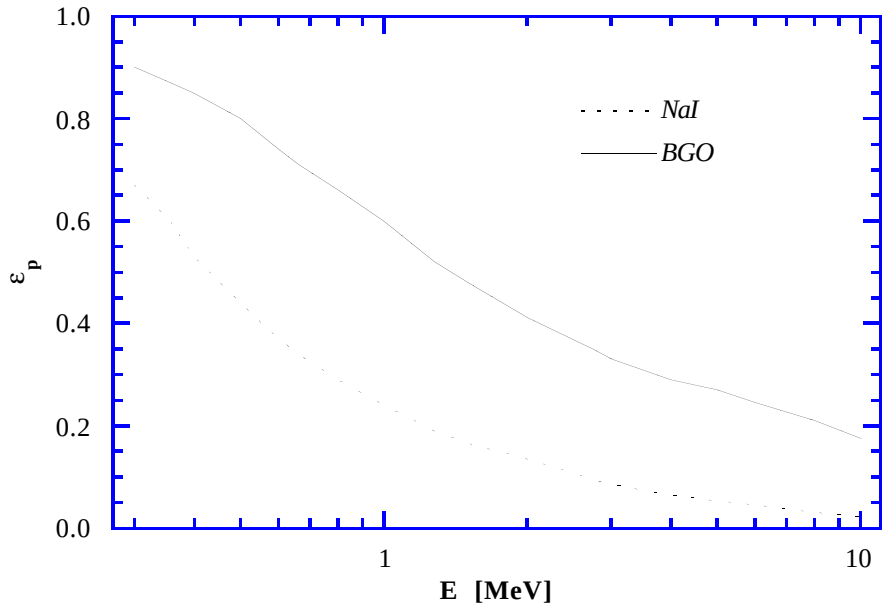

Figure 5.12 Photopeak detection efficiency ε_p (interaction ratio × photofraction) versus photon energy E, for 3" × 3" (height × diameter) NaI and BGO detectors, with an isotropic source at 10 cm distance from the detector front face; efficiency data are from [24].

This is clearly seen from Figure 5.12, where we have plotted the photopeak detection efficiency ε_p versus photon energy E for bare, uncased 3" × 3" NaI and BGO detectors, for

the case of an isotropic source at 10 cm distance from the detector; the efficiencies have been calculated by Rogers [24].

At 1 MeV photon energy, the photopeak efficiency of the BGO detector is 2.4 times that of the NaI detector, which corresponds to a 50% improvement of the statistical fluctuation uncertainty. Noting that we used NaI photopeak efficiency and photofraction values when considering the effect of detection efficiency on raysum uncertainty and countrate requirement in Section 5.2, we realize that the use of BGO instead of NaI would improve these figures significantly.

Note that neither size nor shape of the detectors in the example above is not necessarily realistic; as we shall see shortly, the detectors used in an imaging system will not be cylinder-shaped, and the detector size could be much smaller than 3" × 3". The latter fact is another reason for choosing BGO over scintillators having smaller detection efficiency, because the (photopeak) efficiency advantage is even more pronounced for smaller devices.

5.3.2. Detector shape and size

The typical shape for a scintillation spectroscopy detector is a right cylinder, as shown in Figure 5.13a below. In an imaging system, however, it is important to select a detector shape which offers the best possible utilization of the available space, in order to maximize the detection efficiency. Three factors relate detection efficiency to detector size and shape:

The first is the geometrical aspect; an increase of the detector front face area increases the number of photons impinging on the detector for an isotropic source at a given distance, since the solid angle subtended by the detector at the source is increased.

The second is the detector interaction ratio; at a given photon energy, this is determined by the thickness of the detector, by the ratios of the detector front face width and length to the source-detector distance, and by the shape of the detector.

The third factor is the detector volume, which influence the photopeak detection efficiency through the fact that if Compton scattered photons are absorbed before they escape from the detector, the number of full energy events in the detector spectrum will increase.

If we now consider the specific case of our flow imaging system, in which a number of detectors are placed edge-to-edge in arrays, we see immediately that the detectors should have rectangular shaped front surfaces. The obvious choice of detector shape would then be the rectangular parallelepiped, as shown in Figure 5.13b below.

However, the detector arrays are arc-shaped, and the available space for each detector is determined by the source-detector distance and by an angular interval equal to the ray spacing, see Section 4.2.2; this interval can only be fully utilized if wedge, or even truncated pyramid shaped detectors are used, see Figure 5.13c. The shape of a truncated pyramid detector is seen to be defined by the source-detector distance (the source position defines the top vertex of pyramid), the detector width and length, and the detector thickness.

This has two advantages compared to the parallelepiped detector shape: Firstly, if a truncated pyramid shape is used, the interaction ratio will be almost completely uniform, because the effective detector thickness is then nearly constant, regardless of where a photon impinges on the detector front face; it is seen from Figure 5.13c that no (source) photons can hit the truncated pyramid detector anywhere else than on its front surface. Thus, the edge effects associated with rectangular parallelepiped detectors are avoided. Secondly, the detector volume is increased, which increases the photopeak efficiency.

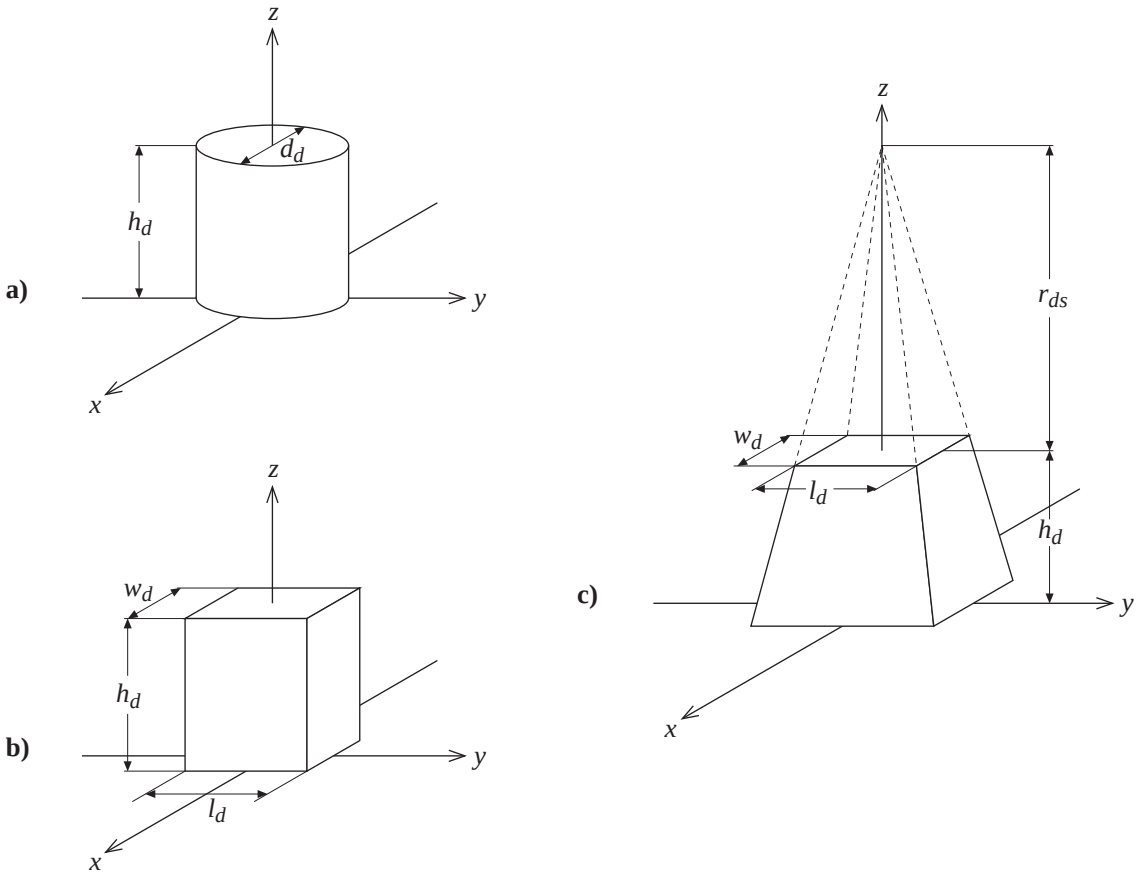

Figure 5.13 Possible detector shapes: a) Right cylinder of diameter d_d and height h_d. b) Rectangular parallelepiped of width w_d, length l_d and height h_d. c) Truncated pyramid, defined by front face width w_d and length l_d, detector height h_d and source-detector distance r_{ds}; the top vertex of the pyramid is defined by the source position.

For these reasons, we conclude that the truncated pyramid shape detector is the ideal choice for use in an imaging system; note, however, that for systems where the ray angular interval is small, the truncated pyramid shape will not be very different from a rectangular parallelepiped. We now proceed to consider the detector dimensions actually encountered in a single energy imaging system.

As we have mentioned already, the maximum permissible front face detector width is determined by the angular interval available for each detector, and the source-detector distance. The available interval is equal to the ray spacing if the detectors are stacked edge-to edge; for the single energy Systems 1 and 4 defined in Chapter 4, i.e. for $m_S = 2n + 1$. The angular ray spacing is then defined by eq 4.23, from which we find the detector angular interval $\Delta\alpha_d$:

$$\Delta\alpha_d = \frac{\pi}{2q}\ , \qquad q \le \frac{n\pi r_s}{d} < q+1 \tag{5.43}$$

Equation 4.6 defines the minimum r_S possible, which is given by:

$$\frac{r_s}{d} = \frac{r_s}{2r_0} = \frac{1}{2\sin(\frac{\pi}{2m_s})} \tag{5.44}$$

Combining this with eq 5.43, we get the following expression for the ray spacing:

$$\Delta\alpha_d = \frac{\pi}{2q}\ , \qquad q \le \frac{n\pi}{2\sin(\frac{\pi}{2m_s})} < q+1 \tag{5.45}$$

To simplify matters a little, we shall use the expression

$$\Delta\alpha_d \approx \frac{\pi}{2nm_s} \tag{5.46}$$

which turns out to produce identical values to eq 5.45 for the detector spacing for all n and m_S except for high n and $m_S \le 5$, in which case 5.46 is still a good approximation.

If we then consider the detector front face width w_d, we find that

$$w_d = 2r_{ds}\tan\left(\frac{\Delta\alpha_d}{2}\right) \tag{5.47}$$

where the detector angular interval $\Delta\alpha_d$ is defined by eq 5.46; using the minimum source-detector distance r_{ds} defined by eq 4.7 (i.e. $r_s = r_d = r_{min}$), we find that w_d is given by:

$$w_d = \frac{4r_0\tan(\frac{\pi}{4nm_s})}{\tan(\frac{\pi}{2m_s})} = \frac{2d\tan(\frac{\pi}{4nm_s})}{\tan(\frac{\pi}{2m_s})} \tag{5.48}$$

Since $n \ge 2$ and $m_S \ge 3$, we may use the following approximation:

$$w_d \approx \frac{4r_0(\frac{\pi}{4nm_s})}{(\frac{\pi}{2m_s})} = \frac{2r_0}{n} = \frac{d}{n} \tag{5.49}$$

which is a little larger than the true w_d, eq 5.49 is accurate to within 10% for m_s = 3 and within 4% for m_s = 5; the error is negligible for higher numbers of views.

At this point, we should mention that by using the *minimum* source-detector distance (eq 4.7) when calculating the detector width, we have ignored the extra space required for placing collimators in front the detectors, although we have tacitly assumed that (multileave) collimators must be used in order to avoid the detection of Compton scattered photons.

However, since detector width is defined by angular interval, and the length is taken to be proportional to the width, the solid angle is independent of r_{ds}; also, we shall see that photopeak efficiency does not vary too rapidly with increasing r_{ds}. Further, if multileave collimators are used, the effective front face area of the detector is reduced, counteracting the increase in photopeak efficiency due to the necessary increase in r_{ds}. For this reason, we have chosen to ignore the use of collimators.

The front face area of the detector also depends on the length l_d, which is normally chosen to be twice the width w_d . Increasing the detector length increases the solid angle subtended at the source by the detector, and hence, the statistical fluctuation uncertainty is lowered, since a higher photon intensity is registered for a given source strength. On the other hand, the detector length should not be very much longer than the width, as this increases the nonuniformity of the beam profile; also, using a detector length several times greater than the width requires a scintillation light readout device of rather awkward shape. The above choice thus represents a reasonable compromise between conflicting requirements.

When we consider the detector height (or thickness), we recall that for a narrow beam (or broad parallel beam) normally incident on a detector of thickness h_d, the interaction ratio (or total detection efficiency) is given by

$$\varepsilon_{tot} = 1 - \exp\left(-\mu_{tot}(E_\gamma)h_d\right) \tag{5.50}$$

which means that for a given h_d, the interaction ratio will decrease with increasing energy in the range we are considering. This will in turn influence the photopeak efficiency, which is our main concern, so to compensate for this effect in our comparison of the suitability of the isotopes in question, we will chose the detector thickness h_d for each energy in such a way that the interaction ratios are the same. For BGO, the thickness required for a 95% interaction ratio is 2.0 cm for ^{133}Ba, 4.5 cm for ^{137}Cs and 7.5 cm for ^{22}Na.

Note that for isotropic sources and truncated pyramid shaped detectors, the interaction ratio will be slightly larger than the value predicted by eq 5.50, since the effective detector thickness increases as the point of photon entry moves towards the edges of the detector front face. This effect is most pronounced when the ratios of w_d and l_d to r_{ds} is at maximum, i.e. along a side edge (corner) of the pyramid; however, for the source-detector distances, detector widths and the 95% interaction ratio encountered here, the increase in interaction ratio is well below 1% in all cases. We may therefore use eq 5.50 for the calculation of interaction ratios, but note that the relative increase would be more pronounced for lower interaction ratios.

Finally, we will consider the slope of the pyramid side faces: As we mentioned above, the detector shape is defined as a truncated pyramid of height h_d, whose top width and length are w_d and l_d, respectively, and the slope of its side faces is such that the vertex of the true pyramid is at a distance r_{ds} from the front face, i.e. the total height of the pyramid is equal to $h_d + r_{ds}$, see Figure 5.13c. Thus the width w_{db} and length l_{db} of the pyramid base surface are given by:

$$w_{db} = w_d\left(1+\frac{h_d}{r_{ds}}\right) \quad ; \quad l_{db} = l_d\left(1+\frac{h_d}{r_{ds}}\right) \tag{5.51}$$

Since z denotes the position along the direction perpendicular to the detector base plane (i.e. towards the source position, or vertex of the pyramid), the detector width (x-direction) and length (y-direction) at a given value of z is given by

$$w_d(z) = w_d\left(1+\frac{h_d - z}{r_{ds}}\right) \quad ; \quad l_d(z) = l_d\left(1+\frac{h_d - z}{r_{ds}}\right) \tag{5.52}$$

for $0 \le z \le h_d$.

5.3.3. DSIM: Monte Carlo detection efficiency calculator

DSIM is a Monte Carlo program which calculates photopeak and total detection efficiencies (and hence, photofractions) for bare, uncased BGO and NaI detectors for photon energies in the range 0 to 10 MeV; the actual accuracy varies within this interval and will be discussed later. The detector may be of right cylinder shape, rectangular parallelepiped shape or truncated pyramid shape, see Figure 5.13; possible source geometries are narrow beam, broad parallel beam and isotropic source at specified distance for cylinder and parallelepiped detectors, and isotropic source only for the truncated pyramid detector.

In all cases, the photons are assumed to be incident on the front face of the detector, i.e. on the surface defined by the plane $z = h_d$; narrow beams hit the detector along the z-axis in the negative direction, the photons of broad parallel beams travel in the same direction, but are equidistributed all over the detector front surface. The isotropic source geometry, however, imply that photons hit the front surface with slightly different directions, and the distribution of source photons is not uniform over the detector front surface; more on this below.

DSIM physics

We will now describe the physical model on which DSIM is based: First of all, it should be noted that charged particle transport is ignored completely, in order to reduce the computation time to manageable proportions. Secondly, we have ignored Rayleigh scattering, since the influence of this interaction process is unimportant compared to other processes in the entire energy range under consideration; see Section 2.3.4. Thus, the only interaction processes included in our model is Compton scattering, photoelectric effect and pair production.

Compton scattering is modelled according to the Klein-Nishina theory, as described in Section 2.4.2. As for the treatment of the photoeffect, we have ignored the generation of fluorescence X rays, since the energy of such photons is below 100 keV and their possibility of escaping from the detector is normally very low, provided that the detector is not too small. This means that the entire energy of the incident photon is assumed to be deposited locally in a photoelectric interaction.

The treatment of pair production includes a simplified model of the annihilation of the positron thus created: Annihilation is assumed to take place locally, and the resulting two 511 keV photons are emitted isotropically, but with each of the 511 keV photons of the annihilation radiation pair in diametrically opposite directions as required by theory.

If we consider the possible error of the simplifications used in this model, it is clear that ignoring charged particle transport is potentially the most serious approximation. However, although photoelectrons, Compton recoil electrons or the pair production electron-positron

pair may acquire considerable kinetic energy in the photon interaction, it is unlikely that large errors are introduced due to the escape of charged particles from the detector. This is because the range of the charged particles normally will be short compared to detector dimensions, except possibly for small detectors and high energy.

It is much more important *how* these charged particles loose kinetic energy within the detector: Much of the charged particle energy loss take place through the generation of bremsstrahlung photons, which have a much higher chance of escaping than the charged particle itself. For this reason, the accuracy of our model must be expected to deteriorate for photon energies above 1 - 2 MeV; at lower energies, however, it should be reasonably accurate. This should be sufficient our purposes, since the highest energy isotope considered in this work is ^{22}Na, which emits 1.275 MeV photons.

DSIM algorithm

The actual calculation of efficiencies is done as indicated in Section 2.4.2, i.e. by generating a large number of photon histories and scoring (tallying) the interesting cases (or successes, in the statistical jargon). Specifically, NI source photons are generated, according to the source geometry selected, and primed in such a way that all impinge on the detector front face. Each source photon is tracked within the detector; if it interacts at all, the variable NTOT is incremented by one. If the photon looses all its energy within the detector, i.e. if no Compton photon or annihilation photon escape, there is a photopeak (full energy) event, and the variable NPH is incremented by one.

The algorithm for the tracking and scoring of one source photon, or photon history, is shown as a flow chart in Figure 5.14 below. This algorithm is performed NI times for a complete calculation, note that the variables NTOT and NPH are initialized to zero before the first history.

The logical variables INTERACTION and ESCAPE control the scoring of one history; if INTERACTION is true and ESCAPE is false after the generation of a photon history, there is a photopeak event, if both are true, the source photon have been registered, but not in the photopeak, if INTERACTION is false, the photon have not been detected.

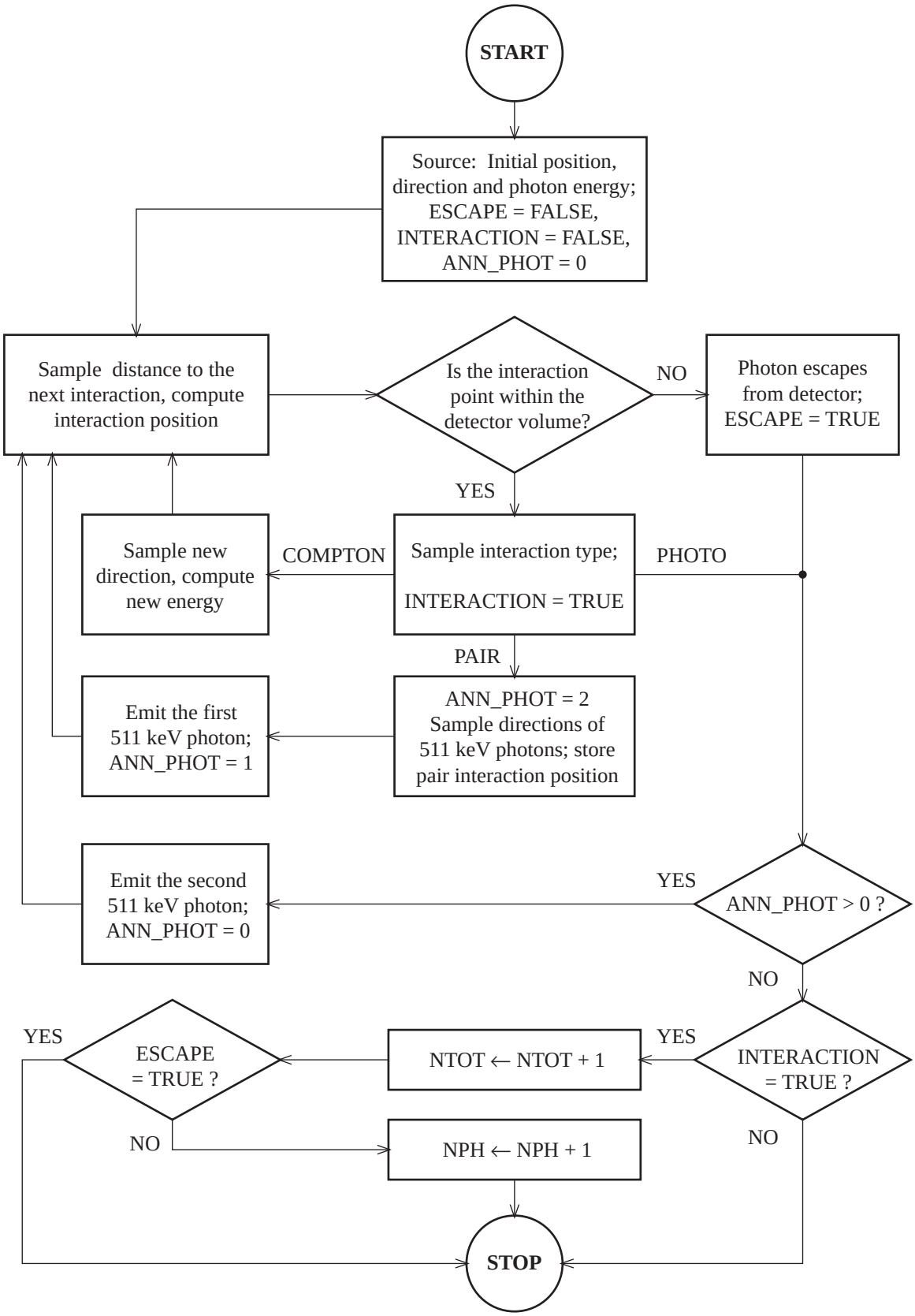

Figure 5.14 Flowchart for a single photon history (iteration) for the Monte Carlo detector efficiency calculator DSIM. Variables NTOT and NPH are initialized to zero before the first iteration; after NI iterations, ε_{tot} = NTOT/NI and ε_p =NPH/NI are computed.

The variable ANN_PHOT controls the generation of annihilation radiation photons; after a pair production interaction, the interaction position is stored, and the directions of the two 511 keV photons are sampled according to an isotropic distribution, see eq. 2.44. The photons are then tracked separately, in opposite directions, but from the same point.

After the completion of NI iterations, the photofraction, the photopeak efficiency and the total detection efficiency are computed as follows:

$$\varepsilon_p = \frac{\mathrm{NPH}}{\mathrm{NI}} \;;\; \varepsilon_{tot} = \frac{\mathrm{NTOT}}{\mathrm{NI}} \;;\; \varepsilon_0 = \frac{\varepsilon_p}{\varepsilon_{tot}} = \frac{\mathrm{NPH}}{\mathrm{NTOT}} \tag{5.53}$$

Representation and computation of photon directions

The methods for sampling the interaction type, the Compton scattering angles, and the distance between interactions were all described in Section 2.4.2, as were the general method for calculating the change in position once the new direction were known. However, we did not describe explicitly how the new photon direction is found from Compton deflection and azimuthal scattering angles, and we will now describe how this is done in DSIM:

If we assume that the current photon direction ω_k (i.e. the direction of travel immediately before interaction k) is defined by spherical coordinates (ν_k,φ_k), the corresponding Carthesian representation of the unit direction vector is given by (see eq 2.33):

$$\boldsymbol{\omega}_k = \begin{bmatrix} \sin\nu_k\cos\varphi_k & \sin\nu_k\sin\varphi_k & \cos\varphi_k \end{bmatrix}^{\mathrm{T}} \tag{5.54}$$

The new photon direction after interaction (scattering) k is determined by the Compton scattering angles θ_k (deflection) and α_k (azimuth). However, since these angles are relative to the current photon direction and *not* to the *xyz*-system, the new photon direction ω_k' given by

$$\boldsymbol{\omega}'_{k+1} = \begin{bmatrix} \sin\theta_k\cos\alpha_k & \sin\theta_k\sin\alpha_k & \cos\theta_k \end{bmatrix}^{\mathrm{T}} \tag{5.55}$$

is not relative to he *xyz*-system, but to the orthonormal system spanned by the vectors $\mathbf{u}_k$, $\mathbf{v}_k$ and $\mathbf{w}_k$, which together constitute the basis matrix $\mathbf{B}_k$:

$$\mathbf{B}_k = \begin{bmatrix} \mathbf{u}_k & \mathbf{v}_k & \mathbf{w}_k \end{bmatrix} = \begin{bmatrix} \cos\nu_k\cos\varphi_k & -\sin\varphi_k & \sin\nu_k\cos\varphi_k \\ \cos\nu_k\sin\varphi_k & \cos\varphi_k & \sin\nu_k\sin\varphi_k \\ -\sin\nu_k & 0 & \cos\nu_k \end{bmatrix} \tag{5.56}$$

It is seen that the current photon direction ω_k is equal to $\mathbf{w}_k$, which together with $\mathbf{u}_k$ and $\mathbf{v}_k$ define a right-handed coordinate system. The new photon direction ω_{k+1} relative to the *xyz*-system is then given by:

$$\boldsymbol{\omega}_{k+1} = \mathbf{B}_k \boldsymbol{\omega}'_{k+1} \tag{5.57}$$

where $\mathbf{B}_k$ and ω_k' are defined by eq 5.55 and 5.56, respectively.

We see that in general, we need the basis matrix $\mathbf{B}_k$ to compute the new photon direction from the Compton scattering angles. However, since spherical direction coordinates (ν_k,φ_k) are normally not used, except for specifying the source function (see below), it is inconvenient to compute $\mathbf{B}_k$ using eq 5.56. Instead, we utilize the fact that the new basis matrix $\mathbf{B}_k'_{+1}$ relative to the current basis $\mathbf{B}_k$ is given by

$$\mathbf{B}'_{k+1} = \left[\mathbf{u}'_{k+1} \;\; \mathbf{v}'_{k+1} \;\; \mathbf{w}'_{k+1}\right] = \begin{bmatrix} \cos\theta_k \cos\alpha_k & -\sin\alpha_k & \sin\theta_k \cos\alpha_k \\ \cos\theta_k \sin\alpha_k & \cos\alpha_k & \sin\theta_k \sin\alpha_k \\ -\sin\theta_k & 0 & \cos\theta_k \end{bmatrix} \tag{5.58}$$

i.e. $\mathbf{w}_k'$ is equal to ω_k'; the new basis matrix $\mathbf{B}_{k+1}$ relative to the *xyz*-system is then simply:

$$\mathbf{B}_{k+1} = \mathbf{B}_k \mathbf{B}'_{k+1} \tag{5.59}$$

The computation of photon directions in DSIM is done as follows: The initial (source) direction of the photon is specified by spherical coordinates $(\nu_0,\varphi_0) = (\nu_1,\varphi_1)$, and the basis matrix is computed using eq 5.56; the initial direction ω_1 is then equal to the matrix component vector $\mathbf{w}_1$. The new photon direction after a scattering interaction is then found by computing $\mathbf{B}_{k+1}$ using eq 5.59, and with $\mathbf{B}_k'_{+1}$ as defined by eq 5.58; the new direction vector ω_{k+1} is equal to the $\mathbf{w}_{k+1}$ component of $\mathbf{B}_{k+1}$. Note that it is possible to avoid our matrix formalism altogether by deriving explicit expressions for the new spherical direction coordinates $(\nu_{k+1},\varphi_{k+1})$ from the previous ones and the scattering angles [10, p. 774]; however, the use of vectors and matrices produces cleaner equations, whose computer implementation is just as efficient.

Source specification

We will now consider the source specifications for the various detector geometries; it is assumed that the detectors are symmetrical with respect to the *z*-axis, as indicated in Figure 5.13. For the *narrow beam* case, the initial direction is represented by

$$\boldsymbol{\omega}_0 = \boldsymbol{\omega}_0(\nu,\varphi)\,; \quad \begin{cases} \nu = \pi \\ \varphi = 0 \end{cases} \tag{5.60}$$

and the initial position by:

$$\mathbf{r}_0 = \begin{bmatrix} 0 & 0 & h_d \end{bmatrix}^{\mathrm{T}} \tag{5.61}$$

In the case of a *broad parallel beam*, the initial direction is as for the narrow beam case, i.e. as in eq 5.60, but the initial position, or point of entry, should be uniformly distributed over the detector front face. For a *rectangular parallelepiped detector*, this is accomplished by sampling the initial position as follows:

$$\mathbf{r}_0 = \begin{bmatrix} w_d(\rho_1 - \frac{1}{2}) \\ l_d(\rho_2 - \frac{1}{2}) \\ h_d \end{bmatrix} \tag{5.62}$$

where ρ_1 and ρ_2 are uniform random numbers.

For a *right cylinder detector*, the sampling of the initial position is done as follows:

$$\mathbf{r}_0 = \begin{bmatrix} d_d\sqrt{\rho_1}\cos(2\pi\rho_2)/2 \\ d_d\sqrt{\rho_1}\sin(2\pi\rho_2)/2 \\ h_d \end{bmatrix} \tag{5.63}$$

Again, ρ_1 and ρ_2 are uniform random numbers.

We note that in the case of narrow and broad parallel beams, initial direction and position are determined independently, this is not the case, however, for an *isotropic source function*: Generally, eq 2.44 would be used directly for the sampling of ν and φ to get isotropically distributed directions. However, only photons that hit the detector front face are of interest to us, so to avoid rejecting a large number of source photons travelling in the "wrong" directions, we will modify eq 2.44 a little. For the *right cylinder detector*, it is seen that restricting ν to lie within the interval

$$\nu_{\min} < \nu \le \pi \quad ; \qquad \nu_{\min} = \pi - \arctan\left(\frac{d_d}{2r_{ds}}\right) \tag{5.64}$$

ensures that all photons hit the detector front surface, see Figure 5.13a. The initial direction is then sampled as follows:

$$\boldsymbol{\omega}_0 = \boldsymbol{\omega}_0(\nu,\varphi)\ ; \quad \begin{cases} \nu = \arccos\left(\rho_1\left[\cos\nu_{\min} + 1\right] - 1\right) \\ \varphi = 2\pi\rho_2 \end{cases} \tag{5.65}$$

The position $\mathbf{r}_0$ on the front surface where the photon impinges on the detector is found by solving the equation

$$\mathbf{r}_0 = \mathbf{r}_s + t\boldsymbol{\omega}_0 \tag{5.66}$$

for the source - entry point distance t, using the fact that the z-coordinate of this point should be h_d ($\mathbf{r}_s$ denotes the source position). This yields the following result:

$$\mathbf{r}_0 = \begin{bmatrix} t\sin\nu\cos\varphi \\ t\sin\nu\sin\varphi \\ h_d \end{bmatrix} \quad ; \quad t = -\frac{r_{ds}}{\cos\nu} \ , \ \cos\nu \neq 0 \tag{5.67}$$

The cylinder detector case is relatively straightforward, which is because the front surface is circular; when we consider the *rectangular parallelepiped* and *truncated pyramid* detectors, however, we find that matters are a little more complicated, due the fact that these detectors have rectangular front surfaces. We solve this problem by the use of rejection sampling (see Section 2.4.2): We start by redefining the angle $\nu_{\min}$ as follows:

$$\nu_{\min} = \pi - \arctan\left(\frac{\sqrt{w_d^2 + l_d^2}}{2r_{ds}}\right) \tag{5.68}$$

The direction is then sampled using eq 5.65, and the detector entry point is found using eq 5.67. The resulting $\mathbf{r}_0$ will then lie on the plane $z = h_d$, within a circle containing the rectangular front surface of the detector. If the conditions

$$|x_0| \leq \tfrac{1}{2} w_d \quad , \quad |y_0| \leq \tfrac{1}{2} l_d \tag{5.69}$$

are fulfilled, the sampled direction is accepted; otherwise, a new direction is sampled using eq 5.65 (with a new pair of random numbers!) and the process is repeated.

The only other part of the DSIM flow chart which requires further comment, is the checking of whether or not the next point of interaction is within the detector volume. For a *right cylinder detector*, the interaction point (x,y,z) is within the detector if the following conditions are true:

$$4x^2 + 4y^2 \leq d_d^2 \qquad , \quad 0 \leq z \leq h_d \tag{5.70}$$

For the *rectangular parallelepiped detector*, the conditions are:

$$|x| \leq \tfrac{1}{2} w_d \quad , \quad |y| \leq \tfrac{1}{2} l_d \quad , \quad 0 \leq z \leq h_d \tag{5.71}$$

Finally, the conditions for the *truncated pyramid detector* are as follows:

$$|x| \leq \tfrac{1}{2} w_d(z) \quad , \quad |y| \leq \tfrac{1}{2} l_d(z) \quad , \quad 0 \leq z \leq h_d \tag{5.72}$$

where $w_d(z)$ and $l_d(z)$ are given by eq 5.52.

Estimating DSIM statistical uncertainty

As we mentioned in Section 2.4.2, a Monte Carlo simulation resembles an experiment in the sense that its result contains a certain degree of statistical uncertainty, due to the random nature of the method. This uncertainty may be estimated using the expression for the standard deviation of a variable which follows a binomial distribution. Alternatively, we may run the simulator several times for each case, use the average efficiency value as the result, and use the observed standard deviation of the average value to estimate the uncertainty [24] Initially, we chose to implement both methods, since this provided an opportunity of checking that the program operates correctly; the two uncertainty estimates should not differ too dramatically.

At this point, we might remark that although Monte Carlo statistical fluctuation uncertainty decreases as the number of generated histories is increased, the accuracy can never be better than permitted by the accuracy of the physical model and the cross section data used. Since the cross section data are accurate to within a few percent only, it follows that it is futile to generate an extreme number of photon histories in the hope of obtaining results of very high accuracy. For example, if photopeak efficiencies are calculated as the averages of 10 runs of 10000 photon histories each, we estimate (using the expression for the standard deviation for the binomial distribution, see eq 2.57) the relative uncertainty in the efficiencies (three times the standard deviation) to be below 3% for detection efficiency values greater than 0.1, below 2% for efficiencies greater than 0.2, and below 1% for efficiencies greater than 0.5.

Some aspects of DSIM implementation

DSIM has been implemented as a Think Pascal 4.0 program on a Macintosh Quadra 700 computer; apart from the photon tracking algorithm itself, the program contains routines for generating pseudorandom numbers, and for calculating linear attenuation coefficients from tabulated cross section data. Using the number of runs (10) and photon histories per run (10000) mentioned above, the calculation of a single set of detection efficiencies (ε_p, ε_{tot} and ε_0) takes about 4 minutes.

The linear attenuation coefficients for NaI and BGO are calculated from the attenuation coefficients of their constituents using the “mixture formula” derived in Section 2.3.3; the cross section data for the separate elements are taken from [12]. The attenuation coefficients needed during the simulation are computed from a previously prepared table, using linear interpolation. Note that since the photoeffect cross section decreases quite sharply with increasing energy, the tabulated photoeffect values have been normalized by E^3 (energy in MeV), and are renormalized accordingly after interpolation, to ensure better interpolation accuracy.

The generation of pseudorandom numbers is accomplished using a Pascal translation of the C routine **ran3** [15]; this routine was originally written by Knuth [30].

5.3.4. Verification of DSIM

To verify that DSIM produces the correct detection efficiencies, the results should really be compared to experimentally determined values; because we have not performed such measurements, we must content ourselves with comparing DSIM behaviour with the results of other simulation tools capable calculating detector response functions. The most advanced system available is the EGS simulator developed at Stanford University [31]; in contrast to DSIM, EGS includes the modelling of charged particle transport, and it also handles a greater energy range.

Rogers [24] has used EGS for calculating NaI and BGO photofractions and total efficiencies for cylinder shaped detectors and several source geometries. Some of the calculations are for bare, uncased detectors, and are therefore suitable for direct comparison with DSIM results. Furthermore, since other simulations use more realistic models (i.e. including the effect of the detector casing), and these results agree nicely with experimental data, we feel confident that EGS is suitable as a benchmark for testing DSIM performance.

We shall now present comparisons of DSIM and EGS results for a few different cases; note that the results apply to bare, uncased detectors only. This may be said to be a shortcoming of DSIM, as the detection efficiencies generally will be affected by the detector casing, however, the effect is believed to be insignificant for our purposes: In this work, we will use the calculated detection efficiencies for estimation of statistical uncertainty and required countrate for raysum measurement, and as we have used several other approximations in these estimates, the accuracy of the detection efficiency values used is not too critical.

The first example we shall consider, is the photofraction ε_0 for a $3'' \times 3''$ NaI detector, for an isotropic source at 10 cm distance, and for photon energies in the range from 0.32 MeV to 10 MeV. The EGS data, which are computed both with and without electron transport included in the model, are taken from Table 1 in [24]. DSIM values are computed as the averages of 10 runs each of NI = 1000 photon histories. The results are plotted against the photon energy in Figure 5.15, the uncertainties are equal to three times the estimated standard deviation. DSIM and EGS numerical values are given in Table A.1 in Appendix A.

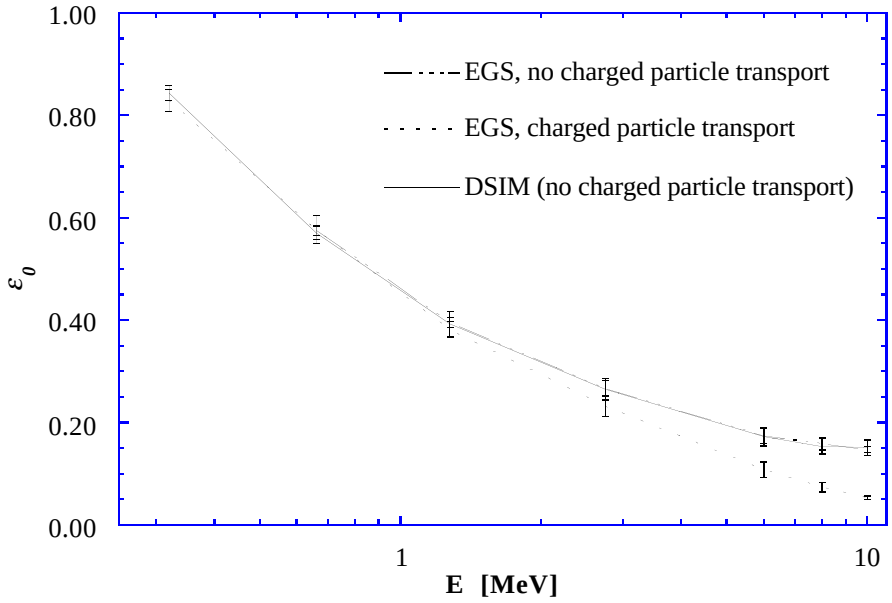

Figure 5.15 EGS and DSIM calculations of the photofraction ε_0 for a 3" × 3" NaI detector illuminated by an isotropic source at 10 cm distance.

The results are interesting for two reasons: Firstly, it is seen that there is excellent agreement between the DSIM data and the values computed using non-charged particle transport EGS simulation; this shows that the DSIM program behaves correctly.

Secondly, we see that photofraction values may be computed accurately for photon energies up to about 1.5 MeV, without including charged particle transport in the model: The discrepancy for higher energies is probably caused by the fact that the amount of escaping bremsstrahlung radiation becomes large enough to reduce the number of photopeak events significantly, and hence, reduce the photofraction as well.

This picture is confirmed by the photofraction results shown in Figure 5.16, which are also for a 3″ × 3″ NaI detector, but for the case of a broad parallel photon beam. The EGS results, which are taken from Rogers' Table 4 [24], are computed using a model which includes charged particle transport. Statistical uncertainties shown are three times the estimated standard deviation of the photofraction values; again, the DSIM - EGS agreement is good for photon energies lower than 1.5 MeV. The photofraction values are given in Table A.2 in Appendix A, where we have also included the DSIM and EGS results for the total detection efficiency ε_{tot}; although it is completely trivial to compute this for a parallel beam, using the attenuation formula, it provides an extra check of the accuracy of the interpolation algorithm used for calculating the required attenuation coefficients.

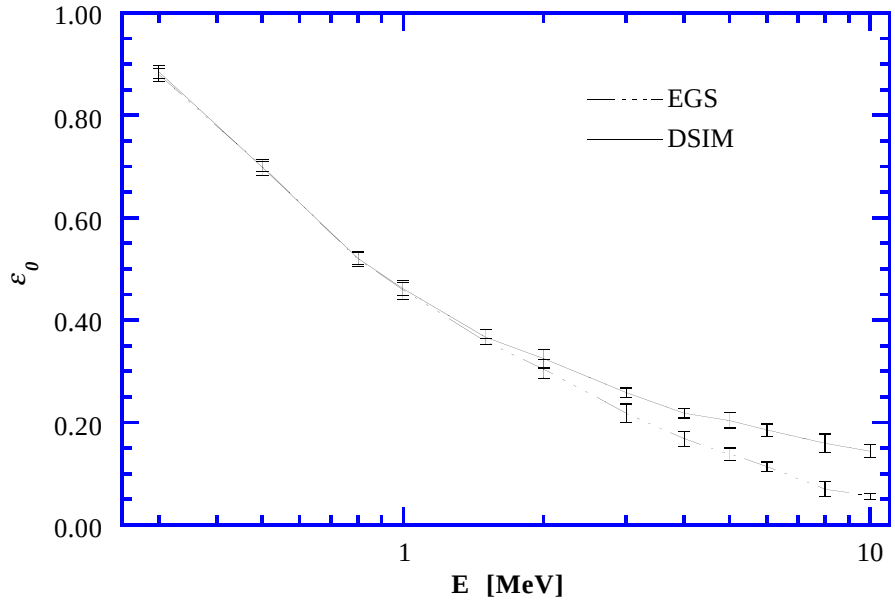

Figure 5.16 EGS and DSIM calculations of the photofraction ε_0 for a 3" × 3" NaI detector illuminated by a broad parallel beam.

Finally, we include a comparison of DSIM and EGS calculations of the photopeak efficiency of 3″ × 3″ NaI and BGO detectors illuminated by an isotropic source at 10 cm distance, for photon energies from 0.3 to 10 MeV. The results are shown in Figure 5.17 below; the EGS data is taken from Rogers' Figure 13, and the plotted EGS uncertainties are reading uncertainties, while DSIM uncertainties are estimated as described earlier. Note that the EGS results are also plotted in Figure 5.12; DSIM and EGS numerical values are given in Table A.3 in Appendix A.

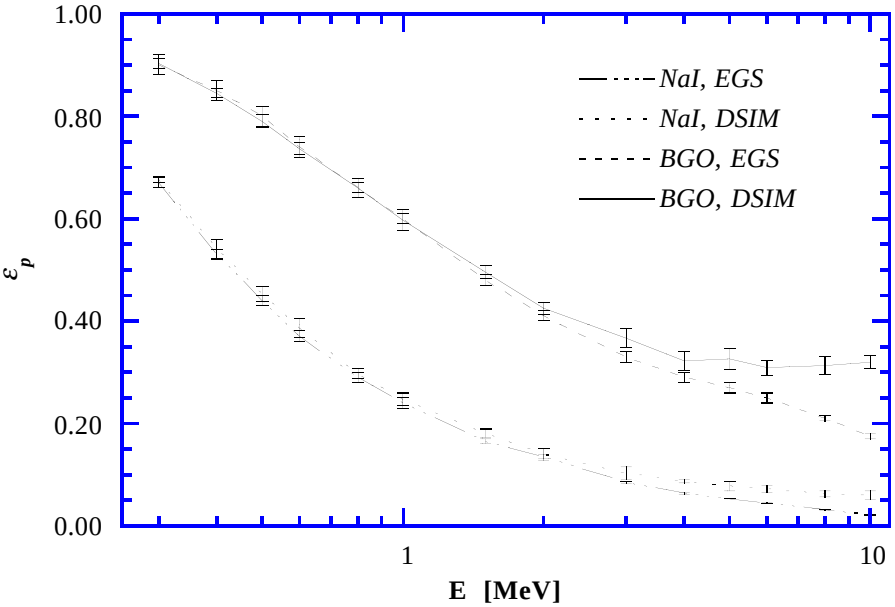

Figure 5.17 EGS and DSIM calculations of the photopeak (full energy) detection efficiency ε_p for 3" × 3" NaI and BGO detectors illuminated by an isotropic source at 10 cm distance.

The DSIM-EGS agreement is still good for the lower part of the energy range; also, the relative discrepancy between the charged particle transport model (EGS) and the simpler DSIM model is greater for NaI than for BGO. The reason for this is that the higher detection efficiency of BGO means that fewer bremsstrahlung photons are allowed to escape, so the reduction of the photopeak efficiency will be less severe than for NaI.

The conclusion of our comparison of EGS and DSIM calculations is that we feel quite confident that DSIM produces reliable detection efficiency estimates for photon energies below 1.5 MeV; this is adequate for our purposes, since the highest photon energy which we have considered for raysum measurement is 1.275 MeV (^{22}Na).

5.3.5. Simulations

Because detector photofractions and photopeak efficiencies are required for estimating the countrate requirement and the statistical uncertainty for the raysum measurements, and because the efficiencies are system geometry dependent, it is necessary to compute detector efficiencies for all possible choices of grid resolution, number of views, pipe diameter and isotope energy, in order to be able to study the performance of different systems. In this section, we will use DSIM to compute the necessary photofraction and photopeak efficiency values; note that while detector width and length are determined by the system geometry, the detector height is chosen so that the nominal interaction ratio is 95%, see Section 5.3.2 and eq 5.50: We repeat the values here for convenience; h_d is 2.0 cm for 356 keV (^{133}Ba), 4.5 cm for 661.6 keV (^{137}Cs) and 7.5 cm for 1.275 MeV (^{22}Na).

We have already established that the truncated pyramid detector shape is optimal for our flow imaging system; note, however, that the slope of the side surfaces depend on the ratios of the detector front face width (and length) to the source-detector distance, i.e. the slope depend on the grid size n and the number of views used, m_s. The size of the detector, i.e. the front face width and length also depends on these parameters (see eq 5.48; also, recall that we have chosen $l_d = 2w_d$), but in addition, it is a function of the pipe diameter.

In Chapter 4, we considered values of n ranging from 2 to 16, and odd-valued m_s from 3 to 15, which means that 105 different detection efficiencies must be computed for every value of the pipe diameter and for every photon energy considered, which is a little time consuming. However, the computational burden may be reduced significantly by introducing two approximations:

First, we note that the detector width w_d (and hence, the length,l_d) is very nearly independent of the number of views, m_s, see eq 5.49. Next, we note that a rectangular parallelepiped detector illuminated by a broad parallel beam of photons should have roughly the same

detection efficiency as a truncated pyramid detector illuminated by an isotropic source of equal height and front face width and length, provided that the source-detector distance is not too small. The reason for introducing these approximations, is that the photopeak efficiency for the parallelepiped detector is then independent of the number of views used, since the detector size is assumed to be m_s independent and so is the shape, since a broad parallel beam is assumed. In this way, we have reduced the number of efficiencies to be computed, by a factor of seven, i.e. the number of different m_s.

To establish the validity of the parallelepiped approximation for a truncated pyramid detector, we first note that the interaction ratio would be nearly identical in the two cases, see Section 5.3.2, so no edge effects should be present. Thus the only remaining factor capable of causing photopeak efficiency differences between the two cases, is the fact that the truncated pyramid detector will have a larger volume, and hence, a larger efficiency: Since the truncated pyramid volume approaches the parallelepiped volume for large source-detector distances, it follows that the photopeak efficiencies should also approach each other. The question is then to determine the minimum source-detector distance for which the parallelepiped shape is a reasonable approximation, or alternatively, to determine the maximum error committed when using the approximation on the present problem.

From eq 5.46 and eq 5.47, we see that the maximum ratio of the detector width w_d to the source-detector distance r_{ds} occurs for the minimum number of views (and minimum gridsize n). Thus, the maximum error in the estimated photopeak efficiency due to the parallelepiped approximation will occur for $m_s = 3$; also, the errors would be larger for higher photon energy and smaller pipe diameter. On the other hand, the approximation used for w_d produces values somewhat greater that the exact one (but for low m_s only), see eq 5.48 and eq 5.49, so this will counteract the decrease in volume by the parallelepiped approximation.

To study the combined effect of these two approximations, we have computed the ratio of the parallelepiped detection efficiency (using eq 5.49 for w_d) to the exact value (truncated pyramid detector and isotropic source, and eq 5.48 for w_d), for all three isotopes in question, for m_s = 3, and for pipe diameters ranging from 5 cm and upwards. It turns out that the maximum error in the estimated photopeak efficiency at 1.275 MeV photon energy (^{22}Na) is -7% for d = 5 cm and -2% at d = 7.5 cm; the error is negligible for larger pipe diameters. For 661.6 keV photon energy (^{137}Cs), the error is -2% for d = 5 cm and negligible for larger pipe diameters; at 356 keV (^{133}Ba) the errors are negligible in all cases.

While the -7% error for ^{22}Na is far from negligible as such, it should be remembered that using this high energy isotope for raysum measurement for small diameter pipes is not very realistic anyway, see our previous discussion of statistical uncertainty (Section 5.2.1) and

detector countrate requirement (Section 5.2.2). Also, recall that in the analysis of statistical raysum uncertainty, it is the inverse of the square root of the photopeak detection efficiency value that enters in the uncertainty expression, so a -7% error in the efficiency value results in a 3.7% error only in the uncertainty estimate. Finally, it is seen from the results of Section 5.3.4 that DSIM efficiency values are maybe a little too high at 1.275 energy anyway, due to the omission of charged particle transport in our model. Therefore, we find that the approximations are acceptable, and we have thus removed the m_s dependence of the photopeak efficiencies (and also the photofractions) from the calculations.

Using the above approximations, we have computed BGO photopeak detection efficiencies ε_p for each of the three isotopes under consideration, for the gridsize range of n = 2 to 16, and for pipe diameter values ranging from 2.5 to 30 cm. Photopeak efficiency values for ^{133}Ba (356 keV), ^{137}Cs (661.6 keV) and ^{22}Na (1.275 MeV) are presented in Appendix A, in Table A.4, Table A.5 and Table A.6, respectively. The presented detection efficiencies are averages of 10 DSIM runs, each of 10000 photon histories, so the relative statistical uncertainty of the photopeak efficiencies are below 2% for efficiencies above 0.2 and below 1% for efficiencies larger than 0.5, see the discussion of DSIM uncertainty in Section 5.3.3.

To illustrate the n and d influence on the photopeak efficiencies, we have plotted ε_p against the pipe diameter, and with the grid size as a parameter below: The data in Figures 5.18, 5.19 and 5.20 are for ^{133}Ba, ^{137}Cs and ^{22}Na, respectively.

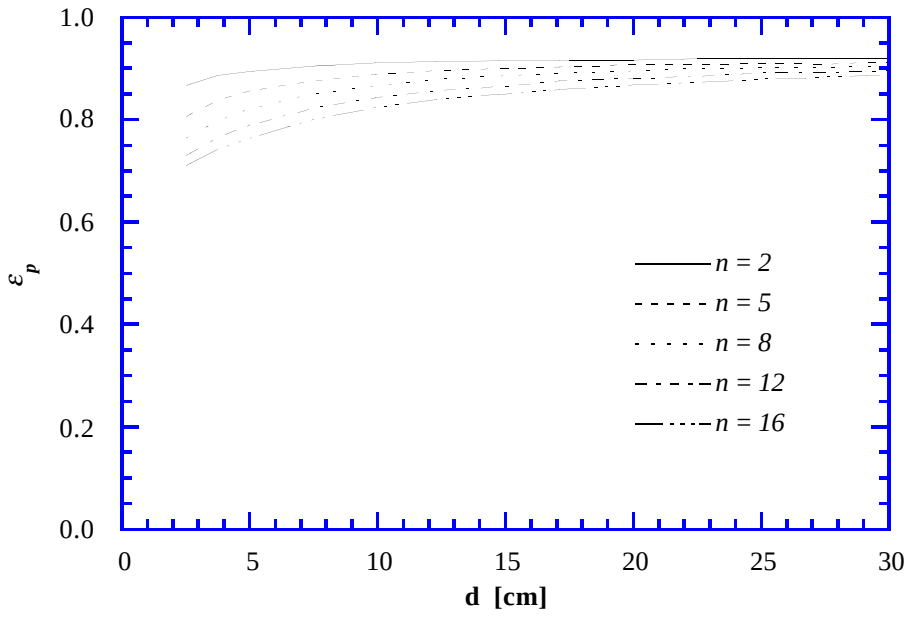

Figure 5.18 BGO photopeak detection efficiency ε_p versus pipe diameter d, with reconstruction gridsize n as a parameter, for E_γ = 356 keV (^{133}Ba). Detector thickness is 2.0 cm, which corresponds to a nominal ε_{tot} value of 95%.

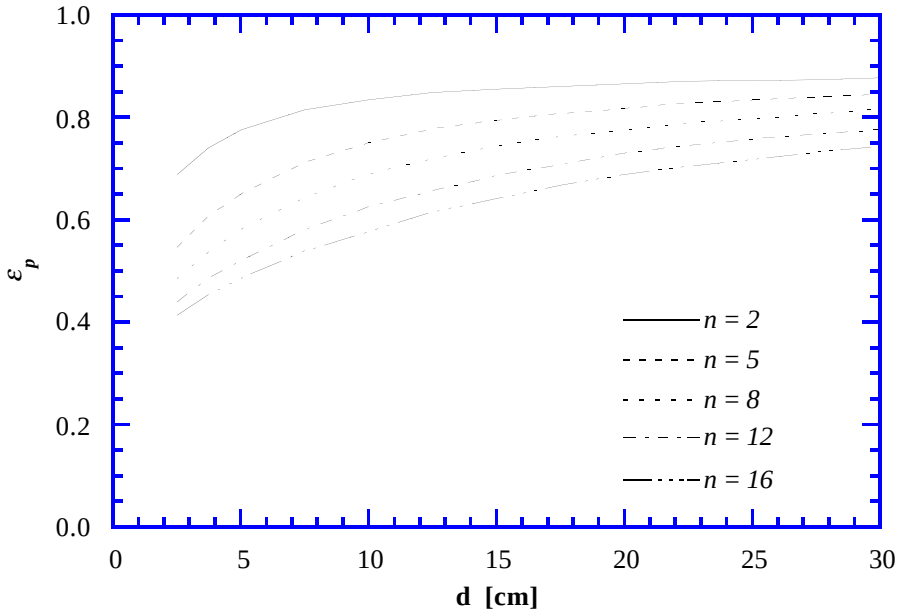

Figure 5.19 BGO photopeak detection efficiency ε_p versus pipe diameter d, with reconstruction gridsize n as a parameter, for E_γ = 661.6 keV (^{137}Cs). Detector thickness is 4.5 cm, which corresponds to a nominal ε_{tot} value of 95%.

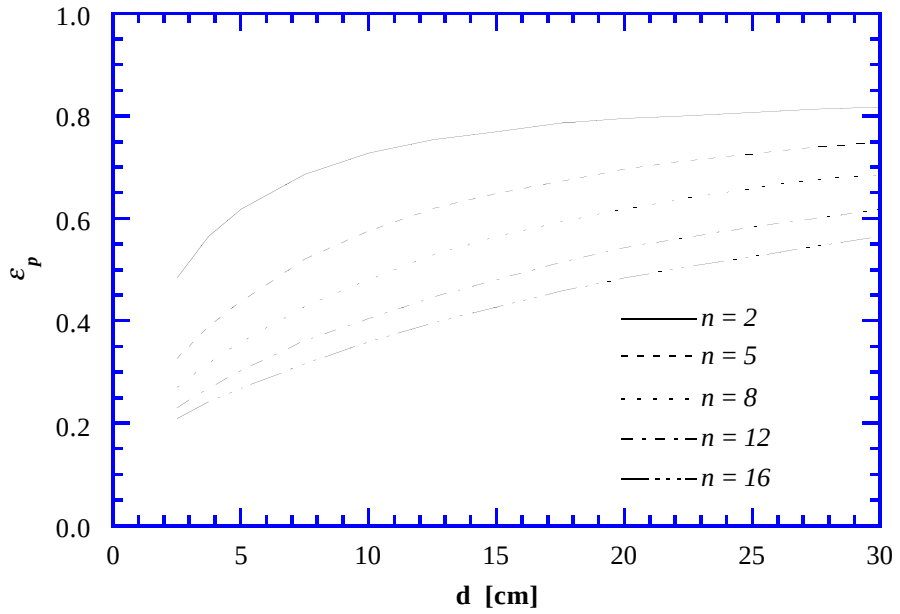

Figure 5.20 BGO photopeak detection efficiency ε_p versus pipe diameter d, with reconstruction gridsize n as a parameter, for E_γ = 1.275 MeV (^{22}Na). Detector thickness is 7.5 cm, which corresponds to a nominal ε_{tot} value of 95%.

The DSIM results show that very reasonable detection efficiencies are possible using BGO detectors: For ^{133}Ba, the photopeak efficiency is greater than 0.7 in all cases, and is nearly 0.9 for an n = 8 system at 15 cm pipe diameter. A similar system using ^{137}Cs has an ε_p value

of 0.75, and for a ^{22}Na system ε_p is 0.55; while the latter value is considerably smaller than the ideal value of one, it is still much better than what is possible using e.g. NaI detectors.

Another feature of the plots shown, is that the sensitivity of the photopeak efficiency to gridsize and photon energy variations is seen to become greater for small pipe diameters, which is due to the reduced detector size. To show the detector size and energy dependence of the photopeak efficiency more explicitly, we have plotted the calculated ε_p values against detector size (represented by detector front surface width w_d), with the isotope (photon energy) as a parameter in Figure 5.21.

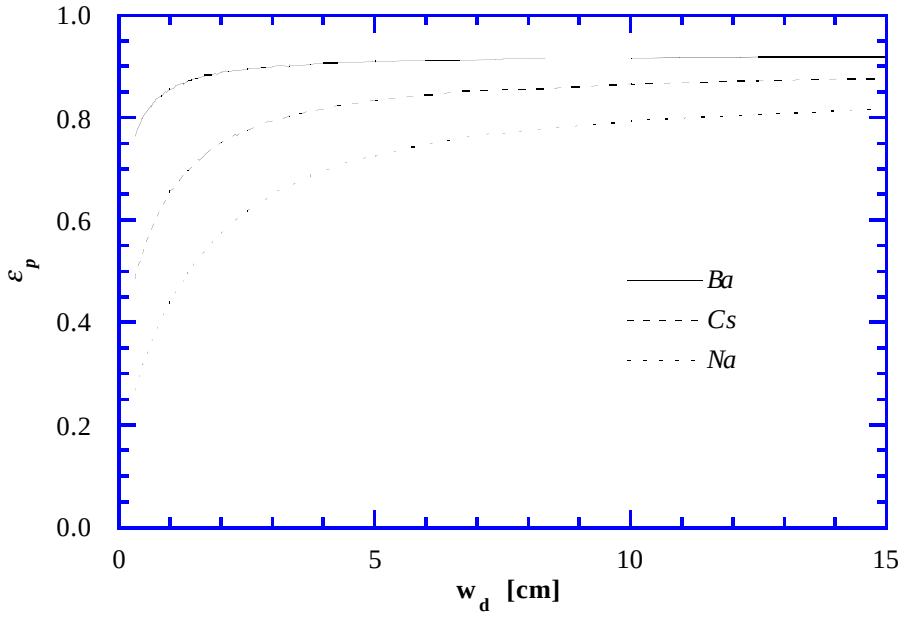

Figure 5.21 BGO photopeak detection efficiency ε_p versus detector front face width w_d for photon energies of 356 keV (^{133}Ba), 661.6 keV (^{137}Cs) and 1.275 MeV (^{22}Na). The detector front face length l_d is twice the width, and the detector thicknesses are chosen so that ε_{tot} = 95% for each energy.

Photofraction values ε_0 are found by dividing the photopeak detection efficiency ε_p by the nominal interaction ratio ε_{tot}, which is equal to 0.95 for the detector thicknesses used in the above calculations.

5.4. Raysum measurement and isotope choice revisited

Having calculated photopeak efficiencies and photofractions for all necessary d and n variations (ε_p and ε_0 have negligible m_s dependence) of the chosen detector system, we may now proceed to consider the relative levels of raysum statistical uncertainty and detector countrate associated with our single energy flow imaging system; hence, we are now in a

position to decide which isotope is best suited for a certain application. We will first take a look at the relative levels of raysum statistical uncertainty.

5.4.1. Raysum statistical uncertainty

By incorporating the photopeak efficiency for a given system geometry into the expression for the raysum statistical uncertainty, eq 5.17, we can relate the uncertainty to the resolution of the reconstruction grid: Using the BGO photopeak efficiency values calculated in Section 5.3.5, (numerical values are given in Appendix A) we may calculate the uncertainty for each isotope, for varying values of pipe diameter d and gridsize n.

In Figures 5.22, 5.23 and 5.24, we have plotted the quantity $\varepsilon_p^{-1/2}(\sigma_p)_{max}$ against the pipe diameter, with the isotope type as a parameter, for gridsizes n of 2, 8 and 16, respectively. Furthermore, in order to facilitate comparison with Figures 5.3 and 5.5, we have used $k = {}^1/_6$, $r_{rel} = {}^3/_4$ (i.e. $r = {}^{3d}/_8$) and $I_0\tau/\varepsilon_p = 10000$.

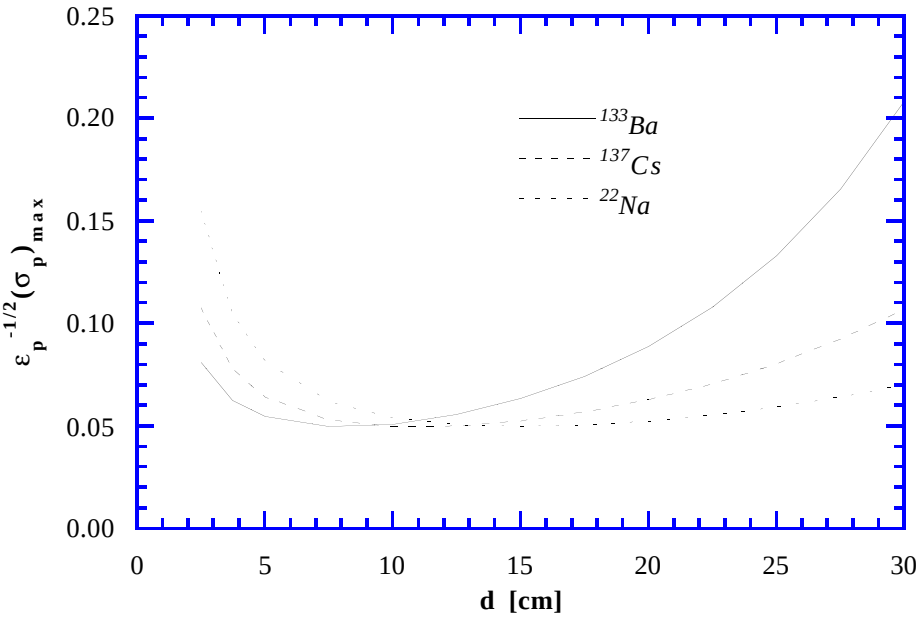

Figure 5.22 Worst-case statistical fluctuation error $\varepsilon_p^{-1/2}(\sigma_p)_{max}$ versus pipe diameter d, for gridsize $n = 2$ and for isotopes ^{133}Ba, ^{137}Cs and ^{22}Na, with $r_{rel} = {}^3/_4$ ($r = {}^{3d}/_8$), $k = {}^1/_6$; the detector type is BGO, see Section 5.3.5. We have used $I_0\tau/\varepsilon_p = 10000$ to facilitate comparison with other uncertainty plots; see also Section 5.2.1.

The plot for the case of $n = 2$, see Figure 5.22, is quite similar to the $(\sigma_p)_{max}$ plot in Figure 5.3, where the detection efficiency have been ignored (i.e. ε_p is assumed to be unity), which is not surprising, since the detection efficiencies are quite high for all energies for this choice of grid resolution, see Figures 5.18 - 5.20.

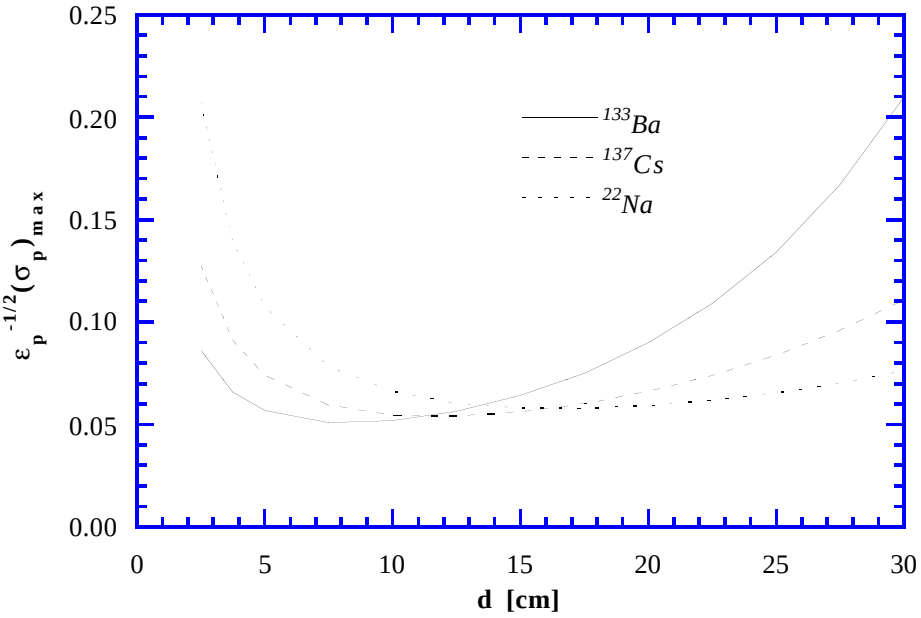

Figure 5.23 Worst-case statistical fluctuation error $\varepsilon_p^{-1/2}(\sigma_p)_{max}$ versus pipe diameter d, for gridsize n = 8 and for isotopes ^{133}Ba, ^{137}Cs and ^{22}Na, with r_{rel} = $^3/_4$ (r = $^{3d}/_8$), k = $^1/_6$; the detector type is BGO, see Section 5.3.5. We have used $I_0\tau/\varepsilon_p$ = 10000 to facilitate comparison with other uncertainty plots; see also Section 5.2.1.

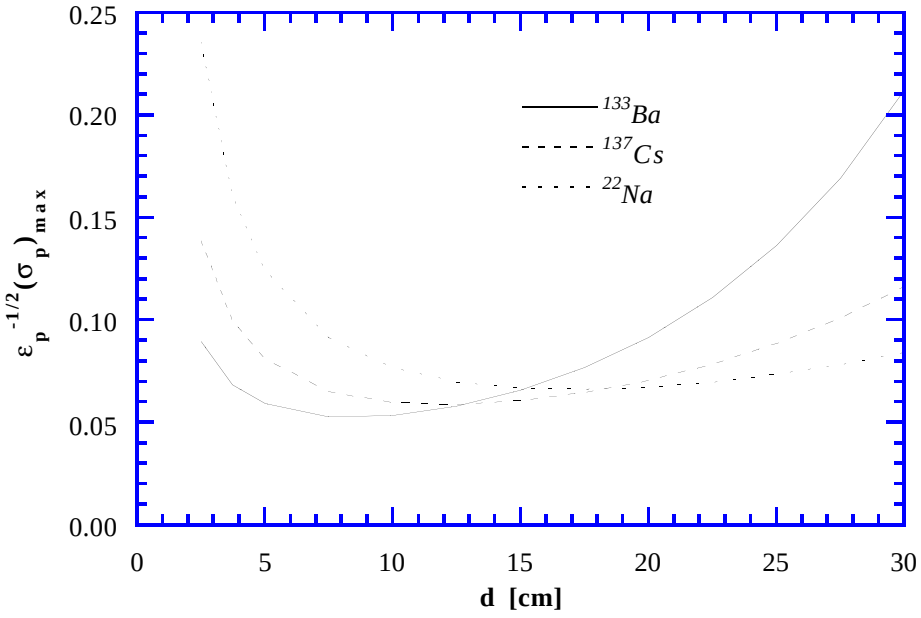

Figure 5.24 Worst-case statistical fluctuation error $\varepsilon_p^{-1/2}(\sigma_p)_{max}$ versus pipe diameter d, for gridsize n = 16 and for isotopes ^{133}Ba, ^{137}Cs and ^{22}Na, with r_{rel} = $^3/_4$ (r = $^{3d}/_8$), k = $^1/_6$; the detector type is BGO, see Section 5.3.5. We have used $I_0\tau/\varepsilon_p$ = 10000 to facilitate comparison with other uncertainty plots; see also Section 5.2.1.

When the grid resolution is increased, however, the picture is altered, because of the reduction in detector size: It is seen from Figures 5.23 and 5.24 that the uncertainty level rises,

especially for small pipe diameters, which corresponds to the smallest detector sizes. Also, the uncertainty increase is almost negligible for ^{133}Ba and very pronounced for ^{22}Na, since the sensitivity of the photopeak efficiency to the detector size is very slight for low photon energy, but is quite strong for higher photon energy, see Figure 5.21.

One important application for the uncertainty plots in Figures 5.22 - 5.24 , is to use them as an aid in the selection of which isotope to use in an imaging system: It is seen that for a moderate grid resolution, n = 8, ^{133}Ba is optimal for smaller pipe diameters, while ^{22}Na is the best choice for large diameters. The remaining isotope, ^{137}Cs, may be regarded as a reasonable compromise for the medium range of diameters, e.g. 7.5 to 17.5 cm; it should also be remembered that this is the isotope having the longest halflife, see Table 5.1.

5.4.2. Detector countrate

As we have mentioned before (see Section 5.2.2), not only the level of statistical uncertainty is important when selecting the isotope, but also the detector countrate requirement. We have also established that the total countrate depends on the detector photofraction; to see the impact of this effect, we have plotted the total countrate $I_{max}\varepsilon_0^{-1}$ in Figures 5.25, 5.26 and 5.27 below; in the expression for I_{max} (eq 5.26) we have used r_{rel} = $^3/_4$, k = $^1/_6$ and $\tau(\sigma_p)^2$ = 1; the photofractions are found from the photopeak efficiencies computed in Section 5.3.5.

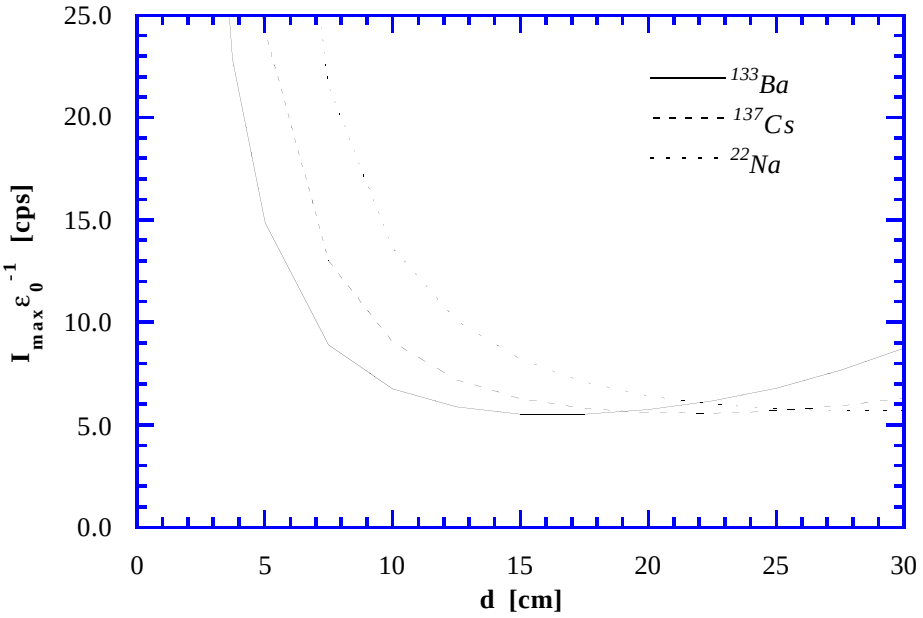

Figure 5.25 Maximum *total* detector countrate $I_{max}\varepsilon_0^{-1}$ (see eq 5.26) versus pipe diameter d for BGO detectors, gridsize n = 2, isotopes ^{133}Ba, ^{137}Cs and ^{22}Na, with r_{rel} = $^3/_4$, k = $^1/_6$, and with the product $\tau(\sigma_p)^2$ equal to one.

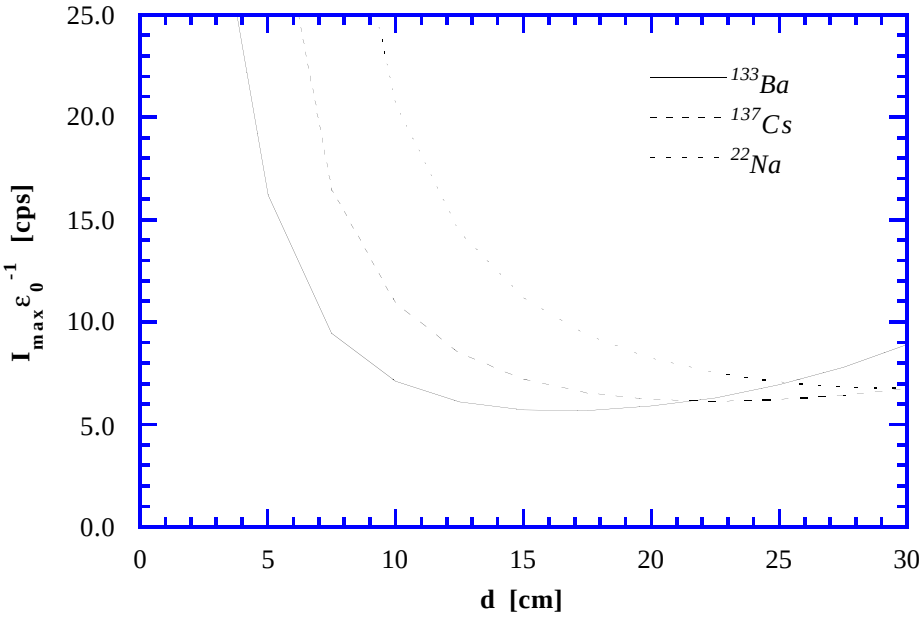

Figure 5.26 Maximum *total* detector countrate $I_{max}\varepsilon_0^{-1}$ (see eq 5.26) versus pipe diameter d for BGO detectors, gridsize n = 8, isotopes ^{133}Ba, ^{137}Cs and ^{22}Na, with r_{rel} = $^3/_4$, k = $^1/_6$, and with the product $\tau(\sigma_p)^2$ equal to one.

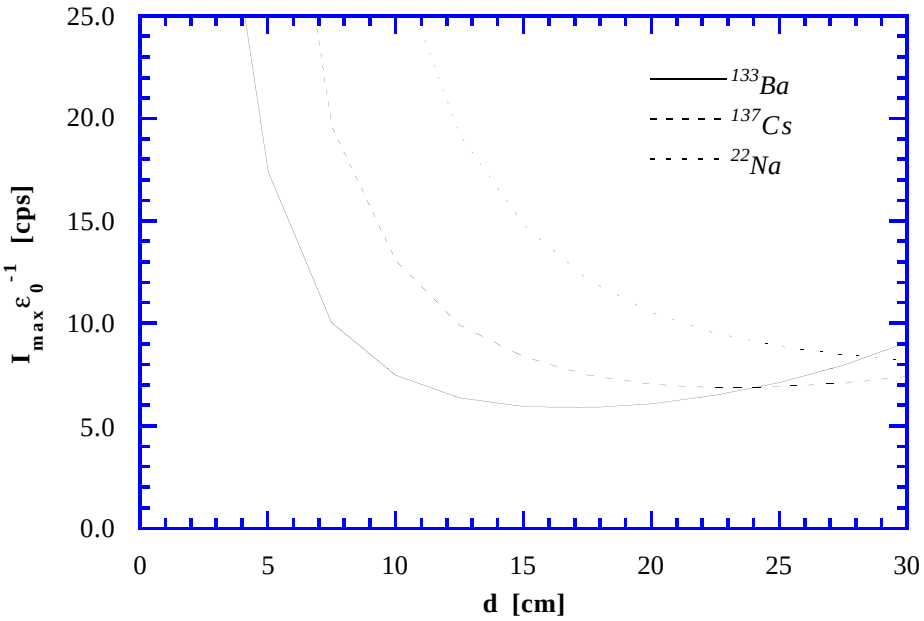

Figure 5.27 Maximum *total* detector countrate $I_{max}\varepsilon_0^{-1}$ (see eq 5.26) versus pipe diameter d for BGO detectors, gridsize n = 16, isotopes ^{133}Ba, ^{137}Cs and ^{22}Na, with r_{rel} = $^3/_4$, k = $^1/_6$, and with the product $\tau(\sigma_p)^2$ equal to one.

It is seen from Figures 5.25, 5.26 and 5.27 that the dependence of the maximum total countrate on the photon energy is quite dramatic for small pipe diameters; also, the energy dependence is seen to become stronger for higher gridsize n, which is a consequence of the greater energy sensitivity of the photopeak efficiency and photofraction for small detectors.

Generally, the detection efficiency influence is seen to be more marked for the countrate requirement than for the raysum uncertainty level; this is because the total countrate is inversely proportional to the photopeak efficiency, while the uncertainty is inversely proportional to the *square root* of ε_p.

The general significance of the presented plots of the total detector countrate, is that the countrate requirement is minimized by choosing the lowest energy isotope, except for very large pipe diameters. This is not surprising, since this is the situation even if the effect of the detector photofraction is ignored, see Figure 5.6, and because the photofraction is a decreasing function of energy.

More importantly, Figures 5.25 - 5.27 may be used for predicting the maximum countrate for a given system, once the measurement time τ and the desired level of raysum uncertainty have been specified. For example, if τ = 1 s and $(\sigma_p)_{max}$ = 0.01, the maximum countrate for a ^{133}Ba system of 15 cm pipe diameter and gridsize n = 8, is about 60 kcps. Also, the countrate capability requirement is seen to become quite extreme for short measurement times and low uncertainty.

5.4.3. Discussion

From the results of the previous two sections, it is clear that if the level of statistical uncertainty in the measured raysum is the most important criterion for isotope choice, a low energy isotope should be chosen for small pipe diameters, and higher energy isotopes for larger diameters; on the other hand, if the detector countrate capability is taken into account, a low energy isotope is desirable.

In addition to these selection criteria, it is necessary to consider some other factors: First of all, it is clear that from a safety point of view, low energy isotopes are preferable, since they require less shielding material than higher energy isotopes. Secondly, from the results of Section 5.2.3 we know that finite beam width raysum errors are minimized by using the isotope corresponding to the lowest possible fluid linear attenuation coefficient; this would normally be the highest energy isotope.

The situation is a little more complicated when we consider the problem of scattered radiation: The relative energy resolution requirement of the detectors is relaxed for higher photon energy, see Figure 5.11; however, the actual intensity of scattered radiation directed into the detectors is impossible to predict without a photon transport model for the entire imaging system, so it is difficult to state which isotope choice, if any, minimizes the raysum measurement error caused by detection of scattered radiation.

If we consider the factors which determine the raysum measurement accuracy, we note that the finite beam width error and the scattered radiation error are systematic errors, which in principle can be reduced using corrections computed from a “raw” first image reconstruction, see Section 5.2.3. The statistical uncertainty, however, can only be lowered by increasing the number of detected photons; this means that, within the countrate capability limits of the detector system, one should choose the isotope which minimizes the statistical uncertainty.

On the basis of the above considerations, it seems that ^{133}Ba or ^{137}Cs would suit most applications[1], with the possible exception of very large pipe diameters; these isotopes also have significantly longer halflives than ^{22}Na.

Finally, it should be noted that the results of Section 5.4.1 and Section 5.4.2 are important from another point of view, since they relate statistical uncertainty level and detector countrate requirement to the gridsize *n*, i.e. to the spatial resolution of the imaging system; this will be exploited below.

---

[1]One possible complication of using ^{133}Ba, is that it emits several photon energies: In addition to the main emission at 356 keV, there are emissions at 303 keV and 384 keV; however, these are of significantly lower intensity than the main emission, and should not cause any problems for raysum measurement, even when detectors of moderate energy resolution are used.

6. Analysis of overall system performance

The main parameters describing the performance and design of a single energy flow imaging system, are image spatial resolution, represented by the gridsize n, the number of sources m_S, the image density resolution σ_f, the dynamic response (or temporal resolution) τ, the pipe diameter d and the source intensity S_0 (see also [5]). The gridsize n is used for representing the spatial resolution, since the relative spatial resolution is $1/n$. Further, since the systems we are considering have relatively low spatial resolution compared to medical CT, the reconstruction time is small compared to the measurement time necessary to ensure a low level of statistical raysum uncertainty, and we may take the system response time to be equal to τ.

In this section, we will develop expressions which relate the main system parameters to each other, and we will also derive a relation between the maximum detector countrate and the other system parameters. Finally, we will consider the possible overall system performance, which is determined by the image density uncertainty referred to above and the reconstruction error analyzed in Chapter 4.

6.1. Density resolution

The starting point for our derivation of the expressions mentioned above is the relation between relative pixel density uncertainty and relative raysum uncertainty (see eq 3.34):

$$\frac{\sigma_f}{f} = \frac{\sigma_p}{p}\sqrt{\frac{n^3}{M}} = \frac{\sigma_p}{p}\sqrt{\frac{n^3}{m_s m_a}} \tag{6.1}$$

where the total number of raysums, M, is simply the product of m_S and m_a; please note that we refer to the standard deviations σ_f and σ_p when speaking of uncertainties.

If it is assumed that there are no other contributions to the raysum uncertainty than the statistical fluctuations in the number of detected photons, we may use eq 5.17 directly for the relative uncertainty (σ_p/p); this is because the equation was derived for the case $p = 1$, so (σ_p/p) = σ_p, and we have:

$$\frac{\sigma_p}{p} = \frac{\exp\left[\frac{1}{2} d_i \left(k'\mu_p + \mu_f\right)\right]}{\mu_f d_i \sqrt{I_0 \tau}} \tag{6.2}$$

Here, it is understood that the parameters d_i and k' are functions of d, k, and r_{rel}, see Section 5.2; as before, we will use $k = 1/6$ and $r_{rel} = 3/4$. Combining eq 6.1 and eq 6.2, we get the following expression for the relative pixel uncertainty:

$$\frac{\sigma_f}{f} = \sqrt{\frac{n^3}{m_s m_a}} \left\{ \frac{\exp\left[\frac{1}{2} d_i \left(k' \mu_p + \mu_f\right)\right]}{\mu_f d_i \sqrt{I_0 \tau}} \right\} \tag{6.3}$$

The pipe diameter d enters in this expression through d_i and k', see eq 5.4 and 5.16, while the remaining main system parameter, S_0, is related to the detected intensity without absorber by the following expression, see eq 5.1:

$$I_0 = S_0 \varepsilon_p \frac{\Omega_d}{4\pi} \tag{6.4}$$

Since the truncated pyramid detector has a rectangular front face shape of width w_d and length $l_d = 2w_d$, the fractional solid angle subtended by the detector at the source is given by:

$$\frac{\Omega_d}{4\pi} = \frac{w_d l_d}{4\pi (r_{ds})^2} = \frac{2}{4\pi} \left(\frac{w_d}{r_{ds}} \right)^2 \tag{6.5}$$

Note that using the ratio of the detector front face area to the square of the source-detector distance for the solid angle Ω_d is really only an approximation; however, it is accurate enough for our purposes, because the ratio between source-detector distance and detector front face width (or length) is several times greater than unity even for small n and m_s.

We now wish to express the fractional solid angle using the system geometry parameters n and m_s: Using eq 5.46 and eq 5.47, the detector width may be written:

$$w_d = 2 r_{ds} \tan\left(\frac{\pi}{4 n m_s} \right) \tag{6.6}$$

Combining eqns 6.5 and 6.6 yields:

$$\frac{\Omega_d}{4\pi} = \frac{2 \tan^2\left(\frac{\pi}{4 n m_s}\right)}{\pi} \tag{6.7}$$

Finally, we note that $n \geq 2$ and $m_s \geq 3$, so $\pi/(4 n m_s) \leq \pi/24$, so we may safely use the approximation

$$\tan\left(\frac{\pi}{4 n m_s} \right) \approx \frac{\pi}{4 n m_s} \tag{6.8}$$

and the fractional solid angle may be expressed as:

$$\frac{\Omega_d}{4\pi} = 2\pi\left(\frac{1}{4nm_s}\right)^2 \tag{6.9}$$

Substituting this in eq 6.4, we find that the detected intensity without absorber is given by:

$$I_0 = 2\pi S_0 \varepsilon_p \left(\frac{1}{4nm_s}\right)^2 \tag{6.10}$$

Combining this with eq 6.3, we find the following expression for the relative pixel uncertainty, or density resolution:

$$\frac{\sigma_f}{f} = \frac{4}{\sqrt{2\pi S_0 \tau \varepsilon_p}} \sqrt{\frac{n^5 m_s}{m_a}} \left\{ \frac{\exp\left[\frac{1}{2} d_i \left(k'\mu_p + \mu_f\right)\right]}{\mu_f d_i} \right\} \tag{6.11}$$

This expression is of fundamental importance, since it relates the main system parameters mentioned above. Thus eq 6.11 may be used to predict the relative density resolution for a given system specification: The necessary photopeak detection efficiencies for our chosen trio of isotopes were calculated in Section 5.3.5; the values are tabulated in Appendix A for grid resolutions n = 2 to 16 and pipe diameter values d from 2.5 to 30 cm. Note that these values apply to the ray spacing used for System 1 and 4 only, see Chapter 4.

Equation 5.83 contains a large number of independent variables, so we will not attempt to undertake a full analysis of its dependence on the various parameters; instead, we will discuss it in general terms, and include some examples where some of the parameters are kept fixed.

First of all, we note that the dependence of the density resolution on the isotope energy used and the pipe diameter is identical to the variation of the raysum uncertainty with the same parameters, which have been discussed thoroughly above. For this reason, we will assume that the isotope ^{137}Cs is used, which is a reasonable compromise with respect to raysum error. Except for very small or very large pipe diameters, the uncertainty levels are very similar for the three isotopes considered, and the n influence on the photon energy dependence of σ_p is relatively slight, since the photopeak efficiency ε_p is not a strong function of n.

However, the expression for the density resolution incorporates the ILST raysum error propagation as well as the effect of detector solid angle, both of which introduces a strong grid resolution dependence. Since the number of rays per view, m_a, is equal to $2n + 1$ for single energy System 1 (see Chapter 4), and approximately 75% of this value for System 4, we see that in general, the relative density resolution is proportional to n^2, if the very slight dependence through the gridsize influence on the photopeak efficiency is ignored. To see the strong n dependence of the density resolution compared to the effect of varying d, we have

plotted (σ_f/f) against the pipe diameter in Figure 6.1, with the grid resolution as a parameter. We have used $m_a = 2n + 1$, $m_s = 7$, $\tau = 1$ s and $S_0 = 100$ mCi, which may be a typical value for the source activity; keep in mind that the total system activity is S_0 multiplied with m_s.

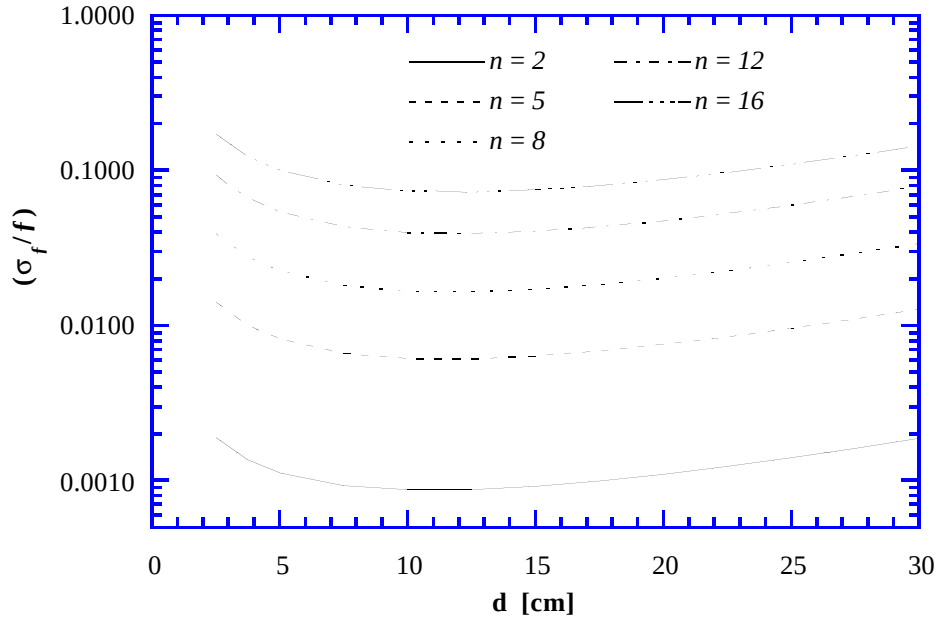

Figure 6.1 Density resolution, or relative pixel density uncertainty, (σ_f/f) versus pipe diameter d with the grid resolution n as parameter, for ^{137}Cs. The source intensity S_0 is 100 mCi, the measurement time τ is 1 s, and the number of sources m_s is 7.

Not surprisingly, the pipe diameter dependence of the density resolution is seen to be very slight compared to the variation with grid size (spatial resolution); for this reason, we will keep the pipe diameter constant and equal to 15 cm for the rest of our discussion of the density resolution. Also, it is seen that quite acceptable density resolution values are possible; for the chosen system parameters, the density resolution is better than 3% for $n = 8$ and 1% for $n = 5$, for a wide range of d.

We will now take a look at the influence of the number of views on the density resolution expression; it is seen that (σ_f/f) is proportional to the square root of m_s. In Figure 6.2, we have plotted the relative pixel density uncertainty, or density resolution, against grid resolution, with the number of views as a parameter: We have used $d = 15$ cm, $\tau = 1$ s and $S_0 = 100$ mCi.

In Chapter 4, we investigated the n and m_s dependence of the reconstruction error R_{abs}, so Figure 6.2 is very interesting because it shows the density resolution dependence on the same parameters: While the pixel error R_{abs} generally decreases with increasing n and m_s, the density uncertainty increases. Thus, low reconstruction error and low density uncertainty due to statistical fluctuations in the measured raysums are conflicting requirements, and a compromise must be made regarding the choice of n and m_s; more on this later.

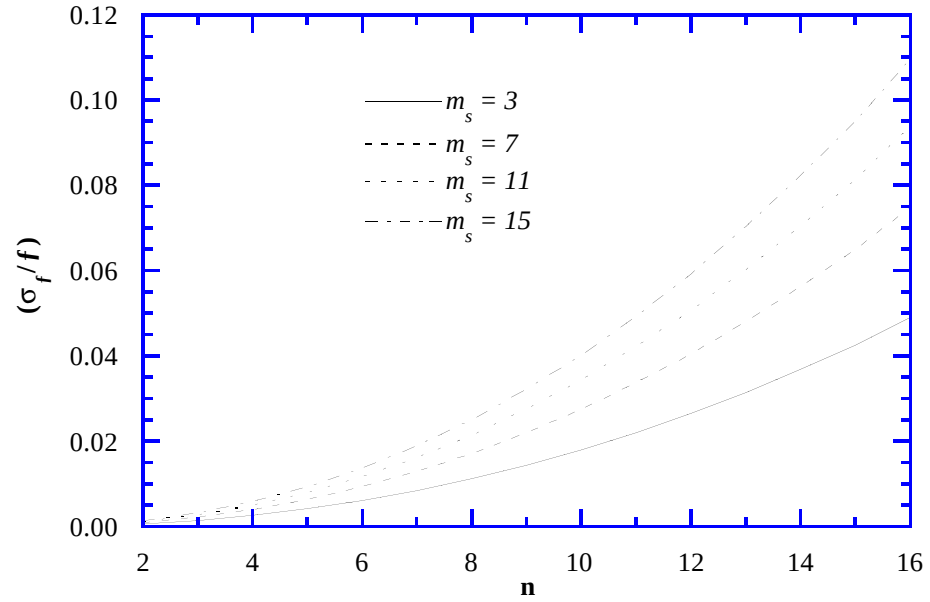

Figure 6.2 Density resolution, or relative pixel density uncertainty, (σ_f/f) versus grid resolution n, with the number of sources, m_s, as parameter, for ^{137}Cs. The source intensity S_0 is 100 mCi, the measurement time τ is 1 s, and the pipe diameter d is 15 cm.

From eq 6.11 we seen that the density uncertainty is inversely proportional to the square root of the measurement time. Since it is interesting to demonstrate the relation between the density, spatial and temporal resolutions, we have plotted (σ_f/f) against n, with τ as a parameter in Figure 6.3. As before, we have used d = 15 cm, m_s = 7 and S_0 = 100 mCi.

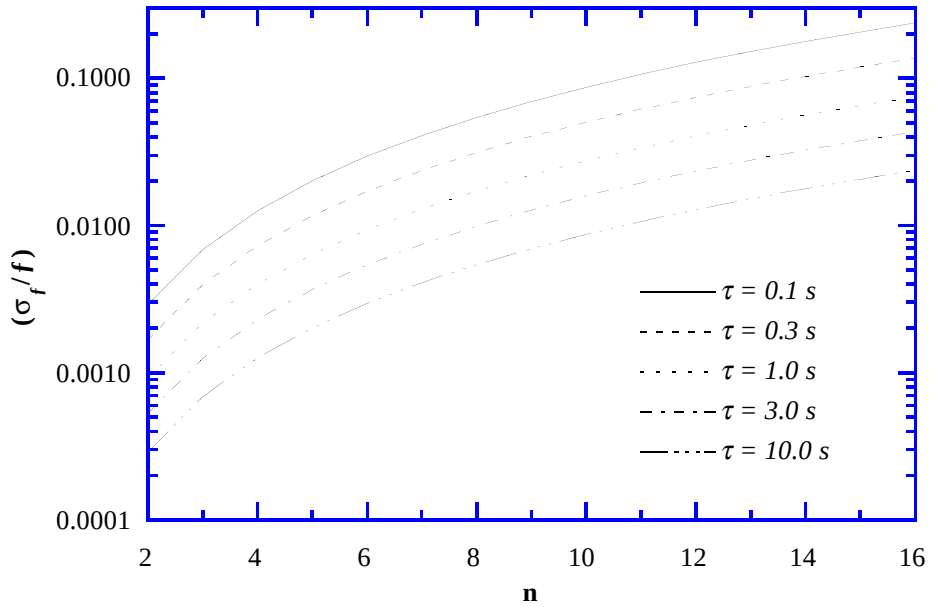

Figure 6.3 Density resolution, or relative pixel density uncertainty, (σ_f/f) versus grid resolution n, with the measurement time τ as a parameter, for ^{137}Cs. The source intensity S_0 is 100 mCi, the number of sources m_s is 7 and the pipe diameter d is 15 cm.

Figure 6.3 shows that quite acceptable values can be achieved for all three resolution parameters; even for measurement times as short as 100 ms, a density uncertainty of 5% is possible at a grid resolution $n = 8$, for the chosen values of d, m_S and S_0. Another implication of this result is that if the dynamic response requirement is relaxed, it is possible to reduce the source activity, while still maintaining good spatial and density resolution.

6.2. Source intensity

We will now take a closer look at the choice of source intensity: By rearranging eq 6.11, S_0 may be expressed as a function of the other system parameters:

$$S_0 = \frac{8}{\pi\tau\varepsilon_p}\left(\frac{\sigma_f}{f}\right)^{-2}\left(\frac{n^5 m_s}{m_a}\right)\left\{\frac{\exp\left[d_i\left(k'\mu_p + \mu_f\right)\right]}{\left(\mu_f d_i\right)^2}\right\} \qquad (6.12)$$

Recalling that m_a is nearly proportional to n, and that the n dependence of ε_p is very slight, we see that the required source intensity is approximately proportional to n^4; also, the source intensity is inversely proportional to the measurement time τ and proportional to the number of sources used, m_S. The latter dependence may seem a little peculiar; however, it is caused by the fact that the solid angle subtended at the source by the detector is inversely proportional to the number of views, see eq 6.9.

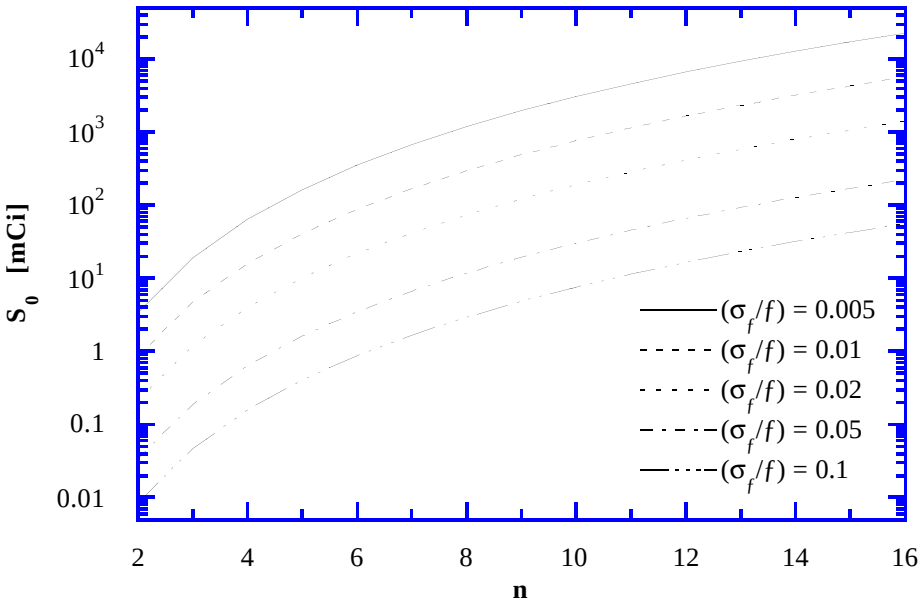

Figure 6.4 Source intensity requirement S_0 versus grid resolution n, with density uncertainty (σ_f/f) as a parameter, for ^{137}Cs. The measurement time τ is 1 s, the pipe diameter d is 15 cm, and the number of sources m_S is 7.

Equation 5.84 is plotted against grid resolution *n* in Figure 6.4, with density resolution (σ_f/f) as a plot parameter; the values of the other parameters are m_s = 7, τ = 1 s and *d* = 15 cm. As one would expect, the required source intensity is quite extreme for high spatial and density resolution; on the other hand, moderate choices of *n* and m_s enable the use of more manageable sources. Note, however, that the total intensity for the whole system is equal to S_0 times m_s.

6.3. Detector countrate

If we consider the maximum total detector countrate $I_{max}\varepsilon_0^{-1}$, we may relate this to the density resolution and the spatial resolution, using eq 6.1 and the expression for the countrate requirement as function of raysum uncertainty level, eq 5.26.

$$\frac{I_{\max}}{\varepsilon_0} = \frac{1}{\varepsilon_0 \tau}\left(\frac{\sigma_f}{f}\right)^{-2}\left(\frac{n^3}{m_a m_s}\right)\left\{\frac{\exp\left(d_i\left[k'\mu_p + \mu_f\right] - kd\mu_p\right)}{\left(\mu_f d_i\right)^2}\right\} \qquad (6.13)$$

The countrate requirement is seen to be it is inversely proportional to the square of (σ_f/f) and roughly proportional to the square of the gridsize *n*. Also, the photon energy (isotope) and pipe diameter dependence is stronger than for the raysum uncertainty based relation eq 6.11; see our earlier discussion of eq 5.26.

Bearing in mind that the countrate gets increasingly pipe diameter and energy sensitive as the grid resolution increases (through photofraction variation), see Figures 5.25 - 5.27, we have chosen the isotope ^{137}Cs for our countrate behaviour examples: In Figure 6.5, we have plotted the total countrate against pipe diameter *d*, with grid resolution *n* as a parameter; the relative density resolution (σ_f/f) is 0.02, the measurement time τ = 1 s and the number of sources m_s is 7.

In Figure 6.6, we have plotted the total countrate $I_{max}\varepsilon_0^{-1}$ as a function of the grid resolution *n*, with the relative density resolution as a parameter, and for 15 cm pipe diameter; as above, 7 sources are used, and the measurement time is one second.

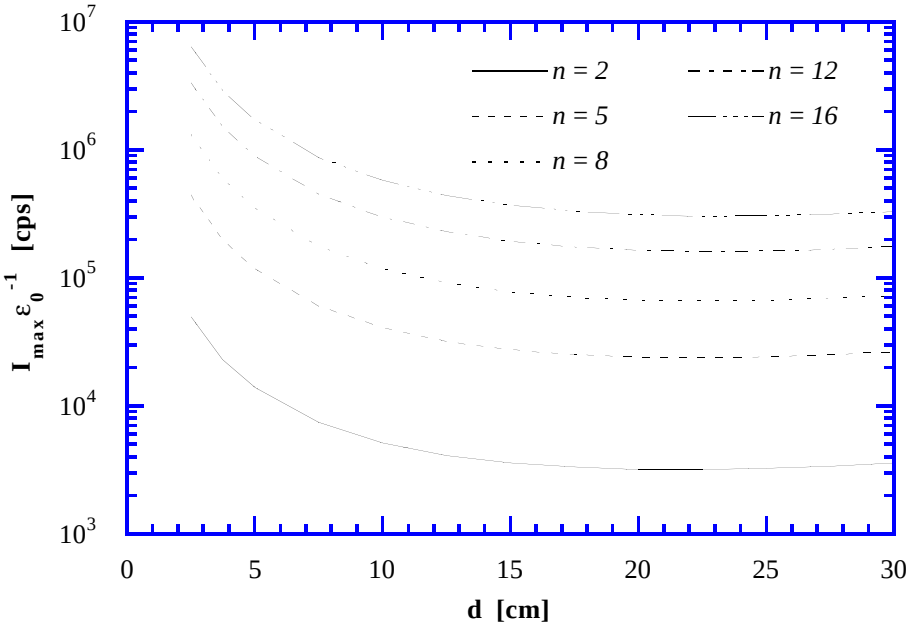

Figure 6.5 The maximum total countrate $I_{max}\varepsilon_0^{-1}$ versus pipe diameter d, and with grid size n as a parameter. The isotope used is ^{137}Cs, the measurement time τ is 1 s, the relative density resolution (σ_f/f) is 0.02, and the number of views m_s is 7.

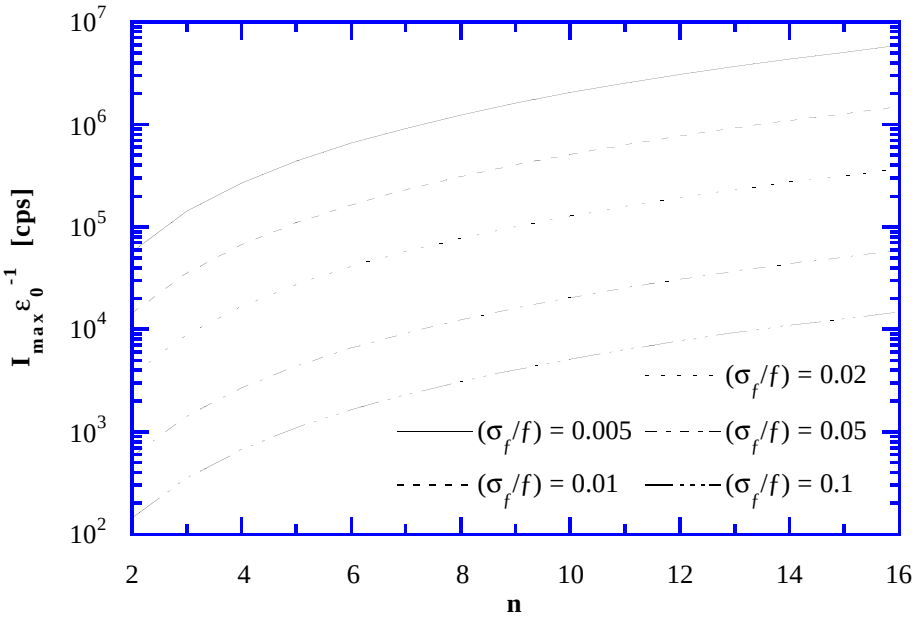

Figure 6.6 The maximum total countrate $I_{max}\varepsilon_0^{-1}$ versus grid size n, and with relative density resolution (σ_f/f) as a parameter. The isotope used is ^{137}Cs, the measurement time τ is 1 s, the pipe diameter d is 15 cm, and the number of views m_s is 7.

Figure 6.5 is a reminder that the isotope should be chosen with care; for small pipe diameters, the countrate requirement rises sharply, and a lower energy isotope should be chosen. Also, the strong grid resolution dependence is clearly shown. Figure 6.6 shows typical countrate levels for a reasonably intelligent choice of isotope for the pipe diameter in question, for different levels of density resolution, or relative pixel density uncertainty; it is seen that high

spatial and density resolution require detectors of extreme countrate capability; however, quite good performance may be achieved with more standard detectors.

The photofraction values used are for BGO detectors, which have a scintillation decay time of 300 ns. In pulse counting mode, the readout circuit time constant would be chosen so that the pulse width would be about a microsecond, and the maximum useful detector countrate would then be limited to a few hundred thousand counts per second. While such a countrate capability is fully adequate for i.e. a relative density uncertainty of 0.01, with a grid resolution *n* equal to 8, and at a measurement time of one second, it is realized that improvement of any of the resolution parameters (density, spatial, temporal) with the others kept constant, requires detectors having better countrate capability.

The countrate problem as such could be solved by using current-mode detector readout; unfortunately, this would also remove the possibility of minimizing raysum measurement errors due to scattered photons by discriminating detected photons by energy. The only possibility left is then to devise an scatter correction algorithm, which adjusts the measured raysums using a preliminary image reconstructed from raw raysum data, and then uses the corrected raysums to generate the final (improved) image. It is clear that a careful study of the photon transport in the imaging system would then be required.

Another option is to select a detector material having shorter scintillation decay time; since good detection efficiency is also required, the only realistic choice is GSO: If the loss of detection efficiency (compared to BGO) is acceptable, GSO offers superior countrate capability, since its decay time is 5 times shorter than that of BGO.

6.4. Overall system performance

In the above analysis, we have taken the density resolution of the imaging system to be equal to the relative uncertainty in the pixel densities caused by the propagation of raysum measurement statistical fluctuation uncertainty into the reconstruction image. We have thus ignored the possible effects of other types of raysum measurement errors, i.e. finite beam width errors and errors caused by detection of scattered radiation: The impact of these errors may be minimized by taking suitable precautions, such as using relatively narrow detectors, and by using collimators and energy discriminating detectors.

Under these assumptions, the relative density resolution is given by eq 6.11: However, the overall pixel density precision of the system is not determined by the above defined density resolution alone, but also by the average reconstruction error per pixel, R_{abs}, defined in Chapter 4. When comparing these contributions, it must be noted that since eq 6.11 have

been derived for the case of (normalized) raysum values p equal to unity, the image pixel densities would be equal to unity as well. This means that the *absolute* (normalized) pixel density resolution is in fact equal to the *relative* value given by eq 6.11, and (σ_f/f) and R_{abs} are directly comparable quantities.

In Chapter 4, several systems (single and dual energy) were analyzed with respect to the reconstruction error; in our above analysis of the density resolution, we have used system parameters corresponding to single energy System 1, and a direct comparison with this system is therefore possible:

In Figure 4.18, the R_{abs} values for System 1 are plotted against grid resolution n and with the number of sources (views) as a parameter, and in Figure 6.2 (σ_f/f) have been plotted in the same way. The striking feature of these two plots is the fact that while the reconstruction error decreases with increasing grid resolution and number of sources, the density uncertainty increases; as we have mentioned before, this means that a compromise must be made when choosing the grid resolution and the number of sources, since low density uncertainty and low reconstruction error are seen to be conflicting requirements.

While the density uncertainty values given in Figure 6.2 are for one specific choice of pipe diameter (15 cm), source intensity (100 mCi) and measurement time (1 s), and thus represent a rather arbitrary chosen example, it is interesting to note that at n = 8 and m_s = 7, the density uncertainty and the pixel error are both approximately equal to 0.016, which is a very satisfactory level of pixel precision.

Unfortunately, System 1 is not practically realizable, since it requires the fans of rays to cover the entire pipe cross section, which cannot be done in practice, since the raysums measured close to the pipe periphery would contain excessive uncertainty, see Figure 5.2. However, single energy System 4 (see Section 4.2.2) is more realistic, since in this case, the fans cover only about 75% of the pipe cross section. In this system, the number of rays per view, m_a, is nominally 75% of the value for System 1, but otherwise the systems are identical. Therefore, the density uncertainty level for System 4 may be found from eq 6.11, simply by correcting for the different m_a value, i.e.by dividing σ_f (= σ_f/f) by the square root of 0.75, which causes an absolute uncertainty increase of about 15%[1].

For our system example above (n = 8 and m_s = 7), this means that the density uncertainty rises to about 0.018; the System 4 reconstruction error (see Figure 4.24), however, is about

---

[1]Also note that the lower number of rays per view cause the required source intensity and maximum detector countrate to be 33% greater for System 4 than for System 1, see eq 6.12 and eq 6.13.

twice this value; recall that the reconstruction error is quite sensitive to a reduction of the fan coverage of the pipe. A closer look at Figures 4.24 and 5.29 reveals that using a higher number of sources would be better in this case; at m_S = 11, the density uncertainty and the average reconstruction error are both approximately equal to 0.024, which is still a quite good pixel precision level: If we consider the case of gas-oil-water flow, the (relative) oil density would normally be about 0.9 compared to the water component, and the system specified above would in fact be able to distinguish between the (separated) oil and water components.

The above discussion applies to the accuracy with which the individual pixel densities may be determined. However, as described in Chapter 4, the void fraction may be estimated using the weighted average of the pixel densities. The reconstruction error contribution to the precision of this estimate, E_{void}, were analyzed in Chapter 4; the contribution from statistical fluctuation measurement error, however, is roughly equal to pixel density uncertainty divided by the square root of the number of pixels. For the System 1 example above, with n = 8 and m_S = 7, the reconstruction void fraction error is 0.006, while the pixel density uncertainty (standard deviation) is about 0.002; for System 4, the figures are similar. It is seen that very precise void fraction measurement is possible, although one would rarely use a complex imaging system as a void fraction gauge.

The system examples discussed above clearly represent realistic systems as far as source intensity requirement and detector countrate are concerned; also, the performance offered with respect to pixel density precision, spatial resolution and dynamic response is clearly quite respectable. For other system requirements, the picture may change considerably, and because of the large number of independent variables in eq 6.11, it is difficult to produce plots covering all possible combinations of system parameters. However, using eq 6.11, the accompanying relations for source intensity (eq 6.12) and detector countrate (eq 6.13), and the reconstruction error graphs presented in Chapter 4, the performance and design parameters of a wide range of single energy flow imaging systems may be established.

7. Summary, conclusion and further work

Summary and conclusion

In this work, we have performed a theoretical analysis of the design and performance of nonrotating, multisource, multidetector γ-ray systems for flow imaging; to provide the groundwork for this analysis, we have described the basics of γ-ray theory and CT mathematics in Chapters 2 and 3, respectively.

The basic geometry relations for these systems have been derived in Chapter 4, where we also have analyzed the image errors associated with the reconstruction algorithm, with the grid resolution and with the raysum measurement strategy. For this purpose, we have developed the simulator TOM1, which has turned out to be an indispensable tool in the analysis process. The conclusion of the measurement strategy analysis is that using a single energy system is clearly the better choice; for dual (or triple) energy systems, the advantage gained by the increased number of measured raysums, is lost because of the nonideal distribution of the rays across the pipe interior. For single energy systems, the use of a higher reconstruction grid resolution and a higher number of sources (views) generally improves the precision of the image.

After having described how the actual raysum measurement is done in practice, we have done a survey of the factors contributing to the raysum measurement uncertainty (Chapter 5); these are finite beam width effects, detection of scattered radiation, and statistical fluctuations in the number of detected photons. We have investigated the latter contribution thoroughly, and it is shown how it influences the choice of isotope and detector system for a given pipe dimension; to minimize the uncertainty, high energy isotopes (such as ^{22}Na) should be chosen for large pipe dimensions, while lower energy isotopes (such as ^{137}Cs or ^{133}Ba) are used for smaller pipes. It also turns out that the detector countrate capability requirement is minimized in this way.

In any event, the detector system should have the best possible detection efficiency; this dictates the use of high-Z high-density scintillation detectors such as BGO. In order to be able to compute the actual levels of raysum uncertainty for a given system, and the detector countrate capability required, it is necessary to know the photopeak detection efficiency of the detectors used. For this reason, we have developed the Monte Carlo simulation program called DSIM, which can compute detection efficiencies for NaI and BGO detectors of various shapes, and for different source geometries. DSIM have not been verified directly against

experimental data; however, for the photon energy range of interest to us, its results agree nicely with those of the state-of-the art radiation transport simulator EGS, and we feel confident that DSIM behaves correctly.

Using DSIM, we have calculated the necessary BGO detection efficiency data required for the analysis of raysum uncertainty and detector countrate requirement associated with the single energy systems 1 and 4 described in Chapter 4, and raysum uncertainty levels and detector countrate requirements have been calculated for these systems.

However, our main concern is not the raysum uncertainty in itself, but rather the pixel density uncertainty it causes by propagating through the reconstruction algorithm: In Chapter 6, we have developed an expression relating the pixel density uncertainty to the main system parameters; these are spatial resolution (reconstruction grid resolution), measurement time, pipe diameter, photon energy (isotope), and the number and intensity of the sources used. It turns out that very acceptable levels of density uncertainty may be achieved with our system, even when using a short measurement time and reasonable spatial resolution.

Finally, we consider the overall precision of the reconstructed image pixel densities (see Section 6.4); this is determined by the level of pixel density uncertainty due to raysum uncertainty propagation, *and* by the reconstruction error discussed in Chapter 4. We find that the possible performance of our imaging system is very acceptable: For the System 4 example considered in the previous chapter, the average reconstruction error for a reconstruction grid of 8×8 pixels is about 3.5% of full scale, and the pixel density uncertainty is about 1.8% of full scale, for a 15 cm diameter pipe, using a measurement time of one second and seven 100 mCi ^{137}Cs sources.

We may then conclude that the nonrotating, multisource, multidetector concept analyzed in this work, represents an unique possibility for designing a high-quality flow imaging system.

Further work

Our reconstruction error analyzer, TOM1, only handles relatively simple two-phase regime models, so it is of great interest to modify this program to include the possibility of simulating more complex regimes, including three-component fluid-fluid-gas regimes; this would enable us to obtain a better knowledge of the general reconstruction error level. Also, simply by including the computation of the standard deviations of the reconstruction error estimators, it is possible to determine if there exist systematic differences between the error levels for different classes of regimes, as the simulation results for the “optimal” system may indicate, see Figures 4.16 and 4.17.

Since the amount of available raysum data is low for the systems we have studied, it may also be worthwhile to consider other types of reconstruction algorithms, or modifications of existing ones. For example, one could try to design algorithms which utilize the fact that many flow regimes exhibit strong "piecewise" homogeneity.

In the present work, we have identified several sources of raysum measurement error; however, only the statistical fluctuation errors have been analyzed thoroughly, and then only for one detector type (BGO), one pipe material, and for a limited range of photon energies (isotopes). A simple but very interesting extension to this work would be to consider the use of GSO detectors, which offer improved countrate capability compared to BGO.

It has been established that the finite beam width error is regime dependent, so to study the impact of this effect, one would have to use a technique similar to that used for analyzing the reconstruction error: By using a model which incorporates finite beam width effects in the computation of raysums, and then feeding these raysums to a reconstruction algorithm, the effect on the reconstructed image may be analyzed; the resulting images are compared with ideal images and images reconstructed from ideal raysum values, see Chapter 4.

The scattered radiation raysum errors may be investigated in the same way: In this case, a full photon transport model is required for the entire imaging system, including the detectors, since the detector response function and energy resolution influence the magnitude of scattered radiation errors. For this purpose, Monte Carlo techniques would be used; a model incorporating charged particle transport will probably be required for accurate detector response function modelling. The resulting raysum errors and their impact on image quality are then analyzed in the same way as the finite beam width errors.

As mentioned before, the effect of regime dependent raysum measurement errors could be reduced by adaptive compensation algorithms; such procedures may be devised from the results of the analysis of finite beam width and scattered photon raysum measurement errors.

For model verification purposes, and because detector energy resolution and countrate capability are important parameters in the system analysis, a high stability detector test system should be designed, and suitable detector types should be tested and optimized with respect to countrate capability and energy resolution. This would provide the basis for selection of a suitable detector for the imaging system.

Finally, based on the results of the error analysis and detector development described above, a prototype system should be built, and tested statically and dynamically.

References

[1] Plaskowski, A., Beck, M.S. , Krawaczynski, J.S.:
"Flow imaging for multi-component flow measurement"
Trans. Inst. Meas. Control. **9** (1987) 108-112.

[2] Huang, S.M., Plaskowski, A.B., Xie, C.G., Beck, M.S.:
"Tomographic imaging of two-component flow using capacitance sensors"
J. Phys. E: Sci. Instrum. **22** (1989) 173-177.

[3] Isaksen, Ø.:
"Avbildning av tokomponent rørstrøm ved hjelp av kapasitanssensorer"
Thesis for the Cand. Scient. degree, University of Bergen (1989).

[4] De Vouno, A.C., Schlosser, P.A., Kulacki, F.A., Munshi, P.:
"Design of an isotopic CT scanner for two phase flow measurements"
IEEE Trans. Nucl. Sci. **NS-27** (1980) 814-820.

[5] Schlosser, P.A., De Vouno, A.C., Kulacki, F.A., Munshi, P.:
"Analysis of high-speed CT scanners for non-medical applications"
IEEE Trans. Nucl. Sci. **NS-27** (1980) 788-794.

[6] Olatunbosun, A., Frith, B.:
"Two-phase flow imaging using gamma scattering/transmission technique"
Int. conf. on flow measurement in the mid-80's, vol. 1 (1986).

[7] Hellesø, O.G.:
"Attgjeving av to-fase røyrstraum med gamma-tomografi"
Thesis for the Cand. Scient. degree, University of Bergen (1989).

[8] Mladjenovic, M.:
"Radioisotope and radiation physics"
Academic Press (1973).

[9] Hubbell, J.H.:
"Photon Cross Sections, Attenuation Coefficients and Energy Absorption Coefficients
From 10 keV to 100 GeV"
NSRDS-NBS 29 (1969).

[10] Fano, U., Spencer, L.V., Berger, M.J.:
"Penetration and Diffusion of X Rays" in "Encyclopedia of Physics", Vol. XXXVIII/2
Springer-Verlag (1959).

[11] Evans, R.D.:
"Compton Effect" in "Encyclopedia of Physics", Vol. XXXIV
Springer-Verlag (1958).

[12] Storm, E., Israel, H.I.:
"Photon Cross Sections from 1 keV to 100 MeV for Elements $Z = 1$ to $Z = 100$"
Nuclear Data Tables **A7** (1970) 565-681.

[13] Klein, O,. Nishina, Y.
Z. Physik **52** (1929) 853-868.

[14] Hubbell, J.H., Veigele, W.J., Briggs, E.A.,Brown, R.T.,
Cromer, D.T., Howerton, R.J.:
J. Phys. Chem. Ref. Data **4** (1975) 471-538.

[15] Press, W.H., Flannery, B.P., Teukolsky, S.A., Vetterling, W.T.:
"Numerical Recipies in C"
Cambridge University Press (1988).

[16] Von Neumann, J.:
"Various techniques used in connection with random digits"
NBS Applied Mathematics Series **12** (1951) 36-38.

[17] Hammersley, J.M., Handscomb, D.C.:
"Monte Carlo Methods"
Methuen (1964).

[18] Birks, J.B.:
"The Theory and Practice of Scintillation Counting"
Pergamon Press (1964).

[19] Canberra Nuclear Products Group Catalog, Edition 8.

[20] Brooks, R.A., DiChiro, G.
"Principles of Computer Assisted Tomography (CAT) in Radiographic and
Radioisotopic Imaging"
Phys. Med. Biol. **21** (1976) 689-732.

[21] Natterer, F.:
"The Mathematics of Computerized Tomography"
Wiley (1986).

[22] Goitein, M.:
"Three-dimensional density reconstruction from a series of two-dimensional projections"
Nuclear Instruments and Methods **101** (1972) 509-518.

[23] Herman, G.T.:
"Image reconstruction from projections, the fundamentals of computerized tomography"
Academic Press (1980).

[24] Rogers, D.W.O.:
"More realistic Monte Carlo calculations of photon detector response functions"
Nuclear Instruments and Methods **199** (1982) 531-548.

[25] Johansen, G.A.:
"Development and analysis of silicon based detectors for low energy nuclear radiation"
Thesis for the Dr. Scient. degree, University of Bergen (1990).

[26] Harshaw Radiation Detectors, GE 102 (1984).

[27] Hitatchi Scintillation Single Crystals, AS-E001, 3068.

[28] Holl, I., Lorenz, E., Mageras, G.:
"A measurement of the light yield of common inorganic scintillators"
IEEE Trans. Nucl. Sci. **NS-35** No.1 (1988) 105-109.

[29] Sakai, E.:
"Recent measurements on scintillator-photodetector systems"
IEEE Trans. Nucl. Sci. **NS-34** No.1 (1987) 418-422.

[30] Knuth, D.E.:
"Seminumerical Algorithms" in "The Art of Computer Programming" (2nd ed.),
Addison-Wesley (1981).

[31] Nelson, W.R., Hirayama, H., Rogers, D.W.O.:
SLAC-Report 265,
Stanford Linear Accelerator Center, Stanford University (1985).

Appendix A

This appendix contains the DSIM detection efficiency simulation results: Tables A.1, A.2 and A.3 contain DSIM and EGS data for bare, uncased NaI and BGO detectors; the latter are taken from [24]. The calculated BGO photopeak efficiencies, used in the raysum uncertainty and detector countrate analysis in Chapter 5, are listed in Tables A.4, A.5 and A.6, for E_γ = 356 keV (^{133}Ba), 661.6 keV (^{137}Cs) and 1.275 MeV (^{22}Na), respectively; see Section 5.3 for further explanation.

Table A.1 EGS and DSIM photofractions for bare 3" × 3" NaI detectors, for an isotropic source at 10 cm distance, and for photon energies in the range from 320 keV to 10 MeV. EGS and DSIM statistical uncertainties quoted in brackets are standard deviation estimates in last digit of photofraction value.

E_γ [MeV]	ε_0		
	EGS: No charged particle transport	**EGS:** Charged particle transport	**DSIM:** No charged particle transport
0.320	–	0.829(7)	0.843(5)
0.662	0.575(3)	0.576(9)	0.570(4)
1.28	0.395(3)	0.381(5)	0.392(8)
2.75	0.266(5)	0.232(7)	0.265(7)
6.00	0.174(5)	0.108(5)	0.172(6)
8.00	0.159(4)	0.074(3)	0.153(5)
10.0	0.147(6)	0.053(1)	0.151(5)

Table A.2 EGS and DSIM photofractions and interaction ratios for bare 3" × 3" NaI detectors, for a broad parallel beam normally incident on the detector, and for the photon energies in the range from 300 keV to 10 MeV. EGS model includes charged particle transport, whereas DSIM model does not. EGS and DSIM statistical uncertainties quoted in brackets are standard deviation estimates in last digit of calculated values.

E_γ[MeV]	ε_0		ε_{tot}	
	EGS	**DSIM**	**EGS**	**DSIM**
0.3	0.879(4)	0.884(4)	0.989(5)	0.987(1)
0.5	0.700(3)	0.698(5)	0.926(6)	0.923(2)
0.8	0.519(5)	0.520(4)	0.832(6)	0.838(3)
1.0	0.459(6)	0.461(4)	0.805(5)	0.801(4)
1.5	0.358(2)	0.367(5)	0.725(2)	0.721(6)
2.0	0.304(6)	0.325(6)	0.687(3)	0.690(5)
3.0	0.218(6)	0.258(3)	0.659(6)	0.646(5)
4.0	0.168(5)	0.218(3)	0.626(7)	0.632(6)
5.0	0.138(4)	0.204(5)	0.613(4)	0.625(5)
6.0	0.114(3)	0.185(4)	0.616(6)	0.621(6)
8.0	0.070(5)	0.159(6)	0.626(6)	0.626(5)
10.0	0.056(2)	0.144(4)	0.642(4)	0.639(4)

Table A.3 EGS and DSIM photopeak detection efficiencies for bare 3" × 3" NaI and BGO detectors, for an isotropic source at 10 cm distance, and for photon energies in the range from 300 keV to 10 MeV. EGS values taken from Figure 13 in [24], the quoted uncertainties are reading uncertainties only. DSIM statistical uncertainties quoted in brackets are standard deviation estimates in last digit of calculated values. EGS model includes charged particle transport, whereas DSIM model does not.

E_γ[MeV]	ε_p			
	NaI		**BGO**	
	EGS	**DSIM**	**EGS**	**DSIM**
0.3	0.67±0.01	0.676(2)	0.90±0.02	0.903(3)
0.4	0.53±0.01	0.541(6)	0.85±0.02	0.845(3)
0.5	0.44±0.01	0.453(5)	0.80±0.02	0.790(4)
0.6	0.37±0.01	0.386(6)	0.74±0.02	0.736(4)
0.8	0.29±0.01	0.297(3)	0.66±0.01	0.659(6)
1.0	0.24±0.01	0.247(4)	0.60±0.01	0.597(7)
1.5	0.165±0.005	0.181(3)	0.48±0.01	0.496(4)
2.0	0.135±0.005	0.140(4)	0.41±0.01	0.425(4)
3.0	0.085±0.002	0.103(4)	0.33±0.01	0.366(6)
4.0	0.064±0.002	0.087(1)	0.29±0.01	0.322(6)
5.0	0.053±0.001	0.078(3)	0.27±0.01	0.326(7)
6.0	0.045±0.001	0.072(2)	0.25±0.01	0.309(5)
8.0	0.031±0.001	0.063(2)	0.210±0.005	0.313(6)
10.0	0.0220±0.0005	0.060(3)	0.175±0.005	0.320(4)

Table A.4 DSIM calculated photopeak efficiencies for BGO detectors at 356 keV photon energy (^{133}Ba), for gridsizes ranging from 2 to 16 and pipe diameters ranging from 2.5 to 30 cm; see Section 5.3 for further explanation. Statistical uncertainties are below 1% in all cases, see Section 5.3.5.

(n, d)	ε_p												
	2.50	3.75	5.00	7.50	10.0	12.5	15.0	17.5	20.0	22.5	25.0	27.5	30.0
2	0.866	0.887	0.894	0.904	0.910	0.913	0.915	0.916	0.916	0.919	0.919	0.919	0.919
3	0.841	0.868	0.883	0.897	0.901	0.904	0.910	0.910	0.912	0.913	0.916	0.916	0.916
4	0.823	0.852	0.867	0.885	0.893	0.901	0.905	0.908	0.909	0.913	0.912	0.913	0.914
5	0.806	0.837	0.856	0.876	0.888	0.896	0.900	0.903	0.907	0.908	0.910	0.909	0.912
6	0.790	0.822	0.842	0.868	0.883	0.890	0.895	0.899	0.903	0.905	0.907	0.908	0.909
7	0.774	0.810	0.833	0.857	0.873	0.884	0.890	0.894	0.898	0.901	0.902	0.907	0.907
8	0.764	0.798	0.821	0.850	0.866	0.879	0.886	0.891	0.895	0.900	0.901	0.901	0.905
9	0.757	0.789	0.814	0.843	0.863	0.874	0.880	0.886	0.891	0.895	0.898	0.900	0.901
10	0.745	0.779	0.807	0.836	0.855	0.867	0.877	0.883	0.888	0.890	0.895	0.897	0.900
11	0.734	0.770	0.797	0.831	0.851	0.862	0.873	0.878	0.883	0.890	0.893	0.897	0.897
12	0.730	0.765	0.789	0.822	0.843	0.857	0.865	0.877	0.880	0.884	0.891	0.892	0.895
13	0.722	0.755	0.782	0.817	0.839	0.854	0.863	0.871	0.877	0.882	0.885	0.890	0.891
14	0.715	0.752	0.775	0.811	0.835	0.848	0.857	0.868	0.874	0.879	0.884	0.887	0.890
15	0.713	0.747	0.768	0.806	0.829	0.842	0.855	0.864	0.871	0.877	0.882	0.884	0.890
16	0.710	0.741	0.764	0.800	0.824	0.841	0.850	0.859	0.867	0.872	0.879	0.883	0.886

Table A.5 DSIM calculated photopeak efficiencies for BGO detectors at 661.6 keV photon energy (^{137}Cs), for gridsizes ranging from 2 to 16 and pipe diameters ranging from 2.5 to 30 cm; see Section 5.3 for further explanation. Statistical uncertainties are below 2% in all cases, see Section 5.3.5.

(n, d)	ε_p												
	2.50	3.75	5.00	7.50	10.0	12.5	15.0	17.5	20.0	22.5	25.0	27.5	30.0
2	0.687	0.741	0.775	0.814	0.834	0.848	0.854	0.859	0.865	0.870	0.872	0.873	0.877
3	0.627	0.685	0.727	0.776	0.803	0.822	0.834	0.842	0.851	0.856	0.856	0.861	0.866
4	0.580	0.643	0.689	0.744	0.776	0.799	0.812	0.825	0.833	0.842	0.846	0.852	0.854
5	0.546	0.608	0.650	0.712	0.750	0.778	0.794	0.807	0.817	0.828	0.833	0.840	0.845
6	0.521	0.582	0.625	0.688	0.725	0.755	0.777	0.795	0.806	0.814	0.822	0.828	0.833
7	0.501	0.556	0.599	0.665	0.704	0.736	0.760	0.778	0.791	0.799	0.808	0.819	0.823
8	0.485	0.537	0.581	0.643	0.689	0.719	0.744	0.763	0.775	0.789	0.797	0.806	0.816
9	0.467	0.522	0.564	0.626	0.670	0.704	0.726	0.746	0.764	0.779	0.787	0.797	0.803
10	0.460	0.506	0.547	0.608	0.654	0.689	0.714	0.733	0.752	0.765	0.779	0.786	0.794
11	0.451	0.498	0.532	0.595	0.637	0.675	0.698	0.720	0.741	0.754	0.767	0.777	0.784
12	0.440	0.487	0.520	0.581	0.625	0.657	0.686	0.708	0.730	0.745	0.758	0.767	0.776
13	0.430	0.477	0.513	0.568	0.613	0.646	0.674	0.698	0.719	0.736	0.747	0.757	0.765
14	0.425	0.469	0.500	0.553	0.602	0.638	0.662	0.687	0.707	0.724	0.738	0.750	0.761
15	0.419	0.460	0.494	0.546	0.590	0.624	0.656	0.678	0.697	0.715	0.731	0.740	0.752
16	0.413	0.453	0.485	0.539	0.577	0.615	0.641	0.667	0.689	0.704	0.717	0.732	0.743

Table A.6 DSIM calculated photopeak efficiencies for BGO detectors at 1.275 MeV photon energy (^{22}Na), for gridsizes ranging from 2 to 16 and pipe diameters ranging from 2.5 to 30 cm; see Section 5.3 for further explanation. Statistical uncertainties are below 2% in all cases, see Section 5.3.5.

(n, d)	ε_p												
	2.50	3.75	5.00	7.50	10.0	12.5	15.0	17.5	20.0	22.5	25.0	27.5	30.0
2	0.484	0.565	0.618	0.685	0.727	0.753	0.769	0.785	0.795	0.801	0.806	0.813	0.817
3	0.406	0.482	0.541	0.619	0.668	0.704	0.727	0.747	0.760	0.771	0.779	0.787	0.793
4	0.360	0.429	0.483	0.561	0.619	0.657	0.689	0.711	0.724	0.743	0.751	0.761	0.772
5	0.326	0.390	0.437	0.520	0.575	0.619	0.648	0.672	0.696	0.713	0.725	0.739	0.749
6	0.301	0.359	0.408	0.482	0.540	0.584	0.617	0.643	0.666	0.686	0.702	0.715	0.727
7	0.279	0.335	0.379	0.453	0.512	0.553	0.589	0.614	0.639	0.660	0.679	0.694	0.708
8	0.270	0.317	0.358	0.428	0.480	0.528	0.565	0.593	0.618	0.639	0.659	0.676	0.685
9	0.256	0.300	0.340	0.405	0.460	0.501	0.539	0.571	0.597	0.618	0.636	0.655	0.669
10	0.246	0.288	0.325	0.388	0.440	0.483	0.521	0.546	0.573	0.595	0.618	0.635	0.652
11	0.237	0.277	0.313	0.370	0.423	0.464	0.500	0.530	0.555	0.577	0.600	0.620	0.634
12	0.230	0.269	0.303	0.361	0.404	0.446	0.480	0.513	0.543	0.563	0.583	0.600	0.617
13	0.223	0.261	0.291	0.347	0.394	0.432	0.467	0.499	0.524	0.547	0.566	0.586	0.603
14	0.218	0.252	0.283	0.337	0.380	0.420	0.452	0.483	0.508	0.533	0.552	0.571	0.587
15	0.217	0.249	0.274	0.328	0.370	0.405	0.439	0.470	0.496	0.517	0.540	0.558	0.574
16	0.209	0.241	0.268	0.316	0.358	0.396	0.427	0.457	0.483	0.506	0.525	0.545	0.565